Report No. DTRS56-96-C-0010
Subtask 1.1 Report

VARIATION OF MAGNETIC PROPERTIES IN PIPELINE STEELS

J. B. Nestleroth
Battelle
505 King Avenue
Columbus, Ohio 43201-2693

A. E. Crouch
Southwest Research Institute
6220 Culebra Road
San Antonio, Texas 78228-0510

MARCH 1998

INTERIM REPORT

Contract No. DTRS56-96-C-0010

Prepared for

U.S. Department of Transportation
Office of Pipeline Safety
400 Seventh Street SW
Washington, DC 20590

50272-101

REPORT DOCUMENTATION PAGE	1. REPORT NO. DTRS56-96-C-0010	2.	PB99-138364

4. Title and Subtitle

Variation of Magnetic Properties in Pipeline Steels
(Subtask 1.1 Report)

5. Report Date
March 1998

6.

7. Authors

J. B. Nestleroth and A. E. Crouch

8. Performing Organization Rept. No.

9. Performing Organization Name and Address

Battelle
505 King Avenue
Columbus, Ohio 43201-2693

Southwest Research Institute
6220 Culebra Road
San Antonio, Texas 78228-0510

10. Project/Task/Work Unit No.
G002993-11

11. Contr. (C) or Grant (G) No.
(C) DTRS56-96-C-0010
(G)

12. Sponsoring Organization Name and Address

U. S. Department of Transportation
Office of Pipeline Safety
400 Seventh Street SW
Washington, DC 20590

13. Type of Report & Period Covered
Interim
Jun 1996–Mar 1998

14.

15. Supplementary Notes

16. Abstract (Limit 200 Words)

This report documents the findings of an evaluation of the magnetic, mechanical, chemical, and metallurgical properties of 36 pipeline materials that were removed from gas-transmission service. There were three objectives of the evaluation. The first was to determine whether there were clear correlations between magnetic properties and mechanical properties. The second was to determine whether magnetic properties change significantly with the application of stresses and strains. The last was to assemble a database of both magnetic and mechanical properties for future developmental activities. Each of these goals was met.

The results of this evaluation show that there is no clear correlation between magnetic properties and commonly measured mechanical properties. So, there is no easy way to predict magnetic properties for commonly known mechanical properties. In order to detect mechanical damage, the change in magnetic properties at the damage must be outside the natural variability of typical magnetic properties. The changes in magnetic properties due to compressive stresses and strains are large enough to fall outside the typical scatter band of properties. So, detecting compressive damage may be possible without measuring the magnetic properties of a pipeline steel. The same cannot be said of tensile stresses and strains.

17. Document Analysis a. Descriptors

b. Identifiers/Open-Ended Terms

Pipe, Pipelines, Metal, Magnetic flux leakage, In-line inspection, Mechanical damage

c. COSATI Field/Group

18. Availability Statement	19. Security Class (This Report)	21. No. of Pages
Availability Unlimited	Unclassified	122
	20. Security Class (This Page) Unclassified	22. Price

(See ANSI-Z39.18)

OPTIONAL FORM 272 (4-77)
(Formerly NTIS-35)
Department of Commerce

NOTICE

This document is disseminated under the sponsorship of the Department of Transportation in the interest of information exchange. The United Sates Government assumes no liability for the contents or use thereof.

This report is a work prepared for the United States Government by Battelle. In no event shall either the United States Government or Battelle have any responsibility or liability for any consequences of any use, misuse, inability to use, or reliance on the information contained herein, nor does either warrant or otherwise represent in any way the accuracy, adequacy, efficacy, or applicability of the contents hereof.

CONTENTS

Page

Introduction and Summary 1
Background 1

Measurement Methods 3

Mechanical and Chemical Properties 3
Magnetic Properties Under No-Load Conditions 7
Magnetic Properties Under Compression and Tension 9
Variation of Magnetic Properties Within a Pipe 11

Analysis of Properties 13

Variation of Properties 13
Correlation of Properties 14
Changes in Magnetic Properties with Stress and Strain 15
Comparison of Single-Pipe Variations With Variations Between Pipes 17

Conclusion 18
References 19

Appendix A Magnetic, Chemical, Mechanical, and Metallurgical Properties of 36 Material Samples A-1

Appendix B Results of Compression and Tension Testing of 12 Materials B-1

TABLES

Table 1. Mechanical, metallurgical, magnetic, and chemical properties of 36 gas transmission pipes pulled from service 5

Table 2. Summary of magnetic property changes 9

Table 3. Sample set for compression and tension tests 10

Table 4. Correlation coefficients for each variable against all others 16

Table 5. Magnetic property changes for pipeline steels 18

FIGURES

		Page
Figure 1.	The initial permeability and hysteresis magnetization curves	21
Figure 2.	Magnetic property measurement method based on American Society for Testing and Materials (ASTM) Standard A 773-80	21
Figure 3.	Typical initial permeability curves for Samples 9, 11, 14, 21, 32, and 46	22
Figure 4.	Initial permeability curves for all samples	23
Figure 5.	Full hysteresis loops for all samples	23
Figure 6.	"Dogbone" sample for tensile plastic deformation experiments	24
Figure 7.	The compression test sample	24
Figure 8.	The sample mounted inside restraining collars	25
Figure 9.	Experimental setup for B-H curve measurements under compression	25
Figure 10.	Experimental setup for B-H curve measurements under tension	26
Figure 11.	Apparatus for measuring applied magnetic field H and flux density B without removing samples from the pipe	26
Figure 12.	Battelle's strongback four-point bending apparatus	26
Figure 13.	The magnetization curves for a no-load condition, tension, and compression for all 8 measurement locations on Specimen 31	27
Figure 14.	Radar plots of permeability for Sample 31	28
Figure 15.	Radar plots of permeability for Sample 08	28
Figure 16.	Radar plots of coercivity for Sample 31	29
Figure 17.	Radar plots of coercivity for Sample 08	29
Figure 18.	Distribution of yield strength	30
Figure 19.	Distribution of ultimate strength	30

FIGURES
(Continued)

		Page
Figure 20.	Distribution of elongation	30
Figure 21.	Distribution of Charpy energy	31
Figure 22.	Distribution of hardness	31
Figure 23.	Distribution of grain size	31
Figure 24.	Distribution of carbon	32
Figure 25.	Distribution of manganese	32
Figure 26.	Distribution of phosphorus	32
Figure 27.	Distribution of sulfur	33
Figure 28.	Distribution of silicon	33
Figure 29.	Distribution of aluminum	33
Figure 30.	Distribution of vanadium	34
Figure 31.	Distribution of columbium (also known as niobium)	34
Figure 32.	Distribution of remanence	35
Figure 33.	Distribution of coercivity	35
Figure 34.	Distribution of permeability	35
Figure 35.	Scatter diagrams for ultimate tensile strength and material hardness, hardness and yield strength, and yield strength and ultimate tensile strength	36
Figure 36.	Scatter diagrams for coercive force and hardness, ultimate strength, and yield strength	37
Figure 37.	Scatter diagrams for permeability and Charpy energy, yield strength, ultimate strength, elongation, hardness, carbon, manganese, and columbium	38
Figure 38.	Typical B-H curves for elastic compressive and tensile stresses	41
Figure 39.	Typical B-H curves for compressive and tensile stresses and permanent plastic strains	41

Variation of Magnetic Properties in Pipeline Steels

Introduction and Summary

This report documents the findings of an evaluation of the magnetic, mechanical, chemical, and metallurgical properties of 36 gas transmission pipe samples pulled from service. This evaluation was motivated by a need to understand the variability of the magnetic properties of pipeline steels in order to develop and improve magnetic flux leakage (MFL) inspection techniques for mechanical damage defects.

This evaluation had three goals. The first was to determine whether there were clear correlations between magnetic properties and mechanical properties. The second was to determine whether magnetic properties change significantly with the application of tensile or compressive stresses and strains. The final goal was to assemble a database of both magnetic and mechanical properties for future developmental activities. Each of these goals was met.

While most MFL-based corrosion inspections avoid the effects of magnetic property variations through an increased magnetization level, the detection and assessment of mechanical damage defects requires the measurement of more subtle magnetic variations at lower magnetization levels. Because mechanical damage induces stress and plastic deformation, magnetic properties of 12 samples were examined under tensile and compressive loading, with up to 8 percent plastic deformation. To examine the magnetic properties on a full section of pipe, magnetization curves were measured around the circumference of two pipes under tensile and compressive loading. The magnetic, chemical, and mechanical properties of each sample are presented in Appendix A. The remainder of this report describes the measurement and analysis of these properties.

This evaluation reached a number of conclusions:

- There is no clear correlation between magnetic properties and commonly measured mechanical properties. So, the change in magnetic properties due to mechanical damage must be outside the range of typical magnetic properties in order for the damage to be detected. Also, when assessment of mechanical damage defect signals requires the magnetic properties, these must be measured,

because they cannot easily be recreated using the more commonly known mechanical properties.

- The changes in magnetic properties due to compressive stresses are large enough to fall outside the typical scatter band of properties. So, detecting compressive stresses and strains may be possible without measuring the magnetic properties of a pipeline steel.
- The same cannot be said of tensile stresses. Detecting tensile stresses and strains would require measurements of magnetic properties, because tension causes more subtle signal changes, and there is no clear method of estimating magnetic properties from other commonly known properties.

Background

MFL is the most commonly used pipeline in-line inspection method for the detection of corrosion [1]. The potential for using MFL to inspect for mechanical damage defects has been demonstrated [2]. MFL locates pipeline defects by applying a strong magnetic field in the pipe wall, and then sensing a local change in this applied field near the pipe wall.

The flux leakage response of pipeline anomalies depends on many factors, including the magnetic properties of the pipeline steel and the geometry of the defects. As an example of this process, corrosion converts the ferromagnetic pipe steel into non-ferromagnetic iron oxide. An MFL inspection tool detects a magnetic property change at corrosion defects because the local ability of the pipe to carry magnetic flux is reduced. Detecting mechanical damage works on the same principle, though the change is more subtle. For mechanical damage defects, the flux leakage is due to a change in magnetic properties induced by stress and plastic deformation rather than removed metal. These changes are much smaller and dependent on the steel composition and fabrication. When MFL is used to detect corrosion, high magnetization levels are applied to minimize the effects of the variation in a steel's magnetic properties, thus producing signals from metal loss only. Prior work shows that to detect mechanical damage using MFL, lower magnetization levels must be considered, which requires that the magnetic property variations be addressed [2].

Pipeline steels have evolved from lower strength steels with yield stresses of 25 ksi to modern steels with yield stresses exceeding 80 ksi. To attain this threefold improvement, mechanical performance, chemical composition, and grain structure have been changed. The changes that enhance the mechanical performance also affect the magnetic properties. The general influence of composition and stress on magnetic properties is documented in the classic text *Ferromagnetism* by Bozorth [3]. The recent literature describes many detailed investigations into the effect of stress and composition on modern steels [4–5], including pipeline materials [6]. The effect of stress on MFL signals has also been investigated [4, 7]. The work reported here was designed to complement the prior research by providing relevant magnetic, mechanical, chemical, and metallurgical analyses from a large sample set.

Measurement Methods

The pipe samples used in this study were all previously in service in 24-inch diameter transmission pipelines. During the initial planning of the Gas Research Institute (GRI) Pipeline Simulation Facility flow loop and as part of Battelle's pipe research programs, over 50 joints of different pipe materials were donated by various pipeline companies to the Facility or Battelle [8]. Thirty-six of these joints remain available for use on this program. These materials have been previously characterized mechanically for stress-strain and toughness properties and chemically for composition. The magnetic and metallographic characteristics were determined in this work.

Table 1 shows mechanical, metallurgical, magnetic, and chemical properties of the samples examined. Appendix A contains data sheets for each sample. These data sheets include the full magnetization (B-H) curve, initial permeability, and a photomicrograph of the grain structure along with the numerical values of 21 measurements.

Mechanical and Chemical Properties

Mechanical and chemical property measurements of 33 of the pipe samples were made under a GRI contract during the construction of the Pipeline Simulation Facility. For these pipe

samples, original data sheets were recovered and values of the mechanical and chemical properties were confirmed. The other samples were tested using the same standards and procedures. The goal was to ensure the absolute quality of these data. The procedures used to obtain these measurements are given below.

Tensile Properties. The tensile properties of each pipe section were measured using a flattened transverse strap tensile specimen. The specimens had a 1.5-inch wide by 2.25-inch long reduced section as required by American Petroleum Institute (API) Specification 5L. The specimens were tested in accordance with American Society for Testing and Materials (ASTM) Designation A 370. The cross-head speed was 0.02 inch/minute through yield and 0.25 inch/minute to failure after yielding occurred.

Impact Properties. The impact properties at 150 F were measured using flattened, transverse, full-wall-thickness, Charpy V-notch specimens for each pipe section. The elevated temperature was used in an attempt to measure "upper shelf" energies. Duplicate specimens also were tested. The impact tests were conducted in accordance with ASTM Designation E 23.

For Table 1, the absorbed energy levels were converted to those for full-thickness specimens; that is, the measured energy levels were multiplied by the standard Charpy thickness divided by the test thickness to give equivalent full-size energy levels. Extreme data points were questioned. For example, the Charpy energy values for Specimens 10 and 11 are relatively high for materials with such low tensile properties and which lack microalloying elements. However, these specimens have a fine grain structure consisting of mainly ferrite, and relatively high elongation, which add credence to these measurements. Also, both samples were subjected to two Charpy tests, whose results were within 10 percent of each other. Where 100 percent shear failure did not occur, no corrections were made to convert the measured levels to upper-shelf levels.

Chemical Composition. The chemical composition of each pipe sample was determined using the optical emission spectrographic analysis technique. The weight percent of carbon,

Table 1. Mechanical, metallurgical, magnetic, and chemical properties of 36 gas transmission pipes pulled from service

Specimen ID	Diam. (inch)	Thick. (inch)	Charpy		Tensile			Hardness Rockwell B	Grain Size, ASTM #	Magnetic Measures				Chemical Composition (Percent)							
			Energy (ft-lbs)	Shear (%)	Yield (ksi)	Ultimate (ksi)	Elong. (%)			Saturation Bs From Hysteresis (Gauss)	Remanence Br (Gauss)	Coercivity Hci (Oe)	Permeability MuMax (G/Oe)	C	Mn	P	S	Si	Al	V	Cb
24-6-A	24.03	0.292	22	100	66.79	84.23	30	93	11.5	19,327	12,130	7.11	1,170	0.11	1.33	0.012	0.008	0.290	0.051	0.000	0.003
24-7-A	24.03	0.290	26	100	68.22	85.55	29	91	11.5	18,898	10,860	7.47	950	0.11	1.30	0.011	0.008	0.290	0.053	0.000	0.003
24-8-A	24.03	0.291	28	100	67.48	84.89	31	90	10	19,037	11,210	7.62	1,120	0.11	1.30	0.012	0.008	0.300	0.052	0.000	0.003
24-9-A	24.03	0.288	18	100	74.45	92.36	27	95	12	19,214	11,880	8.12	1,190	0.11	1.37	0.011	0.009	0.310	0.059	0.034	0.004
24-10-A	24.03	0.314	127	100	40.98	55.06	50	66.5	9	19,389	12,080	4.54	1,600	0.10	0.40	0.018	0.009	0.006	0.017	0.000	0.000
24-11-A	24.03	0.314	134	100	45.85	57.41	45	69	9	19,371	12,410	5.15	2,070	0.10	0.39	0.017	0.008	0.005	0.014	0.000	0.000
24-13-A	24.11	0.310	26	100	67.59	83.29	27	91	9.5	18,517	8,130	8.1	840	0.20	1.17	0.009	0.013	0.007	0.000	0.000	0.006
24-14-A	24.11	0.308	30	99	64.93	84.6	32	90	8	18,602	8,250	8.7	740	0.28	1.20	0.009	0.030	0.074	0.000	0.000	0.025
24-15-A	24.11	0.376	26	64	62.77	82.95	33	87	7	18,827	7,520	7.37	770	0.27	0.85	0.027	0.031	0.052	0.000	0.000	0.010
24-17-A	24.11	0.318	33	98	53.97	74.34	31	78	7.5	19,158	7,706	6.01	1,000	0.25	1.01	0.013	0.015	0.028	0.000	0.000	0.003
24-18-A	24.11	0.318	58	100	65.78	83.6	34	87.5	9.5	19,188	7,840	6.37	990	0.14	1.26	0.014	0.009	0.310	0.034	0.000	0.008
24-20-A	24.11	0.277	39	100	45.71	75.63	38	80.5	8.5	18,779	8,790	5.84	1,100	0.26	1.04	0.011	0.016	0.034	0.023	0.000	0.003
24-21-A	24.11	0.337	26	50	62.44	84.38	33	88	6	18,924	7,710	7.46	820	0.26	0.94	0.027	0.017	0.066	0.000	0.000	0.013
24-22-A	24.11	0.303	30	100	67.82	86.32	31	91	10.5	18,692	9,570	8.37	780	0.20	1.19	0.008	0.010	0.029	0.000	0.000	0.008
24-23-A	24.19	0.284	42	100	50.34	79.68	35	82	8.5	18,580	8,900	6.22	960	0.30	1.07	0.012	0.024	0.038	0.005	0.000	0.003
24-27-A	24.11	0.272	18	100	68.67	85.36	26	88	10	18,946	7,910	8.25	660	0.18	1.28	0.013	0.015	0.082	0.000	0.000	0.012
24-28-A	24.11	0.293	38	100	55.19	73.3	38	78.5	8.5	18,590	9,940	6.36	1,210	0.23	1.06	0.008	0.020	0.005	0.001	0.000	0.003
24-30-A	24.11	0.267	23	100	67.71	87.16	27	89	10	18,951	9,130	8.73	1,200	0.24	1.21	0.009	0.011	0.020	0.000	0.000	0.007
24-31-A	24.11	0.293	25	99	55.34	75.63	27	82	8.5	19,312	8,190	5.96	1,110	0.26	0.70	0.011	0.029	0.040	0.000	0.000	0.004
24-32-1	24.19	0.294	42	100	45.4	73	32.5	80	8.5	19,044	9,540	5.85	1,230	0.20	0.88	0.010	0.017	0.033	0.011	0.002	0.004
24-33-1	23.87	0.289	28	100	60	83.5	25	85	10	17,946	8,450	7.98	840	0.26	1.06	0.016	0.044	0.035	0.000	0.001	0.004
24-34-1	23.87	0.289	34	99	59.4	78.7	22	80	8	18,077	7,400	6.21	1,000	0.23	0.82	0.015	0.026	0.036	0.006	0.002	0.003
24-35-1	23.87	0.290	29	100	71.2	94.2	24	94.5	7	18,533	8,410	9.06	780	0.28	1.16	0.013	0.031	0.042	0.000	0.000	0.005
24-36-1	23.87	0.292	31	100	57.8	79.1	28	82.5	9	18,718	7,610	6.25	1,000	0.25	0.98	0.014	0.021	0.031	0.000	0.001	0.002
24-37-1	23.87	0.284	32	99	62.3	86.4	24.5	87.5	9.5	18,151	7,770	7.45	820	0.27	1.14	0.012	0.020	0.055	0.000	0.000	0.005
24-38-1	23.87	0.289	31	100	57.5	82.7	21	87	9.5	18,699	8,050	6.82	920	0.24	0.91	0.015	0.028	0.046	0.000	0.001	0.006
24-39-1	23.87	0.296	31	100	58.3	80.2	24	87	9.5	18,928	7,810	6.55	870	0.23	0.96	0.014	0.018	0.032	0.000	0.001	0.003
24-40-1	23.87	0.320	31	100	60.1	82.5	26.5	86	10	19,137	9,150	5.51	1,340	0.25	0.92	0.016	0.025	0.047	0.000	0.001	0.005
24-41-A	23.87	0.288	31	100	61	85	31	87	9.5	18,395	7,850	7.69	850	0.27	1.08	0.018	0.021	0.050	0.000	0.000	0.008
24-42-1	23.87	0.279	30	100	53.9	76.3	28.5	82	7.5	18,744	8,150	6.45	890	0.24	0.97	0.009	0.027	0.029	0.009	0.001	0.003
24-43-1	23.87	0.317	45	95	50.1	83.9	29.5	88	4	18,937	9,910	6.94	1,010	0.29	0.97	0.011	0.016	0.130	0.002	0.002	0.003
24-44-1	23.87	0.266	49	83	47.6	65.3	29.5	75	7.5	18,682	7,640	4.68	1,320	0.19	0.55	0.011	0.024	0.002	0.005	0.001	0.003
24-45-1	23.87	0.265	28	100	55.9	76.2	24	80	9	18,942	7,820	6.23	860	0.24	0.66	0.026	0.030	0.013	0.002	0.002	0.003
24-46-1	23.87	0.274	26	92	48.5	67.9	30	71	8	19,184	8,060	4.71	1,480	0.20	0.49	0.006	0.021	0.000	0.025	0.000	0.003
24-47-1	23.87	0.317	63	98	63.8	80.8	28	89.5	11	19,049	7,940	5.29	1,100	0.07	1.17	0.017	0.005	0.160	0.049	0.002	0.000
24-50-1	23.87	0.277	33	98	47.8	63.5	32.5	69.5	8	19,017	8,740	4.32	1,590	0.20	0.44	0.008	0.028	0.000	0.001	0.000	0.003

manganese, phosphorus, sulfur, silicon, aluminum, vanadium, and columbium (niobium) are reported in Table 1.

Magnetic Properties Under No-Load Conditions

An MFL tool applies a magnetic field (H) to create a flux density (B) in a pipe, which can "leak" from the pipe material at defects. The relationship between the magnetic field and the flux density is nonlinear and hysteretic. Magnetization curves, or B-H curves, quantify the basic magnetic properties of ferromagnetic materials. These curves relate the applied magnetic field to the flux density in the material.

B-H curves have two parts, the initial permeability and the hysteresis loop, as shown in Figure 1. Common quantifying measures of these curves are also illustrated in Figure 1. Two measures, the coercive force (H_c) and the remanence (B_r), quantify the extent of the hysteresis. The coercive force, H_c, is the direct current (D-C) magnetizing field required to restore the magnetic flux density to zero after the material has been magnetized. Coercivity (H_{cs}, not shown on the figure) is the maximum value of the coercive force that can be attained after the material has been magnetized to saturation. The remanence, B_r, is the maximum value of magnetic flux density, measured while no magnetic field is applied.

Two other common magnetic properties are the saturation flux density (B_s), and D-C permeability (μ). These properties further characterize the overall B-H curve. The saturation flux density has many practical and technical definitions. In this work, the saturation flux density is fundamentally defined as the flux density where changes in hysteresis behavior are negligible with changes in magnetizing field and arbitrarily defined as the flux density at a magnetic field of 200 Oersted. The D-C permeability (μ) is a generic term used to represent the ratio of the magnetic flux density to the magnetic field. In this work, the incremental permeability (i.e., the slope of the magnetization curve) is used. The incremental permeability is the ratio of the change in magnetic flux density (B) to the change in magnetic field (H).

Numerical regression methods were used to generate the incremental permeability values given in the report. Many measures of permeability are possible, because the range of magnetic field (the dependent variable) is a variable. If the measured range of the magnetic field is very

small, the calculated permeability is significantly influenced by small variations in measurements (noise). If the range of the magnetizing field is very large, the value represents an average over that interval. To provide the maximum amount of information, two measurement windows were applied. The maximum permeability values provided in Table 1 are based on a 2-Oersted regression window, which reduces the influence of noise. In the graphs of permeability versus magnetic field shown in Appendix A, a 1-Oersted regression window was used, which preserves some of the more subtle features.

The 36 samples were magnetically characterized following ASTM Standard A 773-80. This method, illustrated in Figure 2, uses a ring sample machined to have an outside diameter of 2.0 inches and a square cross section of 0.15 inches. This provides an 85 percent inside diameter to outside diameter ratio, as required by the ASTM standard. To obtain this sample geometry from the pipe material, a 6-inch by 6-inch coupon was cut from the pipe opposite the seam weld. The 2-inch ring sample was machined from this coupon in a liquid bath to minimize the effect of sample preparation on the magnetic properties.

The ASTM experimental procedure specifies that each ring sample be wound with drive and sense windings. The drive winding, used to generate the magnetic field (H) has a minimum of 140 turns to generate a field strength of 200 Oersted. The sense winding, used to measure the change in flux, has a minimum of 80 turns to attain accurate measurements. The windings were applied by hand, and a few additional turns were added when space was available. Measurements were made using a LDJ model 3500H Hysteresisgraph. Sufficient current was applied to the drive windings to produce 200 Oersted. After demagnetization, the magnetic field and flux density were digitally recorded at increments of nominally 0.2 Oersted for the initial magnetization curve and 0.5 Oersted increments for the hysteresis loop.

Initial permeability curves for samples 9, 11, 14, 21, 32, and 46 are shown in Figure 3. A composite of all initial permeability curves and full hysteresis loops for all samples are shown in Figures 4 and 5, respectively. Individual initial permeability curves and full hysteresis loops for each sample can be found in Appendix A. These figures show significant variation in magnetic properties for all materials, as further quantified in Table 2.

Table 2. Summary of magnetic property changes

Coercive Force (H_c), Oersted	
Mean	6.7
Std Dev	1.2
Max	9
Min	4.5
Maximum Permeability (μ_{max}), Gauss	
Mean	1003
Std Dev	331
Max	2090
Min	580

Magnetic Properties Under Compression and Tension

Sample Set. Twelve of the pipeline steels were used to examine the effects of elastic and plastic strains on magnetic properties. Thick samples were chosen to reduce the risk of buckling during the compressive-load tests. Table 3 lists the samples and shows that they represent a wide range of yield strengths and manufacturing types. Yield strengths ranged from about 40 ksi to more than 70 ksi. It is sometimes expected that magnetic properties will vary with pipe grade. A cursory review of the permeability curves for these 12 samples confirms that such variation may be present, although it is not necessarily a linear relationship.

Specimen Configuration. Two sample configurations were used to measure magnetic properties: a "dogbone" shape for tensile loading and a thin cylinder for compressive loads. Figures 6 and 7 illustrate the two sample configurations. The compression sample required special attention to prevent buckling when under load. Two coaxial cylinders were used to support the sample during compression. The central holes in these cylinders were sized so that they could be slipped smoothly over each end of the sample. Very small clearances were used to prevent lateral buckling of the sample. The sensed area, in the center of the sample, was exposed between the larger coaxial cylinders, as shown in Figure 8.

Table 3. Sample set for compression and tension tests

Sample Number	Type	Yield (ksi)
6	SMLS/ERW	66.79
8	SMLS/ERW	67.48
10	ERW	40.98
11	SMLS/ERW	45.85
13	DSAW	67.59
17	ERW	53.97
18	DSAW	65.78
22	FW	67.82
31	SMLS/ERW	55.34
35	FW	71.20
36	FW	57.80
43	FW	66.79

Legend: SMLS – seamless, ERW – electric resistance weld, DSAW – double submerged arc weld, FW – flash weld

Each sample was prepared with strain gages and with an encircling coil to measure magnetic flux. Hall probes in the vicinity of the sensing area were used to measure the magnetizing force. A large magnetizing coil was placed over the whole arrangement, and load cells within the loading linkage were provided as an alternative measure of specimen loading. Figures 9 and 10 are drawings of the test configurations for compression and tension, respectively.

Test Procedure. Each sample was mounted in the test fixture, which has a scissors-type loading linkage under manual adjustment. A computer-driven magnetic sensing system automatically cycled the magnetic excitation field and collected the data from all sensors. Strain gages were connected to a bridge circuit and read manually.

B-H curve data were collected for each tensile specimen under a half-dozen different applied loads. Each sample was taken to mechanical yielding, and B-H data were collected again for 1 percent plastic deformation plus a range of applied elastic loads. The sample was then further yielded to 2 percent, and the applied loads were cycled again. The process was repeated to a maximum of 5 to 8 percent plastic deformation.

A similar process was carried out with the compressive samples.

Results. The results are presented in sets of 16 graphs (on three pages) for each sample (see Appendix B). The first page of each set shows B-H curves for tensile and compressive loading under several levels of applied stress. Separate graphs cover the cases of zero plastic deformation, 1 percent plastic deformation, and the maximum amount of plastic strain achieved for the particular sample.

The second page shows the incremental permeability variation under similar loading conditions. The final set of four graphs on the third page of each set displays the B-H curve and permeability response to plastic deformation at zero applied stress.

The permeability plots at zero applied stress and zero plastic strain have different peak values after compressive and tensile loading. Since all loads are zero, the plots should be the same. This difference is suspected to be due to the difference in length of the tensile and compressive samples. The shorter sample used in compression tests apparently had an end effect that caused its indicated permeability to be too low. To verify that hypothesis, a dogbone tensile specimen was shortened to the same length as the compression samples and the permeability was remeasured. A reduction was observed that was sufficient to explain the differences between compressive and tensile results.

Variation of Magnetic Properties Within a Pipe

The pipe manufacturing process induces significant mechanical stress and metallurgical variations that can affect the magnetic properties of pipeline steels. With the variation of magnetic properties for various pipeline steels generally established as discussed above, the variation within a pipe sample (around the circumference of the pipe) was examined. The results presented here show a sufficient variation of magnetic properties to affect signals from mechanical damage defects. Compensation for these effects may be required for accurate analyses.

Magnetic Measurements. To avoid releasing the inherent mechanical stress induced during the pipe manufacturing process, a special experimental setup and test method were established. This method measured the applied magnetic field (H) and flux density (B) without

removing samples from the pipe. The variation around the circumference of a pipe was measured for Samples 08 and 31. The measurement apparatus is illustrated in Figure 11.

The magnetic field was measured by a Hall effect sensor mounted on the surface of the pipe. Physical boundary conditions require that the tangential magnetic field in the pipe equal the magnetic field in the air just above the pipe.

The flux density in the pipe was measured by a coil wound though two small holes in the pipe. The holes were made using electric discharge machining (EDM). Ten turns of 32-gage wire were threaded through each hole. Since coils measure the change in magnetic flux, the output was integrated and multiplied by the cross-sectional area to obtain the flux density. Eight locations were instrumented around the circumference of the pipe, as illustrated in Figure 11. EDM allows well controlled geometry and minimal heating of the pipe material, which could affect results. The magnetic field is applied by a U-core electromagnet placed on the pipe, straddling the flux density and field sensors. While this configuration enables in-situ measurement of the flux density and field, the amount of magnetic field in the pipe is limited to approximately 40 Oersted for the pipe materials tested.

Compound Stress Effects. The in-situ magnetic measurement configuration also enabled an examination of the compounding effects of manufacturing stress and axial stress on the magnetic properties in the pipe. These results complement the data on stress effects presented earlier. To apply an axial load, a strongback four-point bending apparatus was used, as illustrated in Figure 12. The two pipe samples were welded together, and 15-foot-long bending arms (0.344 inch wall thickness, 70 ksi pipe) were added to either end. The ends of the pipe were anchored to the reaction frame of the bending apparatus. Equal upward force was hydraulically applied at two locations, producing uniform tension at the top of the pipe samples and uniform compression at the bottom. Four strain gages on each sample were used to set the hydraulic load levels to establish 95 percent measured yield stress in each pipe sample.

Measurement and Analysis. Magnetization curves were measured before loading, at 95 percent of measured yield stress, and after loading. Composite magnetization curves for a no-load condition, tension, and compression are shown in Figure 13 for all the samples. These

results parallel prior results with the largest change in magnetization curves occurring for compression and smaller differences for tension.

Two magnetic parameters—maximum magnetic permeability and coercive force—were examined in detail. Figures 14 and 15 show "radar plots" of permeability for Samples 31 and 08, respectively. The position numbers, 1 through 8, are as shown in Figure 11. A material that had uniform magnetic field independent of circumferential position would produce a perfect octagon in these radar plots. For Specimen 31 without load, the permeability is highest for positions 6 and 7. Under tension, the permeability increases slightly for all measurements and the variation is reduced. Under compression, the permeability decreases significantly for all measurements and the variation is reduced. Sample 08 has similar results, but with less variation without loads. Coercivity is presented in Figures 16 and 17. The plots show similar results with the exception being significant skewing under tension.

Analysis of Properties

There were three objectives to this program. The first was to determine whether there were clear correlations between magnetic properties and mechanical properties. The second was to determine whether magnetic properties change significantly with the application of tensile or compressive stresses and strains. The last was to assemble a database of both magnetic and mechanical properties for future developmental activities. In addition, information was gathered on the range of material properties that might be encountered during an MFL inspection.

Variation of Properties

A wide range of magnetic properties was encountered. In the following discussion, histograms are used to illustrate the range of pipe properties examined. Figure 18 shows the distribution of measured yield strength for the sample set. The mean of all pipe samples is 58 ksi with 95 percent of the values ranging from 42 to 74 ksi. While difficult to quantify, this range of values represents a good sampling of pipe in service in the United States, where X52 is a commonly used pipe material. It should be noted that measured yield strength typically exceeds

the specified minimum yield strength (SMYS) by definition; however the SMYS of each pipe sample was not available for most samples.

The ultimate strength histogram, Figure 19, shows that the most common values are between 75 and 85 ksi, and that the distribution is tighter than that of the yield strength. The elongation is relatively evenly distributed, as shown in Figure 20, with a mean of all pipe samples of 30 percent and 95 percent of the values ranging from 18 to 46 percent. The Charpy results show two materials with toughness that exceeds 100 foot-pounds. Excluding these two samples, the Charpy energy histogram, shown in Figure 21, has a mean for the remaining pipe samples of 30 foot-pounds, with 95 percent of the values ranging from 10 to 50 foot-pounds. The distributions of mechanical hardness and grain size are shown in Figure 22 and 23, respectively.

Chemical properties also affect the magnetic properties of pipeline steel [1]. Histograms of the weight percents of carbon, manganese, phosphorus, sulfur, silicon, aluminum, vanadium, and columbium are given in Figures 24 through 31, respectively.

Based on these results, we can conclude that the samples used in this evaluation represent a wide range of typical pipeline steels.

The variations in the magnetic properties were also examined. Saturation flux density for all pipe materials had a mean of 18,850 gauss with a standard deviation of 350 gauss, a tight distribution. However, a significant variation was observed in the remanence, coercivity, and permeability, as shown in the histograms in Figures 32 to 34, respectively. While the effect of these variations on the mechanical damage signals is not fully known, it has been shown that two dent defects made in different materials with the same internal and external loading profile have different flux leakage signatures. So, understanding the effects of material variations on MFL signals from mechanical damage will be required to develop general signal analysis methods.

Correlation of Properties

One objective that motivated the measurement of material properties was the potential of estimating magnetic properties from the more widely known mechanical and chemical properties. As a first step, correlations between mechanical, metallurgical, chemical, and

magnetic properties were examined. The correlation coefficients for each variable against all others are given in Table 4. The strongest correlation was between ultimate tensile strength and material hardness, with a correlation coefficient of 0.96. This correlation is clearly illustrated by the first scatter diagram in Figure 35. Also illustrated in Figure 35 are the correlations between hardness and yield strength (correlation coefficient = 0.88) and between yield strength and ultimate tensile strength (correlation coefficient = 0.86). The strongest correlations between a magnetic property and mechanical properties were the correlations between coercive force and hardness, ultimate strength, and yield strength with coefficients of 0.83, 0.85, and 0.81, respectively. The scatter plots in Figure 36 illustrate these correlations.

Magnetic permeability is one of the more important parameters that significantly affect the results in magnetic inspection. The results of this study show that most physical measurements had a limited correlation with this magnetic property. Table 4 shows that permeability is most strongly correlated with Charpy energy, yield strength, ultimate strength, elongation, hardness, carbon, manganese, and columbium. However, the correlation coefficients for these eight are low, between 0.48 and 0.76, and the scatter plots in Figure 37 illustrate that only a general trend exists. Table 4 also shows that permeability is somewhat correlated with magnetic saturation, remanence, and coercivity, but again the correlation coefficients are low, between 0.55 and 0.69. The remanence, another important parameter, did not strongly correlate with mechanical, metallurgical, or chemical properties.

Based on these results, we can conclude that there is no clear correlation between magnetic properties and commonly measured mechanical properties. So, the change in magnetic properties due to mechanical damage must be outside the range of typical magnetic properties in order for the damage to be detected. Otherwise, the magnetic properties must be measured because they cannot easily be recreated from mechanical properties.

Changes in Magnetic Properties with Stress and Strain

Figure 38 shows the typical changes in magnetic properties as a function of elastic stress. Compressive stress significantly changes the magnetization curve, while tensile stress does not. Under compression, the flux density decreases up to a magnetizing force of about 80 Oersted. In

Table 4. Correlation coefficients for each variable against all others (shaded boxes indicate higher correlations)

	Energy	Percent Shear	Yield	Ultimate	Elongation	Hardness	Grain Size	Saturation	Remanence	Coercivity	Permeability	Chemical Composition							
												C	Mn	P	S	Si	Al	V	Cb
Energy		0.10	-0.54	-0.69	0.74	-0.58	-0.06	0.34	0.44	-0.52	0.67	-0.44	-0.52	0.17	-0.33	-0.15	0.09	-0.13	-0.35
% Shear	0.10		0.00	-0.02	-0.10	-0.01	0.47	-0.03	0.27	-0.01	0.14	-0.19	0.18	-0.57	-0.12	0.09	0.16	0.07	-0.31
Yield	-0.54	0.00		0.86	-0.52	0.88	0.47	-0.18	-0.04	0.81	-0.57	-0.12	0.80	0.03	-0.16	0.55	0.26	0.29	0.41
Ultimate	-0.69	-0.02	0.86		-0.63	0.96	0.23	-0.35	-0.19	0.85	-0.76	0.24	0.86	0.02	0.02	0.46	0.10	0.25	0.42
Elongation	0.74	-0.10	-0.52	-0.63		-0.55	-0.13	0.41	0.52	-0.40	0.58	-0.31	-0.36	0.05	-0.37	-0.08	0.14	-0.14	-0.11
Hardness	-0.58	-0.01	0.88	0.96	-0.55		0.31	-0.22	-0.05	0.83	-0.70	0.06	0.88	0.01	-0.13	0.55	0.22	0.25	0.40
Grain Size	-0.06	0.47	0.47	0.23	-0.13	0.31		0.11	0.36	0.17	0.04	-0.59	0.43	-0.14	-0.39	0.45	0.54	0.31	-0.14
Saturation	0.34	-0.03	-0.18	-0.35	0.41	-0.22	0.11		0.48	-0.40	0.55	-0.54	-0.23	0.02	-0.54	0.30	0.43	0.16	-0.20
Remanence	0.44	0.27	-0.04	-0.19	0.52	-0.05	0.36	0.48		-0.03	0.56	-0.62	0.04	-0.18	-0.54	0.43	0.57	0.32	-0.31
Coercivity	-0.52	-0.01	0.81	0.85	-0.40	0.83	0.17	-0.40	-0.03		-0.69	0.23	0.76	-0.02	0.03	0.27	-0.06	0.16	0.57
Permeability	0.67	0.14	-0.57	-0.76	0.58	-0.70	0.04	0.55	0.56	-0.69		-0.48	-0.63	-0.16	-0.29	-0.10	0.24	0.07	-0.51
Carbon	-0.44	-0.19	-0.12	0.24	-0.31	0.06	-0.59	-0.54	-0.62	0.23	-0.48		-0.04	0.07	0.71	-0.56	-0.79	-0.26	0.34
Manganese	-0.52	0.18	0.80	0.86	-0.36	0.88	0.43	-0.23	0.04	0.76	-0.63	-0.04		-0.19	-0.29	0.61	0.34	0.22	0.33
Phosphorus	0.17	-0.57	0.03	0.02	0.05	0.01	-0.14	0.02	-0.18	-0.02	-0.16	0.07	-0.19		0.16	-0.04	-0.12	-0.06	0.08
Sulfur	-0.33	-0.12	-0.16	0.02	-0.37	-0.13	-0.39	-0.54	-0.54	0.03	-0.29	0.71	-0.29	0.16		-0.51	-0.61	-0.17	0.22
Silicon	-0.15	0.09	0.55	0.46	-0.08	0.55	0.45	0.30	0.43	0.27	-0.10	-0.56	0.61	-0.04	-0.51		0.83	0.40	0.01
Aluminum	0.09	0.16	0.26	0.10	0.14	0.22	0.54	0.43	0.57	-0.06	0.24	-0.79	0.34	-0.12	-0.61	0.83		0.43	-0.29
Vanadium	-0.13	0.07	0.29	0.25	-0.14	0.25	0.31	0.16	0.32	0.16	0.07	-0.26	0.22	-0.06	-0.17	0.40	0.43		-0.08
Columbium	-0.35	-0.31	0.41	0.42	-0.11	0.40	-0.14	-0.20	-0.31	0.57	-0.51	0.34	0.33	0.08	0.22	0.01	-0.29	-0.08	

this region, the incremental permeability (the slope of the B-H curve), decreases. Above about 80 Oersted, there is little change in flux density or permeability with compression. With tension, there is little change in flux density for the entire magnetization curve. There is an increase in permeability for very low magnetizing forces (below about 30 Oersted).

Figure 39 shows the typical changes in magnetic properties as a function of elastic stress for a case where the material was subjected to 5 percent plastic strain. Here, the effects of compressive and tensile stresses are similar and opposite: the flux density and permeability decrease with compression, while they increase with tension.

Based on these results, we can conclude that elastic compressive stresses should be easier to detect than elastic tensile stresses when there is no permanent plastic deformation. When there is permanent plastic deformation, both compressive and tensile stresses should be equally easy (or hard) to detect.

Comparison of Single-Pipe Variations with Variations Between Pipes

Table 5 shows the mean, standard deviation, maximum, and minimum coercive force and maximum permeability for the 36 samples under no load and the variation of Sample 31 under no load, tension, and compression. This table shows that the standard deviation of the coercive force for all materials (1.2 Oersted) is 2.2 times greater than the standard deviation for pipe Specimen 31 (0.55 Oersted) under no load. The results are similar for the maximum permeability.

For the detection of stress, the variation in magnetic properties due to stress must be greater than the natural variations within a pipe under unloaded conditions. Under tension, the variation of the coercive force and magnetic permeability is within one standard deviation of the natural variation under the no load condition. This will make the detection of tensile stresses difficult. Under compression, the variation of the magnetic properties is beyond two standard deviations of the variation under the no-load condition. This variability should not mask the detection of compressive stresses.

Table 5. Magnetic property changes for pipeline steels

Coercive Force (H_c), Oersted		Sample 31		
	All Materials	No Load	Tension	Compression
Mean	6.7	7.7	7.4	9.7
Std Dev	1.2	0.55	0.8	0.9
Max	9	8.6	8.4	10.9
Min	4.5	7.1	6.3	8.5
Maximum Permeability (μ_{max}), Gauss				
Mean	1003	1297	1425	488
Std Dev	331	142	75	28
Max	2090	1497	1521	549
Min	580	1101	1325	462

Based on these results, we can conclude that the MFL signals from elastic tensile stresses would likely be masked by the natural variations in permeability that occur in any pipe steel. On the other hand, MFL signals due to compressive stresses should be larger than signals caused by natural variations in magnetic properties.

Conclusion

In this work, the variability of magnetic properties of pipeline steels was investigated for a range of material properties that could be encountered during an MFL inspection. The first goal of this work was to determine whether there were clear correlations between magnetic properties and mechanical properties. The second goal was to determine whether magnetic properties change significantly with the application of tensile or compressive stresses and strains. The final goal was to assemble a database of both magnetic and mechanical properties for future developmental activities.

There is no clear correlation between magnetic properties and mechanical properties. So, there is no easy way to predict magnetic properties for commonly known mechanical properties. As a result and in order to detect mechanical damage, the change in magnetic properties at the damage location must be outside the natural variability of typical magnetic properties. Otherwise, the magnetic properties must be measured to provide a baseline for assessing the small signals that are associated with mechanical damage defects.

The changes in magnetic properties due to compressive stresses and strains are large enough to fall outside the natural variability of typical magnetic properties. So, detecting compressive stresses and strains may be possible without a priori knowledge of the magnetic properties of a pipeline steel. These changes in properties are significant for relatively low magnetizing forces—below about 80 Oersted. Above this level, the effects of compressive stress or strain are negligible.

The same cannot be said of tensile stresses and strains. The changes in magnetic properties for tensile stresses are below the natural variability of typical magnetic properties. Detecting tensile stresses and strains would require measurements of magnetic properties because tension causes more subtle MFL signals and there is no clear method of estimating magnetic properties from other commonly known properties. This conclusion holds for the case where there is no net plastic strain. Based on limited results, it may be possible to detect plastic tensile strains with the same amount of effort needed to detect plastic compressive strains.

Finally, the data from this program should help ensure that the mechanical damage detection and characterization functions that are being developed are applicable over a range of pipe materials. Knowledge of the mechanical and chemical properties helps ensure that experimental samples and the conclusions drawn from them represent typical pipeline situations.

References

1. Bubenik, T.A., and J.B. Nestleroth, "Magnetic Flux Leakage (MFL) Technology for Natural Gas Pipeline Inspection," GRI Report 91/0367, 1992.

2. Davis, R.J., et al., "The Feasibility of MFL In-line Inspection as a method to Detect and Characterize Mechanical Damage," GRI Report 95/0369, 1996.

3. Bozorth, R.M., *Ferromagnetism*, D. Van Nostrand, New York, 1951. This classic Bell Laboratories text is available from the IEEE Press, Piscataway, NJ [www.ieee.org].

4. Atherton, D.L., et al., "Effects of Line Pressure Stress, Magnetic Properties, and Test Conditions on Magnetic Flux Leakage Signals," Gas Research Institute Annual Report GRI-96/0197, 1996. The bibliography contains nearly 100 references [www.gri.org].

5. Jiles, D.C. "Effects of Stress on the Magnetic Properties of Steels," *Review of Progress in Quantitative NDE*, Vol 16, Plenum New York, July 1997. A quantitative analysis with references.

6. Crouch, A.E., et al., "Magnetic Flux Leakage Inspection of Gas Pipelines: The Effects of Biaxial Stress," Gas Research Institute Annual Report GRI-95/0484, 1996 [www.gri.org].

7. Richer, F., "Magnetic and Other Physical Properties of X52, X60, X70, and X80 Grade Linepipe Steels," *Steel Research*, Verlag Stahleisen, Duseldorf, No. 9, 1989, pp. 417-424. English translation from German. Two samples of each pipe grade examined.

8. Eiber, R.J., et al., "GRI Nondestructive Evaluation Program: Pipeline Simulation Facility Development," Gas Research Institute Annual Report GRI-92/0141, 1992.

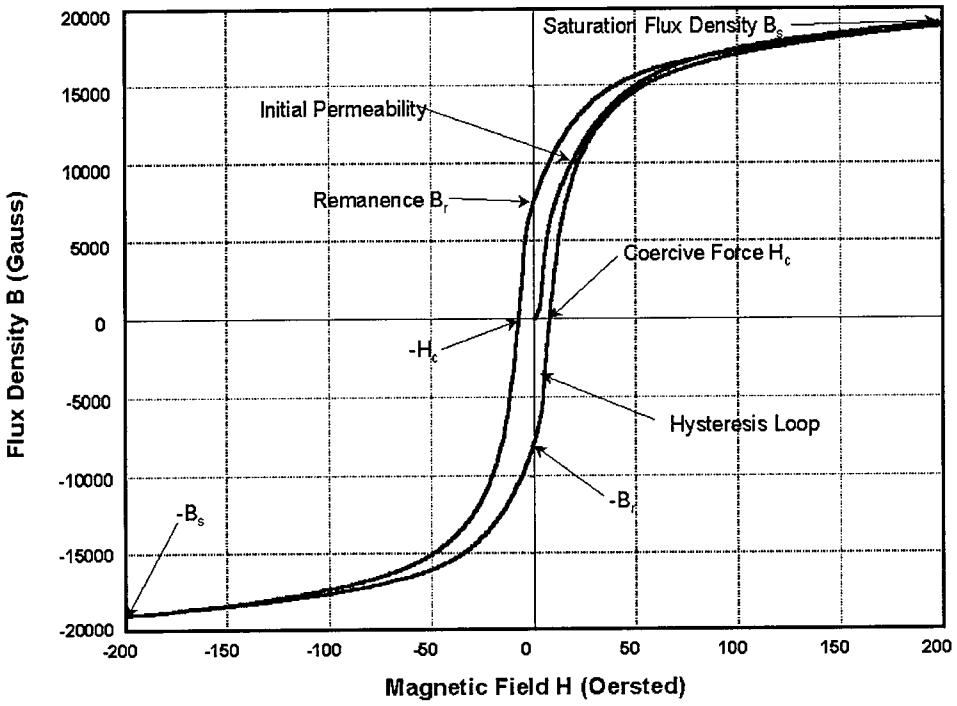

Figure 1. The initial permeability and hysteresis magnetization curves

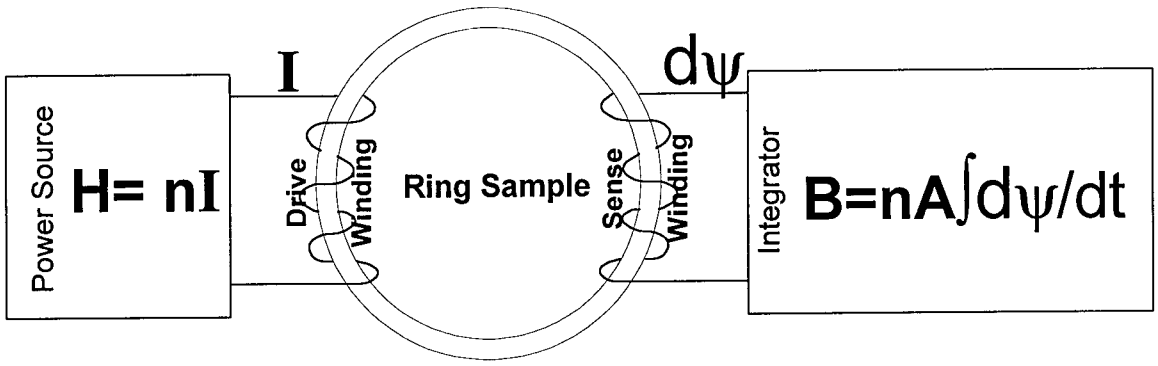

Figure 2. Magnetic property measurement method based on American Society for Testing and Materials (ASTM) Standard A 773-80

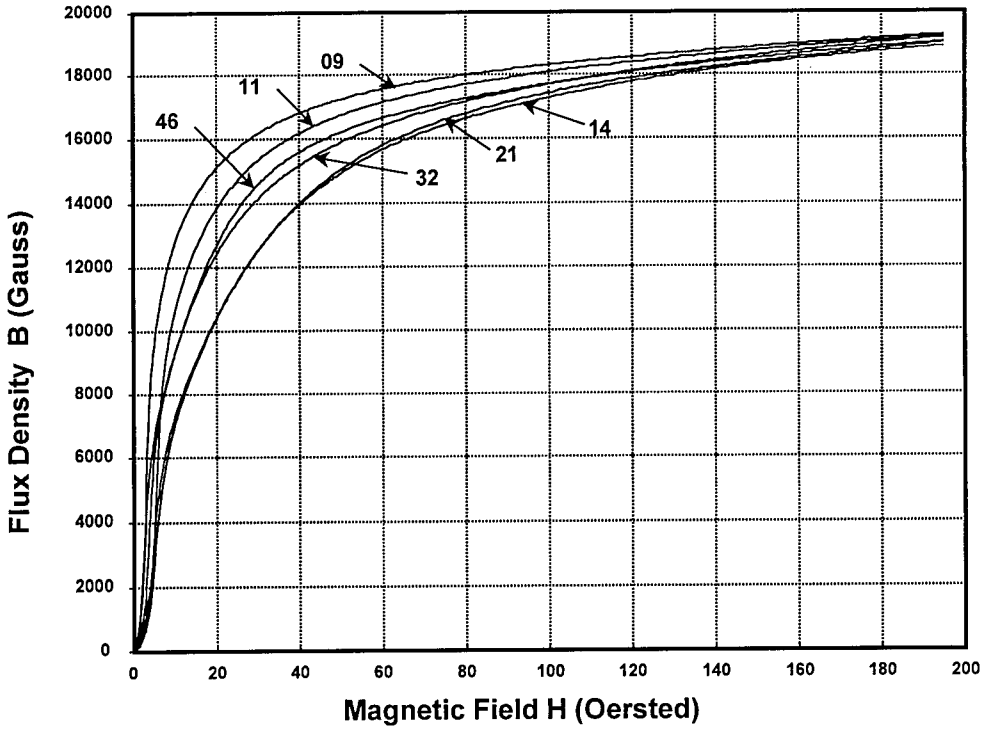

a. Full range measurement

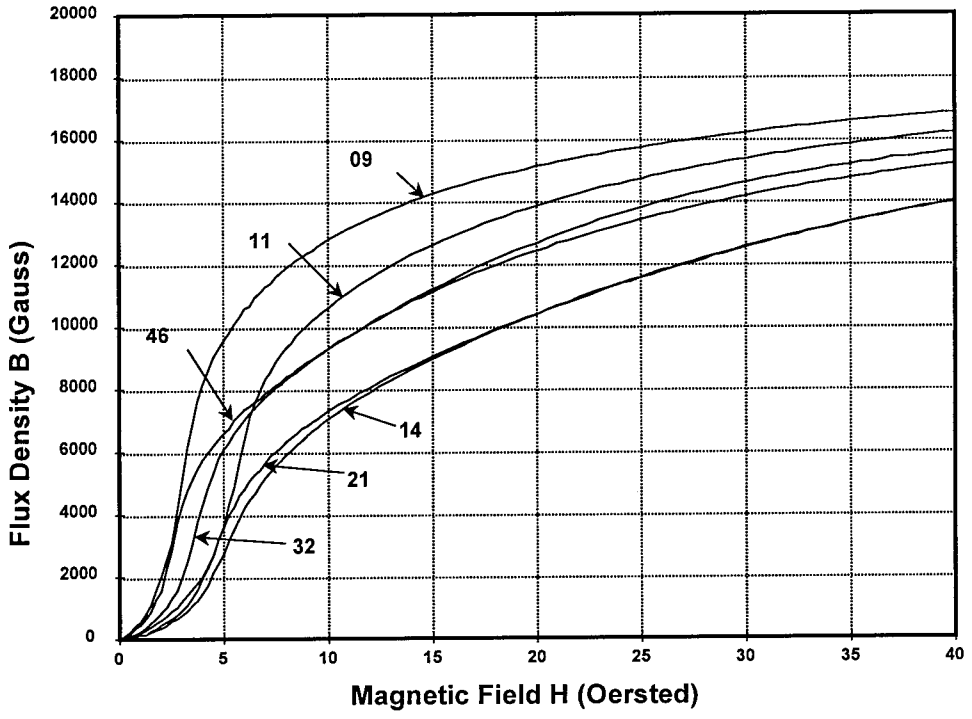

b. Expanded view

Figure 3. Typical initial permeability curves for Samples 9, 11, 14, 21, 32, and 46

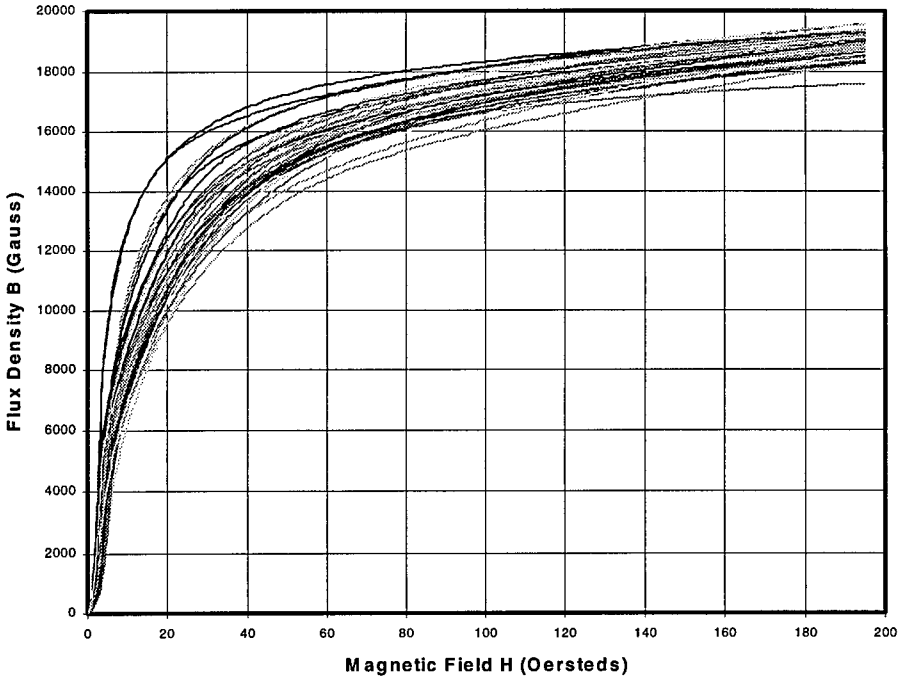

Figure 4. Initial permeability curves for all samples

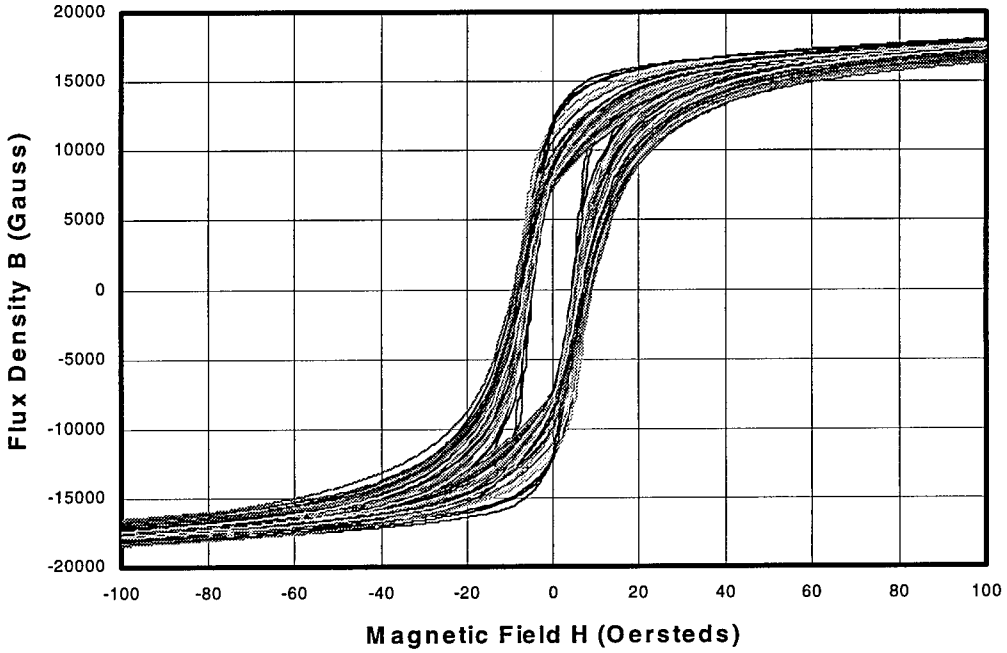

Figure 5. Full hysteresis loops for all samples

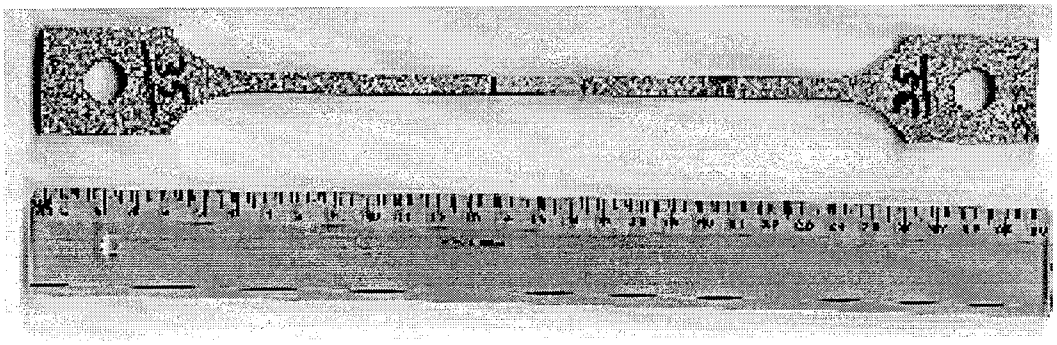

Figure 6. "Dogbone" sample for tensile plastic deformation experiments

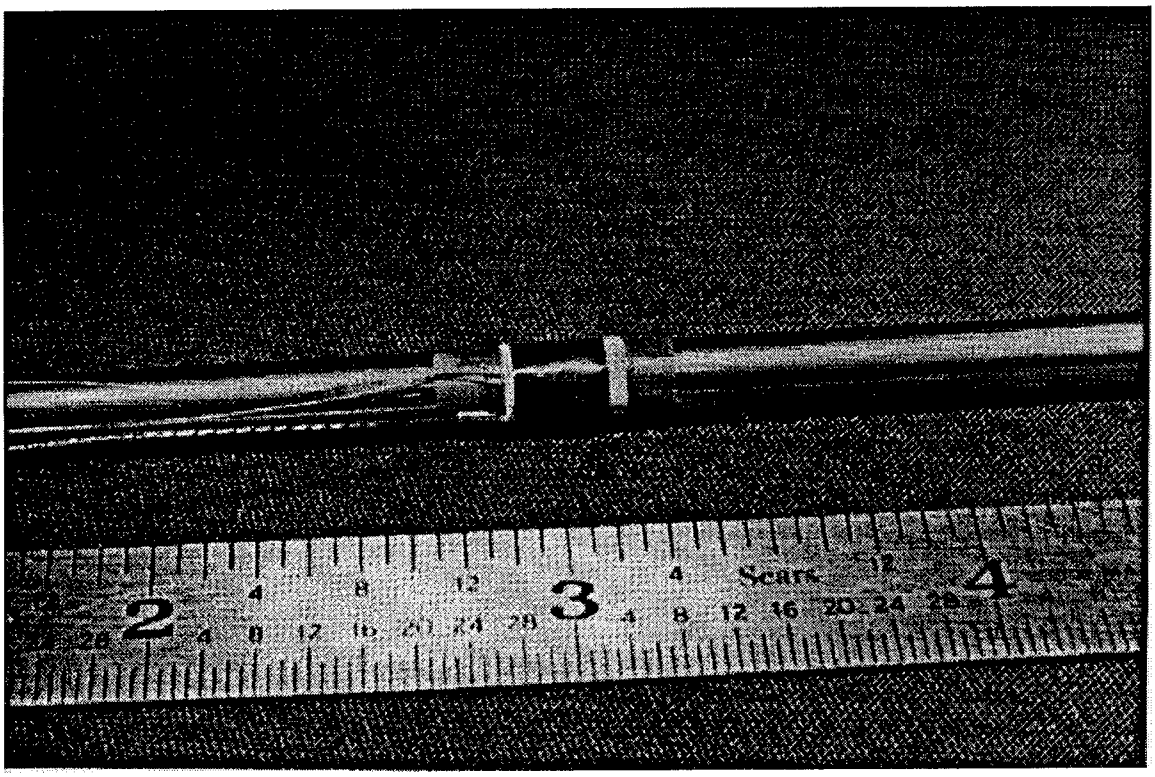

Figure 7. The compression test sample

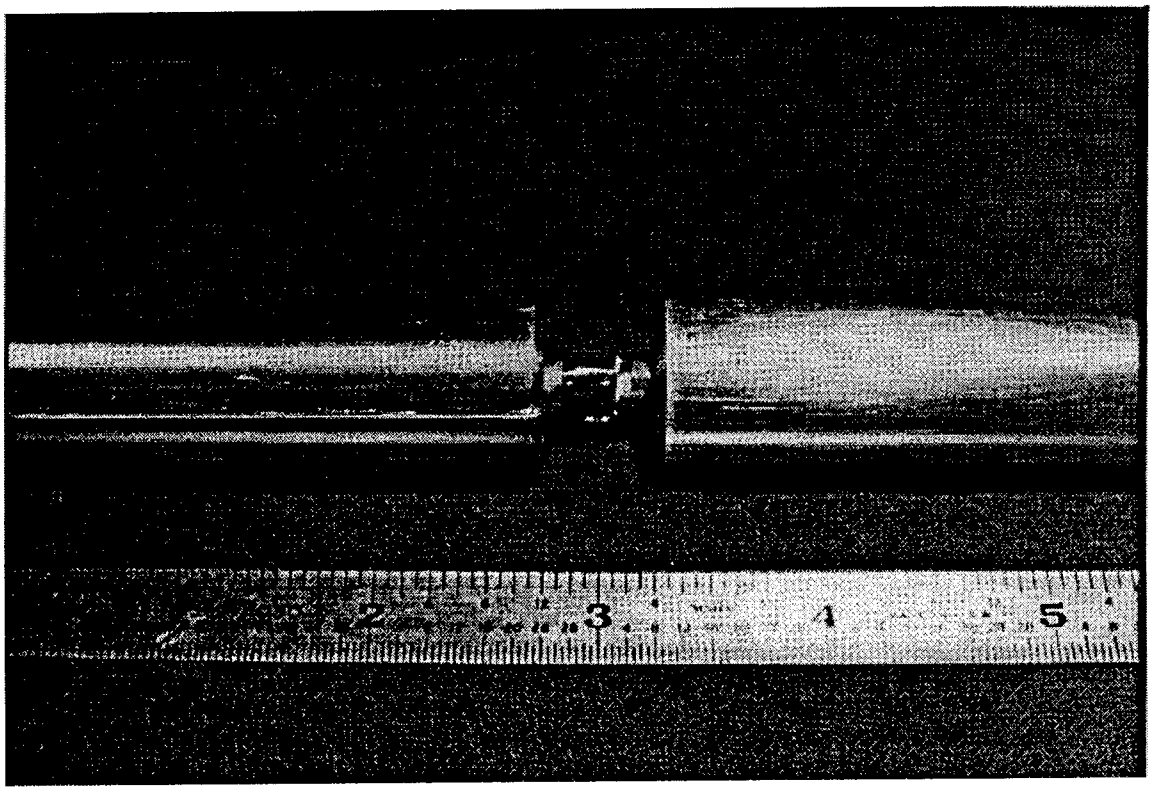

Figure 8. The sample mounted inside restraining collars

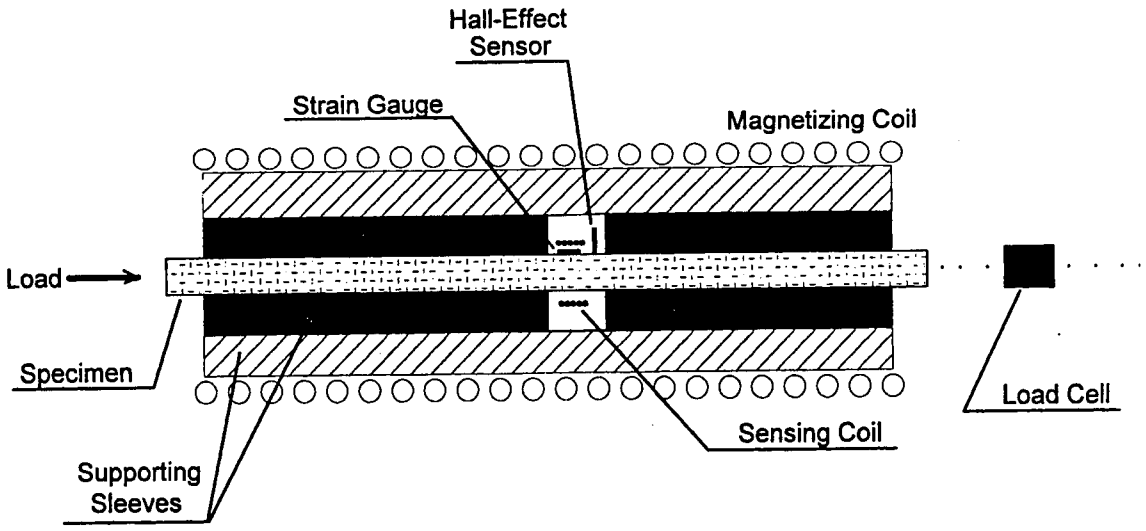

Figure 9. Experimental setup for B-H curve measurements under compression

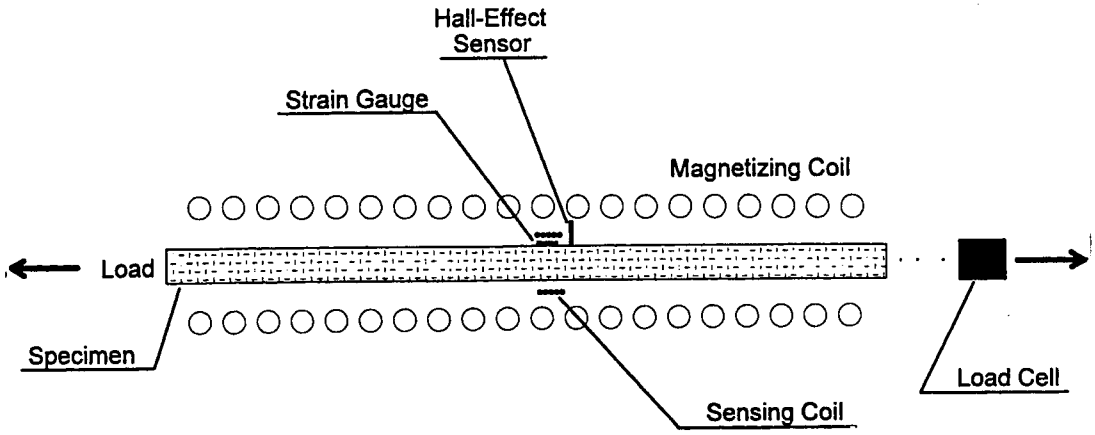

Figure 10. Experimental setup for B-H curve measurements under tension

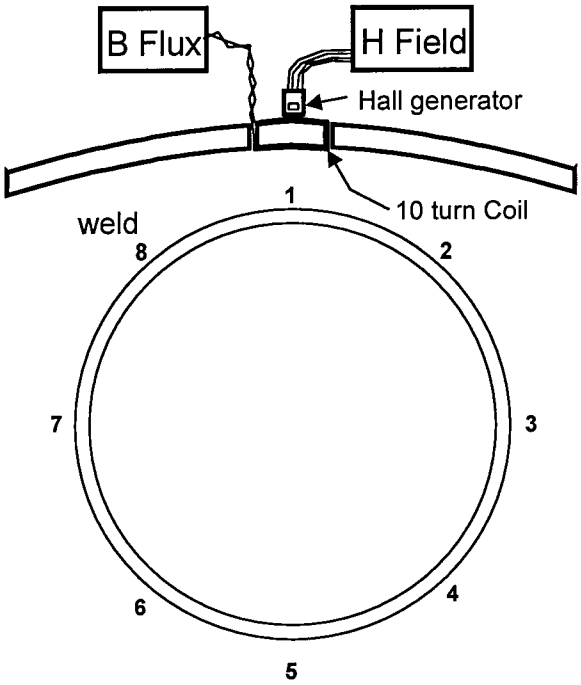

Figure 11. Apparatus for measuring applied magnetic field H and flux density B without removing samples from the pipe

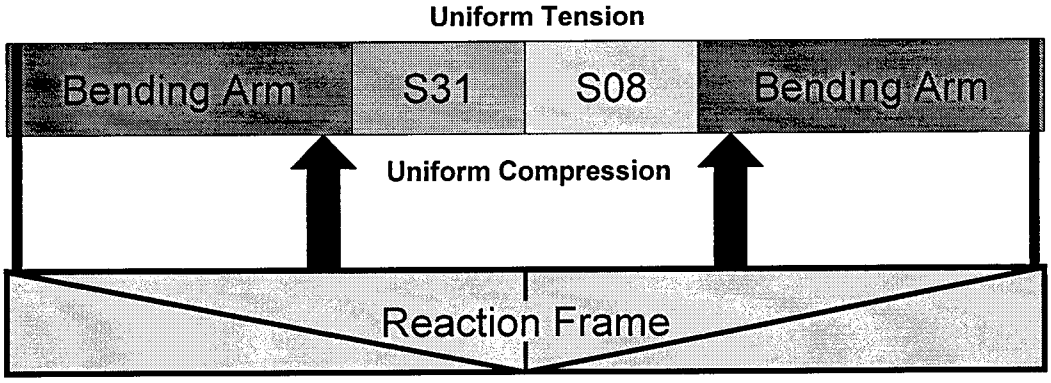

Figure 12. Battelle's strongback four-point bending apparatus

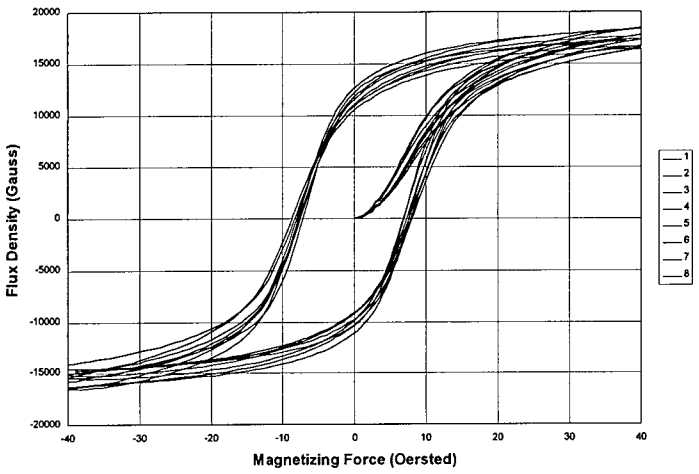

a. No load

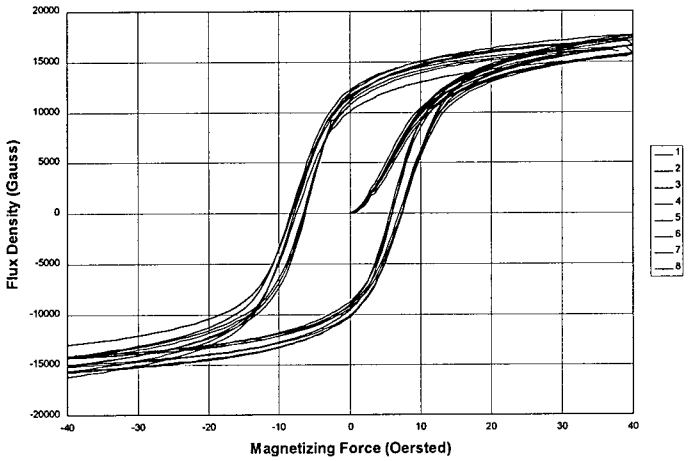

b. Tension

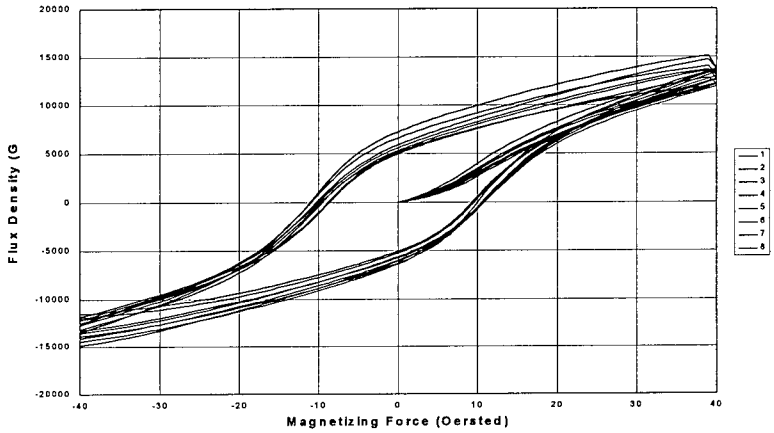

c. Compression

Figure 13. The magnetization curves for a no-load condition, tension, and compression for all 8 measurement locations on specimen 31

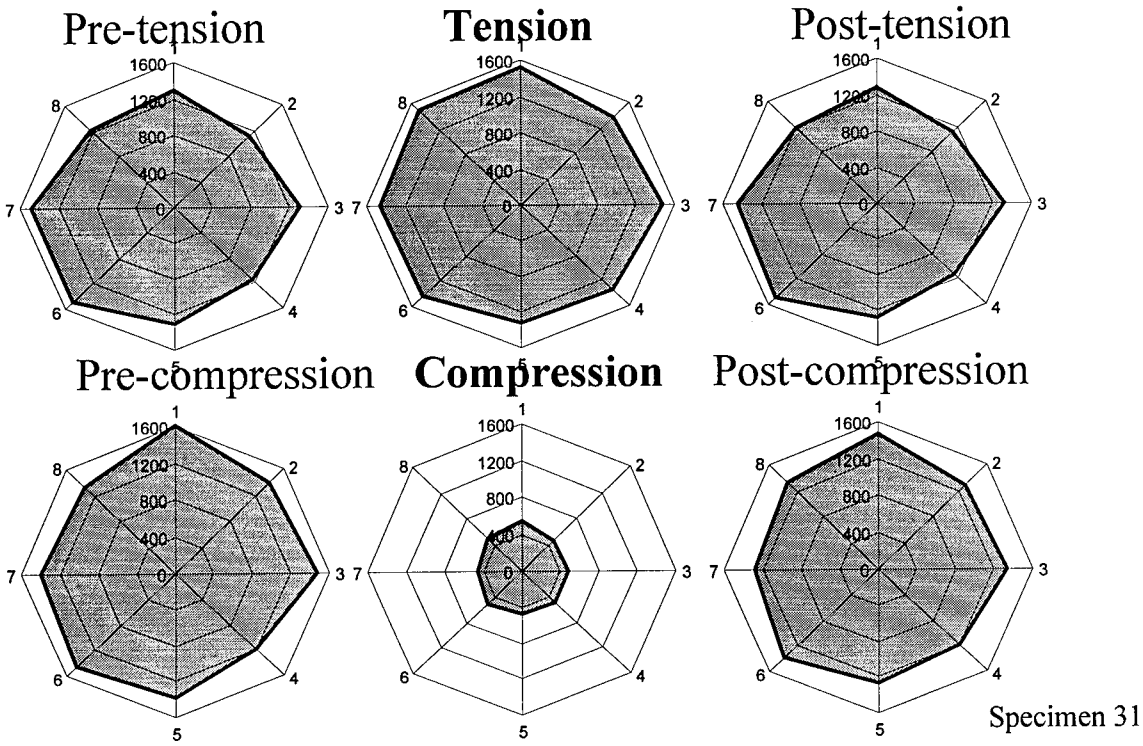

Figure 14. Radar plots of permeability for sample 31

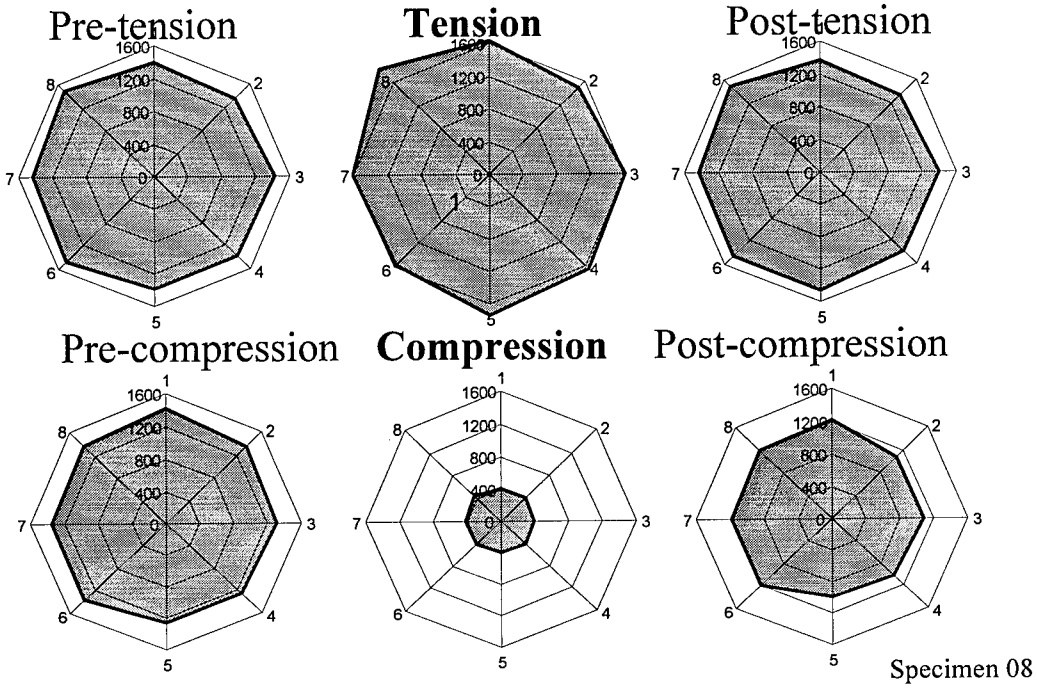

Figure 15. Radar plots of permeability for sample 08

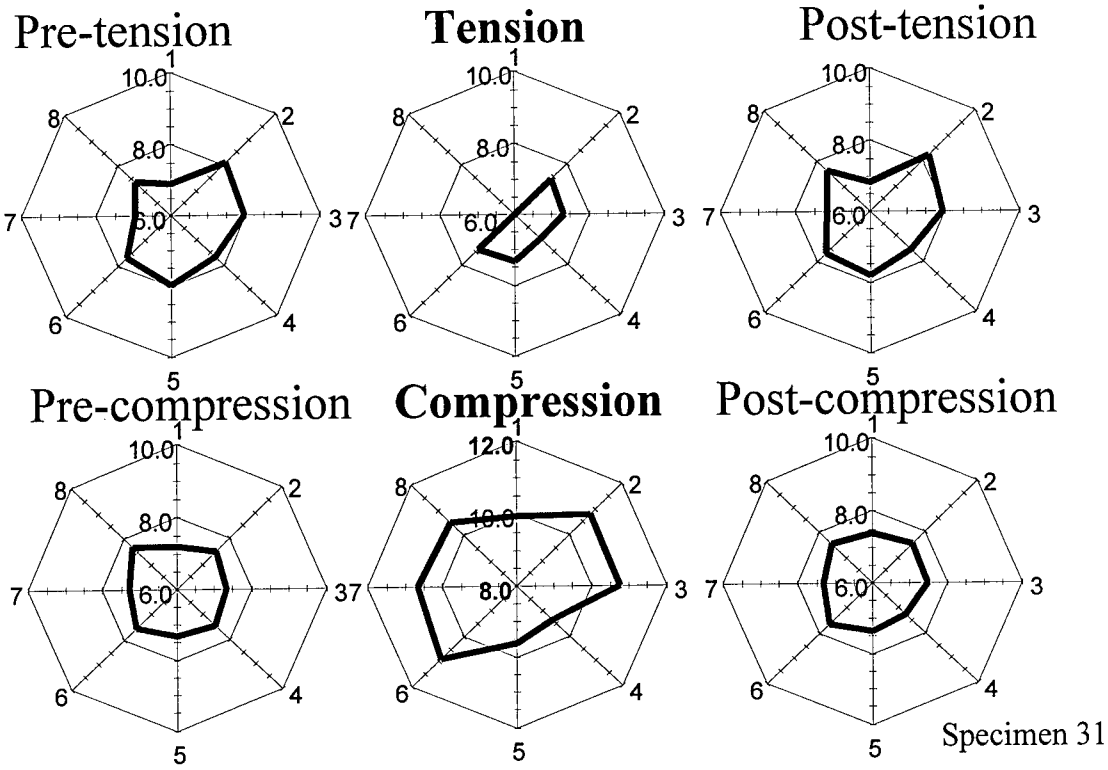

Figure 16. Radar plots of coercivity for sample 31

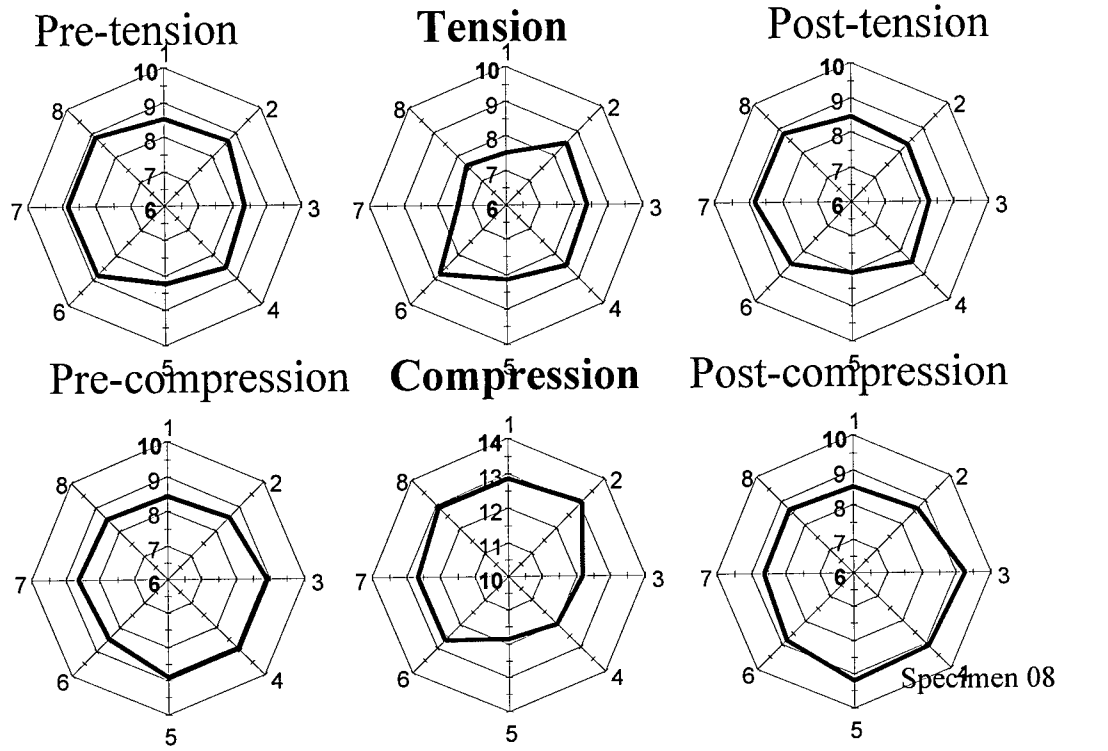

Figure 17. Radar plots of coercivity for sample 08

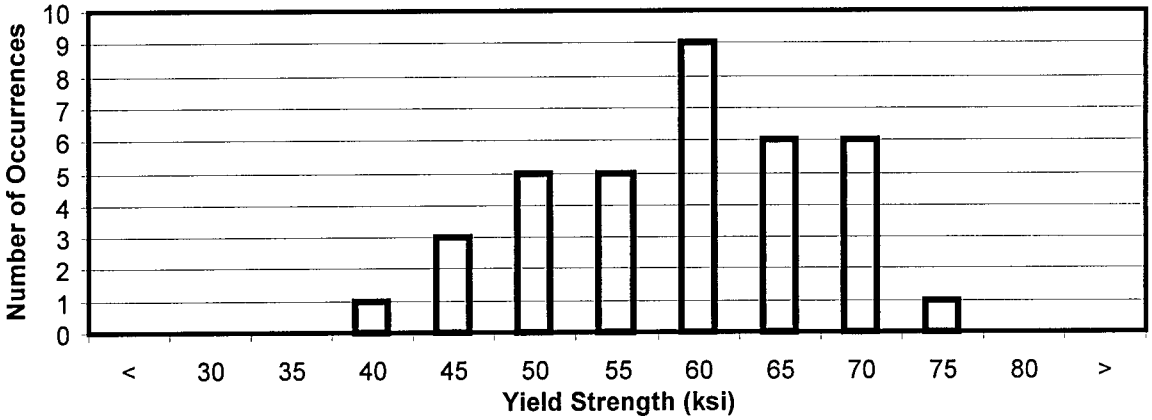

Figure 18. Distribution of yield strength

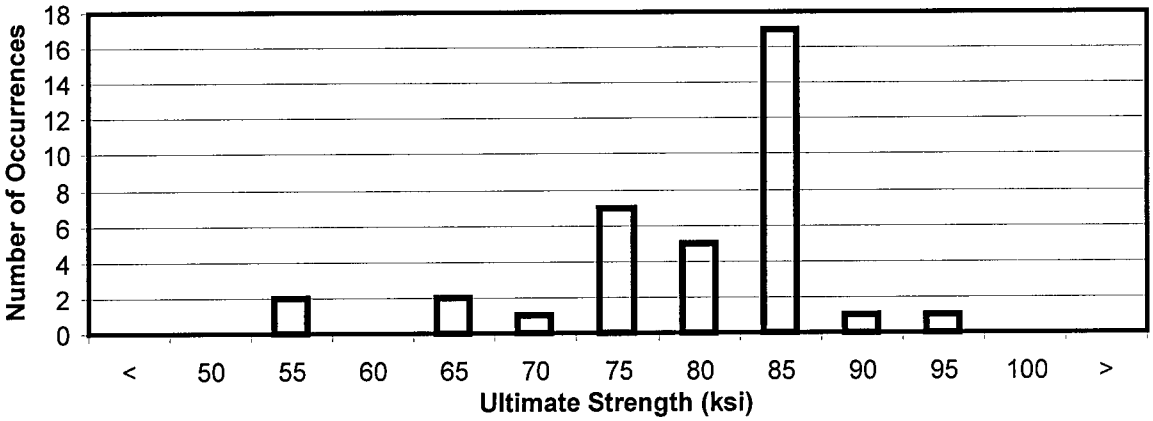

Figure 19. Distribution of ultimate strength

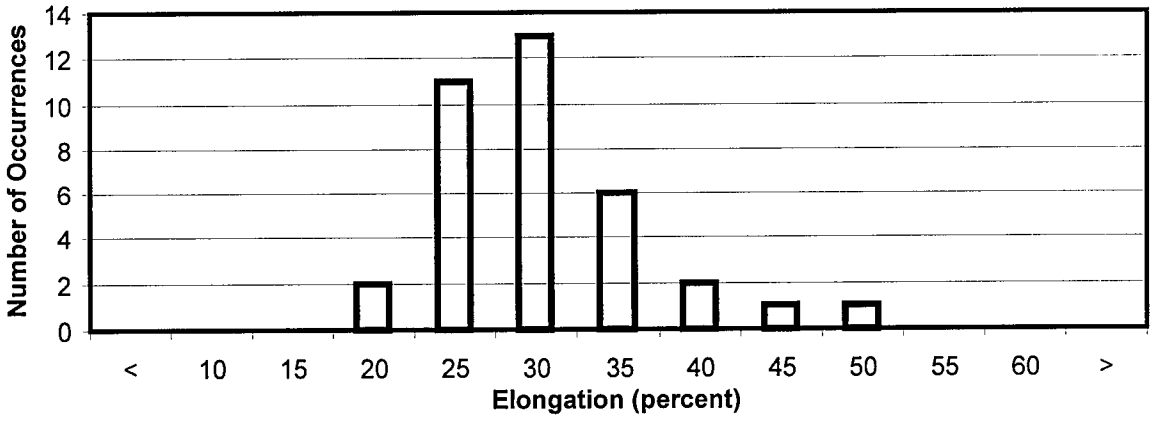

Figure 20. Distribution of elongation

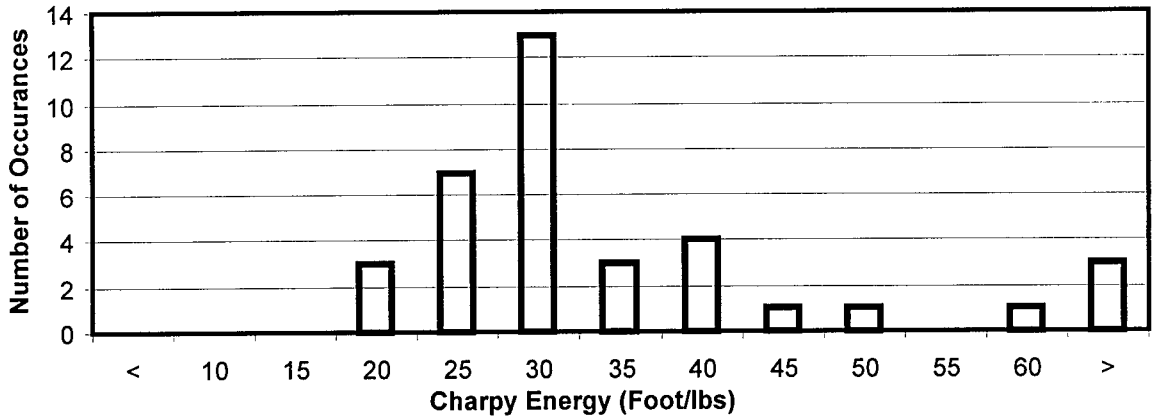

Figure 21. Distribution of Charpy energy

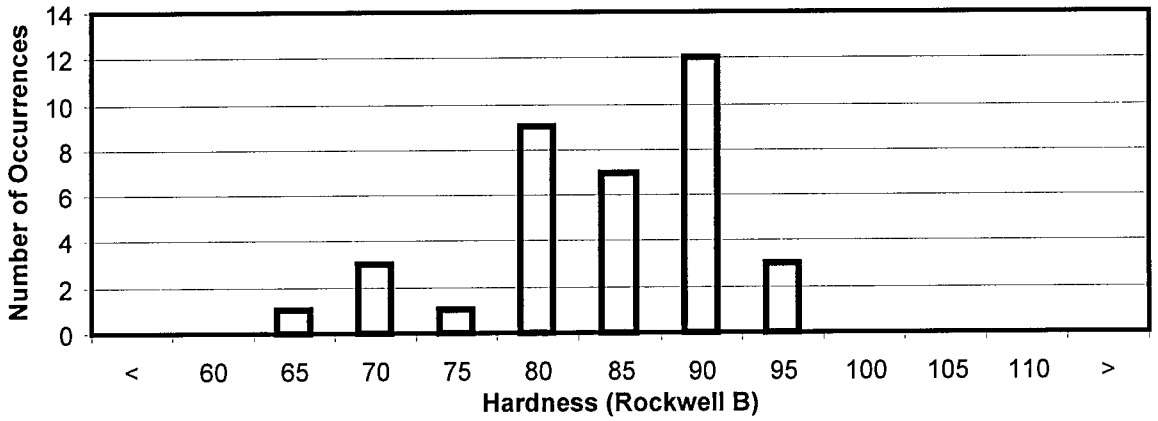

Figure 22. Distribution of hardness

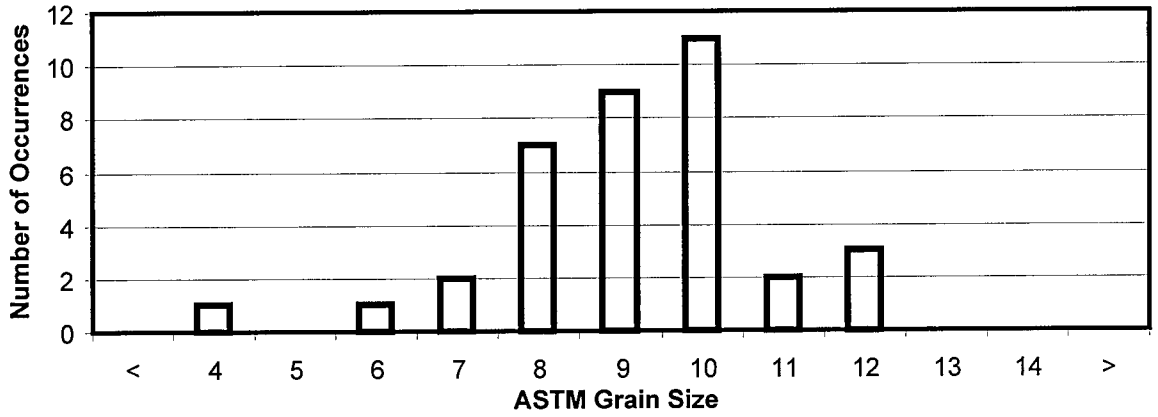

Figure 23. Distribution of grain size

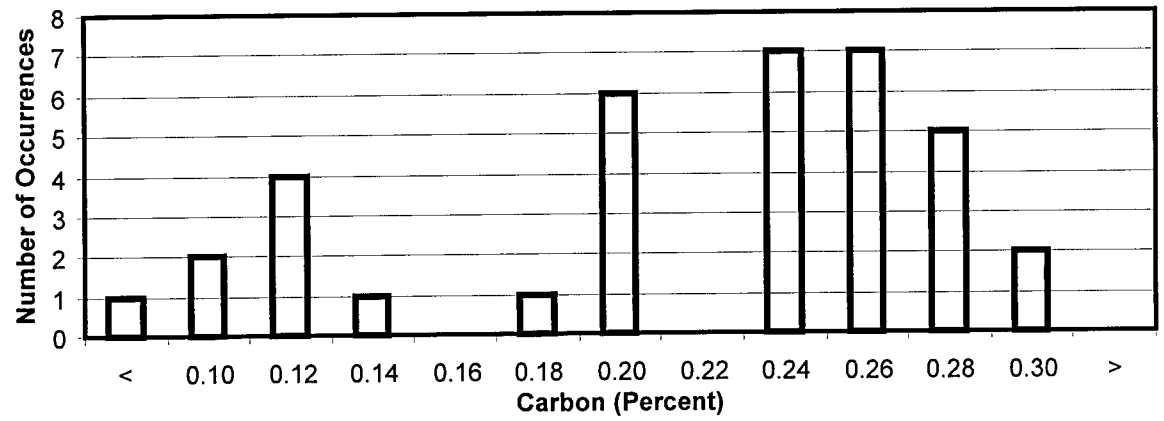

Figure 24. Distribution of carbon

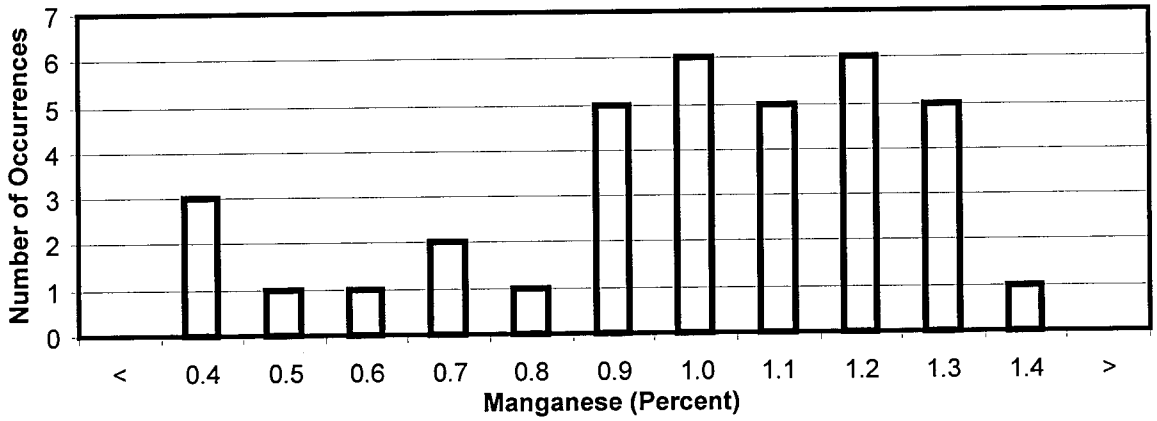

Figure 25. Distribution of manganese

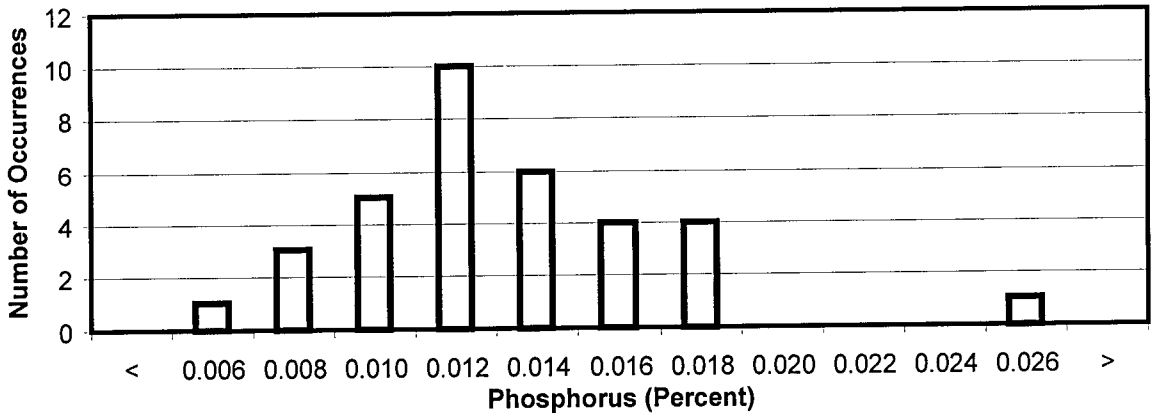

Figure 26. Distribution of phosphorus

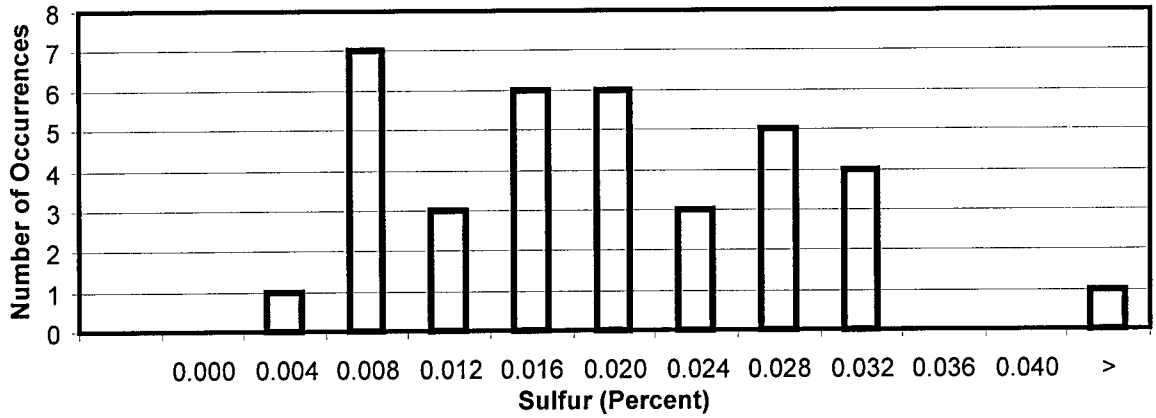

Figure 27. Distribution of sulfur

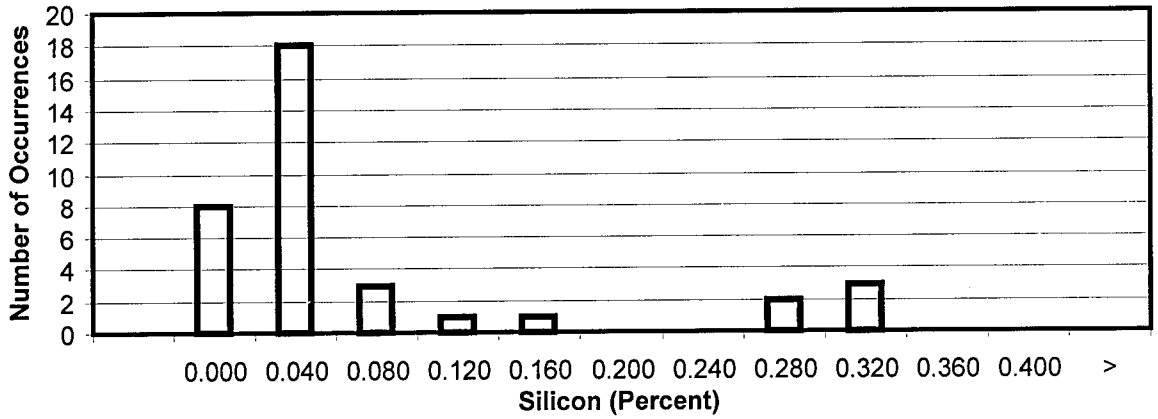

Figure 28. Distribution of silicon

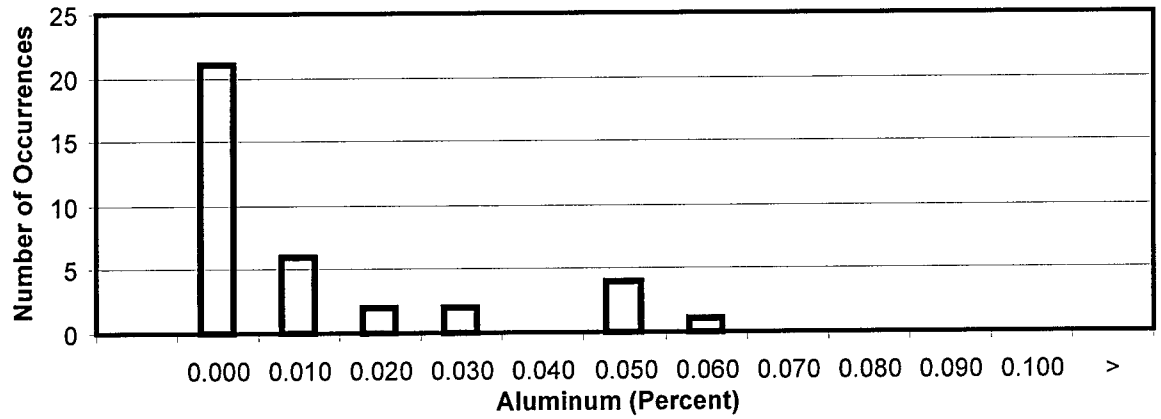

Figure 29. Distribution of aluminum

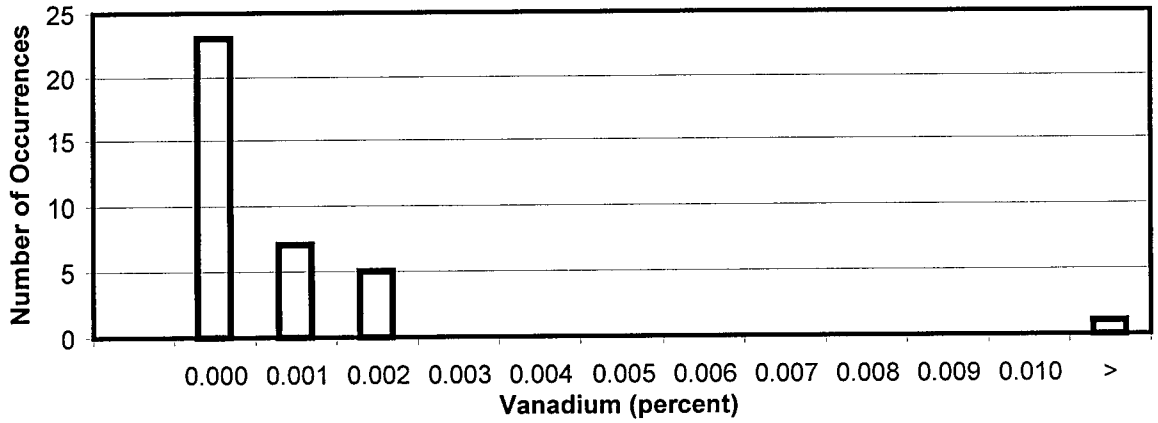

Figure 30. Distribution of vanadium

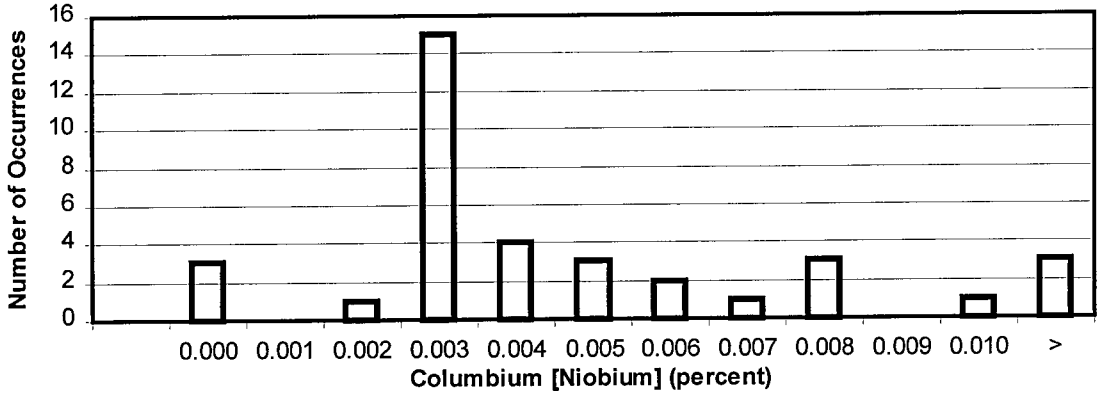

Figure 31. Distribution of columbium (also known as niobium)

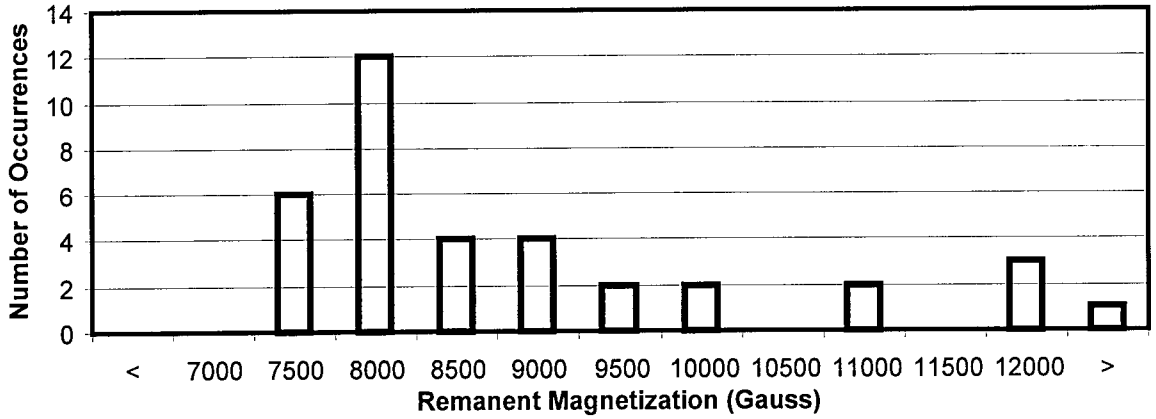

Figure 32. Distribution of remanence

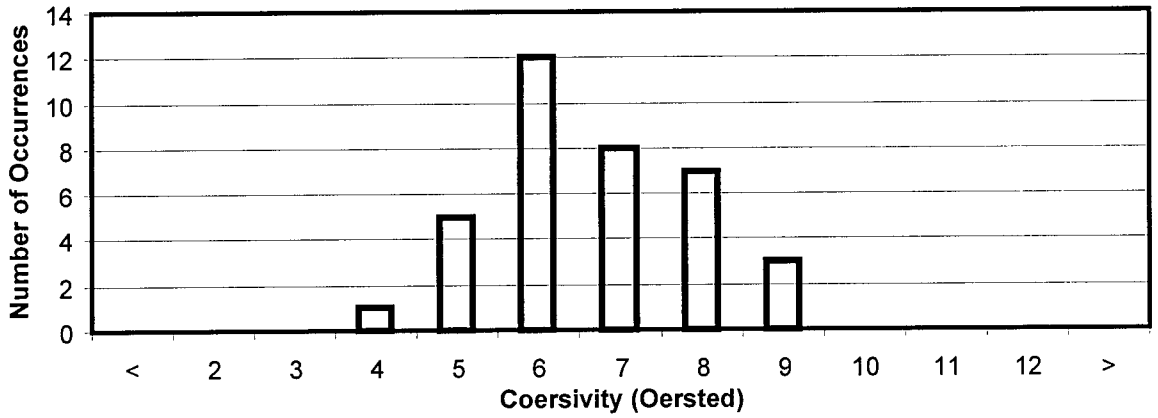

Figure 33. Distribution of coercivity

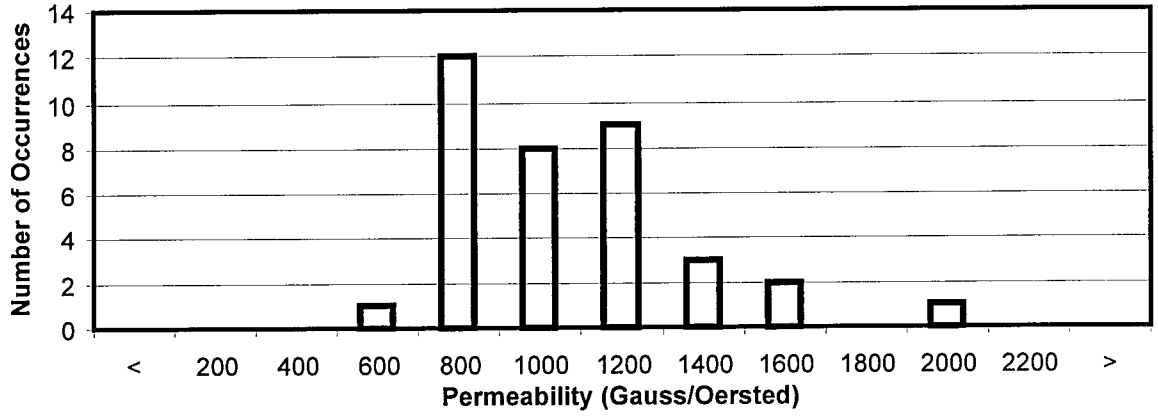

Figure 34. Distribution of permeability

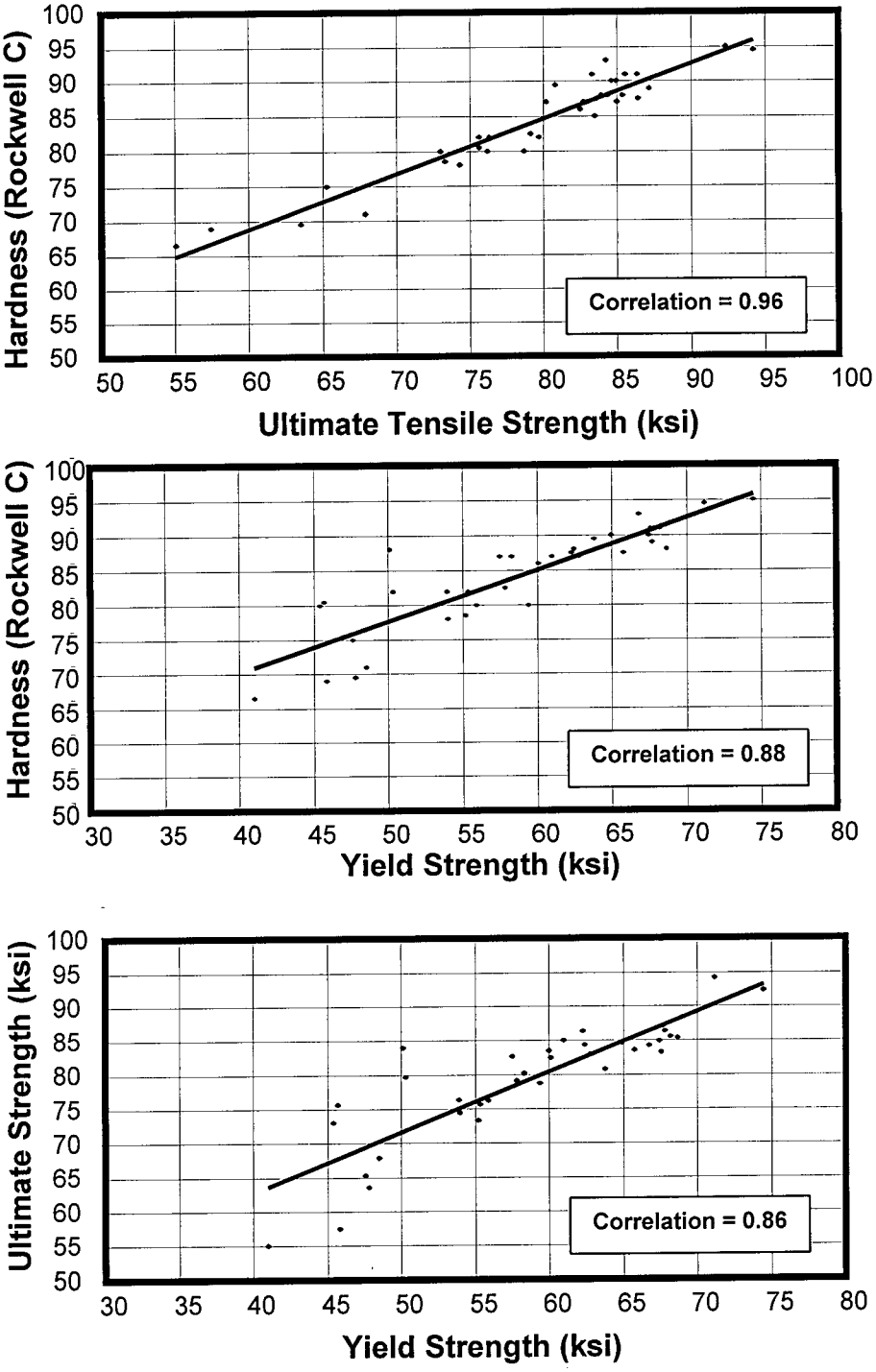

Figure 35. Scatter diagrams for ultimate tensile strength and material hardness, hardness and yield strength, and yield strength and ultimate tensile strength

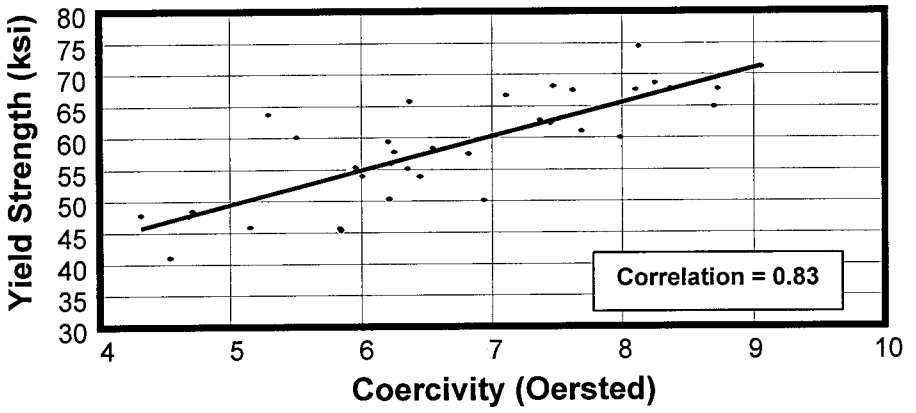

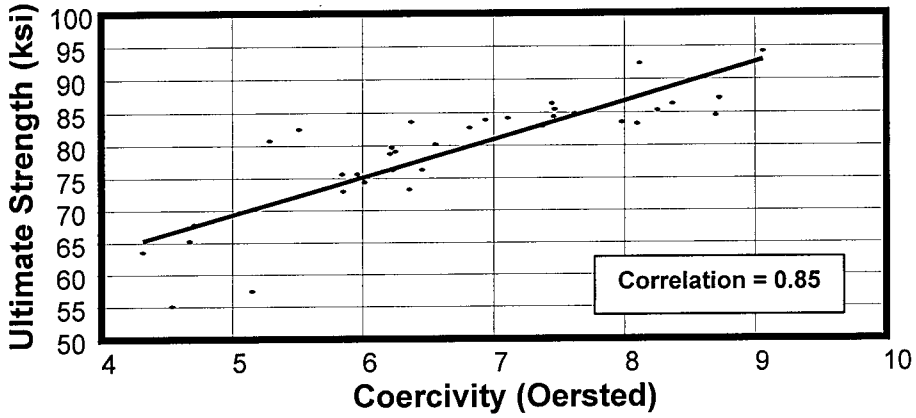

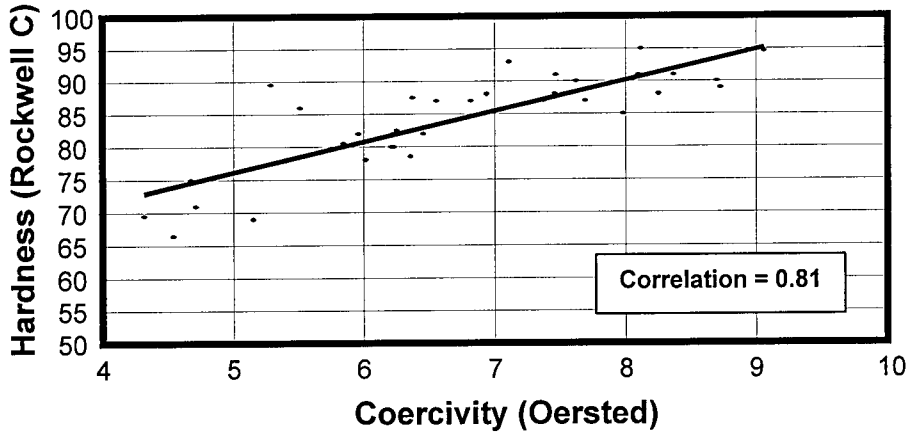

Figure 36. Scatter diagrams for coercive force and hardness, ultimate strength, and yield strength

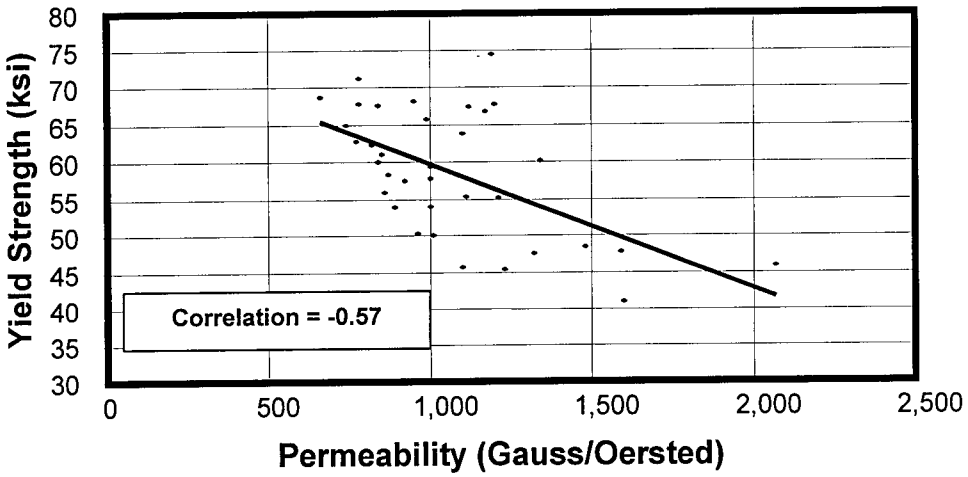

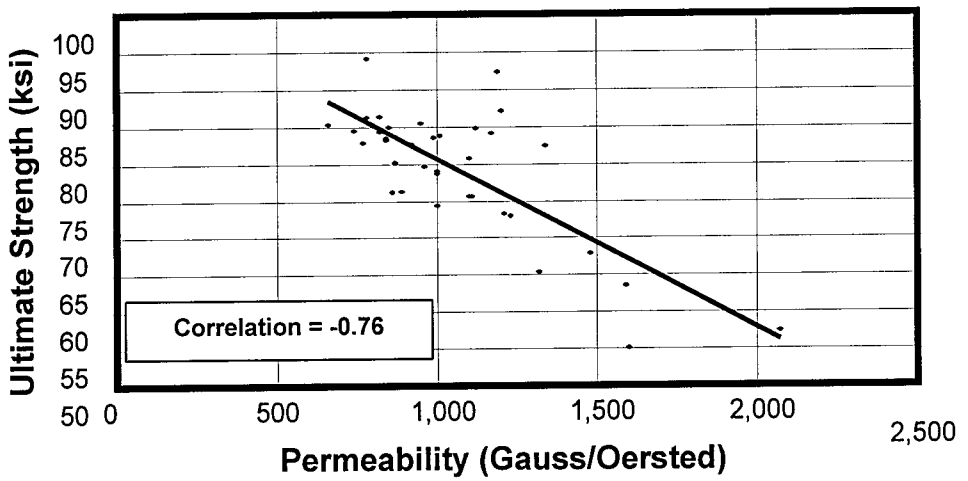

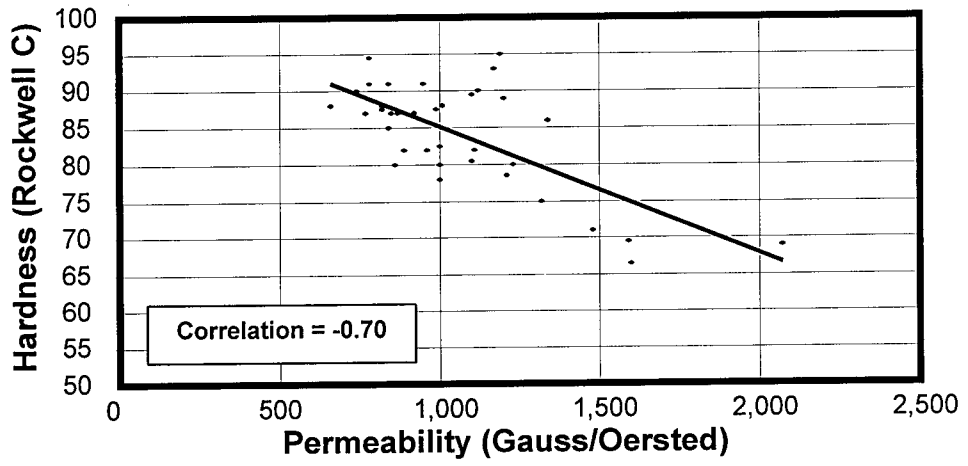

Figure 37. Scatter diagrams for permeability and Charpy energy, yield strength, ultimate strength, elongation, hardness, carbon, manganese, and columbium

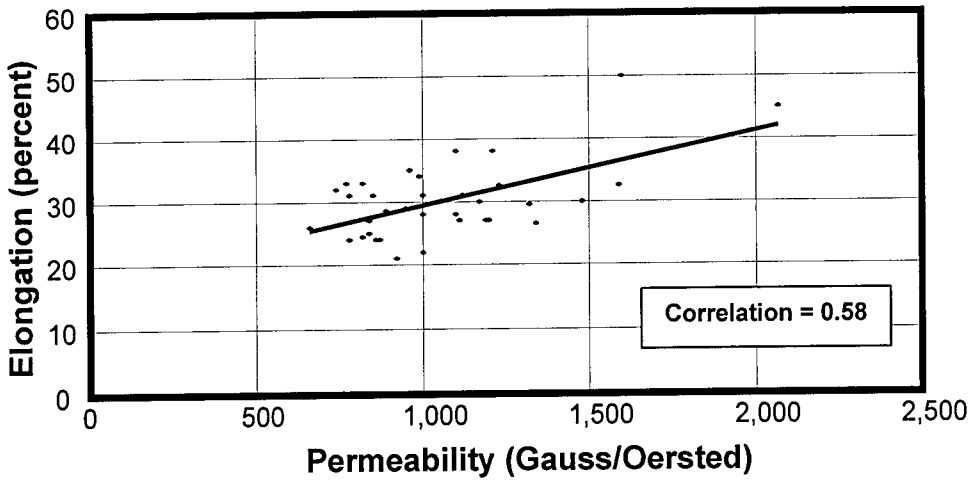

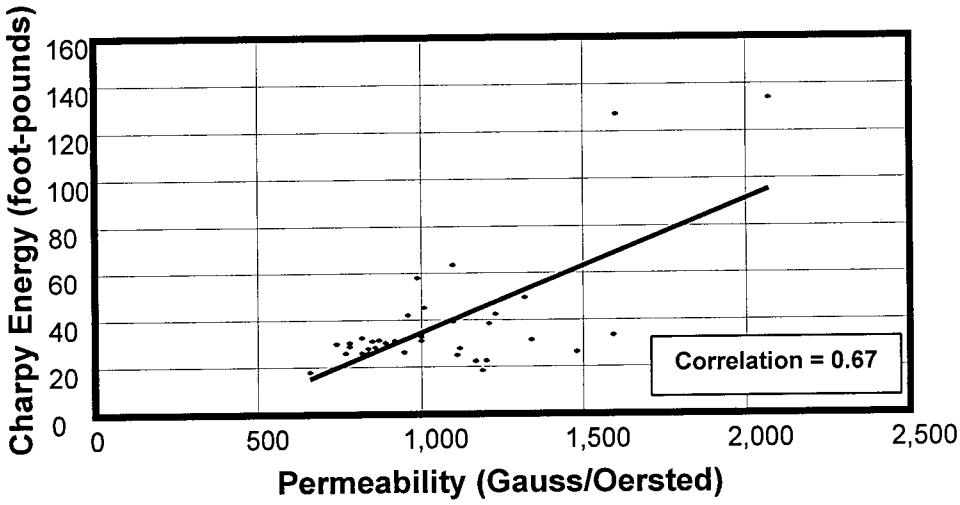

Figure 37. Scatter diagrams for permeability and Charpy energy, yield strength, ultimate strength, elongation, hardness, carbon, manganese, and columbium (continued)

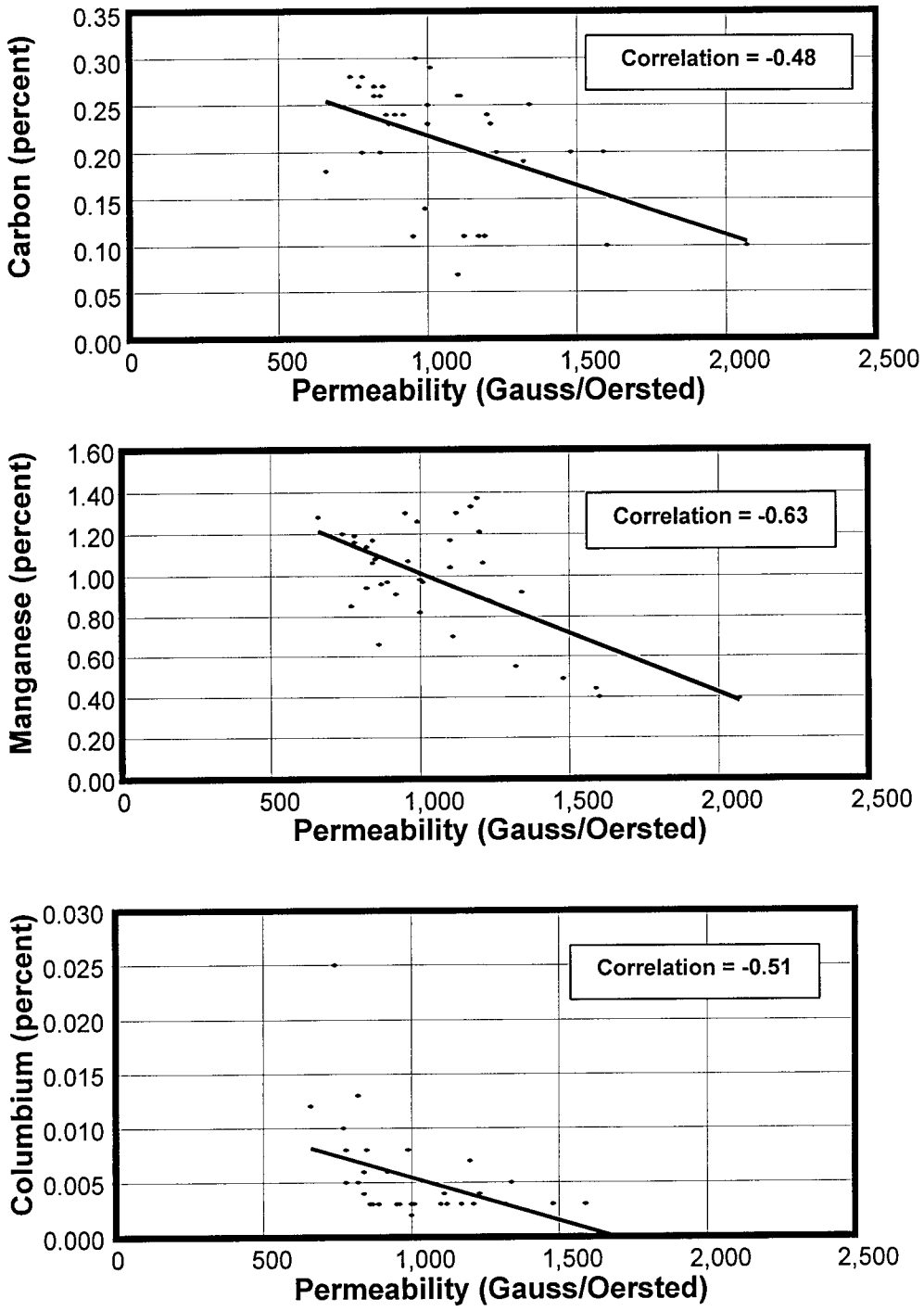

Figure 37. Scatter diagrams for permeability and Charpy energy, yield strength, ultimate strength, elongation, hardness, carbon, manganese, and columbium (continued)

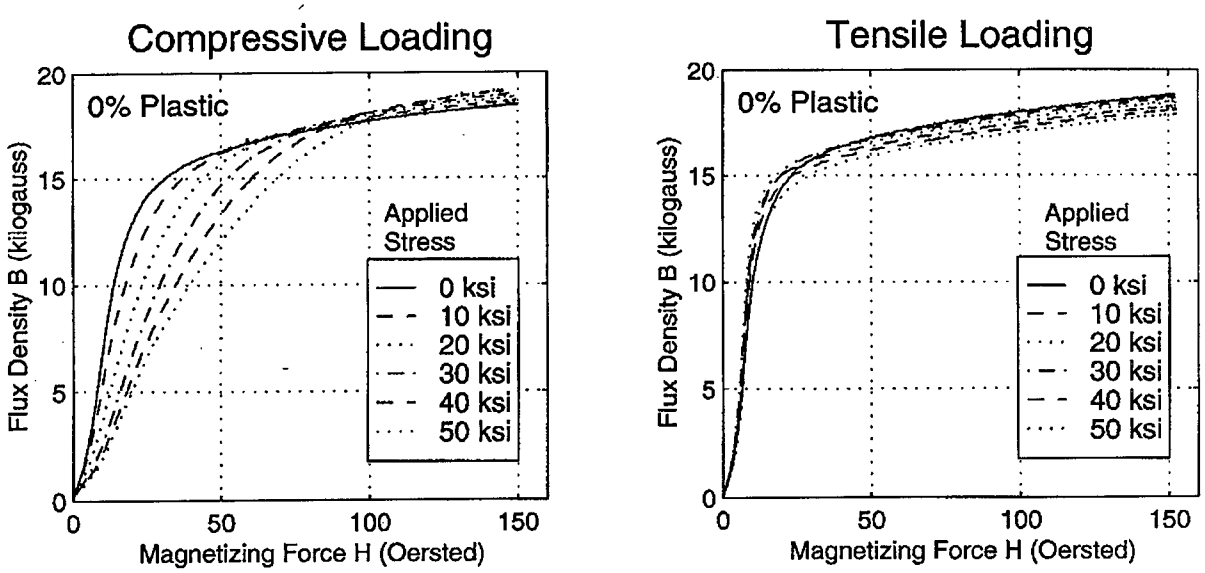

Figure 38. Typical B-H curves for elastic compressive and tensile stresses

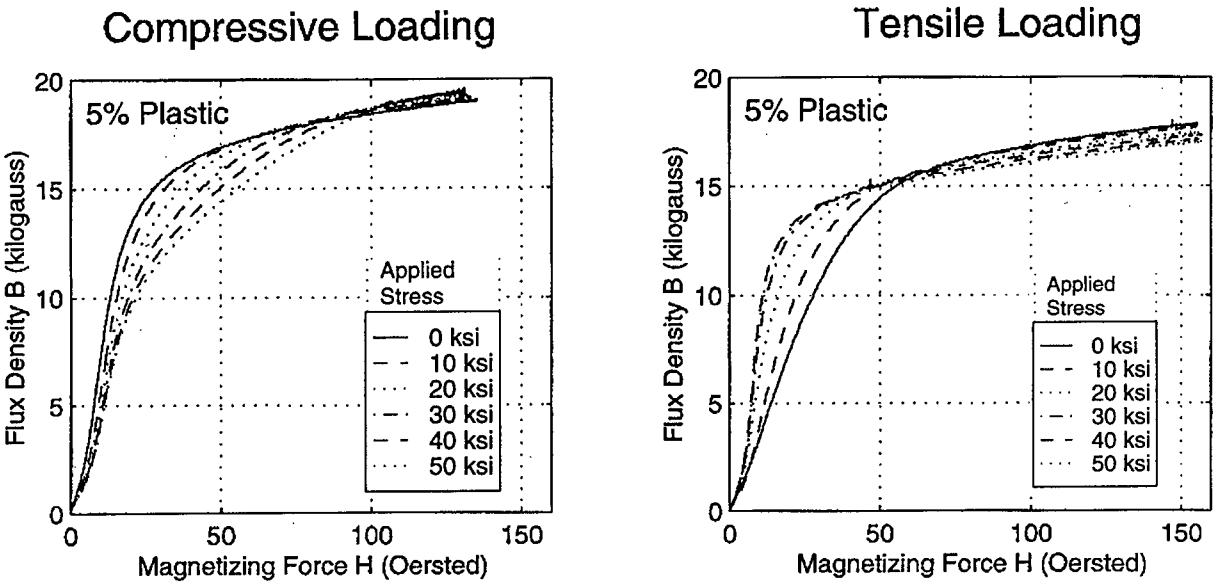

Figure 39. Typical B-H curves for compressive and tensile stresses and permanent plastic strains

Appendix A

Magnetic, Chemical, Mechanical, and Metallurgical Properties of 36 Material Samples

Material 24-06

Numerical Values		
Diameter		24.03 in.
Thickness		0.292 in.
Charpy		
Energy		22 ft-lbs
Shear		100%
Tensile		
Yield		66.79 ksi
Ultimate		84.23 ksi
Elongation		30%
Hardness (Rockwell B)		93
Grain Size (ASTM #)		11.5
Magnetic Measures		
Remanence		12,130 G
Coercivity		7.11 Oe
Permeability		1,170 G/Oe
H at Max Permeability		10 Oe
Chemical Composition		
Carbon	C	0.11%
Manganese	Mn	1.33%
Phosphorus	P	0.012%
Sulfur	S	0.008%
Silicon	Si	0.290%
Aluminum	Al	0.051%
Vanadium	V	0.000%
Columbium	Cb	0.003%

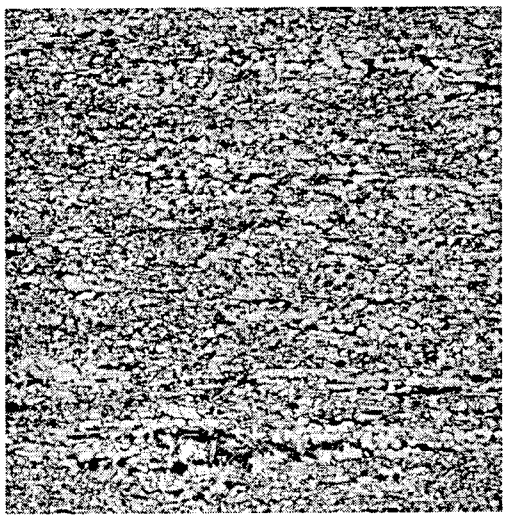

100X Picral + Nital Etch OB366

The microstructure is somewhat banded and consists of a mixture of ferrite and pearlite with perhaps some bainite. The steel exhibits a duplex grain size with the finer grains having a grain size of ASTM 11 and the larger ferrite grains having a grain size of ASTM 8.5. It appears that this steel may have been controlled rolled with a low finishing temperature.

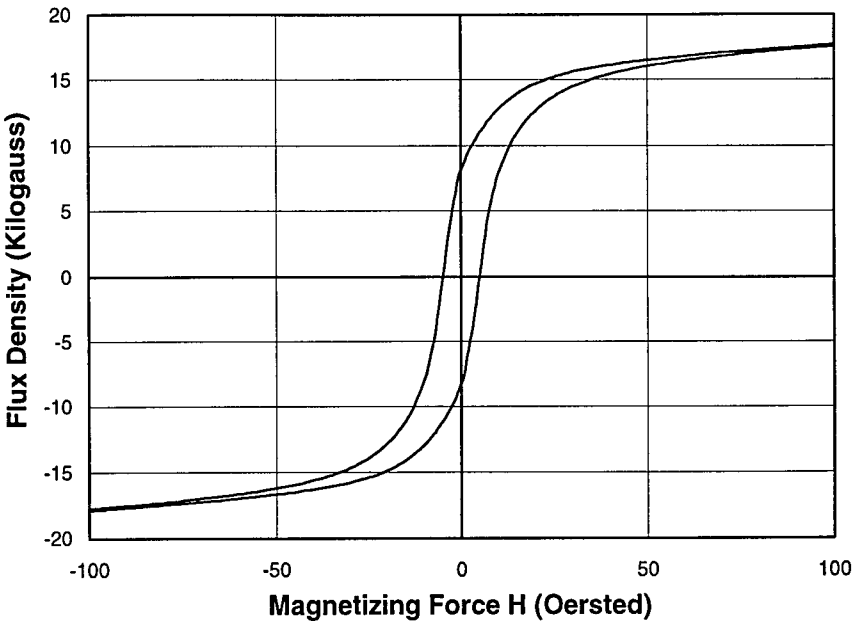

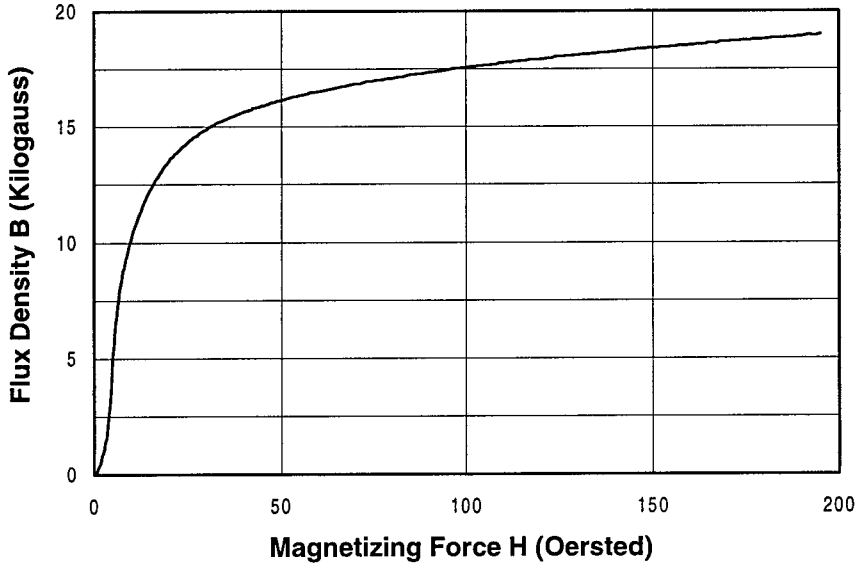

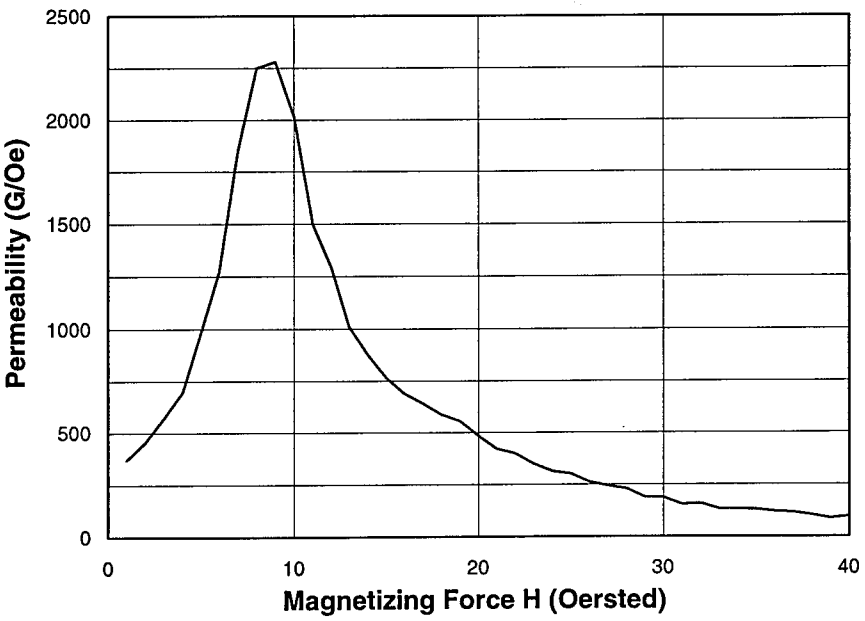

Material 24-07

Numerical Values		
Diameter		24.03 in.
Thickness		0.290 in.
Charpy		
Energy		26 ft-lbs
Shear		100%
Tensile		
Yield		68.22 ksi
Ultimate		85.55 ksi
Elongation		29%
Hardness (Rockwell B)		91
Grain Size (ASTM #)		11.5
Magnetic Measures		
Remanence		10,860 G
Coercivity		7.47 Oe
Permeability		950 G/Oe
H at Max Permeability		10 Oe
Chemical Composition		
Carbon	C	0.11%
Manganese	Mn	1.30%
Phosphorus	P	0.011%
Sulfur	S	0.008%
Silicon	Si	0.290%
Aluminum	Al	0.053%
Vanadium	V	0.000%
Columbium	Cb	0.003%

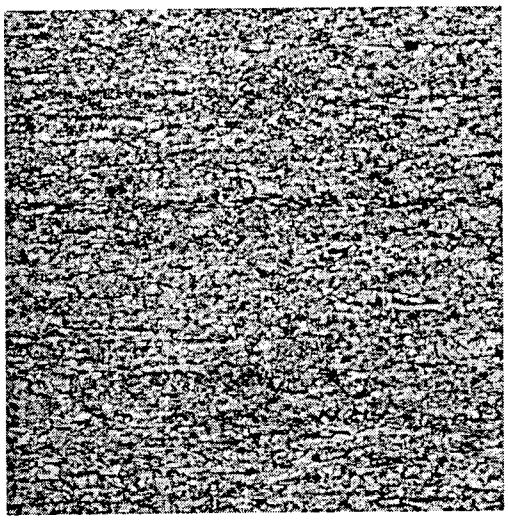

100X Picral + Nital Etch OB367

The microstructure consists of a mixture of fine-grained polygonal and elongated (distorted) ferrite and pearlite/bainite. The grain was judged to be ASTM 11.5. The steel appeared to have been controlled rolled with a low finishing temperature.

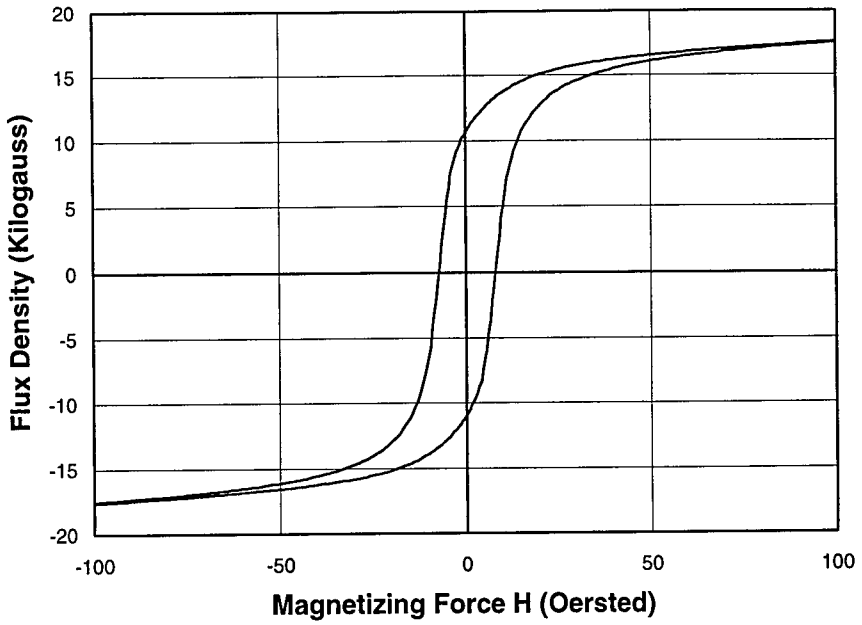

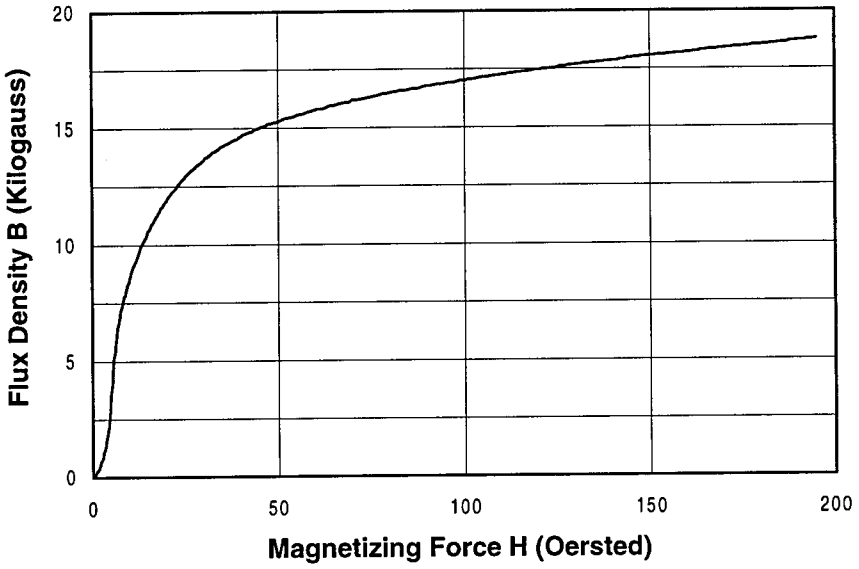

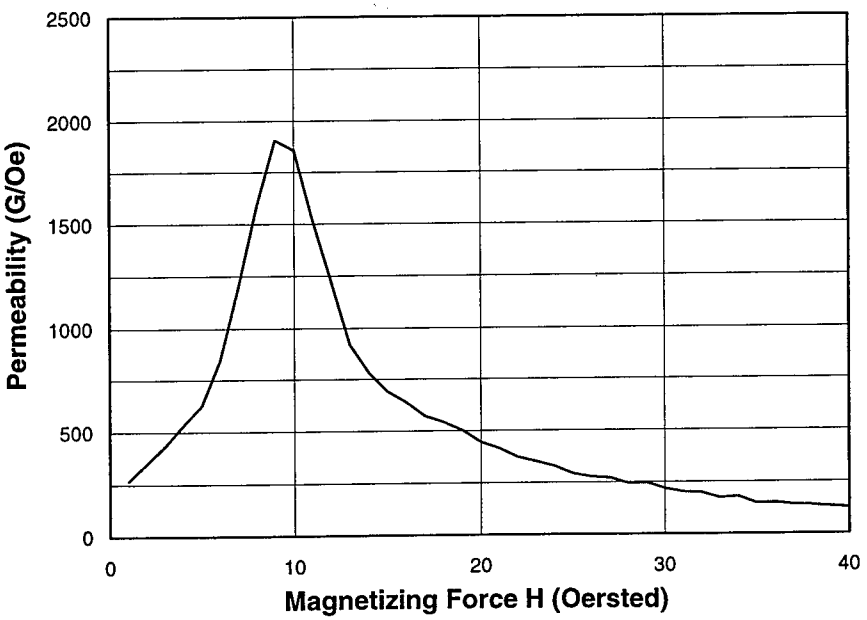

Material 24-08

Numerical Values		
Diameter		24.03 in.
Thickness		0.291 in.
Charpy		
Energy		28 ft-lbs
Shear		100 %
Tensile		
Yield		67.48 ksi
Ultimate		84.89 ksi
Elongation		31%
Hardness (Rockwell B)		90
Grain Size (ASTM #)		10
Magnetic Measures		
Remanence		11,210 G
Coercivity		7.62 Oe
Permeability		1,120 G/Oe
H at Max Permeability		11 Oe
Chemical Composition		
Carbon	C	0.11%
Manganese	Mn	1.30%
Phosphorus	P	0.012%
Sulfur	S	0.008%
Silicon	Si	0.300%
Aluminum	Al	0.052%
Vanadium	V	0.000%
Columbium	Cb	0.003%

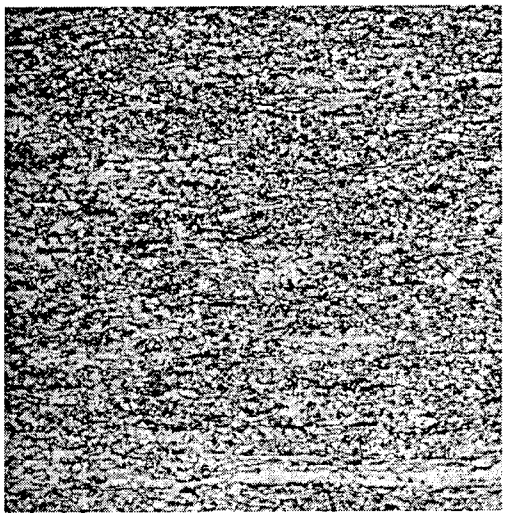

100X Picral + Nital Etch OB368

The microstructure consists of a slightly banded mixture of fine-grained polygonal and elongated ferrite and pearlite/bainite. The ferrite grains exhibit a duplex grain size with finer grains being ASTM 11.5 and the larger grains being ASTM 9. The steel appears to have been controlled rolled with a low finishing temperature.

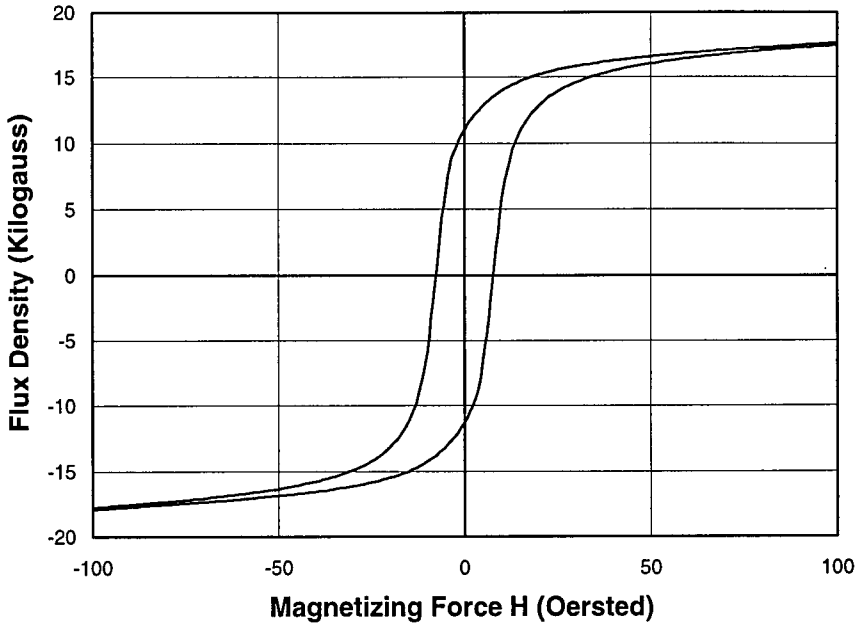

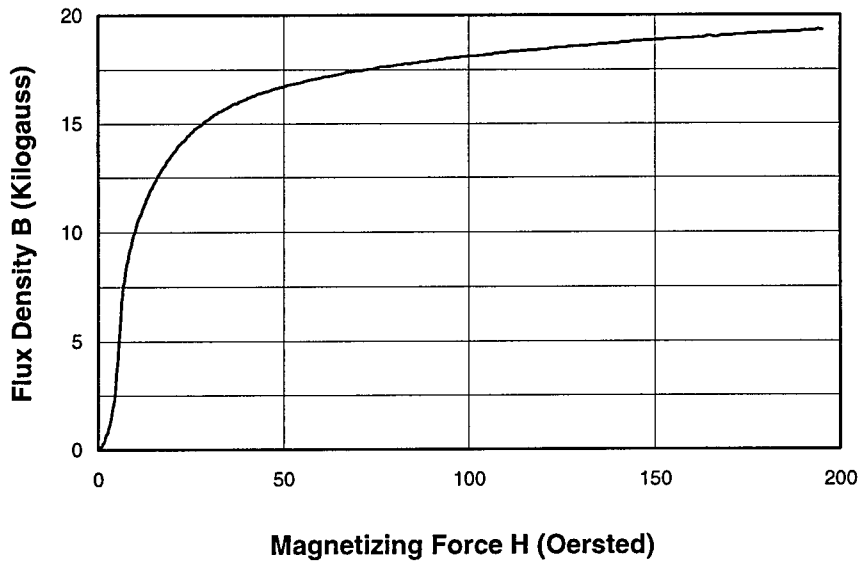

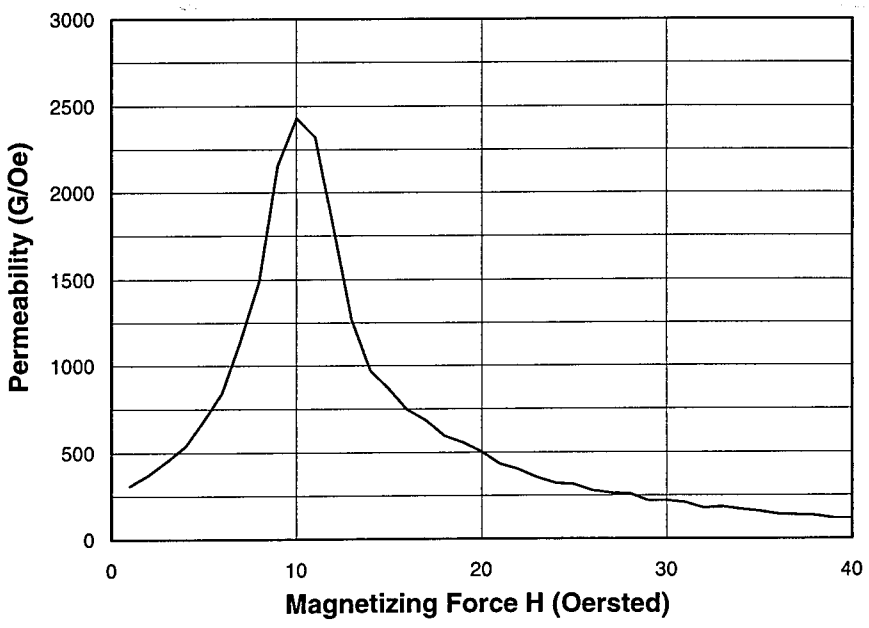

Material 24-09

Numerical Values		
Diameter		24.03 in.
Thickness		0.288 in.
Charpy		
Energy		18 ft-lbs
Shear		100%
Tensile		
Yield		74.45 ksi
Ultimate		92.36 ksi
Elongation		27%
Hardness (Rockwell B)		95
Grain Size (ASTM #)		12
Magnetic Measures		
Remanence		11,880 G
Coercivity		8.12 Oe
Permeability		1,190 G/Oe
H at Max Permeability		11 Oe
Chemical Composition		
Carbon	C	0.11%
Manganese	Mn	1.37%
Phosphorus	P	0.011%
Sulfur	S	0.009%
Silicon	Si	0.310%
Aluminum	Al	0.059%
Vanadium	V	0.034%
Columbium	Cb	0.004%

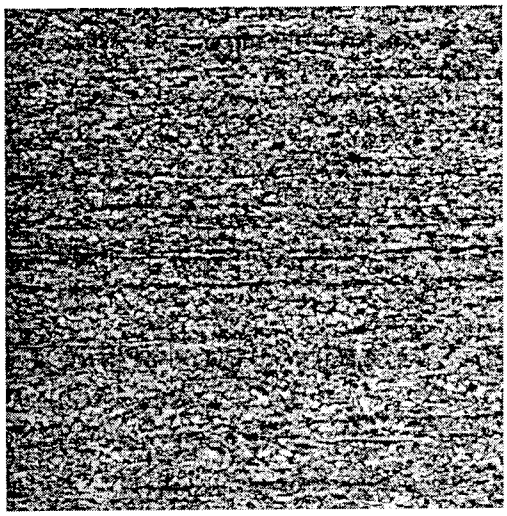

100X Picral + Nital Etch OB369

The microstructure consists of a somewhat banded mixture of fine-grained, somewhat elongated ferrite and pearlite/bainite. The grain size was judged to be ASTM 12. The steel appears to have been controlled rolled with a relatively low finishing temperature.

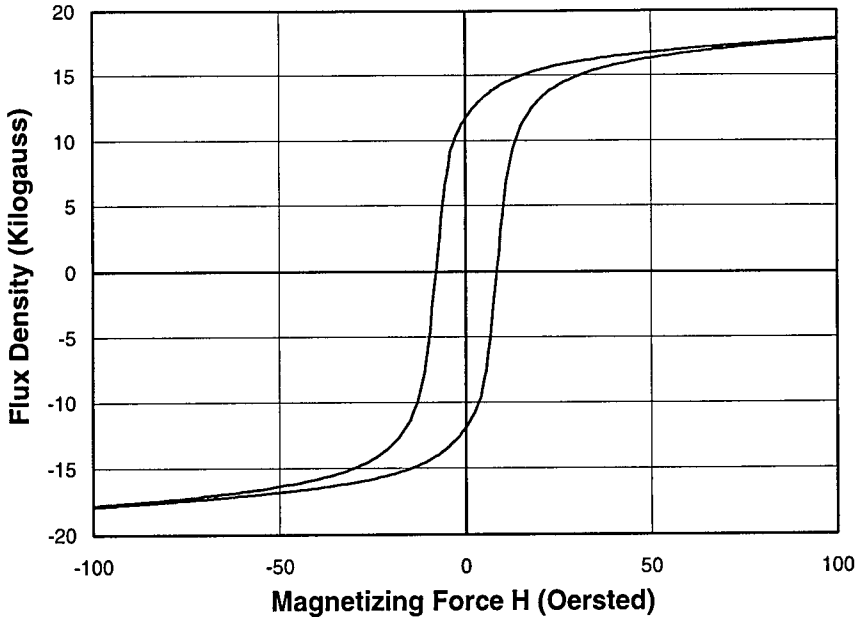

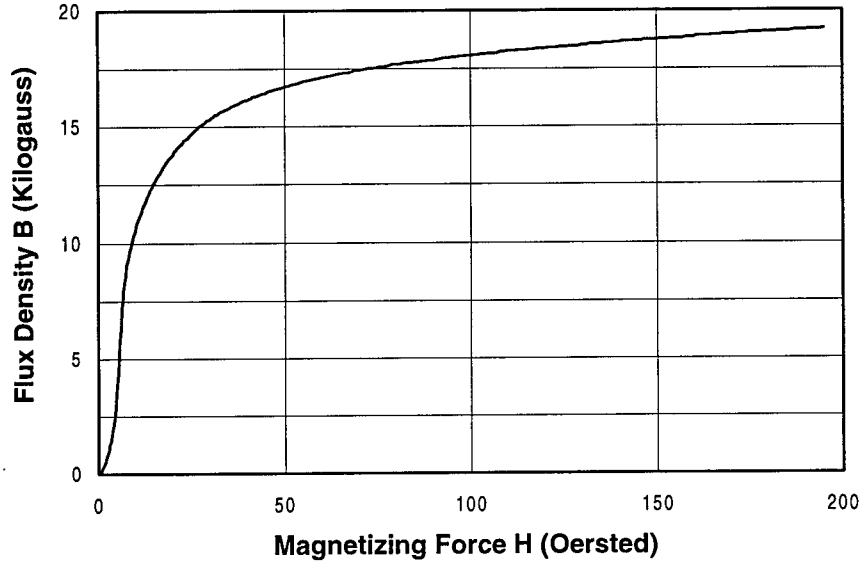

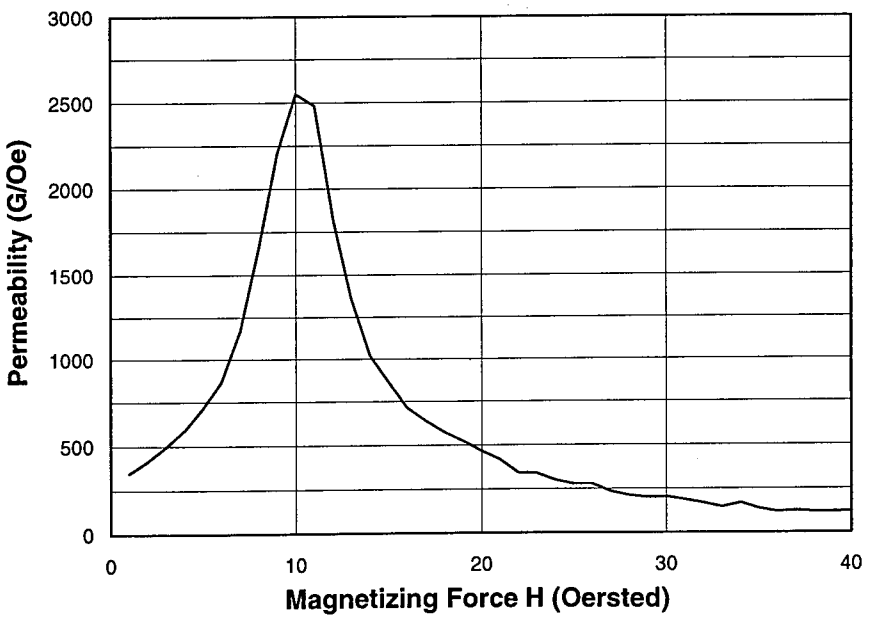

Material 24-10

Numerical Values		
Diameter		24.03 in.
Thickness		0.314 in.
Charpy		
Energy		127 ft-lbs
Shear		100%
Tensile		
Yield		40.98 ksi
Ultimate		55.06 ksi
Elongation		50%
Hardness (Rockwell B)		66.5
Grain Size (ASTM #)		9
Magnetic Measures		
Remanence		12,080 G
Coercivity		4.54 Oe
Permeability		1,600 G/Oe
H at Max Permeability		5 Oe
Chemical Composition		
Carbon	C	0.10%
Manganese	Mn	0.40%
Phosphorus	P	0.018%
Sulfur	S	0.009%
Silicon	Si	0.006%
Aluminum	Al	0.017%
Vanadium	V	0.000%
Columbium	Cb	0.000%

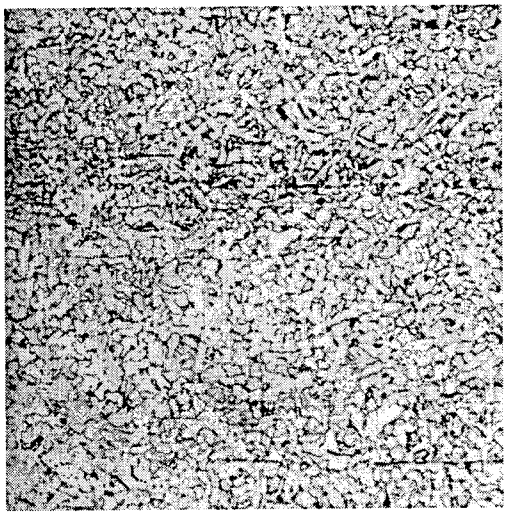

100X Picral + Nital Etch OB370

The microstructure consists of a mixture of equiaxed ferrite and pearlite with a low pearlite content. The ferrite grain size is ASTM 9. There is slight centerline segregation with a band that contains slightly more pearlite than the surrounding steel.

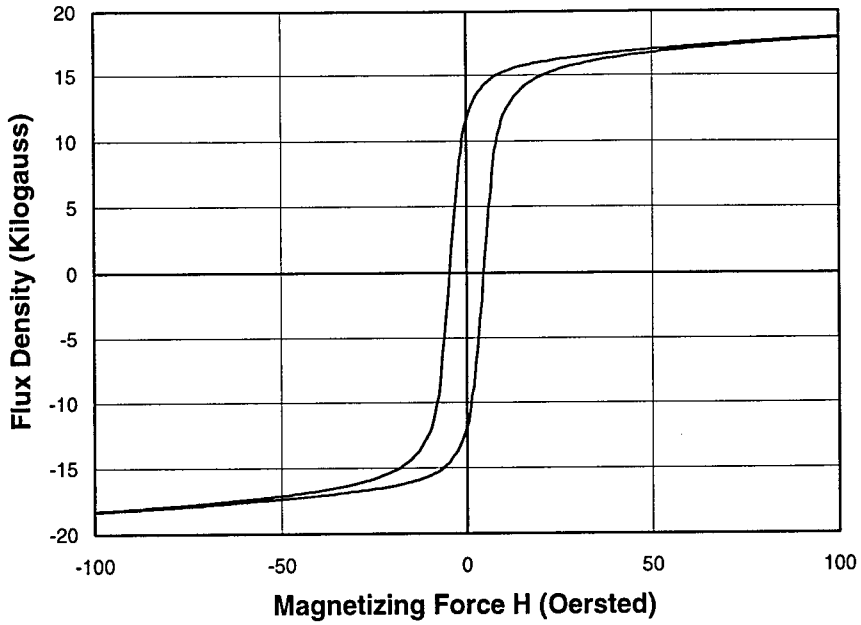

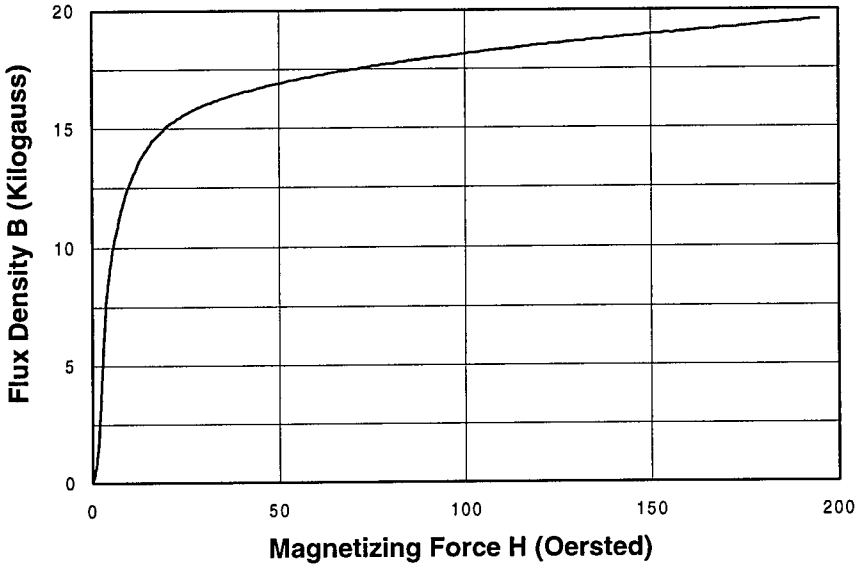

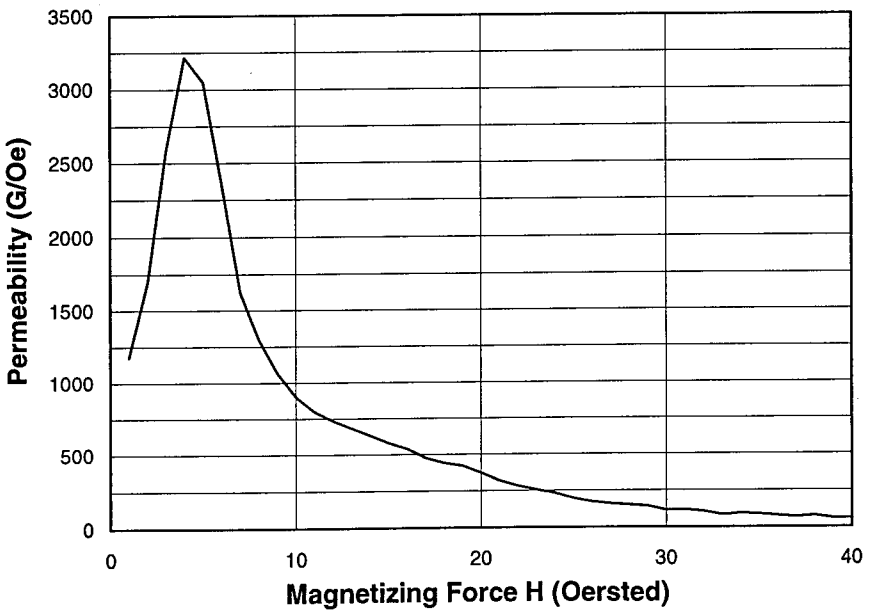

Material 24-11

Numerical Values		
Diameter		24.03 in.
Thickness		0.314 in.
Charpy		
Energy		134 ft-lbs
Shear		100%
Tensile		
Yield		45.85 ksi
Ultimate		57.41 ksi
Elongation		45%
Hardness (Rockwell B)		69
Grain Size (ASTM #)		9
Magnetic Measures		
Remanence		12,410 G
Coercivity		5.15 Oe
Permeability		2,070 G/Oe
H at Max Permeability		6 Oe
Chemical Composition		
Carbon	C	0.10%
Manganese	Mn	0.39%
Phosphorus	P	0.017%
Sulfur	S	0.008%
Silicon	Si	0.005%
Aluminum	Al	0.014%
Vanadium	V	0.000%
Columbium	Cb	0.000%

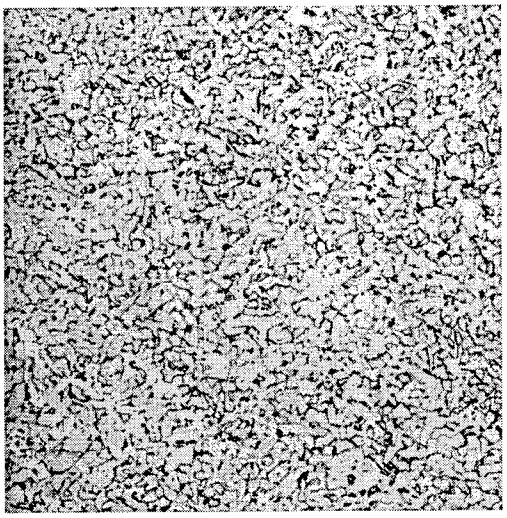

100X Picral + Nital Etch OB371

The microstructure consists of a mixture of equiaxed ferrite and pearlite with a relatively low pearlite content. The ferrite grain size is ASTM 9.

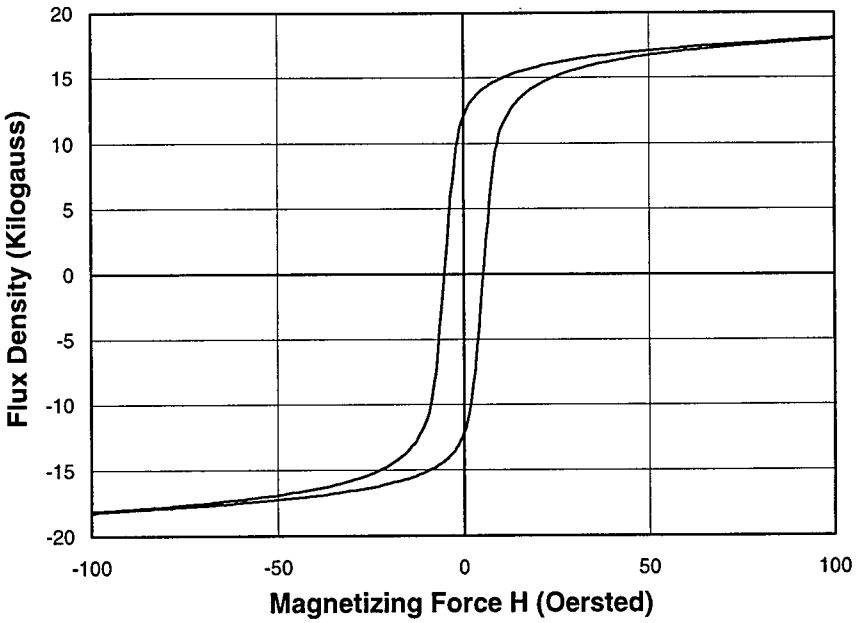

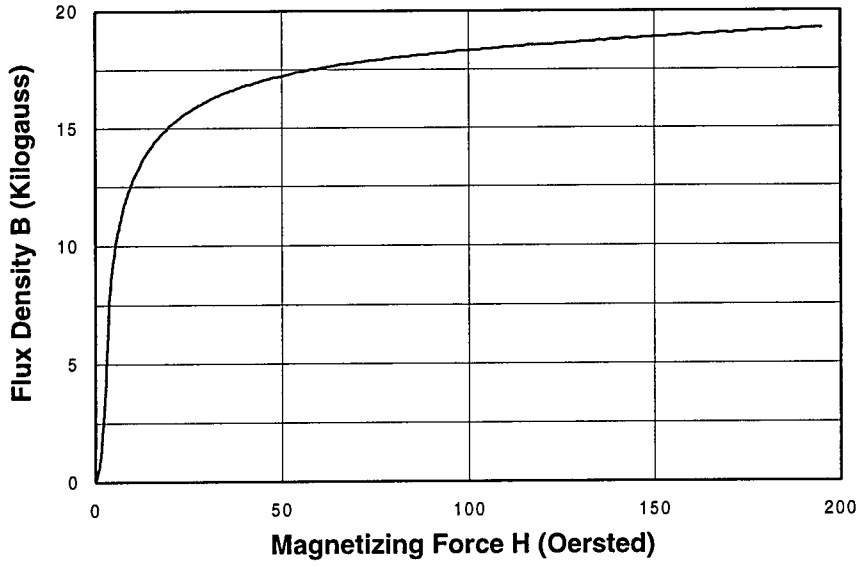

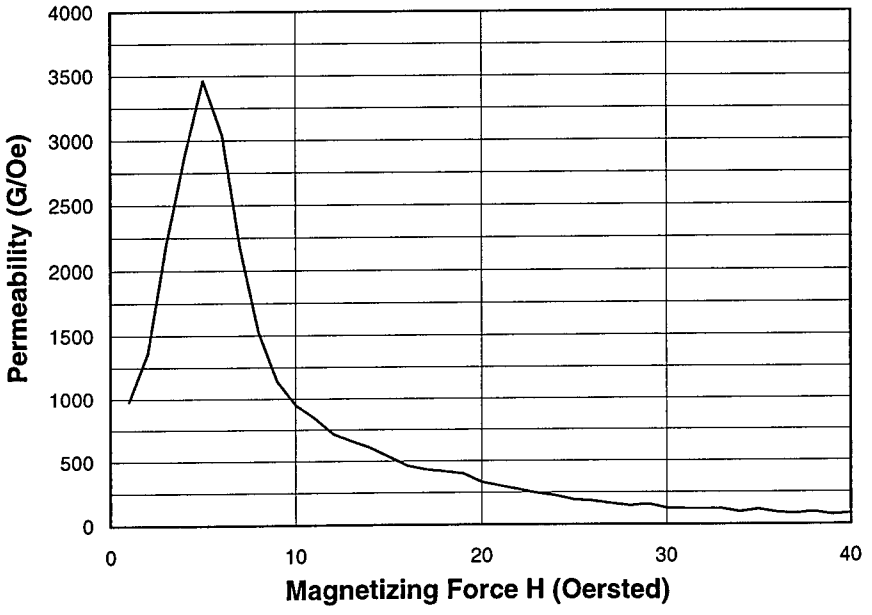

Material 24-13

Numerical Values		
Diameter		24.11 in.
Thickness		0.310 in.
Charpy		
Energy		26 ft-lbs
Shear		100%
Tensile		
Yield		67.59 ksi
Ultimate		83.29 ksi
Elongation		27%
Hardness (Rockwell B)		91
Grain Size (ASTM #)		9.5
Magnetic Measures		
Remanence		8,130 G
Coercivity		8.1 Oe
Permeability		840 G/Oe
H at Max Permeability		10 Oe
Chemical Composition		
Carbon	C	0.20%
Manganese	Mn	1.17%
Phosphorus	P	0.009%
Sulfur	S	0.013%
Silicon	Si	0.007%
Aluminum	Al	0.000%
Vanadium	V	0.000%
Columbium	Cb	0.006%

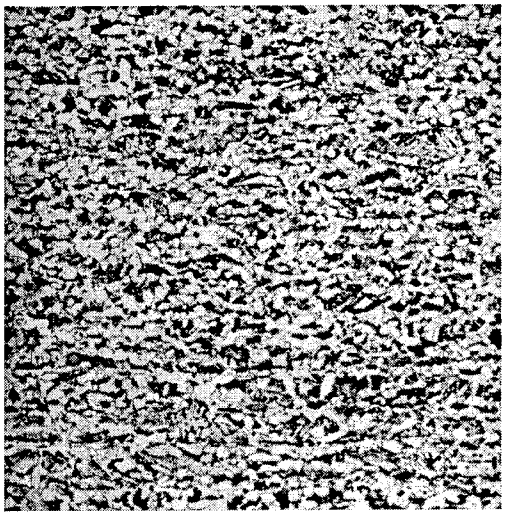

100X Picral + Nital Etch OB373

The microstructure consists of a slightly banded mixture of ferrite and pearlite. The ferrite grain size is ASTM 9.5.

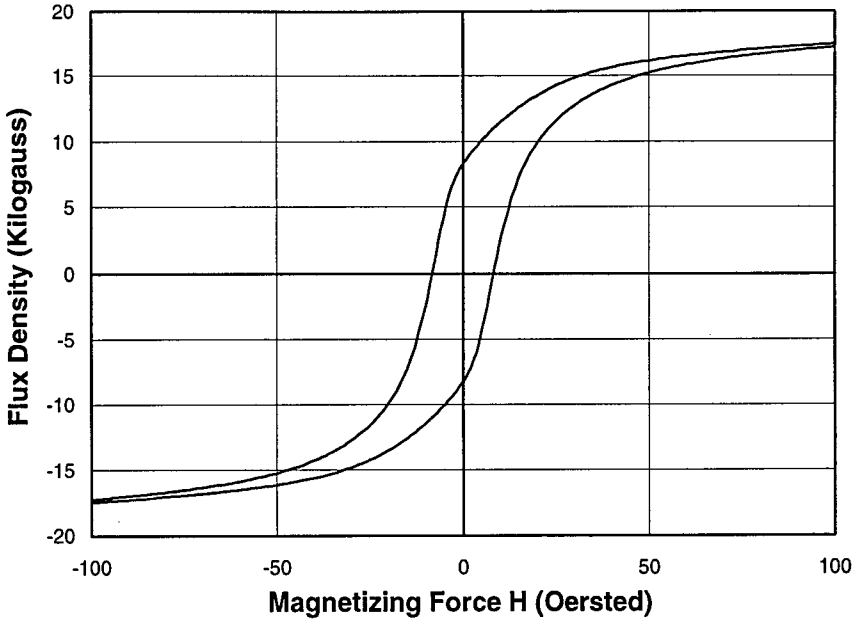

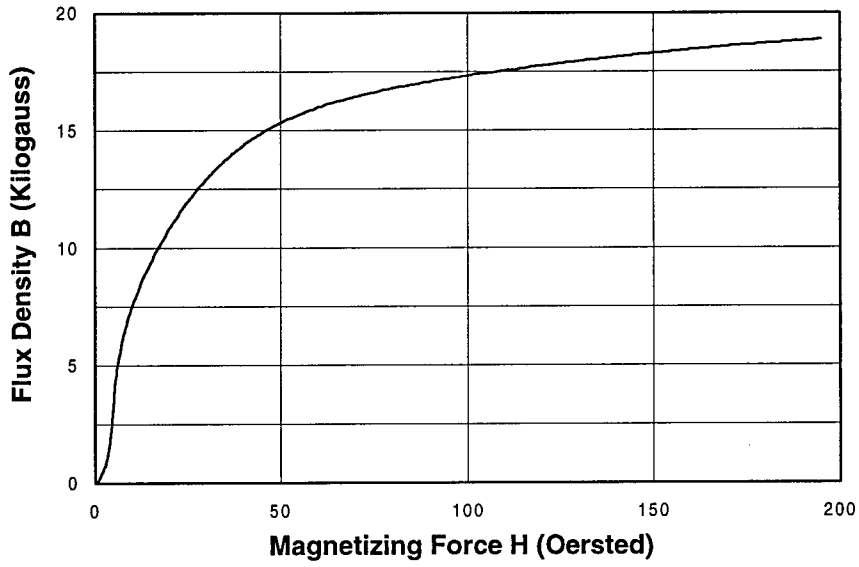

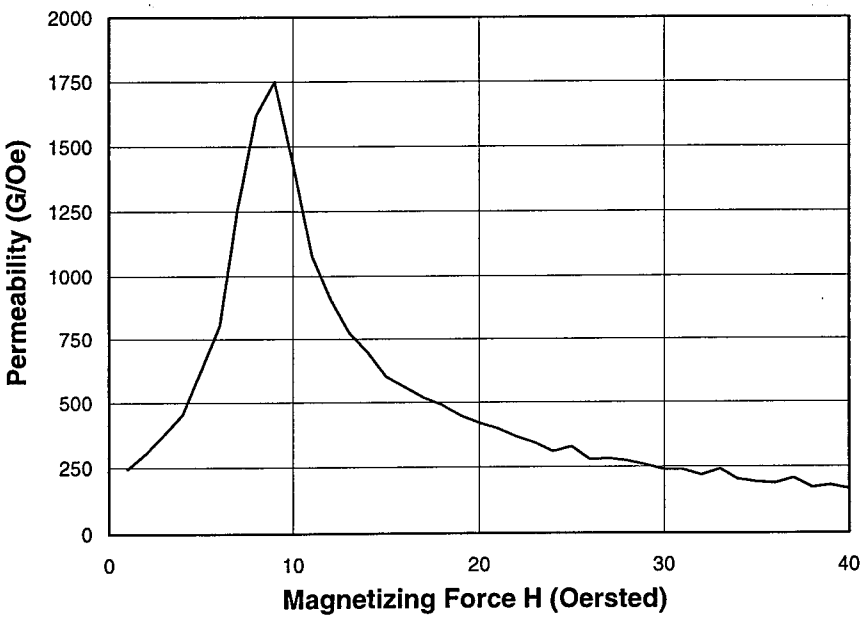

Material 24-14

Numerical Values		
Diameter		24.11 in.
Thickness		0.308 in.
Charpy		
Energy		30 ft-lbs
Shear		99 %
Tensile		
Yield		64.93 ksi
Ultimate		84.6 ksi
Elongation		32%
Hardness (Rockwell B)		90
Grain Size (ASTM #)		8
Magnetic Measures		
Remanence		8,250 G
Coercivity		8.7 Oe
Permeability		740 G/Oe
H at Max Permeability		10 Oe
Chemical Composition		
Carbon	C	0.28%
Manganese	Mn	1.20%
Phosphorus	P	0.009%
Sulfur	S	0.030%
Silicon	Si	0.074%
Aluminum	Al	0.000%
Vanadium	V	0.000%
Columbium	Cb	0.025%

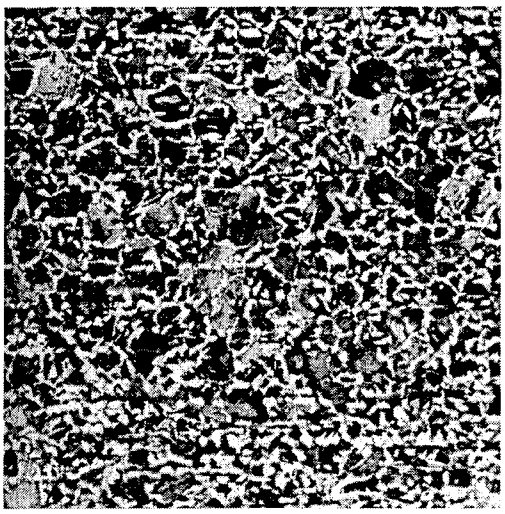

100X Picral + Nital Etch OB375

The microstructure consists of a somewhat banded mixture of equiaxed ferrite and pearlite. Near the centerline there are two bands that contain more and larger pearlite colonies than the surrounding microstructure. The grain size ranges from ASTM 7 (larger pearlite colonies) to ASTM 9 (ferrite).

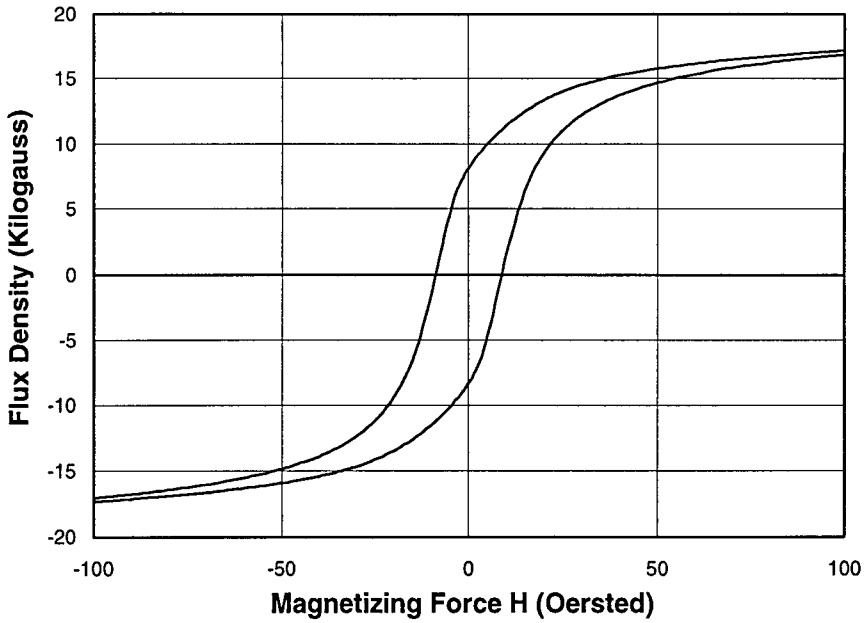

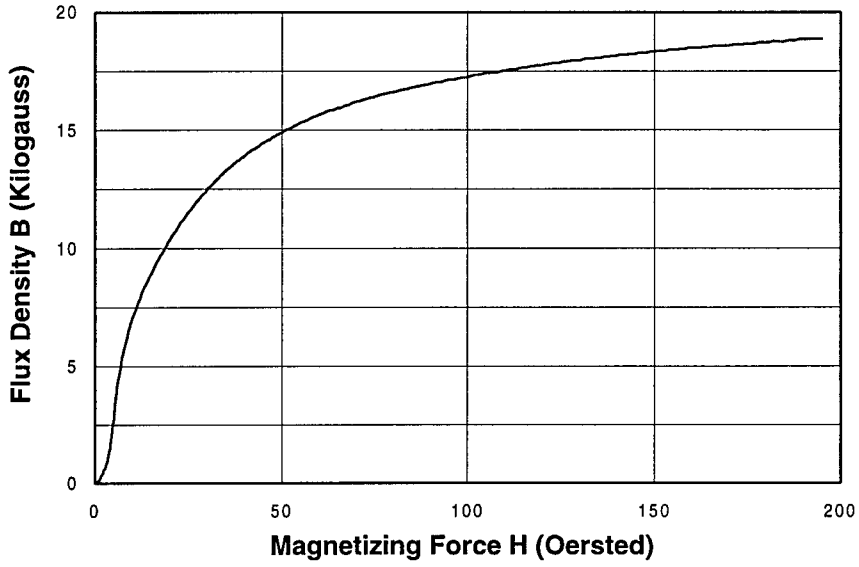

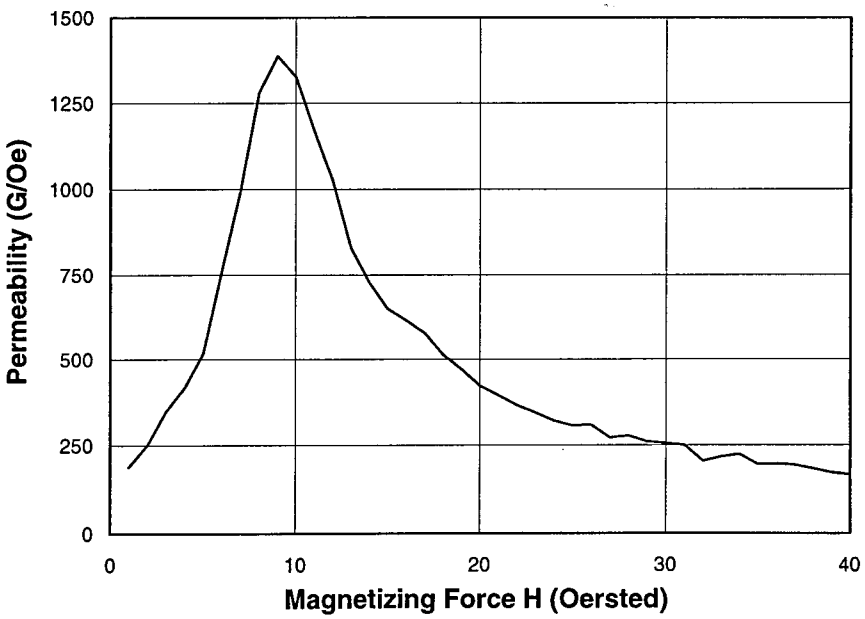

Material 24-15

Numerical Values		
Diameter		24.11 in.
Thickness		0.376 in.
Charpy		
Energy		26 ft-lbs
Shear		64 %
Tensile		
Yield		62.77 ksi
Ultimate		82.95ksi
Elongation		33%
Hardness (Rockwell B)		87
Grain Size (ASTM #)		7
Magnetic Measures		
Remanence		7,520 G
Coercivity		7.37 Oe
Permeability		770 G/Oe
H at Max Permeability		8 Oe
Chemical Composition		
Carbon	C	0.27%
Manganese	Mn	0.85%
Phosphorus	P	0.027%
Sulfur	S	0.031%
Silicon	Si	0.052%
Aluminum	Al	0.000%
Vanadium	V	0.000%
Columbium	Cb	0.010%

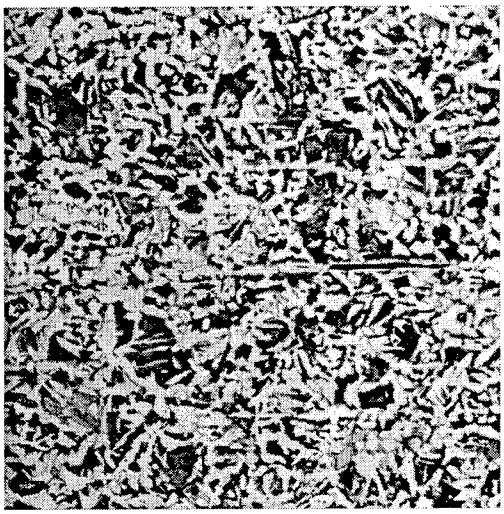

100X Picral + Nital Etch OB376

The microstructure consists of a slightly banded mixture of ferrite and pearlite. The grain size is ASTM 6.5. This steel exhibits some centerline segregation with bands that contain more pearlite.

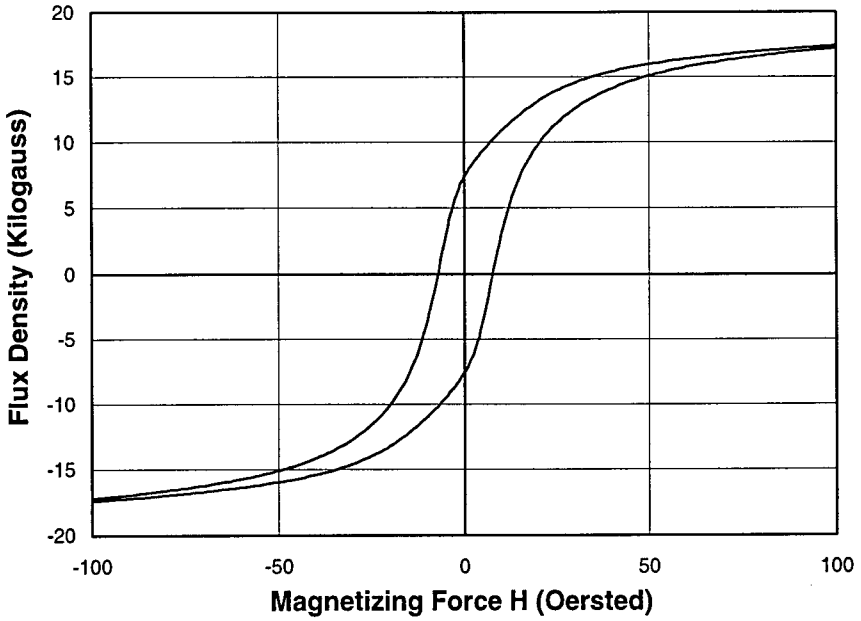

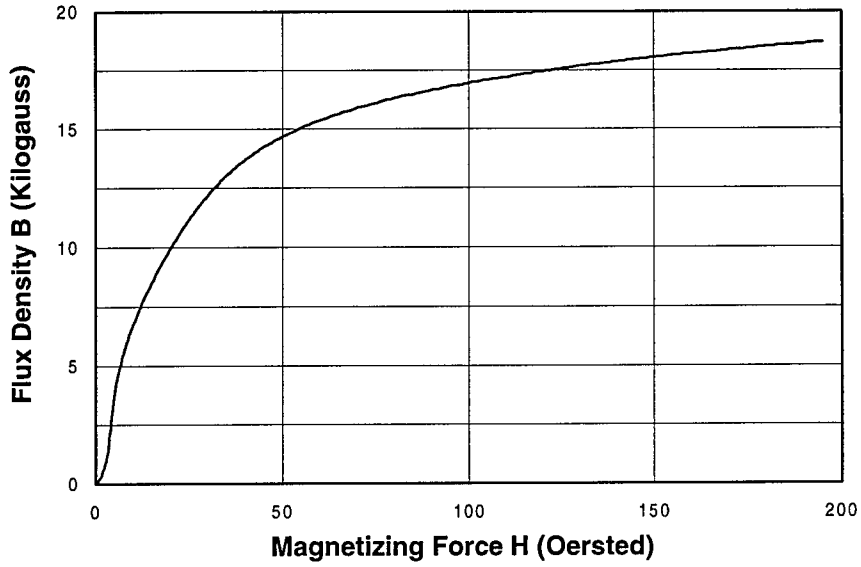

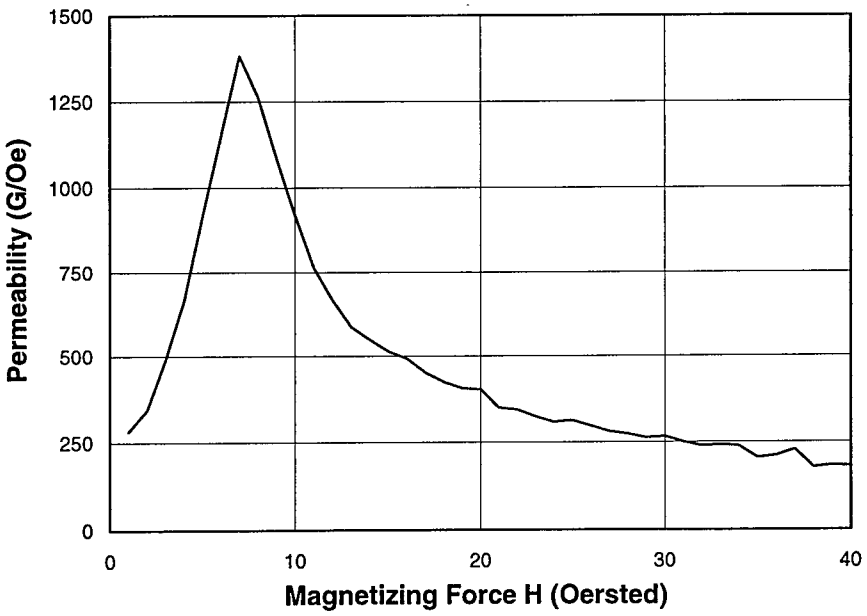

Material 24-17

Numerical Values		
Diameter		24.11 in.
Thickness		0.318 in.
Charpy		
Energy		33 ft-lbs
Shear		98 %
Tensile		
Yield		53.97 ksi
Ultimate		74.34 ksi
Elongation		31%
Hardness (Rockwell B)		78
Grain Size (ASTM #)		7.5
Magnetic Measures		
Remanence		7,706 G
Coercivity		6.01 Oe
Permeability		1,000 G/Oe
H at Max Permeability		7 Oe
Chemical Composition		
Carbon	C	0.25%
Manganese	Mn	1.01%
Phosphorus	P	0.013%
Sulfur	S	0.015%
Silicon	Si	0.028%
Aluminum	Al	0.000%
Vanadium	V	0.000%
Columbium	Cb	0.003%

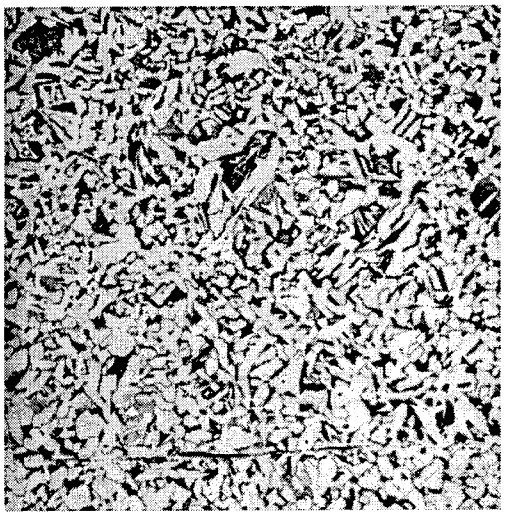

100X Picral + Nital Etch OB377

The microstructure consists of a slightly banded mixture of equiaxed ferrite and pearlite. The grain size is ASTM 7.5.

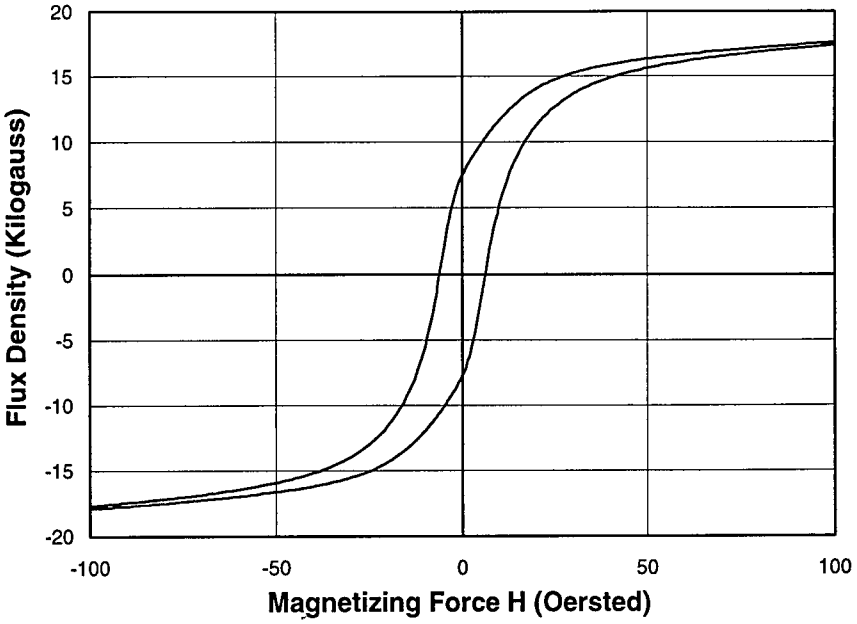

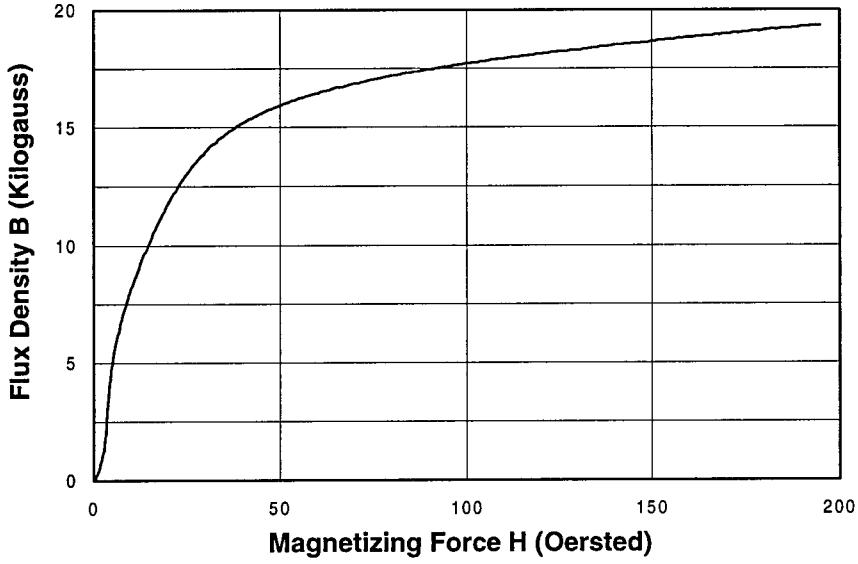

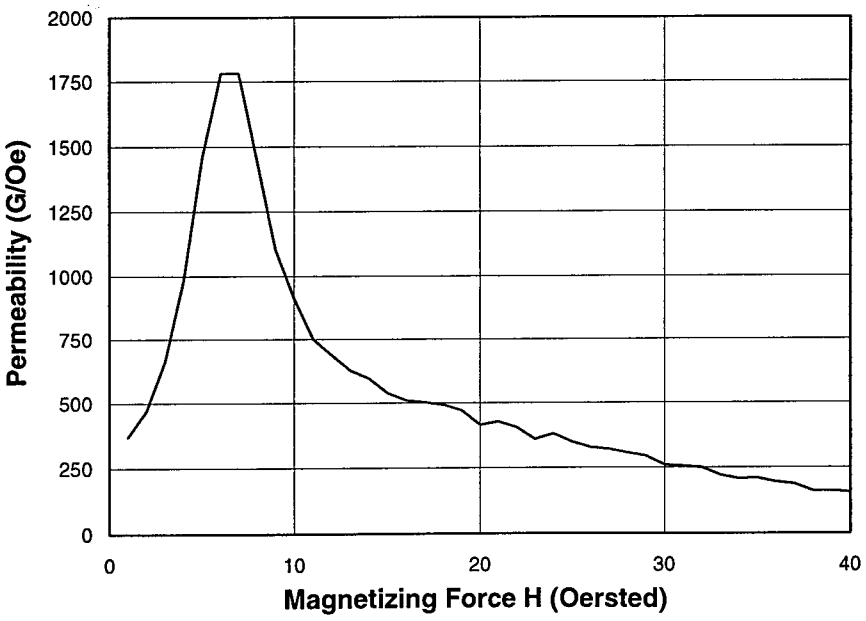

Material 24-18

Numerical Values		
Diameter		24.11 in.
Thickness		0.318 in.
Charpy		
Energy		58 ft-lbs
Shear		100%
Tensile		
Yield		65.78 ksi
Ultimate		83.6 ksi
Elongation		34%
Hardness (Rockwell B)		87.5
Grain Size (ASTM #)		9.5
Magnetic Measures		
Remanence		7,840 G
Coercivity		6.37 Oe
Permeability		990 G/Oe
H at Max Permeability		8 Oe
Chemical Composition		
Carbon	C	0.14%
Manganese	Mn	1.26%
Phosphorus	P	0.014%
Sulfur	S	0.009%
Silicon	Si	0.310%
Aluminum	Al	0.034%
Vanadium	V	0.000%
Columbium	Cb	0.008%

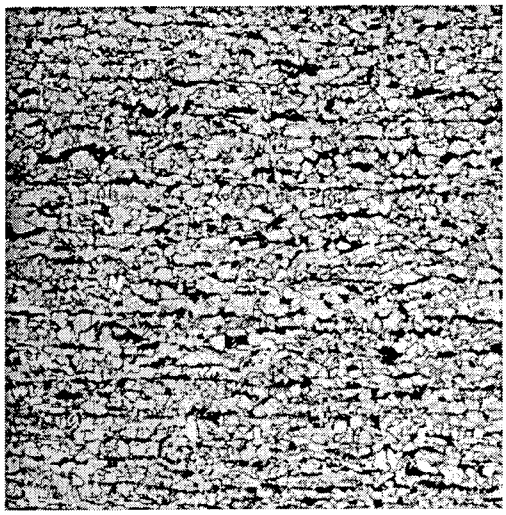

100X Picral + Nital Etch OB378

The microstructure consists of a somewhat banded mixture of equiaxed ferrite and pearlite. The ferrite grain size is ASTM 9.5. The microstructure also contains some angular carbonitride particles.

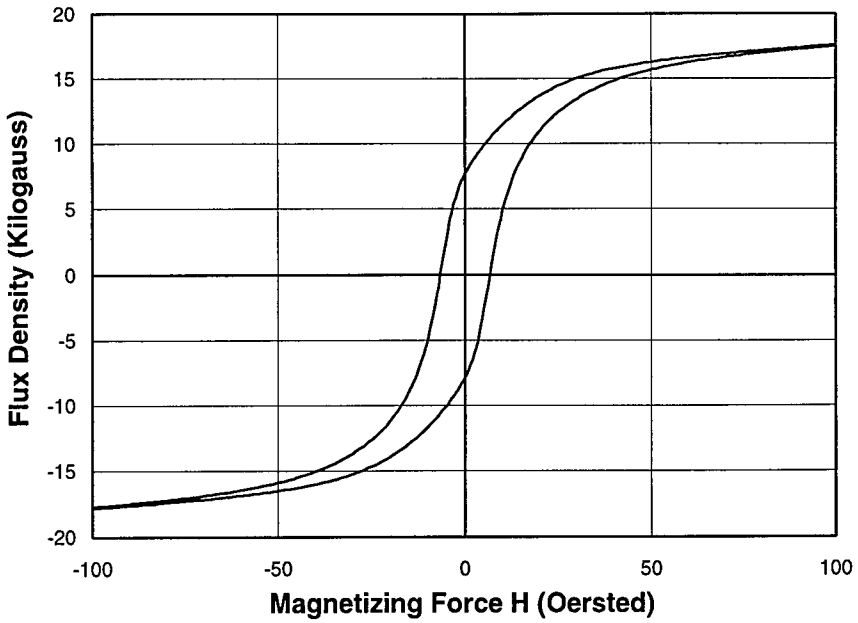

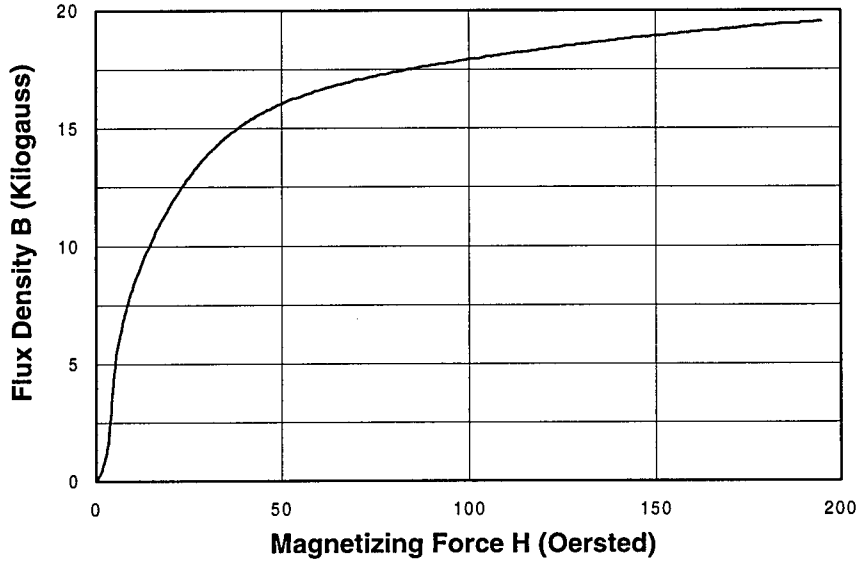

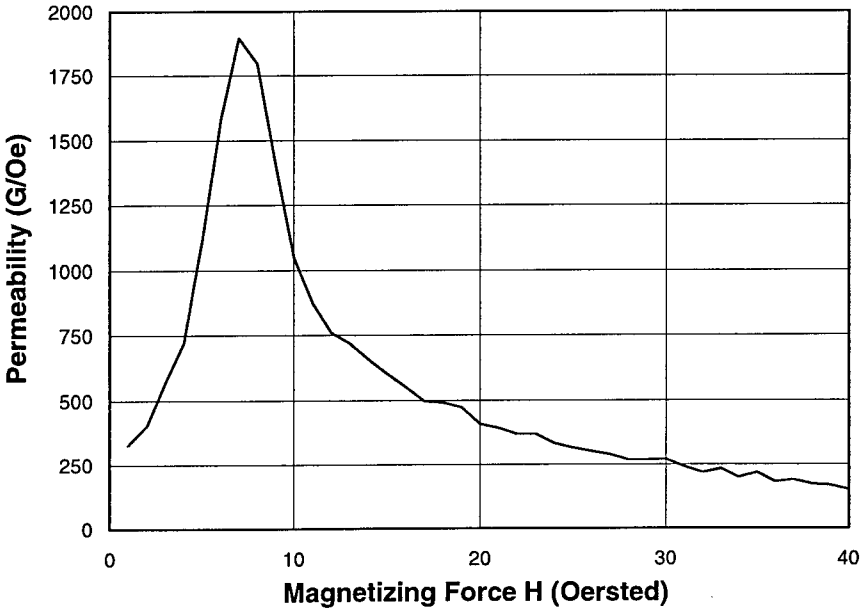

Material 24-20

Numerical Values		
Diameter		24.11 in.
Thickness		0.277 in.
Charpy		
Energy		39 ft-lbs
Shear		100%
Tensile		
Yield		45.71 ksi
Ultimate		75.63 ksi
Elongation		38%
Hardness (Rockwell B)		80.5
Grain Size (ASTM #)		8.5
Magnetic Measures		
Remanence		8,790 G
Coercivity		5.84 Oe
Permeability		1,100 G/Oe
H at Max Permeability		7 Oe
Chemical Composition		
Carbon	C	0.26%
Manganese	Mn	1.04%
Phosphorus	P	0.011%
Sulfur	S	0.016%
Silicon	Si	0.034%
Aluminum	Al	0.023%
Vanadium	V	0.000%
Columbium	Cb	0.003%

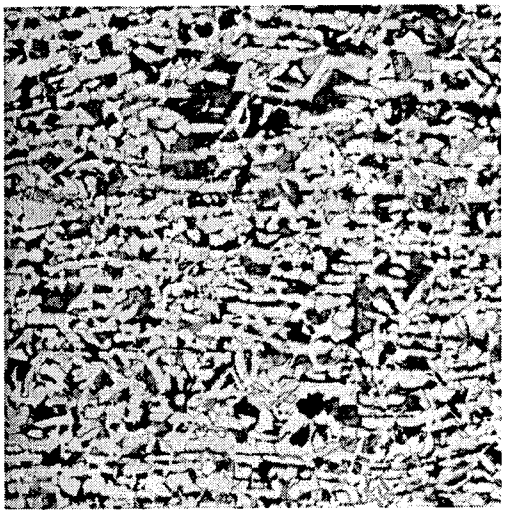

100X Picral + Nital Etch OB379

The microstructure consists of a banded mixture of equiaxed ferrite and pearlite; note that the banding is somewhat wavy. Some larger pearlite colonies are present. The grain size is ASTM 8.5.

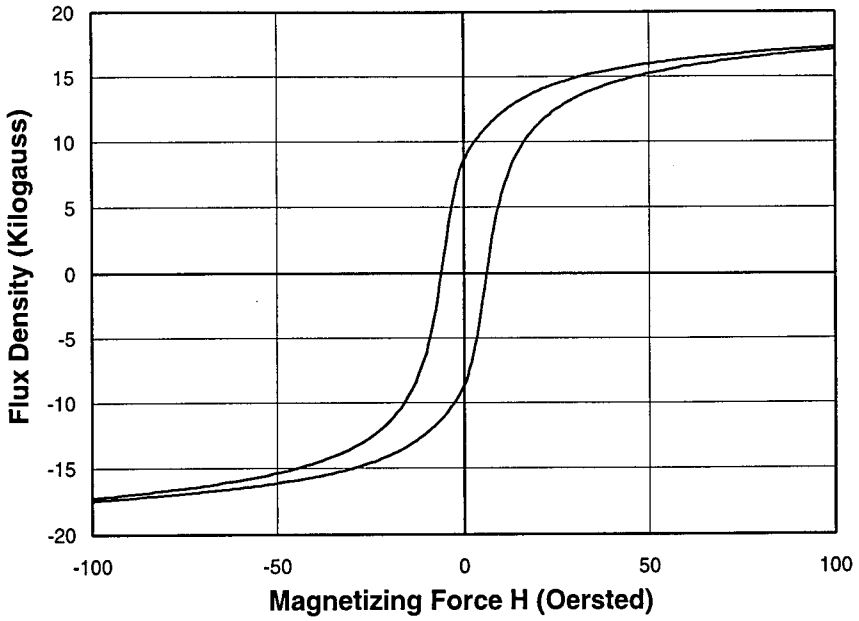

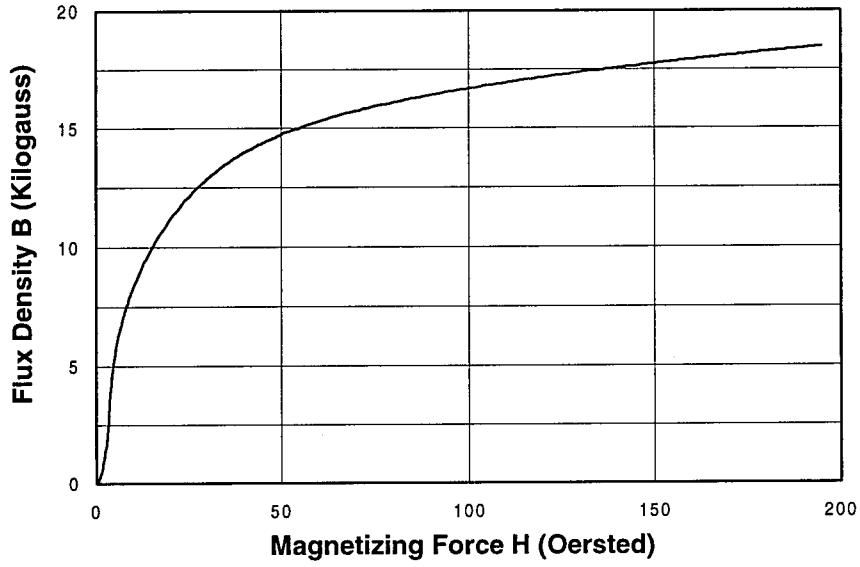

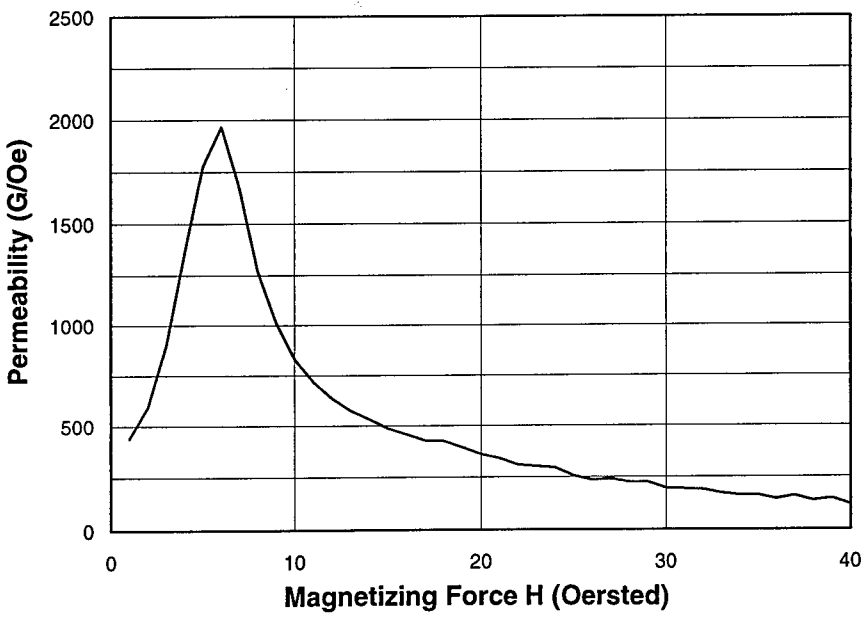

Material 24-21

Numerical Values		
Diameter		24.11 in.
Thickness		0.337 in.
Charpy		
Energy		26 ft-lbs
Shear		50%
Tensile		
Yield		62.44 ksi
Ultimate		84.38 ksi
Elongation		33%
Hardness (Rockwell B)		88
Grain Size (ASTM #)		6
Magnetic Measures		
Remanence		7,710 G
Coercivity		7.46 Oe
Permeability		820 G/Oe
H at Max Permeability		9 Oe
Chemical Composition		
Carbon	C	0.26%
Manganese	Mn	0.94%
Phosphorus	P	0.027%
Sulfur	S	0.017%
Silicon	Si	0.066%
Aluminum	Al	0.000%
Vanadium	V	0.000%
Columbium	Cb	0.013%

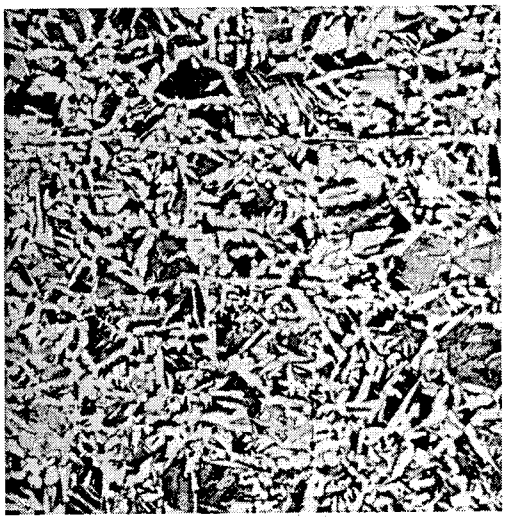

100X Picral + Nital Etch OB380

The microstructure consists of a slightly banded mixture of equiaxed ferrite and relatively large pearlite colonies, some of which exhibit a Widmanstätten structure. The grain size is ASTM 6.

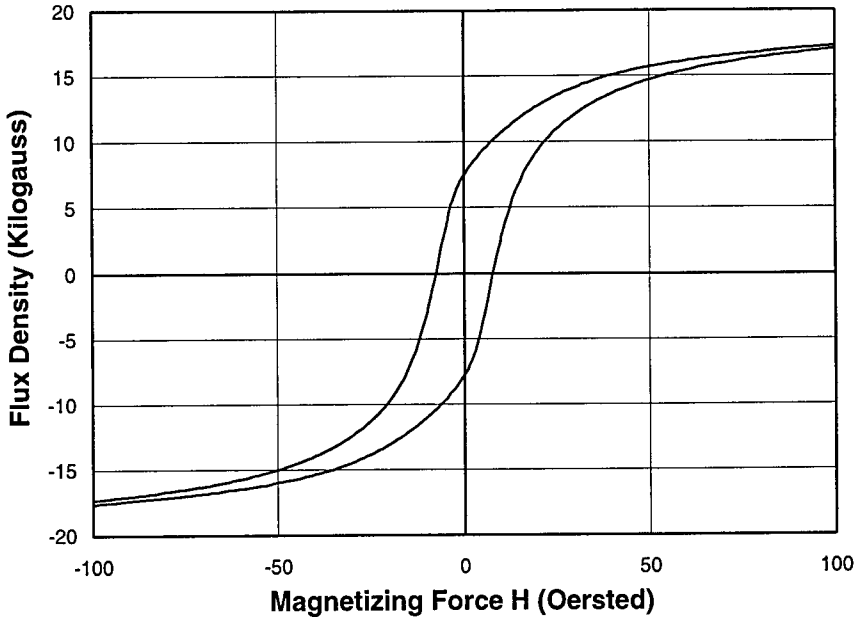

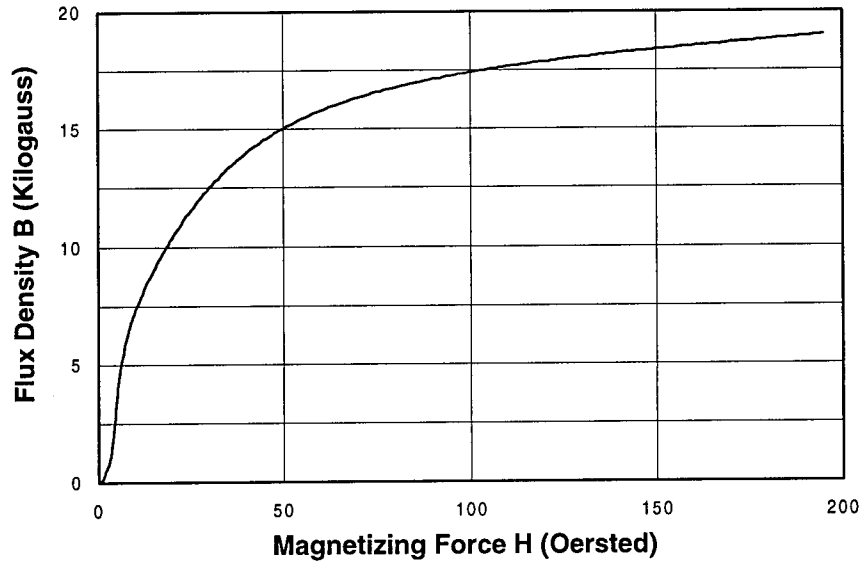

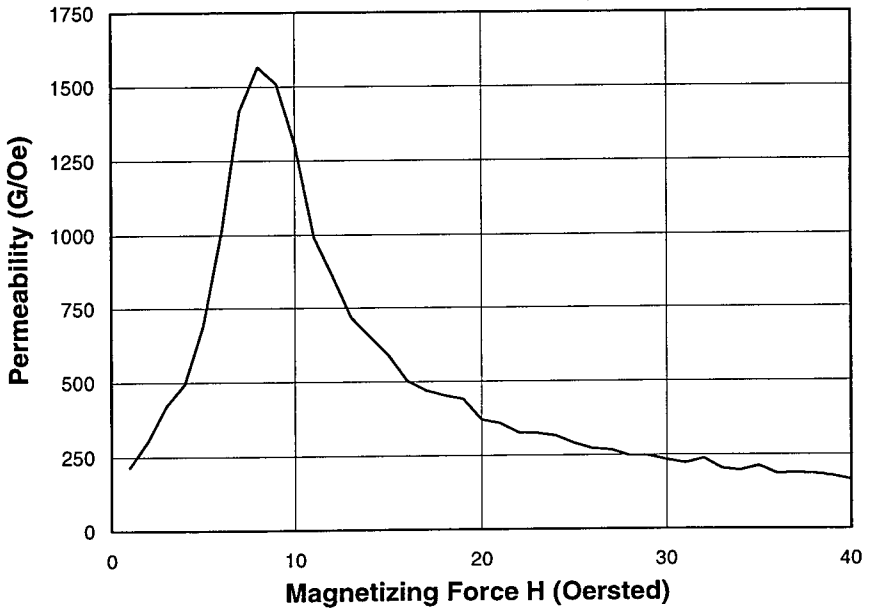

Material 24-22

Numerical Values		
Diameter		24.11 in.
Thickness		0.303 in.
Charpy		
Energy		30 ft-lbs
Shear		100%
Tensile		
Yield		67.82 ksi
Ultimate		86.32 ksi
Elongation		31%
Hardness (Rockwell B)		91
Grain Size (ASTM #)		10.5
Magnetic Measures		
Remanence		9,570 G
Coercivity		8.37 Oe
Permeability		780 G/Oe
H at Max Permeability		9 Oe
Chemical Composition		
Carbon	C	0.20%
Manganese	Mn	1.19%
Phosphorus	P	0.008%
Sulfur	S	0.010%
Silicon	Si	0.029%
Aluminum	Al	0.000%
Vanadium	V	0.000%
Columbium	Cb	0.008%

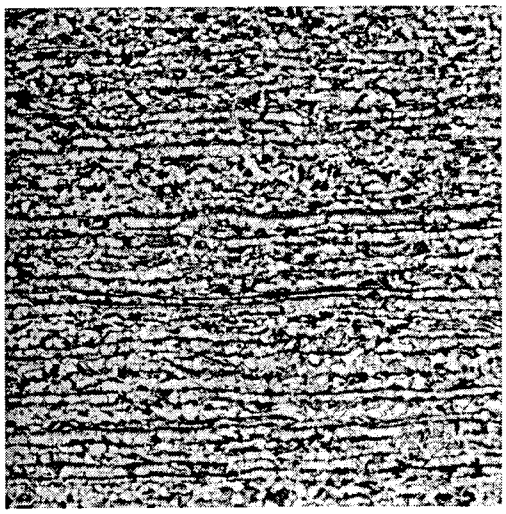

100X Picral + Nital Etch OB381

The microstructure consists of a banded mixture of equiaxed fine-grained ferrite and pearlite. The grain size is ASTM 10.5.

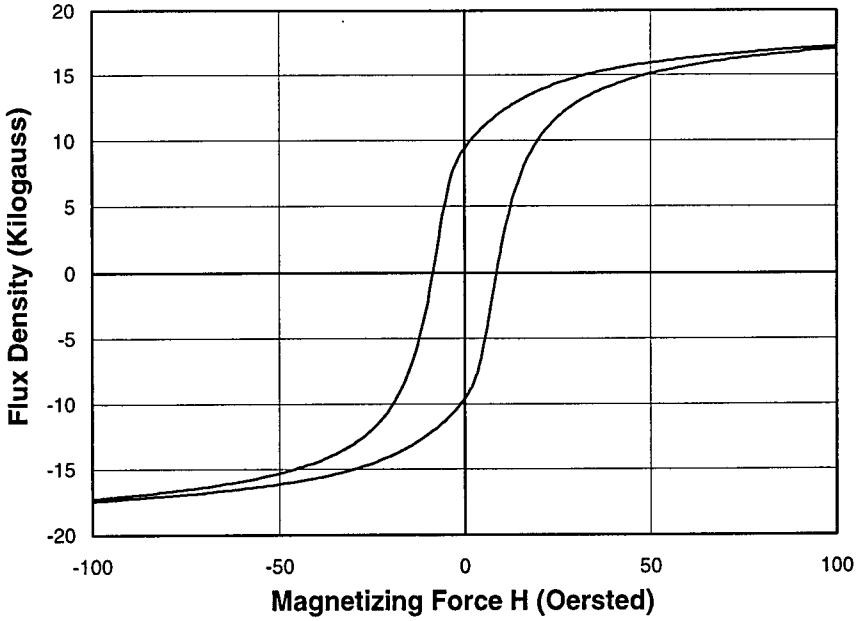

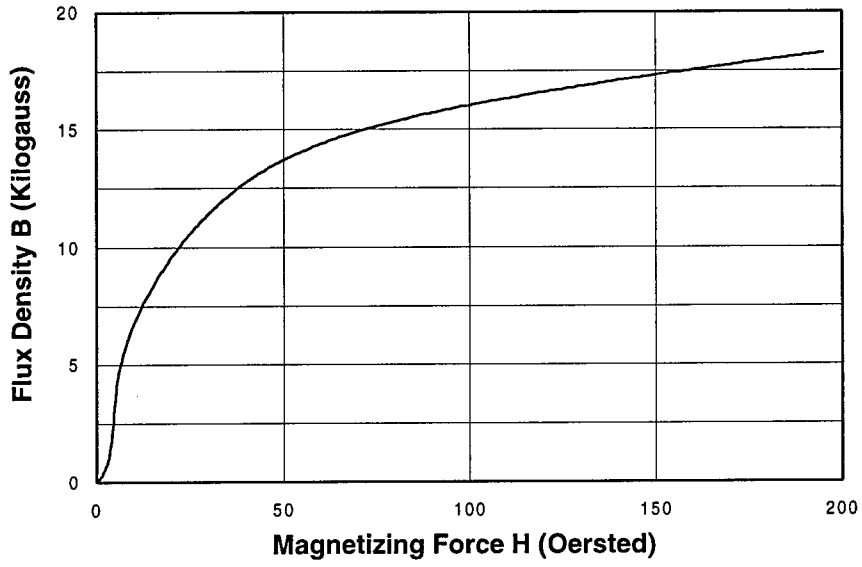

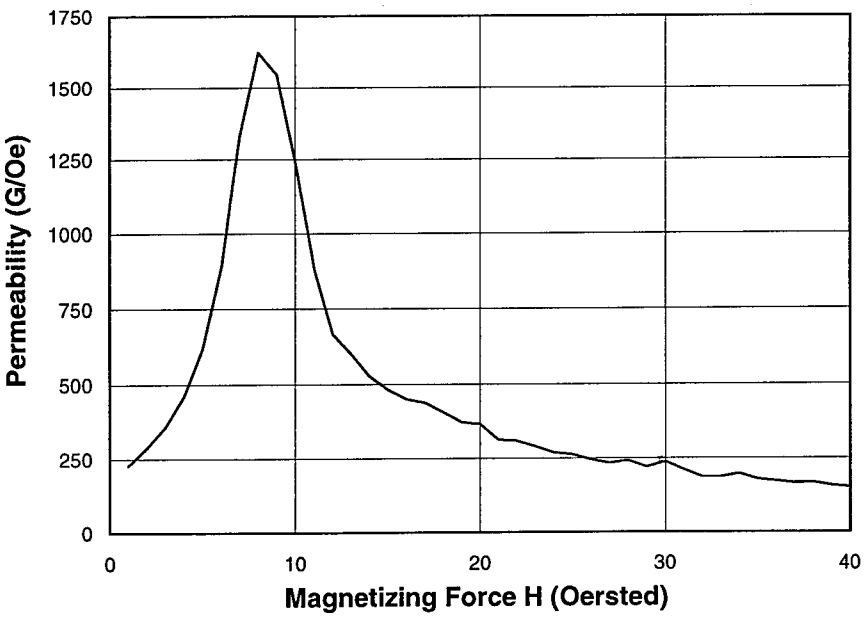

Material 24-23

Numerical Values		
Diameter		24.19 in.
Thickness		0.284 in.
Charpy		
Energy		42 ft-lbs
Shear		100%
Tensile		
Yield		50.34 ksi
Ultimate		79.68 ksi
Elongation		35%
Hardness (Rockwell B)		82
Grain Size (ASTM #)		8.5
Magnetic Measures		
Remanence		8,900 G
Coercivity		6.22 Oe
Permeability		960 G/Oe
H at Max Permeability		7 Oe
Chemical Composition		
Carbon	C	0.30%
Manganese	Mn	1.07%
Phosphorus	P	0.012%
Sulfur	S	0.024%
Silicon	Si	0.038%
Aluminum	Al	0.005%
Vanadium	V	0.000%
Columbium	Cb	0.003%

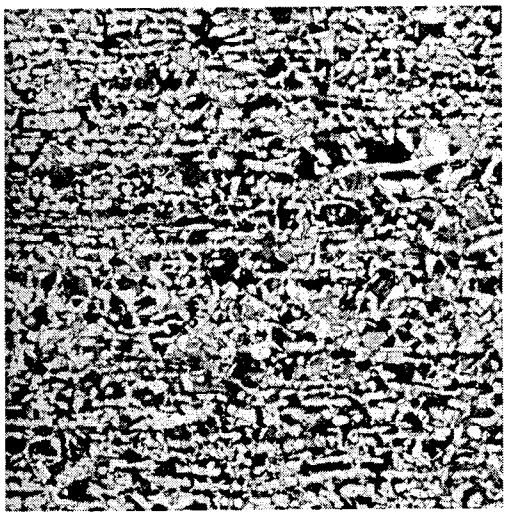

100X Picral + Nital Etch OB382

The microstructure consists of a banded mixture of fine-grained, equiaxed ferrite and pearlite. The grain size is ASTM 9.

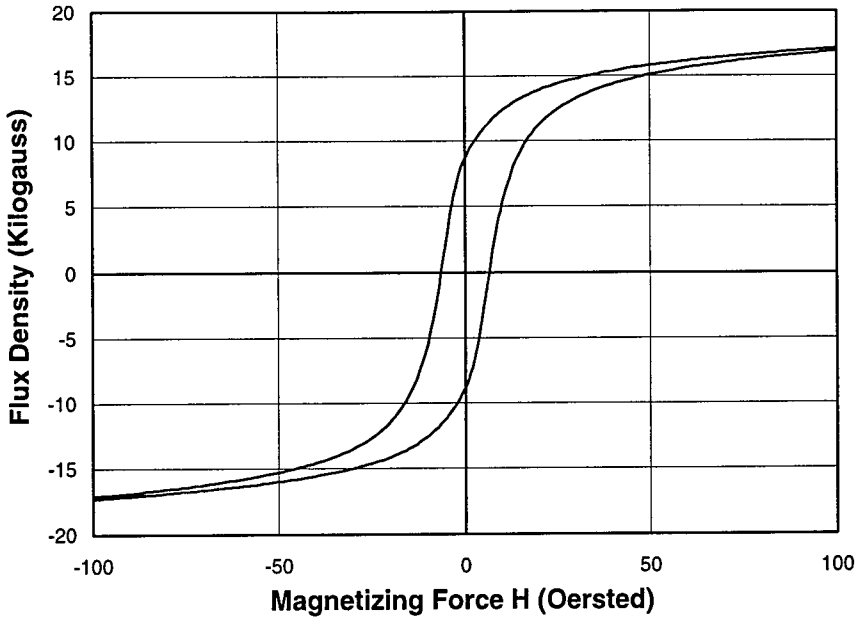

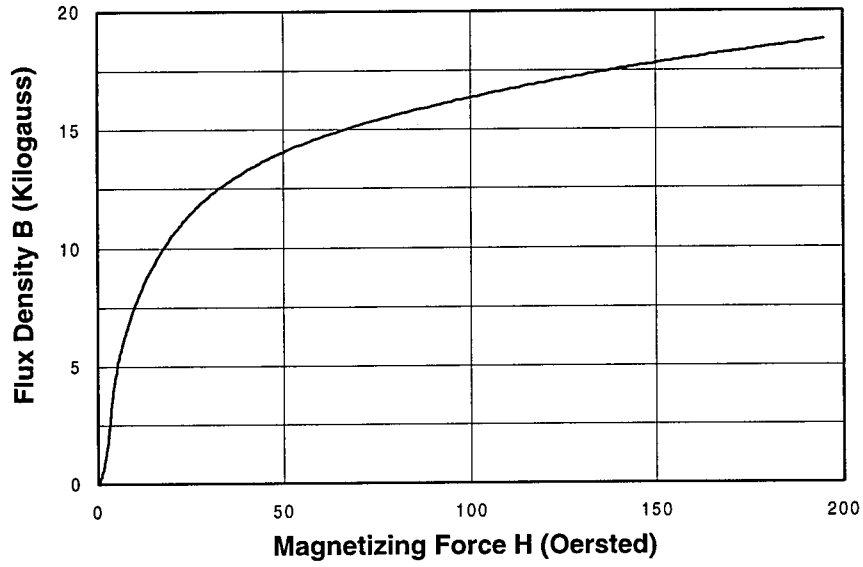

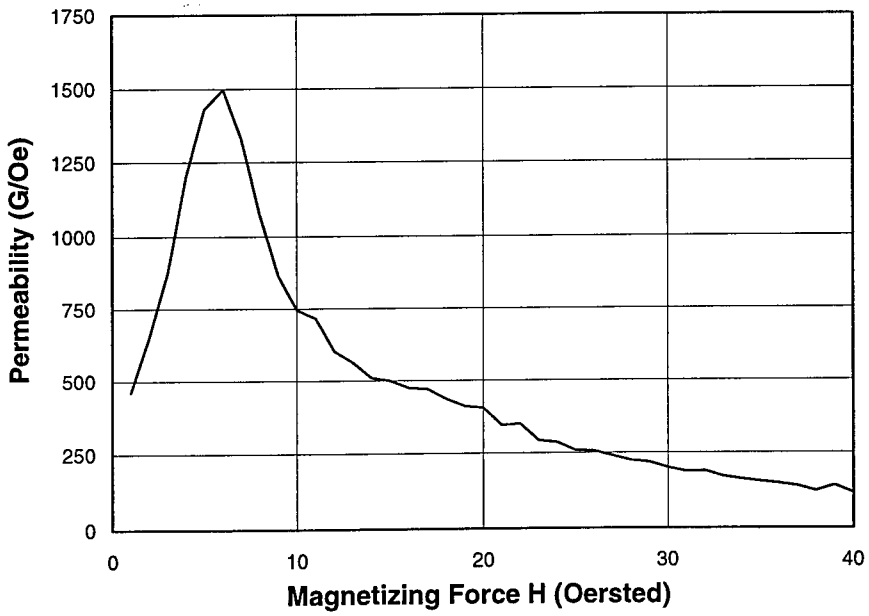

Material 24-27

Numerical Values		
Diameter		24.11 in.
Thickness		0.272 in.
Charpy		
Energy		18 ft-lbs
Shear		100%
Tensile		
Yield		68.67 ksi
Ultimate		85.36 ksi
Elongation		26%
Hardness (Rockwell B)		88
Grain Size (ASTM #)		10
Magnetic Measures		
Remanence		7,910 G
Coercivity		8.25 Oe
Permeability		660 G/Oe
H at Max Permeability		10 Oe
Chemical Composition		
Carbon	C	0.18%
Manganese	Mn	1.28%
Phosphorus	P	0.013%
Sulfur	S	0.015%
Silicon	Si	0.082%
Aluminum	Al	0.000%
Vanadium	V	0.000%
Columbium	Cb	0.012%

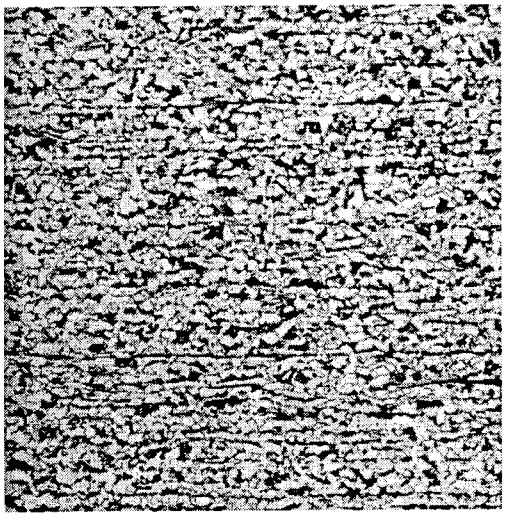

100X Picral + Nital Etch OB383

The microstructure consists of a banded mixture of relatively fine-grained, equiaxed ferrite and pearlite. The grain size is ASTM 9.5.

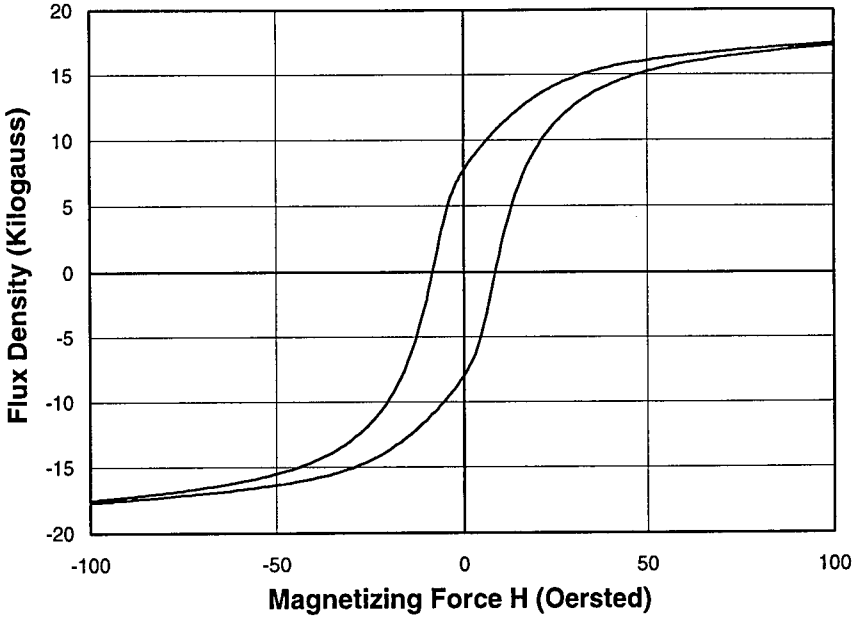

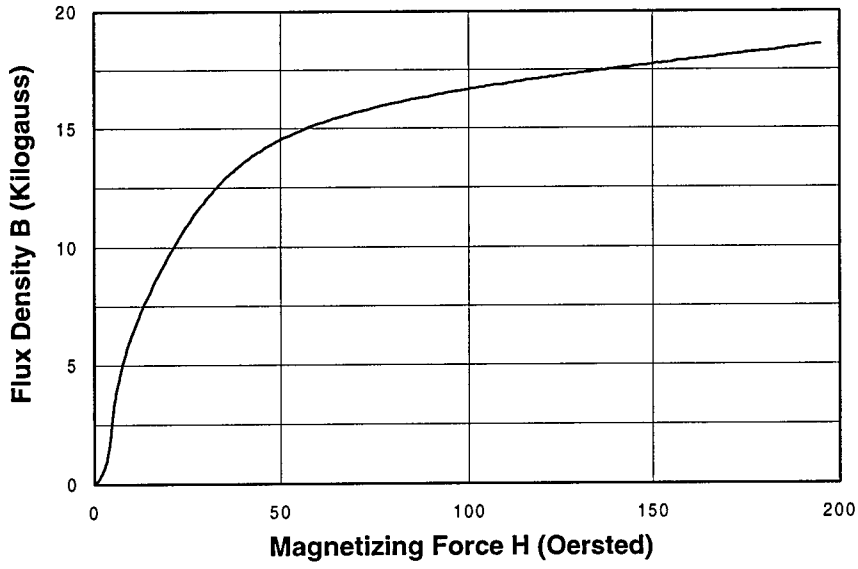

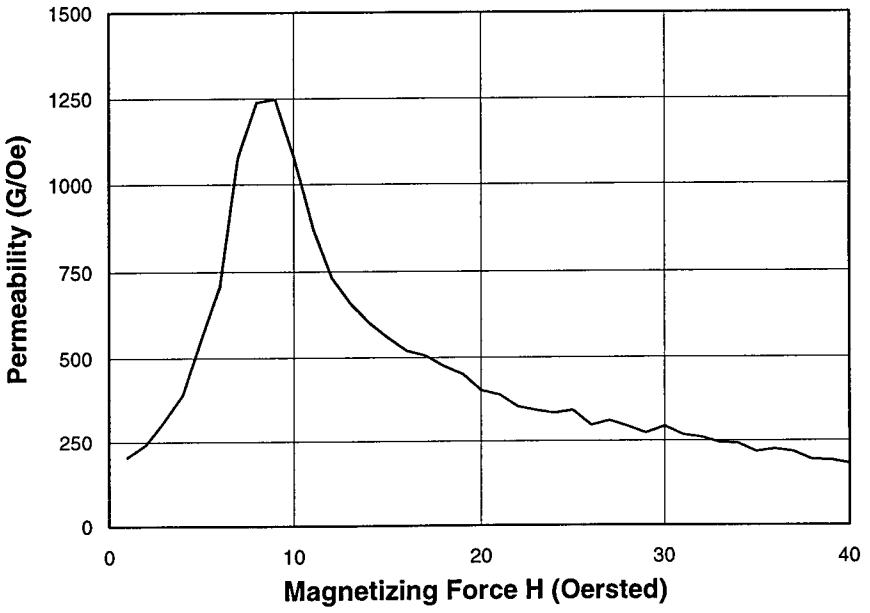

Material 24-28

Numerical Values		
Diameter		24.11 in.
Thickness		0.293 in.
Charpy		
Energy		38 ft-lbs
Shear		100%
Tensile		
Yield		55.19 ksi
Ultimate		73.3 ksi
Elongation		38%
Hardness (Rockwell B)		78.5
Grain Size (ASTM #)		8.5
Magnetic Measures		
Remanence		9,940 G
Coercivity		6.36 Oe
Permeability		1,210 G/Oe
H at Max Permeability		8 Oe
Chemical Composition		
Carbon	C	0.23%
Manganese	Mn	1.06%
Phosphorus	P	0.008%
Sulfur	S	0.020%
Silicon	Si	0.005%
Aluminum	Al	0.001%
Vanadium	V	0.000%
Columbium	Cb	0.003%

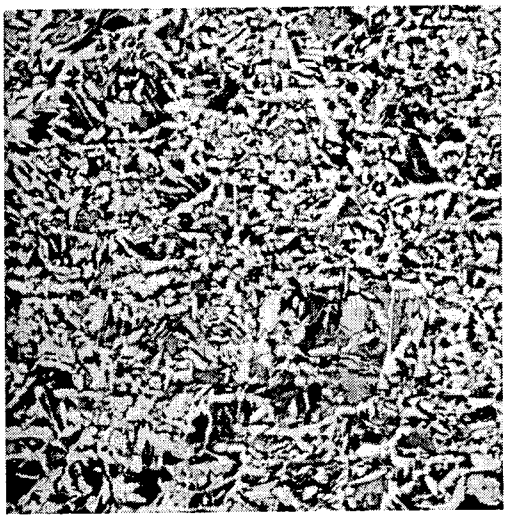

100X Picral + Nital Etch OB384

The microstructure consists of a banded mixture of relatively fine-grained, equiaxed ferrite and pearlite with some relatively large pearlite colonies. The grain size is primarily ASTM 9 with the larger pearlite colonies being rated as ASTM 7.

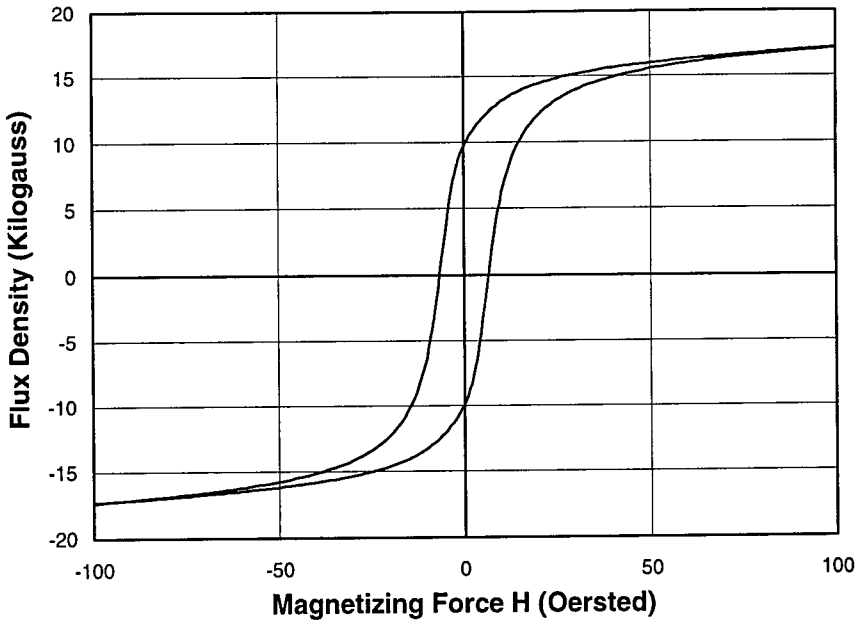

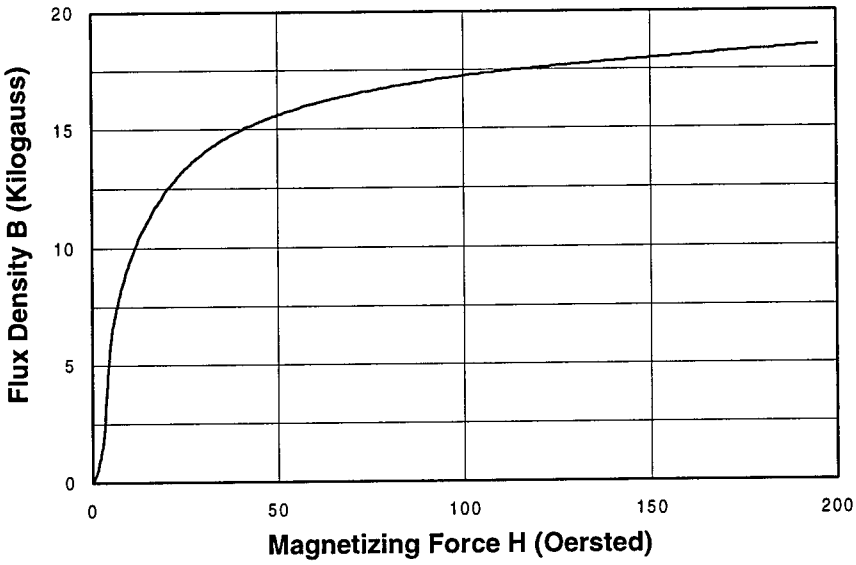

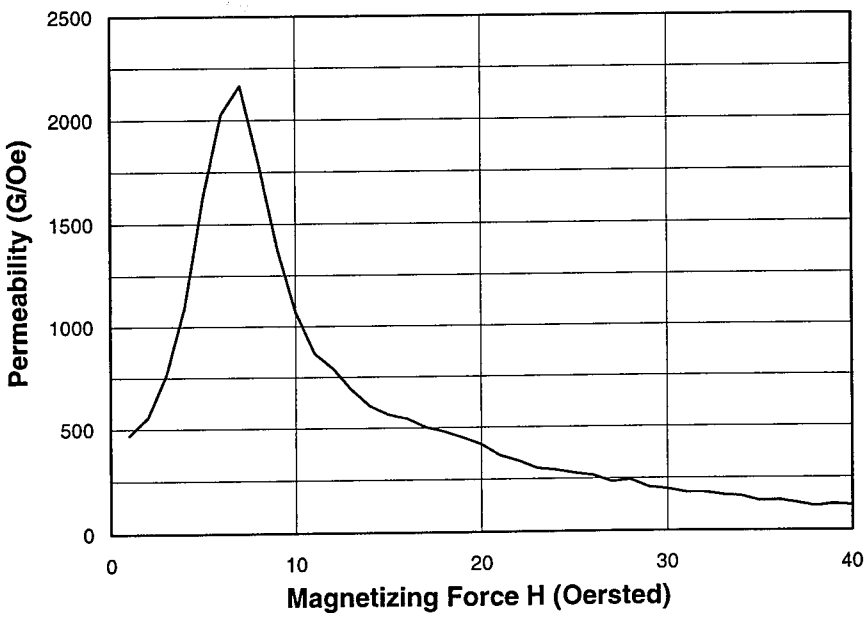

Material 24-30

Numerical Values		
Diameter		24.11 in.
Thickness		0.267 in.
Charpy		
Energy		23 ft-lbs
Shear		100%
Tensile		
Yield		67.71 ksi
Ultimate		87.16 ksi
Elongation		27%
Hardness (Rockwell B)		89
Grain Size (ASTM #)		10
Magnetic Measures		
Remanence		9,130 G
Coercivity		8.73 Oe
Permeability		1,200 G/Oe
H at Max Permeability		11 Oe
Chemical Composition		
Carbon	C	0.24%
Manganese	Mn	1.21%
Phosphorus	P	0.009%
Sulfur	S	0.011%
Silicon	Si	0.020%
Aluminum	Al	0.000%
Vanadium	V	0.000%
Columbium	Cb	0.007%

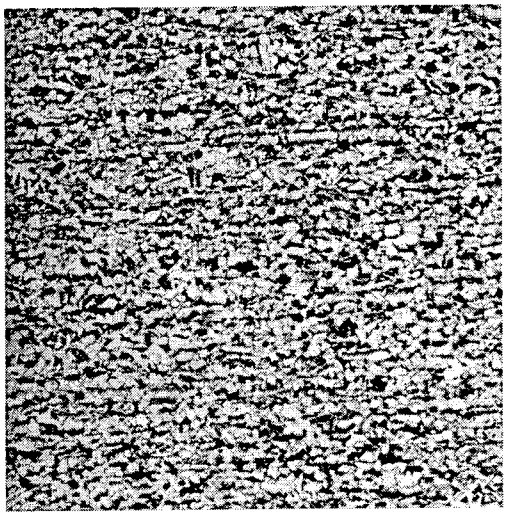

100X Picral + Nital Etch OB385

The microstructure consists of a somewhat banded mixture of fine-grained, equiaxed ferrite and pearlite. The grain size is ASTM 9.5.

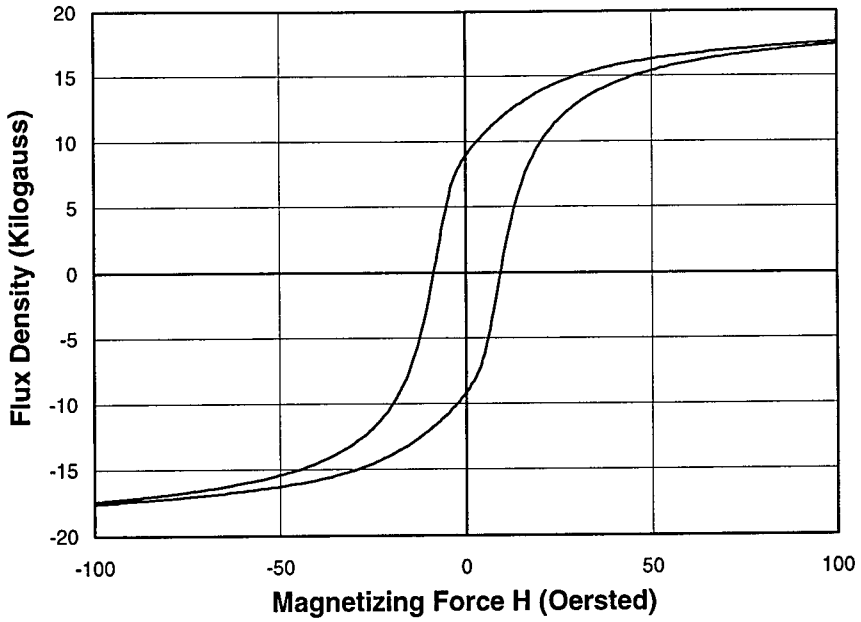

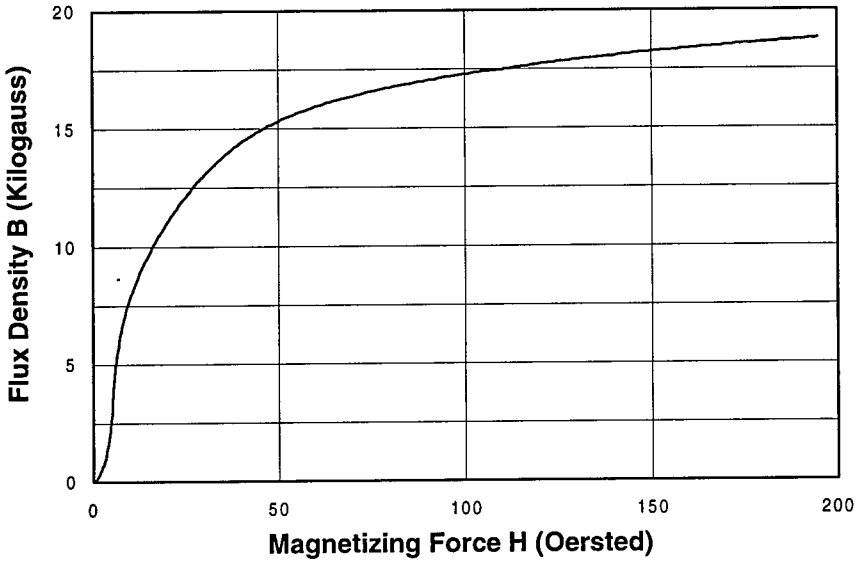

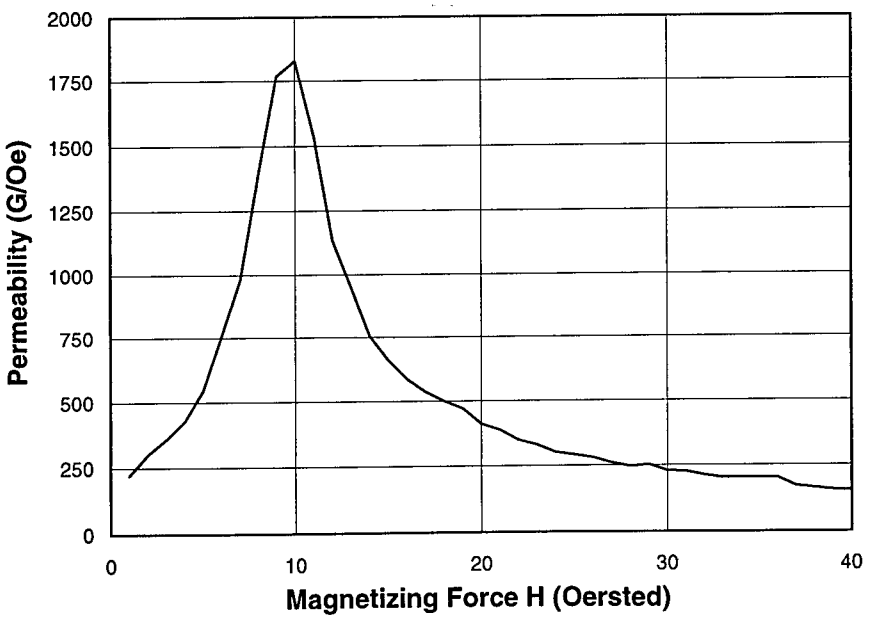

Material 24-31

Numerical Values		
Diameter		24.11 in.
Thickness		0.293 in.
Charpy		
Energy		25 ft-lbs
Shear		99%
Tensile		
Yield		55.34 ksi
Ultimate		75.63 ksi
Elongation		27%
Hardness (Rockwell B)		82
Grain Size (ASTM #)		8.5
Magnetic Measures		
Remanence		8,190 G
Coercivity		5.96 Oe
Permeability		1,110 G/Oe
H at Max Permeability		7 Oe
Chemical Composition		
Carbon	C	0.26%
Manganese	Mn	0.70%
Phosphorus	P	0.011%
Sulfur	S	0.029%
Silicon	Si	0.040%
Aluminum	Al	0.000%
Vanadium	V	0.000%
Columbium	Cb	0.004%

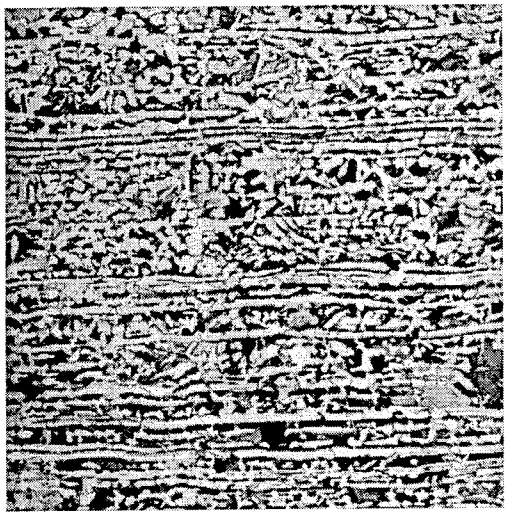

100X Picral + Nital Etch OB386

The microstructure consists of a distinctly banded mixture of ferrite and pearlite with pronounced narrow ferrite bands across the wall thickness. The grain size ranges from ASTM 8 to 9.

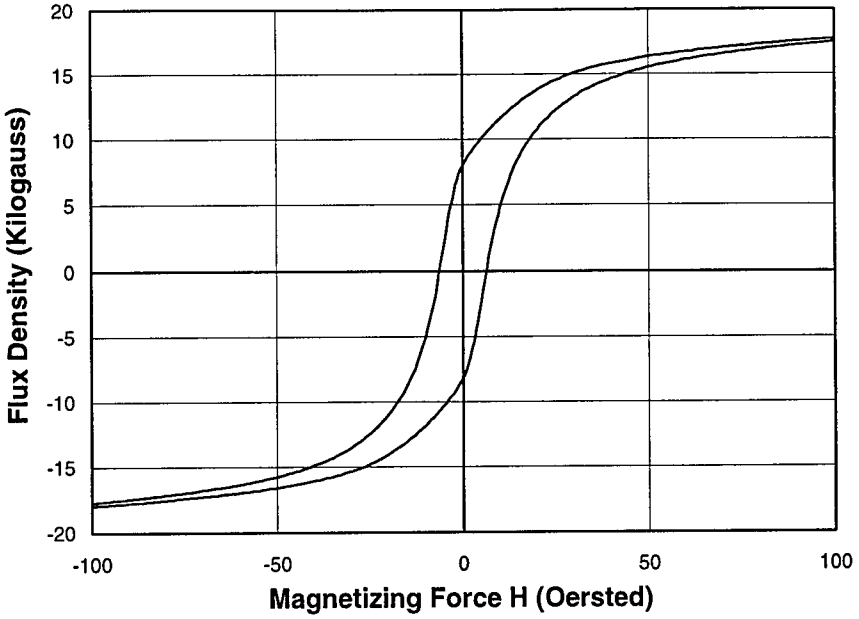

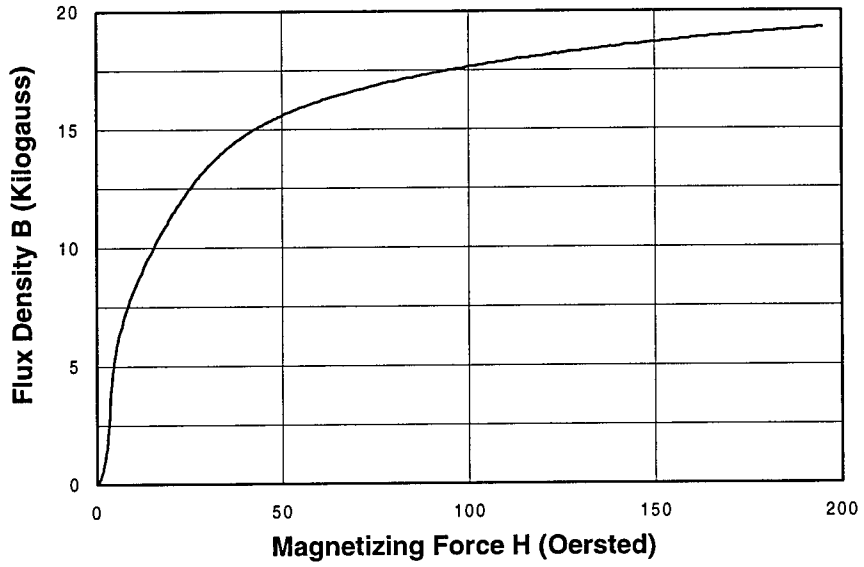

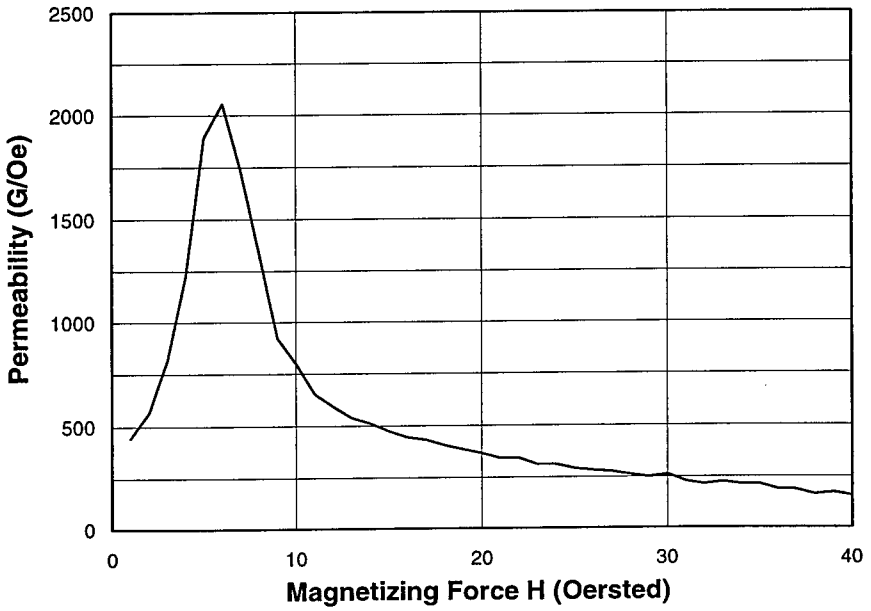

Material 24-32

Numerical Values		
Diameter		24.19 in.
Thickness		0.294 in.
Charpy		
Energy		42 ft-lbs
Shear		100%
Tensile		
Yield		45.4 ksi
Ultimate		73 ksi
Elongation		32.5%
Hardness (Rockwell B)		80
Grain Size (ASTM #)		8.5
Magnetic Measures		
Remanence		9,540 G
Coercivity		5.85 Oe
Permeability		1,230 G/Oe
H at Max Permeability		8 Oe
Chemical Composition		
Carbon	C	0.20%
Manganese	Mn	0.88%
Phosphorus	P	0.010%
Sulfur	S	0.017%
Silicon	Si	0.033%
Aluminum	Al	0.011%
Vanadium	V	0.002%
Columbium	Cb	0.004%

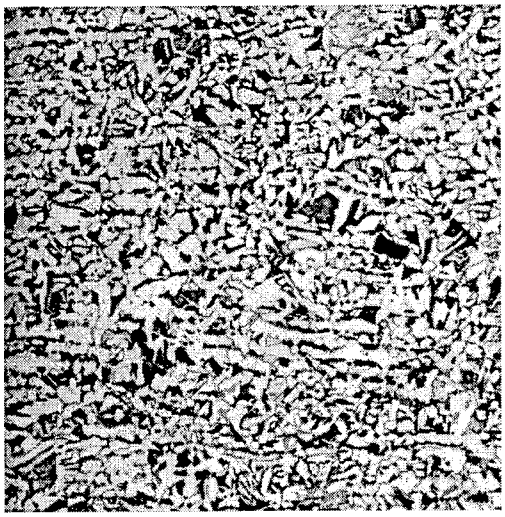

100X Picral + Nital Etch OB387

The microstructure consists of a somewhat banded mixture of equiaxed ferrite and pearlite; note that some of the bands are wavy. From the centerline toward one surface of the specimen, the microstructure contains more pearlite. The grain size is ASTM 8.

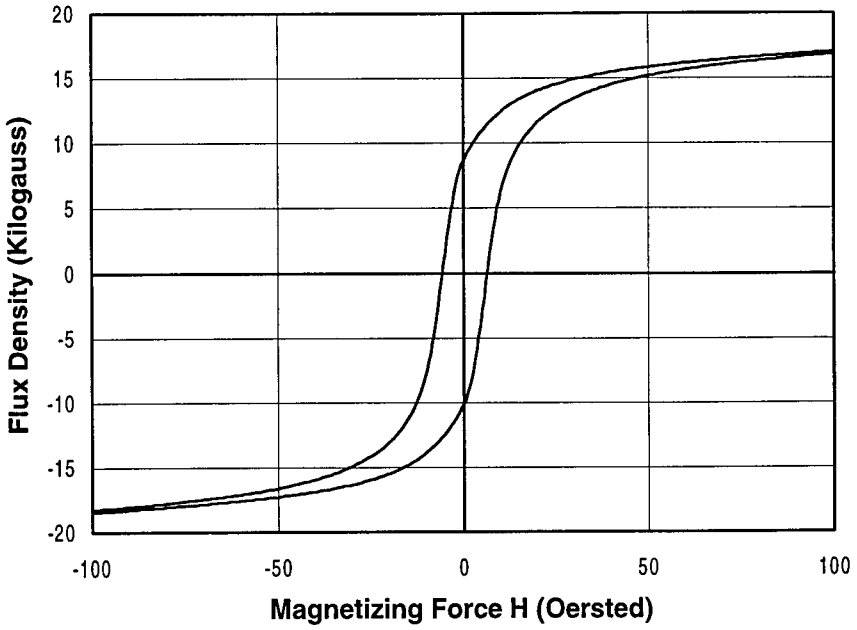

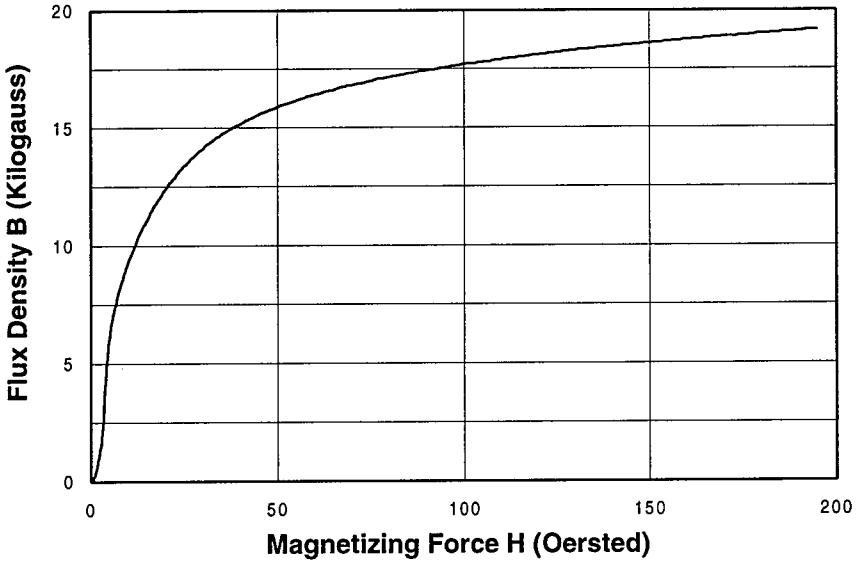

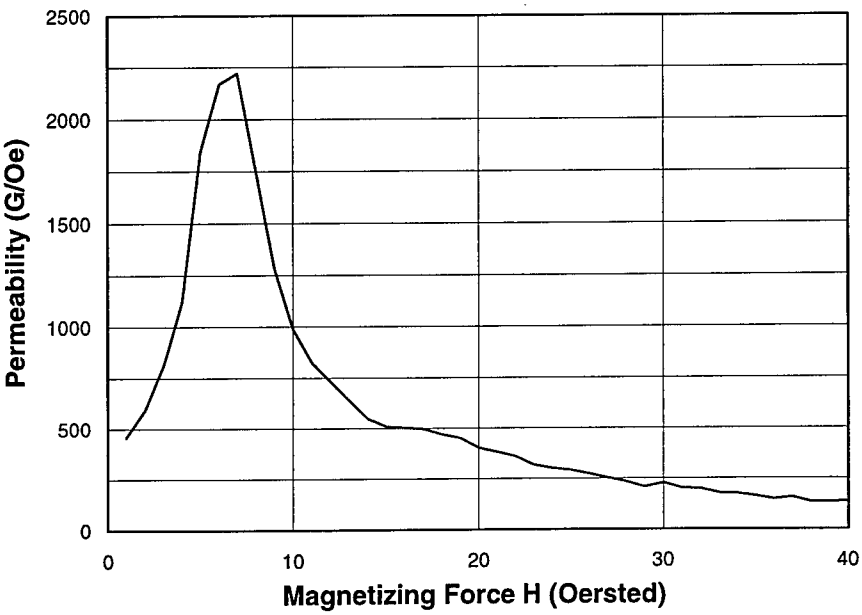

Material 24-33

Numerical Values		
Diameter		23.87 in.
Thickness		0.289 in.
Charpy		
Energy		28 ft-lbs
Shear		100%
Tensile		
Yield		60 ksi
Ultimate		83.5 ksi
Elongation		25%
Hardness (Rockwell B)		85
Grain Size (ASTM #)		10
Magnetic Measures		
Remanence		8,450 G
Coercivity		7.98 Oe
Permeability		840 G/Oe
H at Max Permeability		10 Oe
Chemical Composition		
Carbon	C	0.26%
Manganese	Mn	1.06%
Phosphorus	P	0.016%
Sulfur	S	0.044%
Silicon	Si	0.035%
Aluminum	Al	0.000%
Vanadium	V	0.001%
Columbium	Cb	0.004%

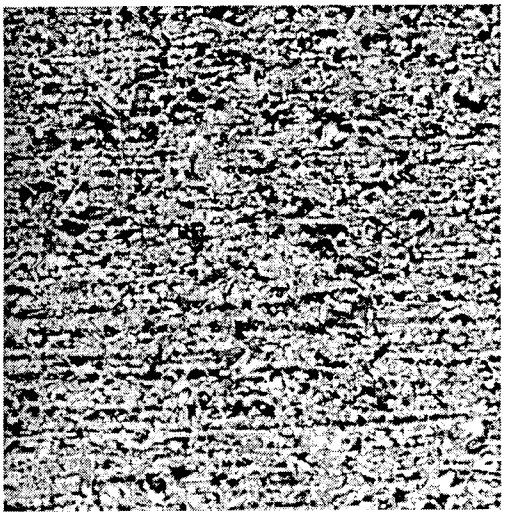

100X Picral + Nital Etch OB388

The microstructure consists primarily of a banded mixture of relatively fine-grained, equiaxed ferrite and pearlite with a grain size of ASTM 9.5. However, toward the inside surface there is evidence of segregation with more pearlite present in that region.

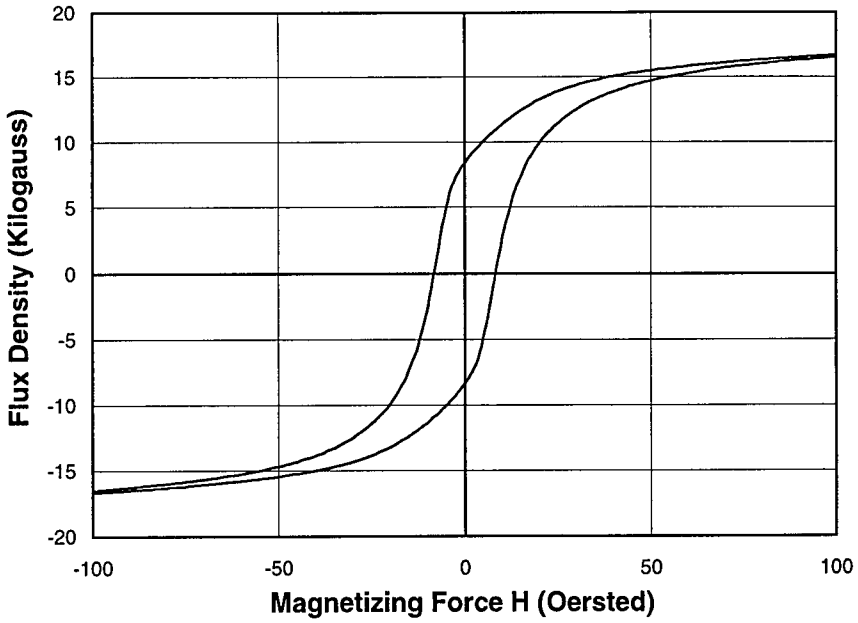

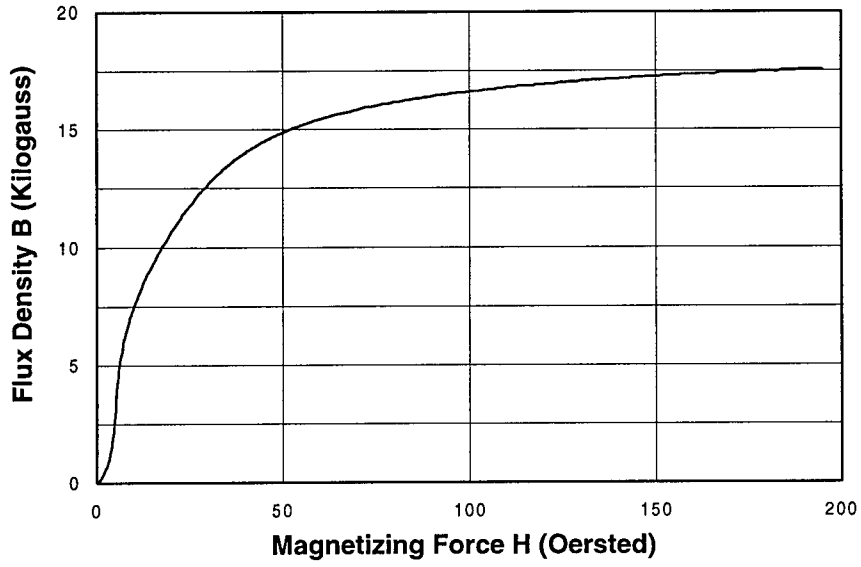

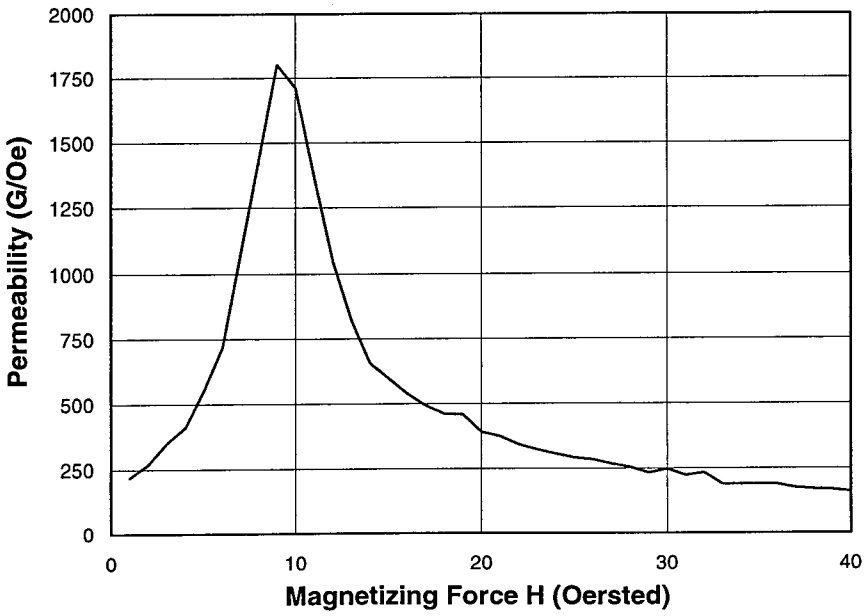

Material 24-34

Numerical Values		
Diameter		23.87 in.
Thickness		0.289 in.
Charpy		
Energy		34 ft-lbs
Shear		99%
Tensile		
Yield		59.4 ksi
Ultimate		78.7 ksi
Elongation		22%
Hardness (Rockwell B)		80
Grain Size (ASTM #)		8
Magnetic Measures		
Remanence		7,400 G
Coercivity		6.21 Oe
Permeability		1,000 G/Oe
H at Max Permeability		8 Oe
Chemical Composition		
Carbon	C	0.23%
Manganese	Mn	0.82%
Phosphorus	P	0.015%
Sulfur	S	0.026%
Silicon	Si	0.036%
Aluminum	Al	0.006%
Vanadium	V	0.002%
Columbium	Cb	0.003%

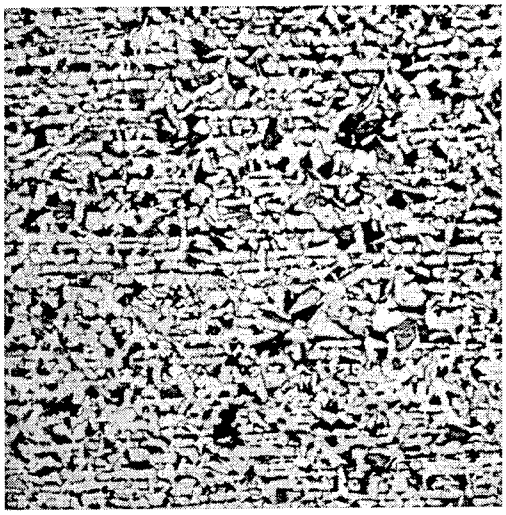

100X Picral + Nital Etch OB389

The microstructure consists of a somewhat banded mixture of equiaxed ferrite and pearlite. Some ferrite bands are distinct. The grain size is ASTM 8.

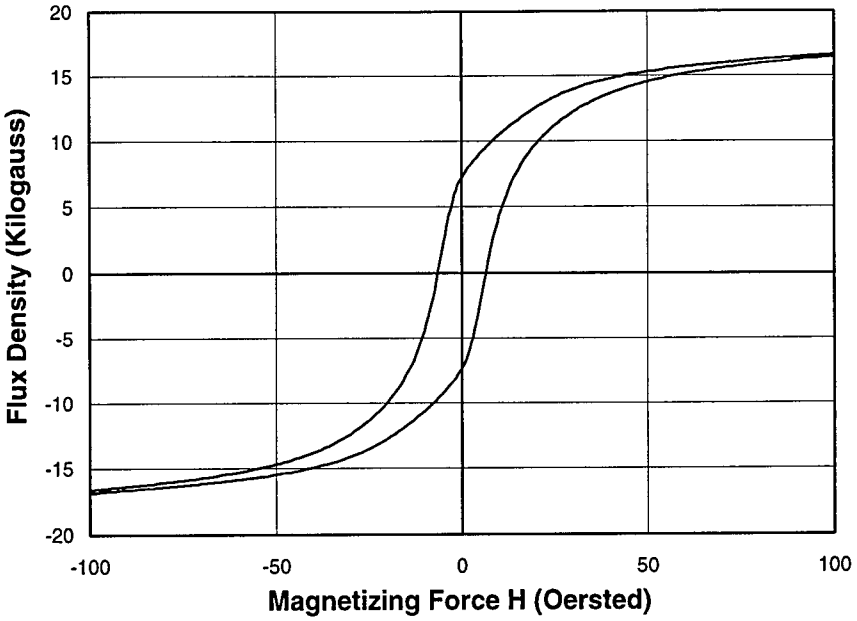

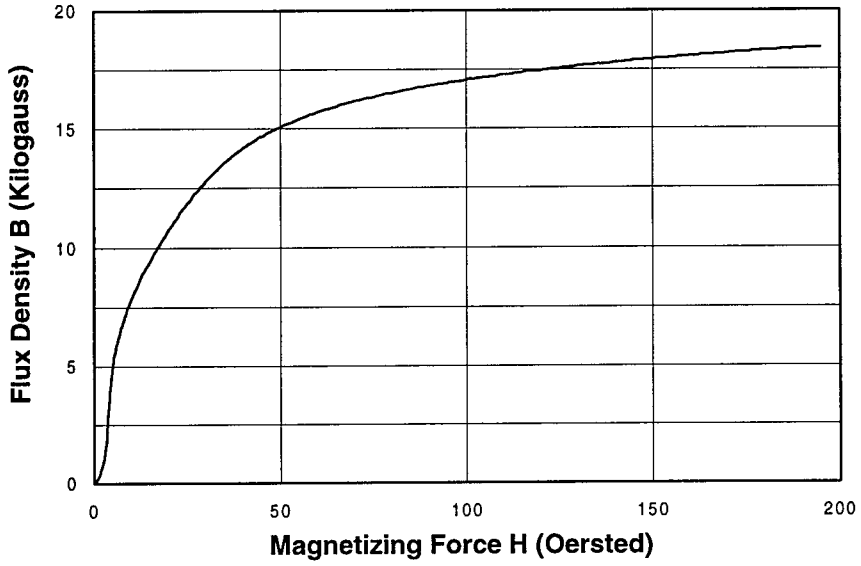

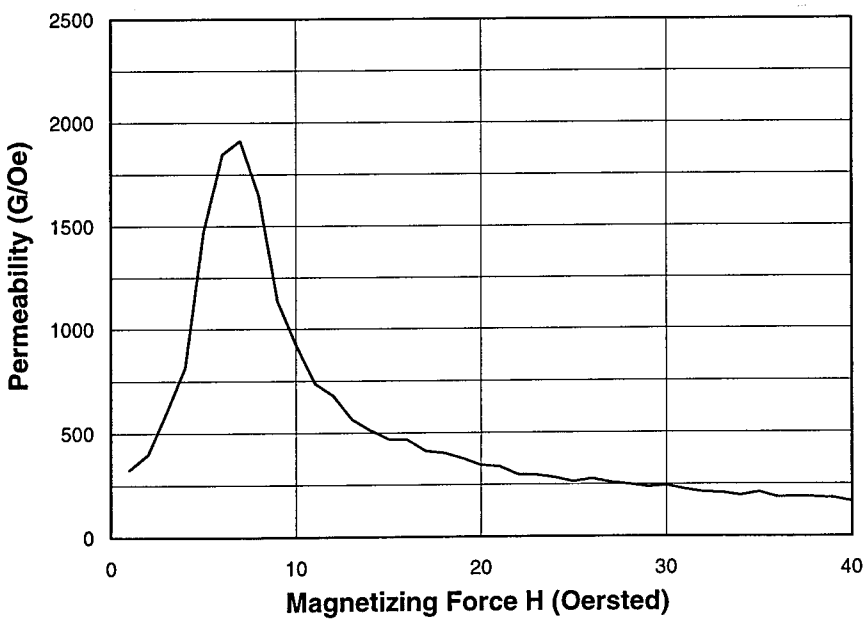

Material 24-35

Numerical Values		
Diameter		23.87 in.
Thickness		0.290 in.
Charpy		
Energy		29 ft-lbs
Shear		100%
Tensile		
Yield		71.2 ksi
Ultimate		94.2 ksi
Elongation		24%
Hardness (Rockwell B)		94.5
Grain Size (ASTM #)		7
Magnetic Measures		
Remanence		8,410 G
Coercivity		9.06 Oe
Permeability		780 G/Oe
H at Max Permeability		10 Oe
Chemical Composition		
Carbon	C	0.28%
Manganese	Mn	1.16%
Phosphorus	P	0.013%
Sulfur	S	0.031%
Silicon	Si	0.042%
Aluminum	Al	0.000%
Vanadium	V	0.000%
Columbium	Cb	0.005%

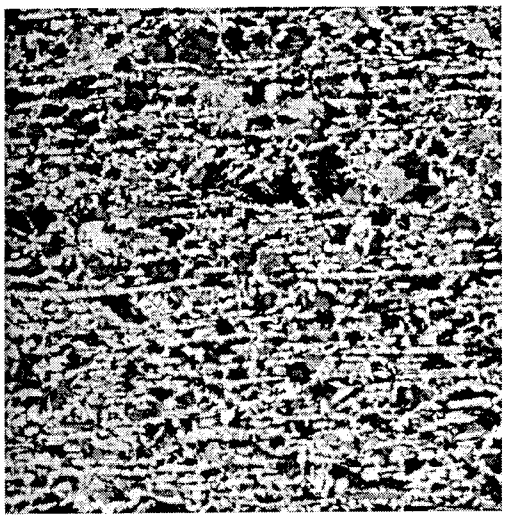

100X Picral + Nital Etch OB390

The microstructure consists of a banded mixture of equiaxed ferrite and pearlite with a relatively high pearlite content. The ferrite bands tend to be distinct. The grain size is ASTM 7. This pipe steel exhibits centerline segregation with centerline region containing a higher percentage (70 percent) of pearlite and relatively large pearlite colonies.

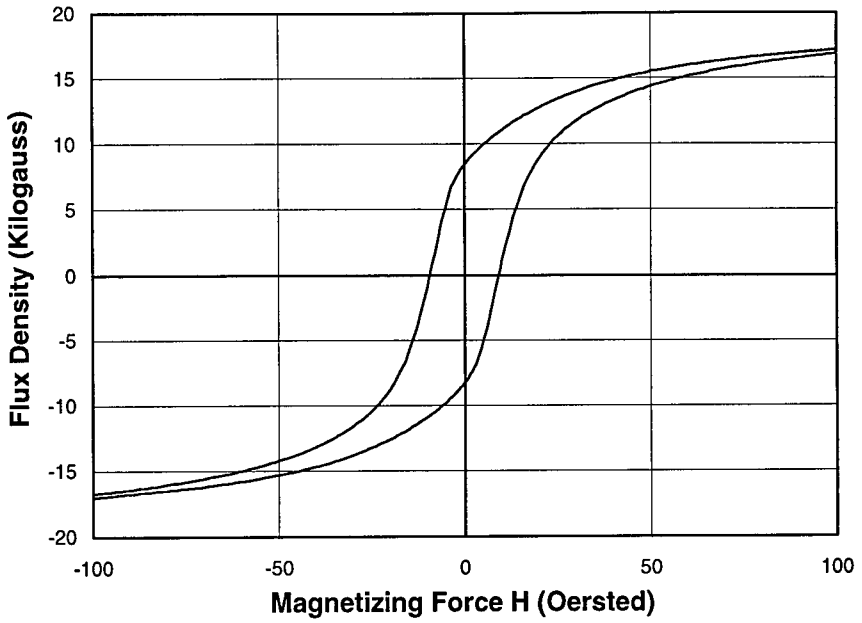

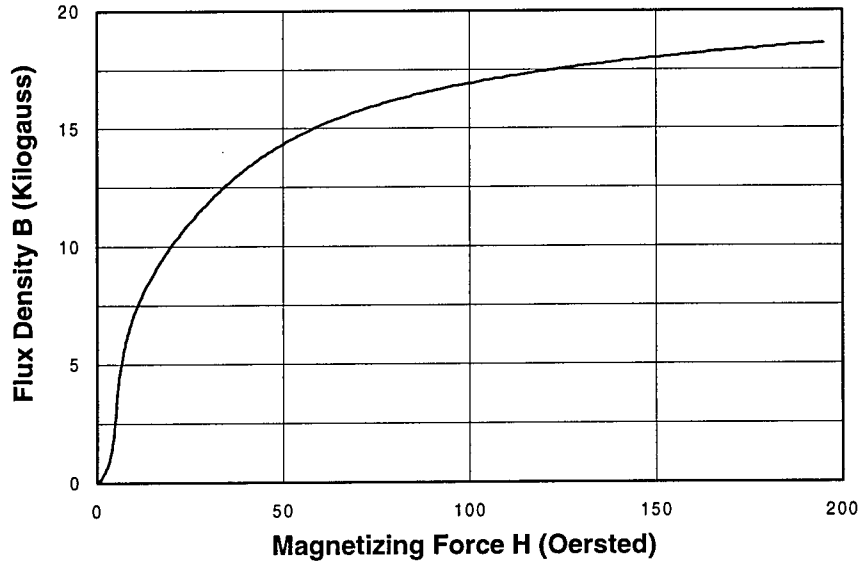

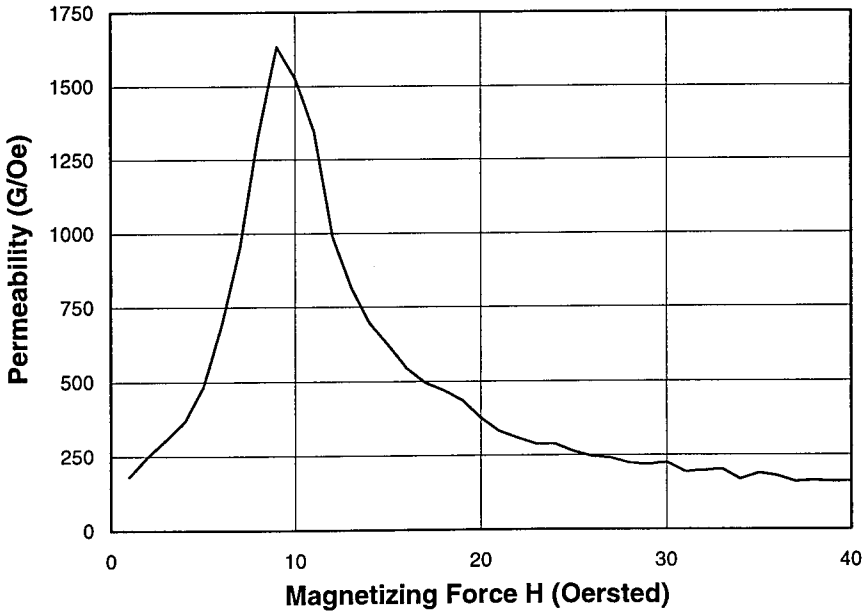

Material 24-36

Numerical Values		
Diameter		23.87 in.
Thickness		0.292 in.
Charpy		
Energy		31 ft-lbs
Shear		100%
Tensile		
Yield		57.8 ksi
Ultimate		79.1 ksi
Elongation		28%
Hardness (Rockwell B)		82.5
Grain Size (ASTM #)		9
Magnetic Measures		
Remanence		7,610 G
Coercivity		6.25 Oe
Permeability		1,000 G/Oe
H at Max Permeability		7 Oe
Chemical Composition		
Carbon	C	0.25%
Manganese	Mn	0.98%
Phosphorus	P	0.014%
Sulfur	S	0.021%
Silicon	Si	0.031%
Aluminum	Al	0.000%
Vanadium	V	0.001%
Columbium	Cb	0.002%

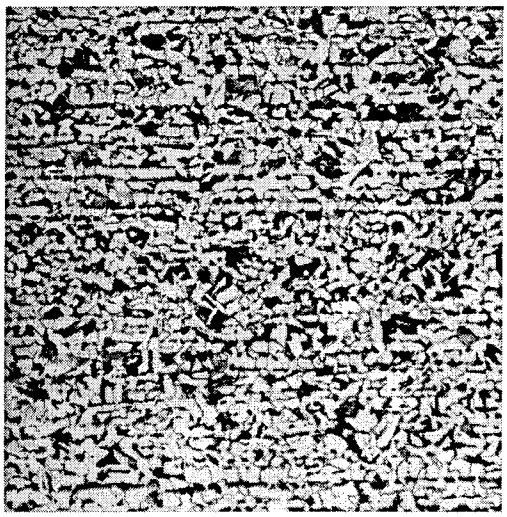

100X Picral + Nital Etch OB391

The microstructure consists of a banded mixture of relatively fine-grained, equiaxed ferrite and pearlite. The grain size is ASTM 8.5. There are two bands visible to the unaided eye near the centerline. Those bands have somewhat higher pearlite contents than the remainder of the microstructure. Also, there is a layer of distorted microstructure at the outside surface of the pipe. That structure most likely resulted from grit blasting prior to coating.

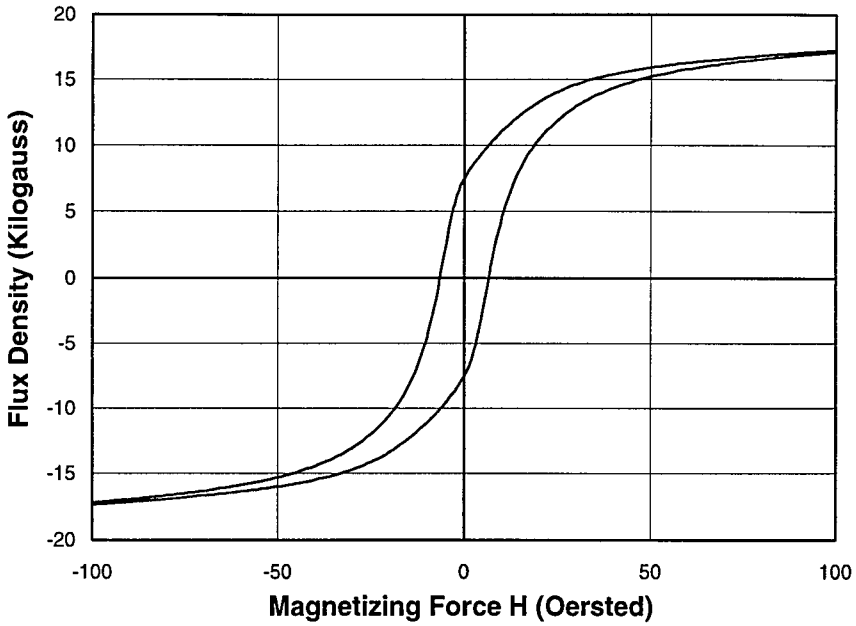

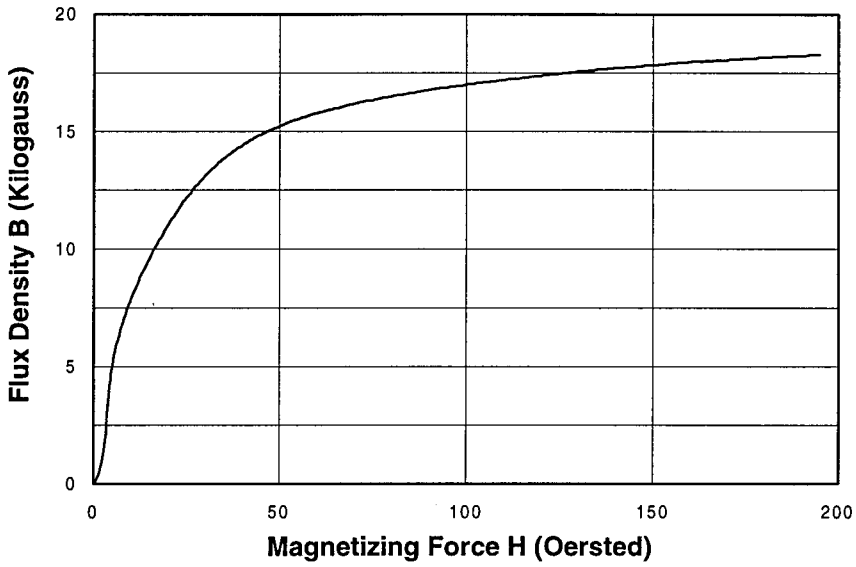

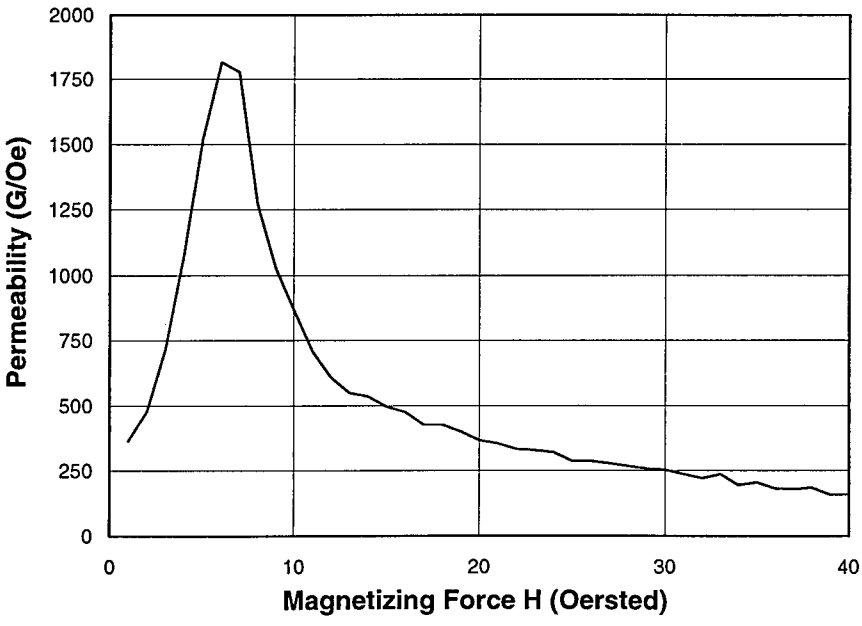

Material 24-37

Numerical Values		
Diameter		23.87 in.
Thickness		0.284 in.
Charpy		
Energy		32 ft-lbs
Shear		99%
Tensile		
Yield		62.3 ksi
Ultimate		86.4 ksi
Elongation		24.5%
Hardness (Rockwell B)		87.5
Grain Size (ASTM #)		9.5
Magnetic Measures		
Remanence		7,770 G
Coercivity		7.45 Oe
Permeability		820 G/Oe
H at Max Permeability		9 Oe
Chemical Composition		
Carbon	C	0.27%
Manganese	Mn	1.14%
Phosphorus	P	0.012%
Sulfur	S	0.020%
Silicon	Si	0.055%
Aluminum	Al	0.000%
Vanadium	V	0.000%
Columbium	Cb	0.005%

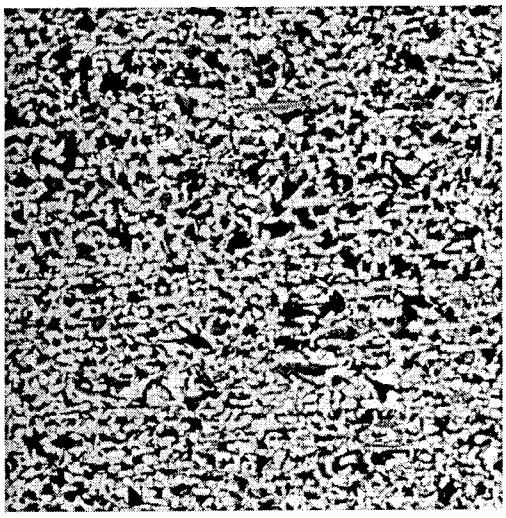

100X Picral + Nital Etch OB393

The microstructure consists of a banded mixture of relatively fine-grained, equiaxed ferrite and pearlite. The grain size is ASTM 9. There is evidence of centerline segregation with two bands with higher pearlite contents near the centerline.

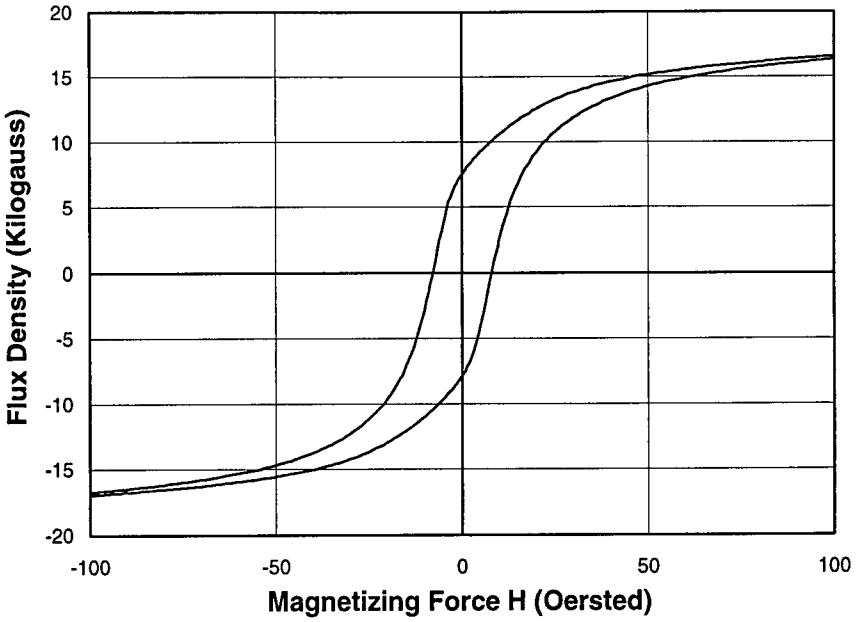

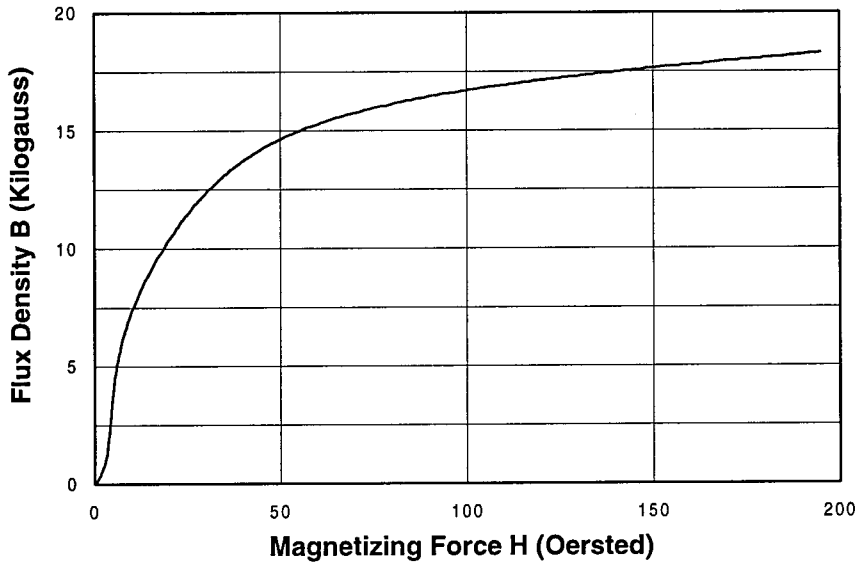

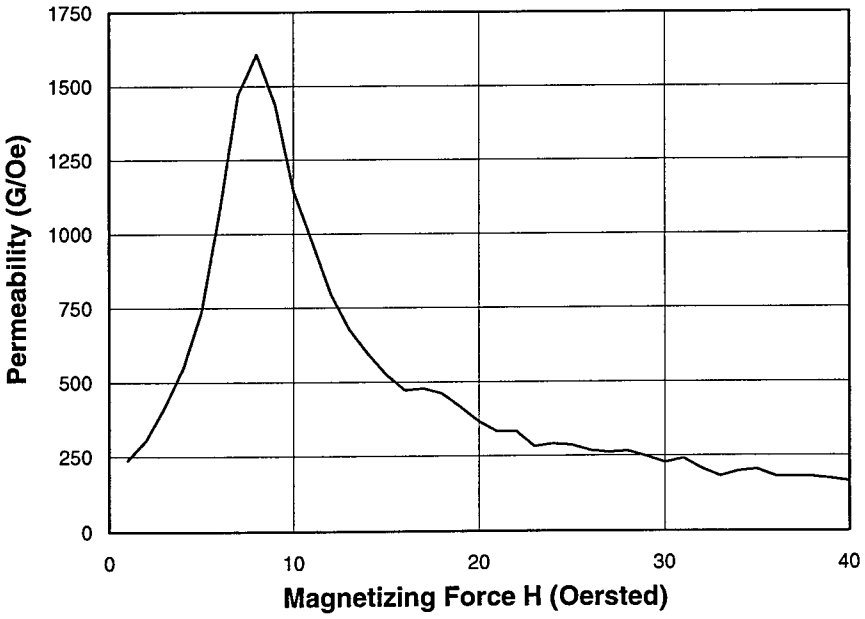

Material 24-38

Numerical Values		
Diameter		23.87 in.
Thickness		0.289 in.
Charpy		
Energy		31 ft-lbs
Shear		100%
Tensile		
Yield		57.5 ksi
Ultimate		82.7 ksi
Elongation		21%
Hardness (Rockwell B)		87
Grain Size (ASTM #)		9.5
Magnetic Measures		
Remanence		8,050 G
Coercivity		6.82 Oe
Permeability		920 G/Oe
H at Max Permeability		8 Oe
Chemical Composition		
Carbon	C	0.24%
Manganese	Mn	0.91%
Phosphorus	P	0.015%
Sulfur	S	0.028%
Silicon	Si	0.046%
Aluminum	Al	0.000%
Vanadium	V	0.001%
Columbium	Cb	0.006%

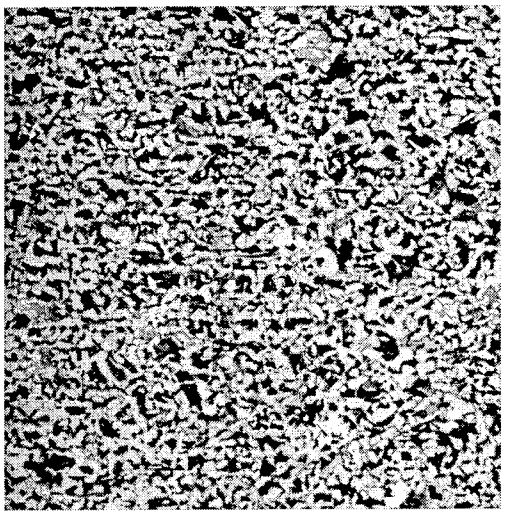

100X Picral + Nital Etch OB394

The microstructure consists of a slightly banded mixture of relatively fine-grained, equiaxed ferrite and pearlite. The grain size is ASTM 9.

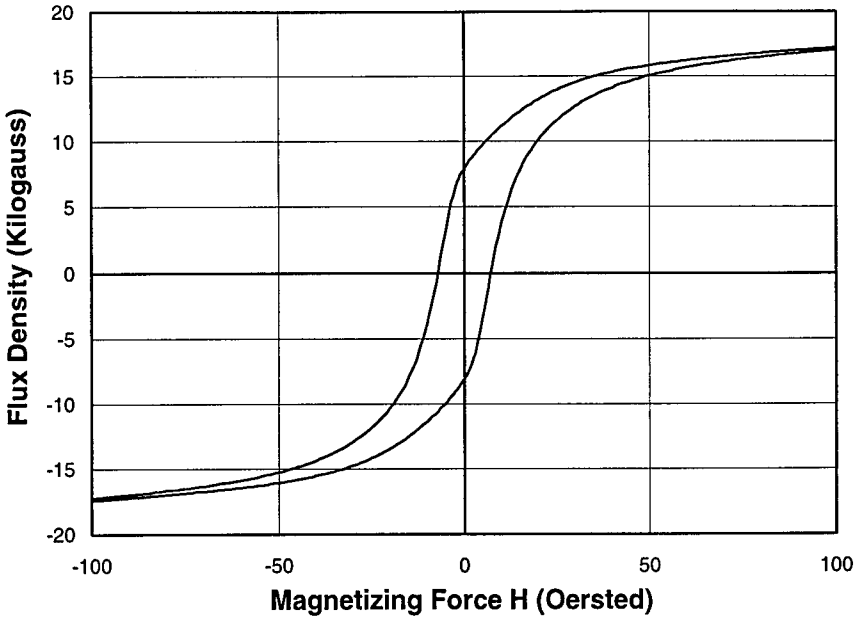

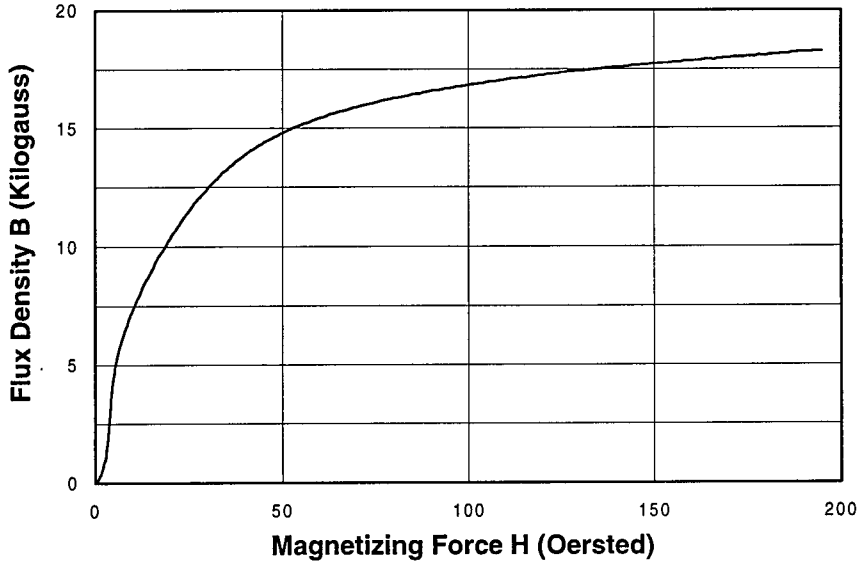

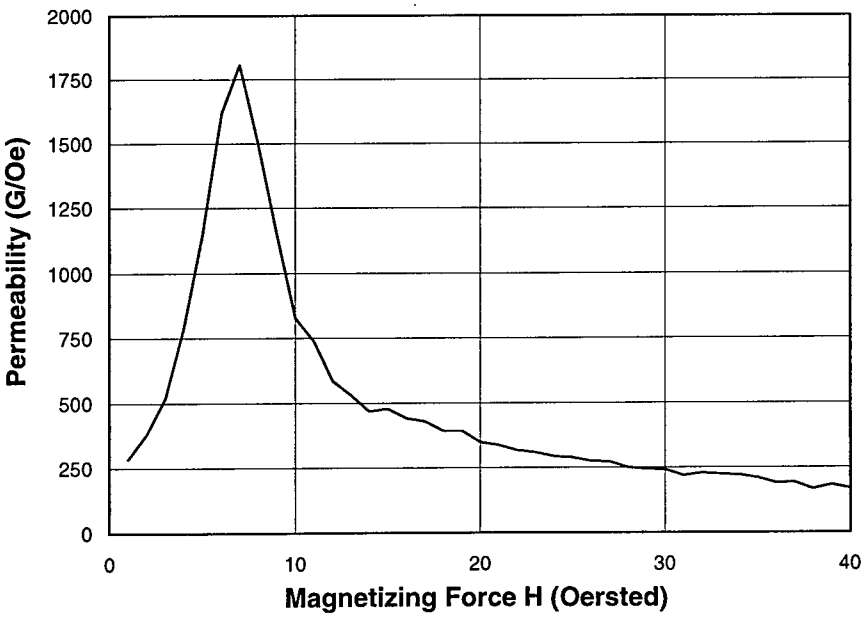

Material 24-39

Numerical Values		
Diameter		23.87 in.
Thickness		0.296 in.
Charpy		
Energy		31 ft-lbs
Shear		100%
Tensile		
Yield		58.3 ksi
Ultimate		80.2 ksi
Elongation		24%
Hardness (Rockwell B)		87
Grain Size (ASTM #)		9.5
Magnetic Measures		
Remanence		7,810 G
Coercivity		6.55 Oe
Permeability		870 G/Oe
H at Max Permeability		8 Oe
Chemical Composition		
Carbon	C	0.23%
Manganese	Mn	0.96%
Phosphorus	P	0.014%
Sulfur	S	0.018%
Silicon	Si	0.032%
Aluminum	Al	0.000%
Vanadium	V	0.001%
Columbium	Cb	0.003%

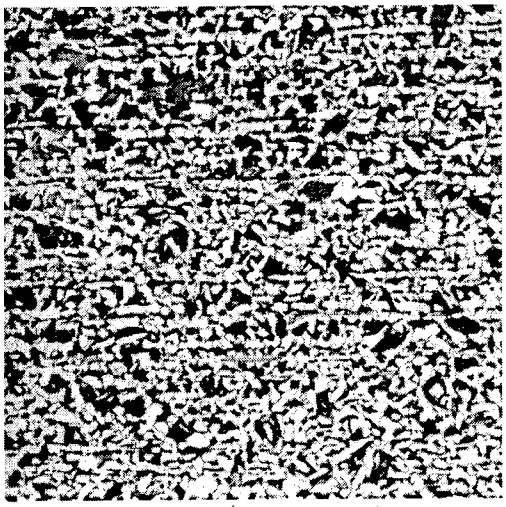

100X Picral + Nital Etch OB395

The microstructure consists of a moderately banded mixture of relatively fine-grained, equiaxed ferrite and pearlite. The grain size is ASTM 9. There is evidence of some centerline segregation with bands that contain somewhat higher pearlite contents in that region.

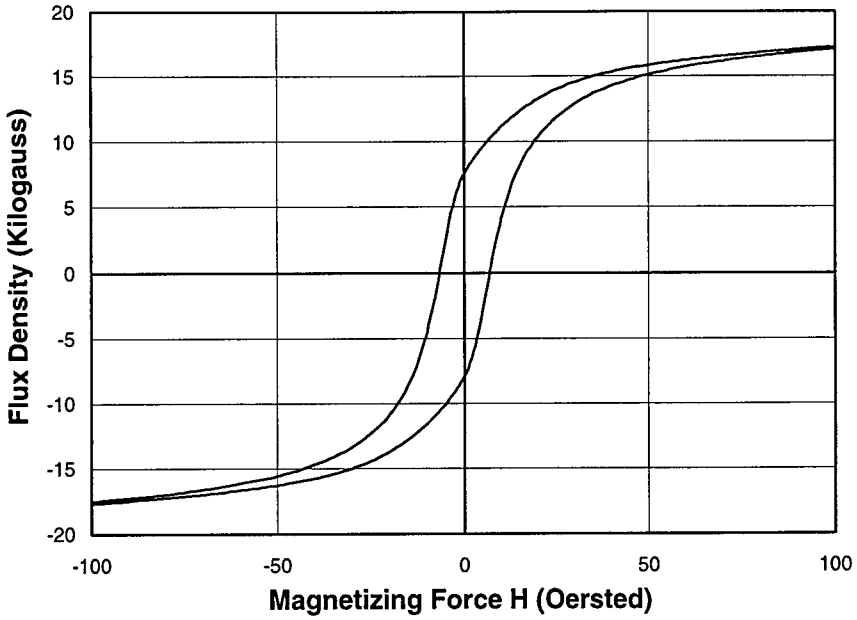

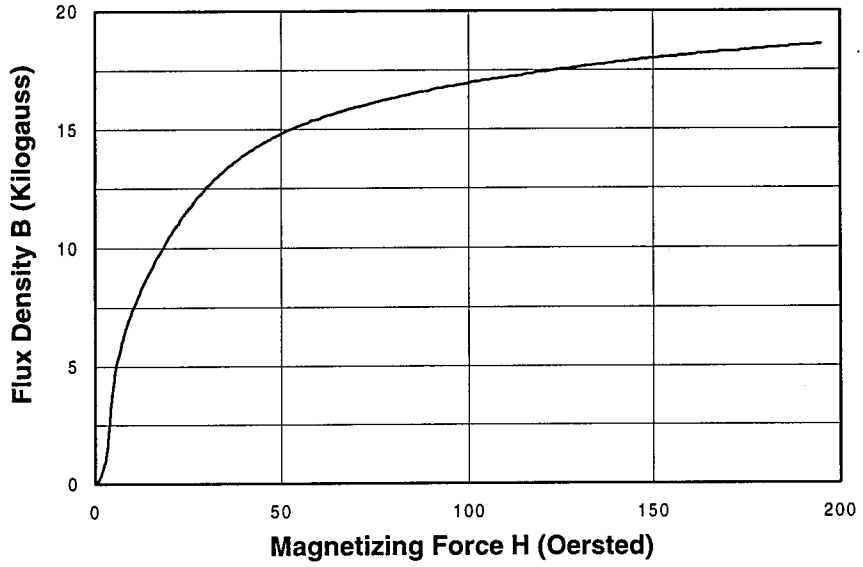

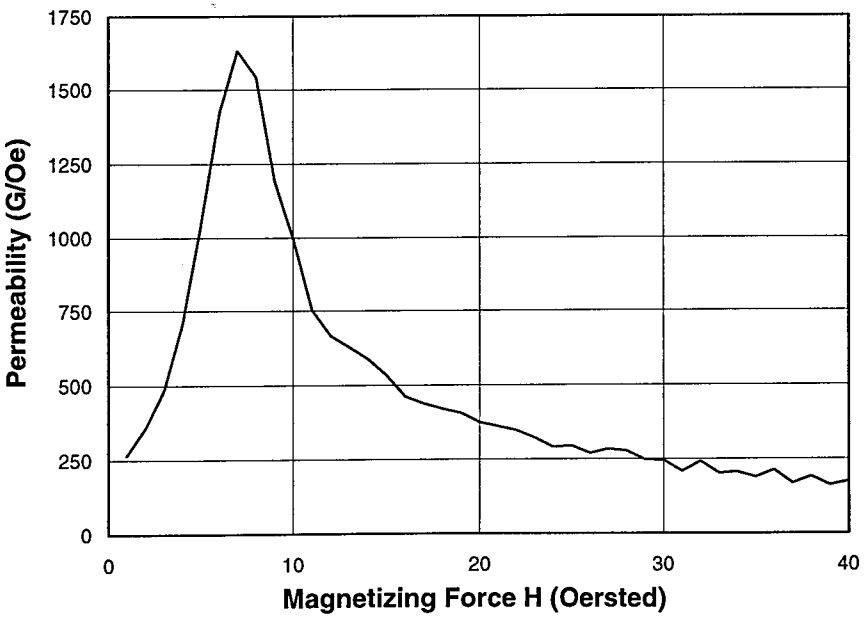

Material 24-40

Numerical Values		
Diameter		23.87 in.
Thickness		0.320 in.
Charpy		
Energy		31 ft-lbs
Shear		100%
Tensile		
Yield		60.1 ksi
Ultimate		82.5 ksi
Elongation		26.5%
Hardness (Rockwell B)		86
Grain Size (ASTM #)		10
Magnetic Measures		
Remanence		9,150 G
Coercivity		5.51 Oe
Permeability		1,340 G/Oe
H at Max Permeability		7 Oe
Chemical Composition		
Carbon	C	0.25%
Manganese	Mn	0.92%
Phosphorus	P	0.016%
Sulfur	S	0.025%
Silicon	Si	0.047%
Aluminum	Al	0.000%
Vanadium	V	0.001%
Columbium	Cb	0.005%

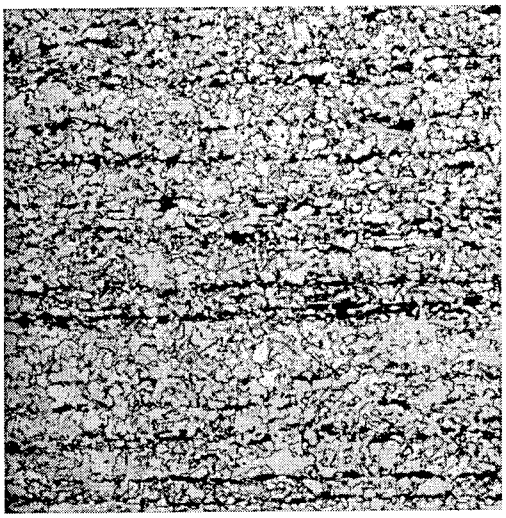

100X Picral + Nital Etch OB396

The microstructure consists of a banded mixture of fine-grained ferrite and pearlite. The pearlite colonies etched very dark. The grain size is ASTM 10. The centerline region contains a band that is mostly ferrite.

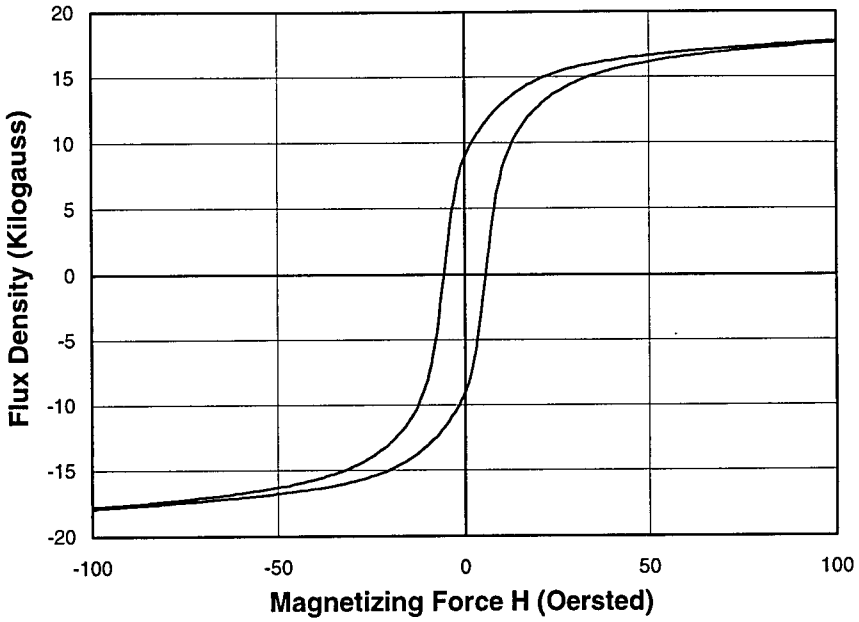

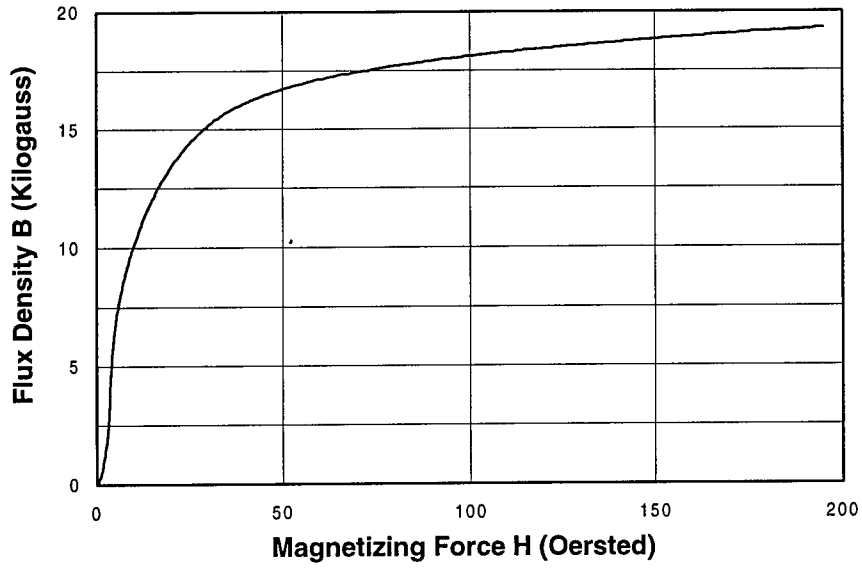

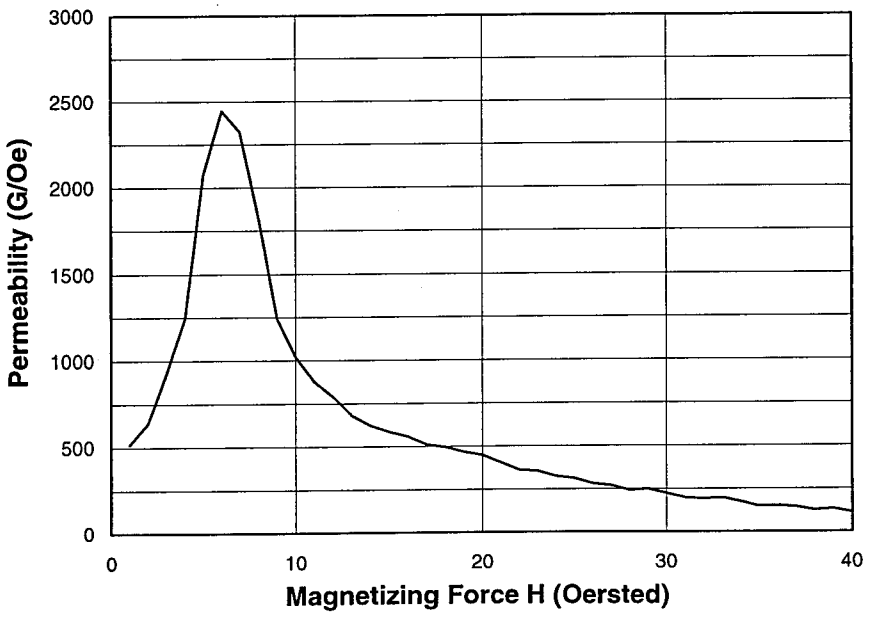

Material 24-41

Numerical Values		
Diameter		23.87 in.
Thickness		0.288 in.
Charpy		
Energy		31 ft-lbs
Shear		100%
Tensile		
Yield		61 ksi
Ultimate		85 ksi
Elongation		31%
Hardness (Rockwell B)		87
Grain Size (ASTM #)		9.5
Magnetic Measures		
Remanence		7,850 G
Coercivity		7.69 Oe
Permeability		850 G/Oe
H at Max Permeability		8 Oe
Chemical Composition		
Carbon	C	0.27%
Manganese	Mn	1.08%
Phosphorus	P	0.018%
Sulfur	S	0.021%
Silicon	Si	0.050%
Aluminum	Al	0.000%
Vanadium	V	0.000%
Columbium	Cb	0.008%

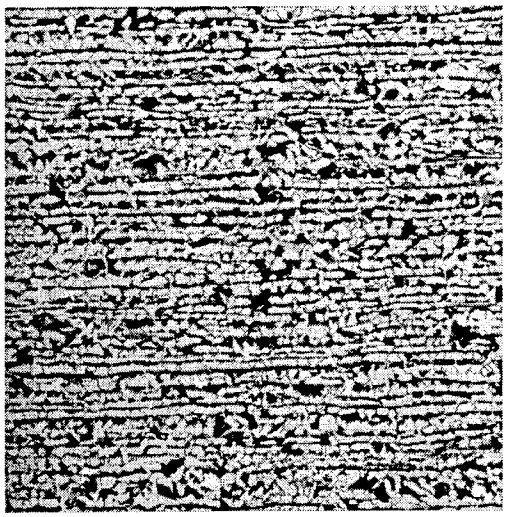

100X Picral + Nital Etch OB397

The microstructure consists of a banded mixture of relatively fine-grained, equiaxed ferrite and pearlite. The grain size is ASTM 9.5.

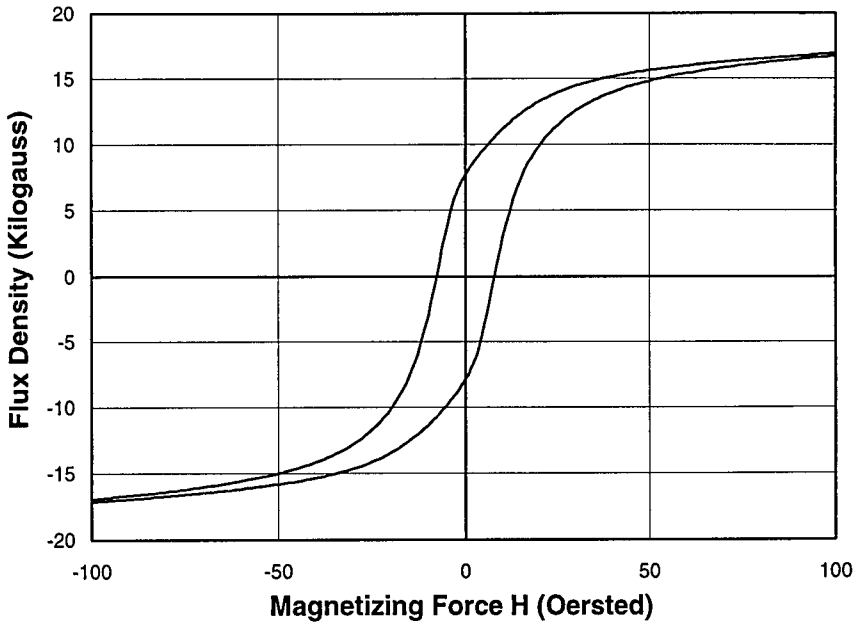

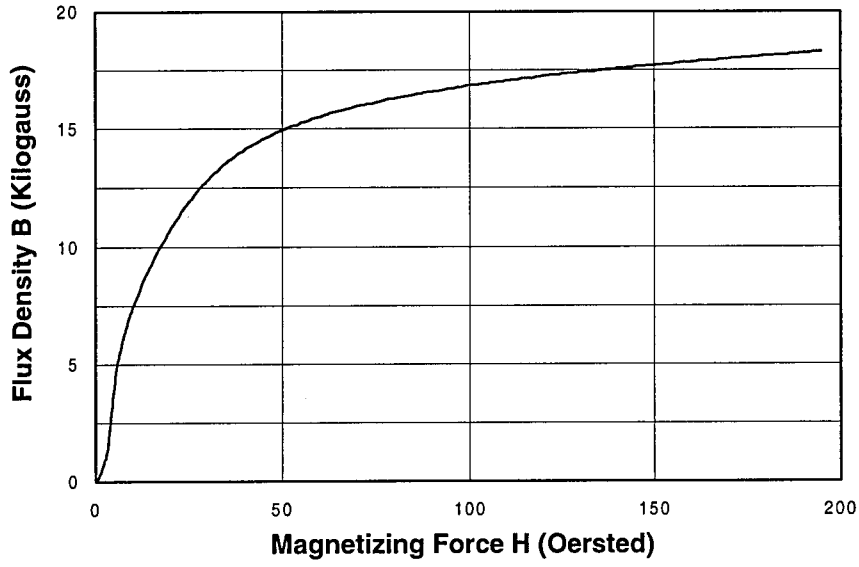

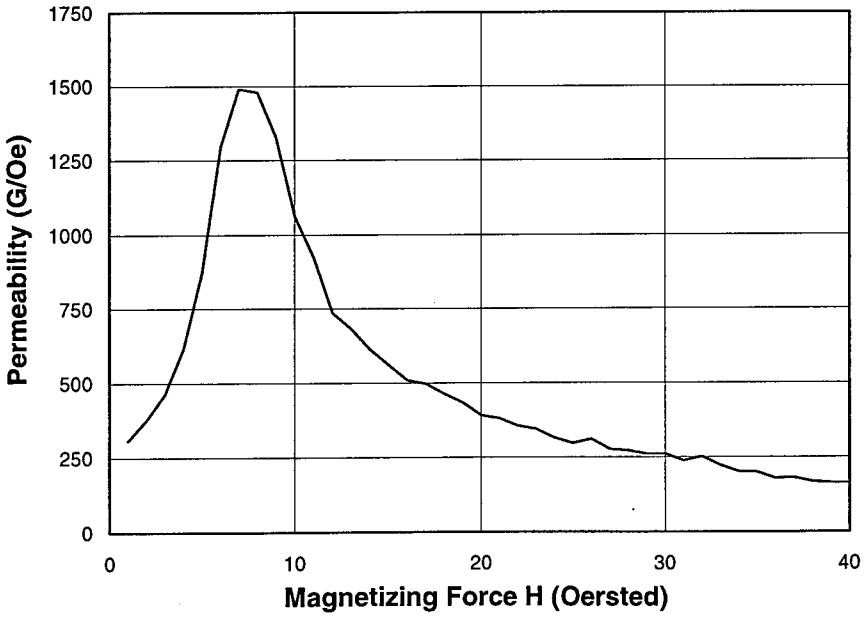

Material 24-42

Numerical Values		
Diameter		23.87 in.
Thickness		0.279 in.
Charpy		
Energy		30 ft-lbs
Shear		100%
Tensile		
Yield		53.9 ksi
Ultimate		76.3 ksi
Elongation		28.5%
Hardness (Rockwell B)		82
Grain Size (ASTM #)		7.5
Magnetic Measures		
Remanence		8,150 G
Coercivity		6.45 Oe
Permeability		890 G/Oe
H at Max Permeability		7 Oe
Chemical Composition		
Carbon	C	0.24%
Manganese	Mn	0.97%
Phosphorus	P	0.009%
Sulfur	S	0.027%
Silicon	Si	0.029%
Aluminum	Al	0.009%
Vanadium	V	0.001%
Columbium	Cb	0.003%

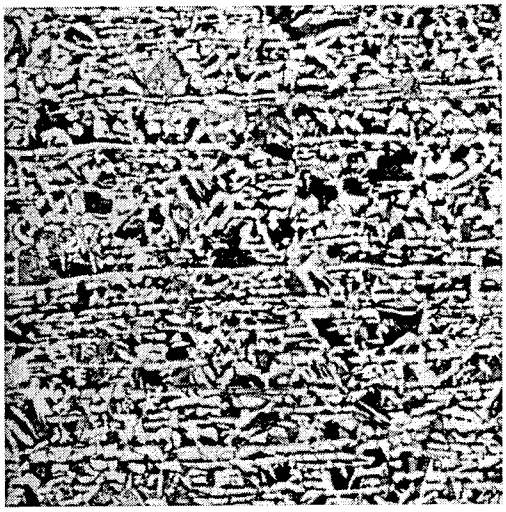

100X Picral + Nital Etch OB398

The microstructure of the steel consists of a banded mixture of equiaxed ferrite and pearlite. Some of the bands are thin and distinct. Some of the pearlite colonies are relatively large compared to the pearlite colonies in the narrow bands. The grain size is ASTM 7.5.

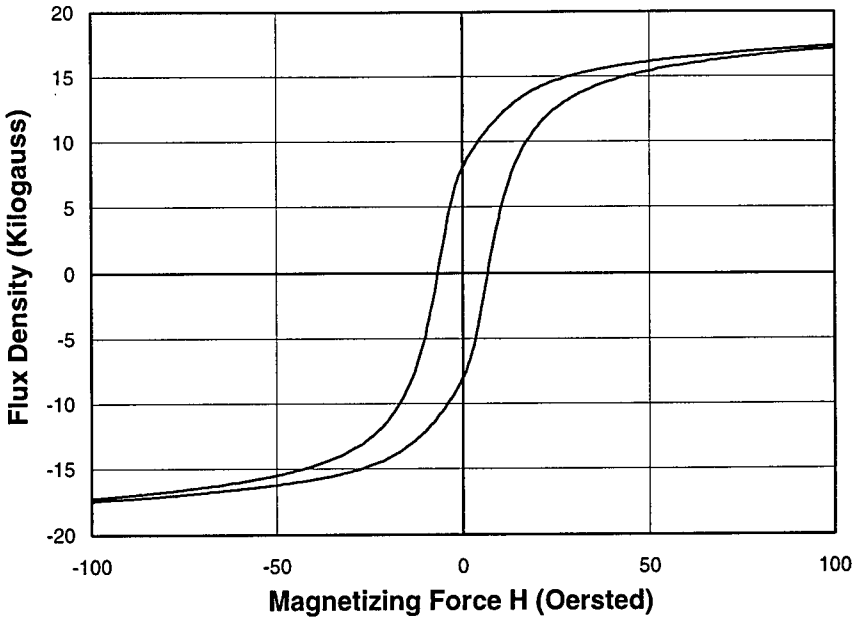

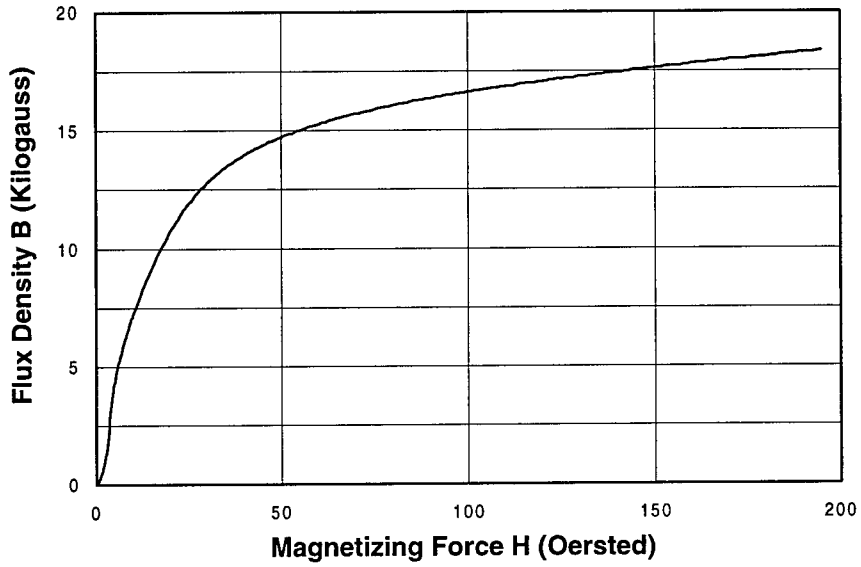

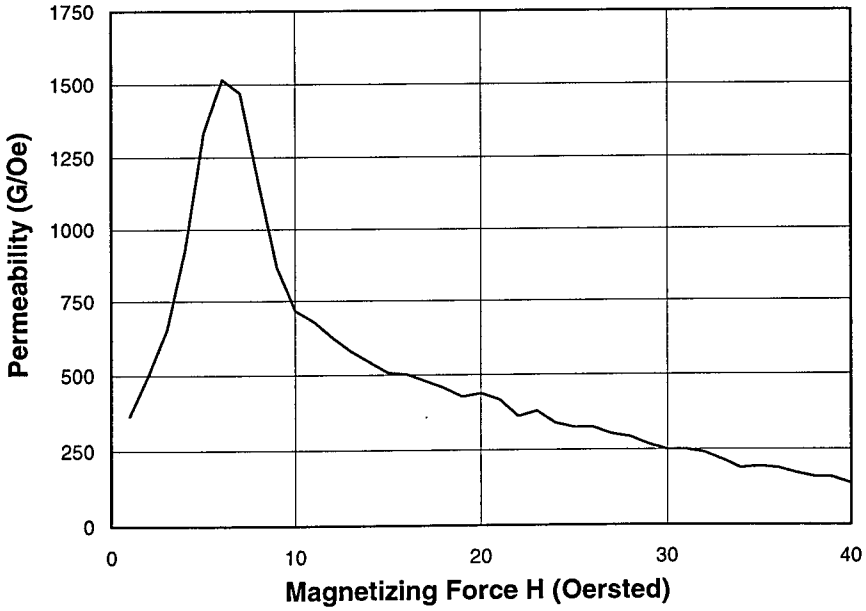

Material 24-43

Numerical Values		
Diameter		23.87 in.
Thickness		0.317 in.
Charpy		
Energy		45 ft-lbs
Shear		95%
Tensile		
Yield		50.1 ksi
Ultimate		83.9 ksi
Elongation		29.5%
Hardness (Rockwell B)		88
Grain Size (ASTM #)		4
Magnetic Measures		
Remanence		9,910 G
Coercivity		6.94 Oe
Permeability		1,010 G/Oe
H at Max Permeability		8 Oe
Chemical Composition		
Carbon	C	0.29%
Manganese	Mn	0.97%
Phosphorus	P	0.011%
Sulfur	S	0.016%
Silicon	Si	0.130%
Aluminum	Al	0.002%
Vanadium	V	0.002%
Columbium	Cb	0.003%

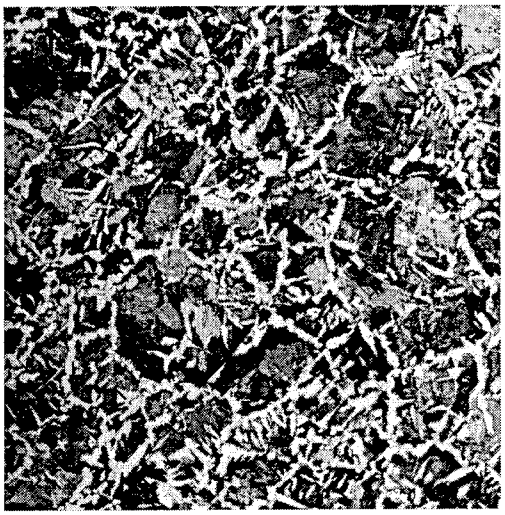

100X Picral + Nital Etch OB399

The microstructure consists of relatively large pearlite colonies with ferrite networks at the prior austenite grain boundaries. The grain size is ASTM 3.5.

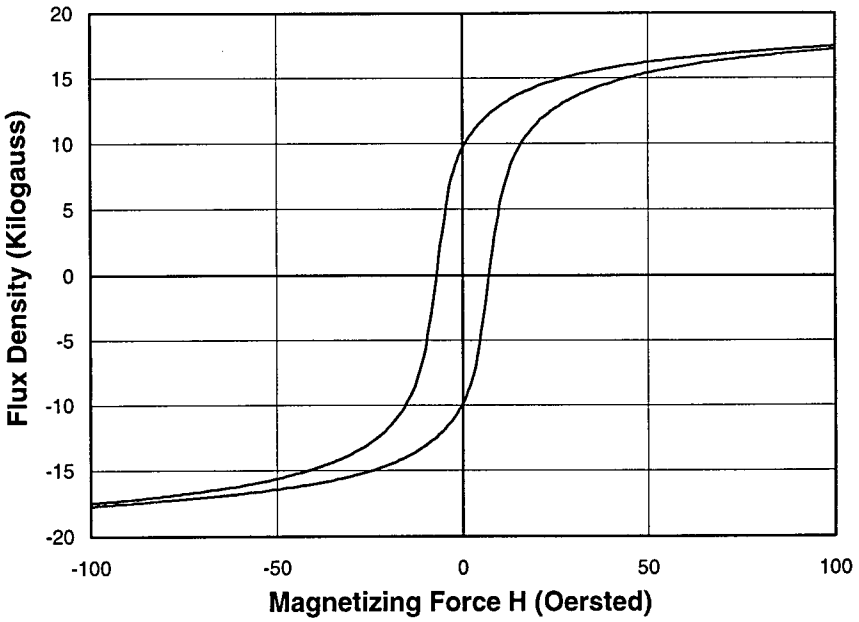

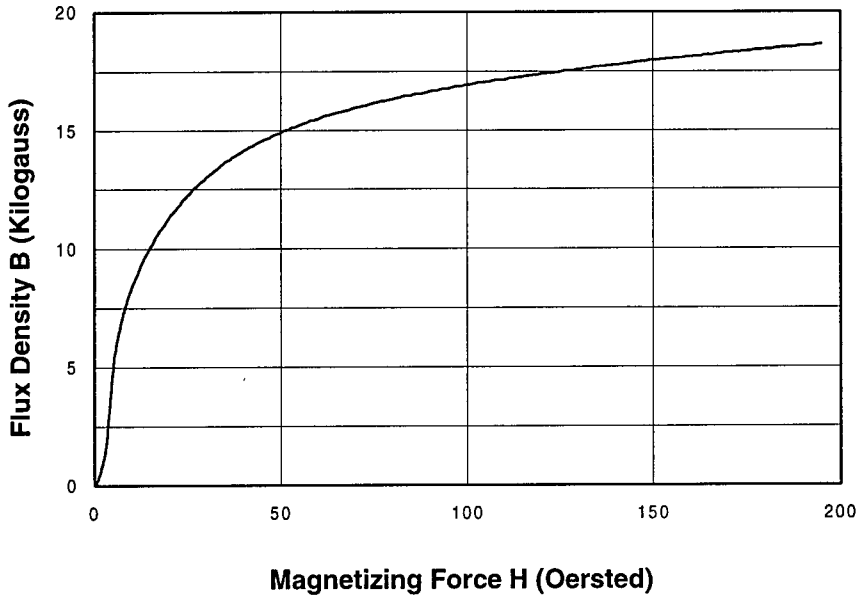

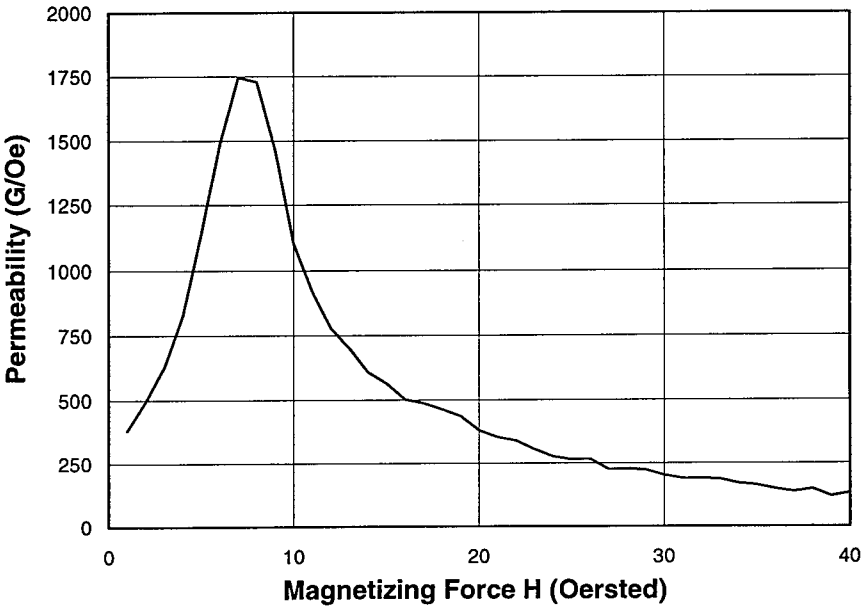

Material 24-44

Numerical Values		
Diameter		23.87 in.
Thickness		0.266 in.
Charpy		
Energy		49 ft-lbs
Shear		83%
Tensile		
Yield		47.6 ksi
Ultimate		65.3 ksi
Elongation		29.5%
Hardness (Rockwell B)		75
Grain Size (ASTM #)		7.5
Magnetic Measures		
Remanence		7,640 G
Coercivity		4.68 Oe
Permeability		1,320 G/Oe
H at Max Permeability		5 Oe
Chemical Composition		
Carbon	C	0.19%
Manganese	Mn	0.55%
Phosphorus	P	0.011%
Sulfur	S	0.024%
Silicon	Si	0.002%
Aluminum	Al	0.005%
Vanadium	V	0.001%
Columbium	Cb	0.003%

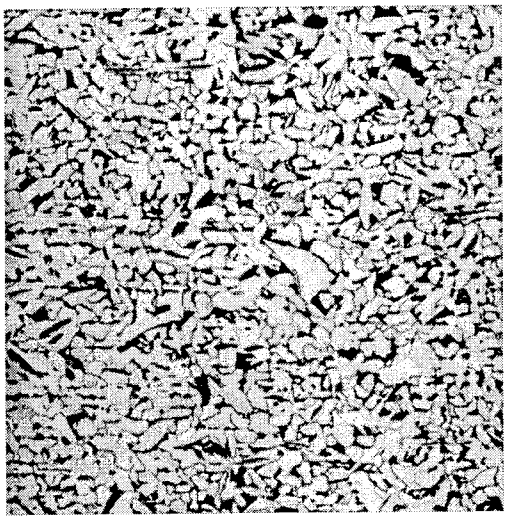

100X Picral + Nital Etch OB400

The microstructure consists of a slightly banded mixture of equiaxed ferrite and pearlite. The grain size is ASTM 7. This steel exhibits some centerline segregation with the microstructure in that region exhibiting more pronounced banding.

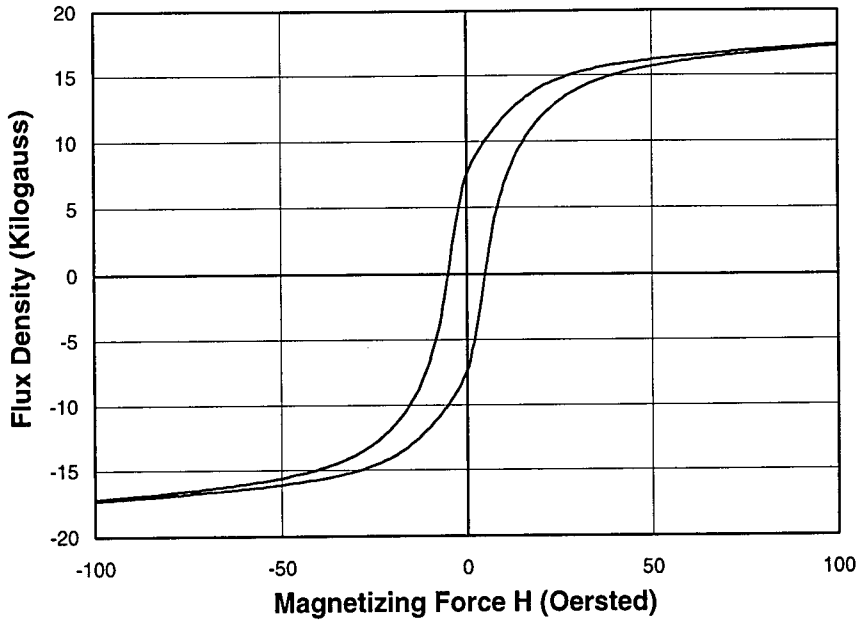

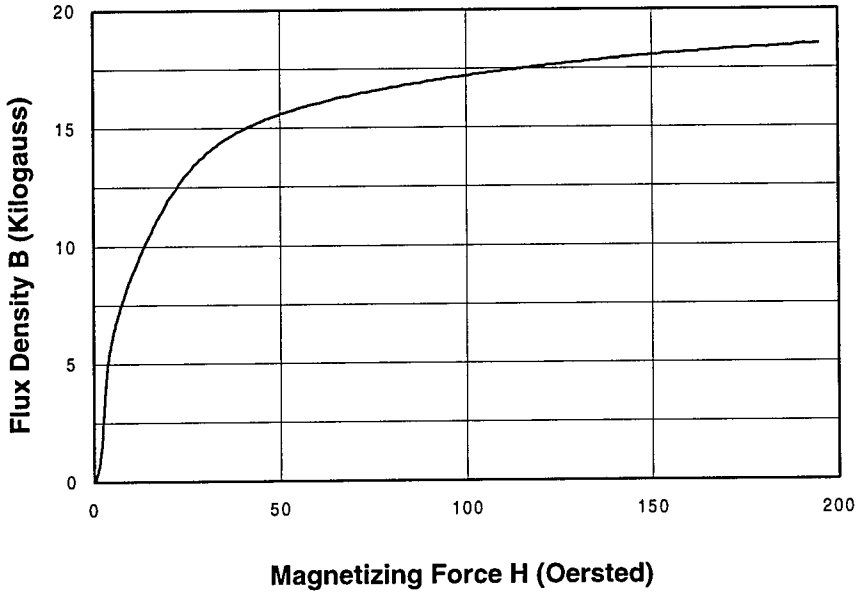

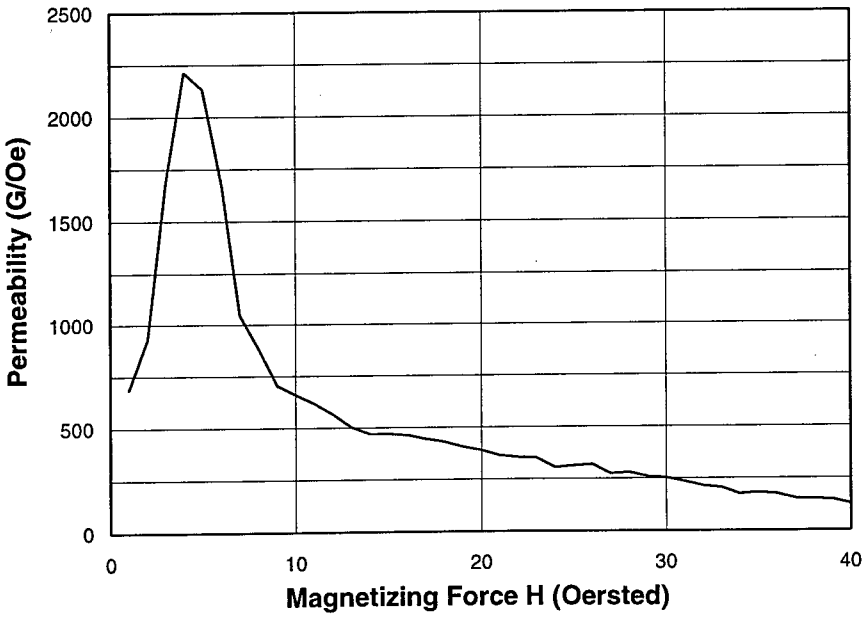

Material 24-45

Numerical Values		
Diameter		23.87 in.
Thickness		0.265 in.
Charpy		
Energy		28 ft-lbs
Shear		100%
Tensile		
Yield		55.9 ksi
Ultimate		76.2 ksi
Elongation		24%
Hardness (Rockwell B)		80
Grain Size (ASTM #)		9
Magnetic Measures		
Remanence		7,820 G
Coercivity		6.23 Oe
Permeability		860 G/Oe
H at Max Permeability		7 Oe
Chemical Composition		
Carbon	C	0.24%
Manganese	Mn	0.66%
Phosphorus	P	0.026%
Sulfur	S	0.030%
Silicon	Si	0.013%
Aluminum	Al	0.002%
Vanadium	V	0.002%
Columbium	Cb	0.003%

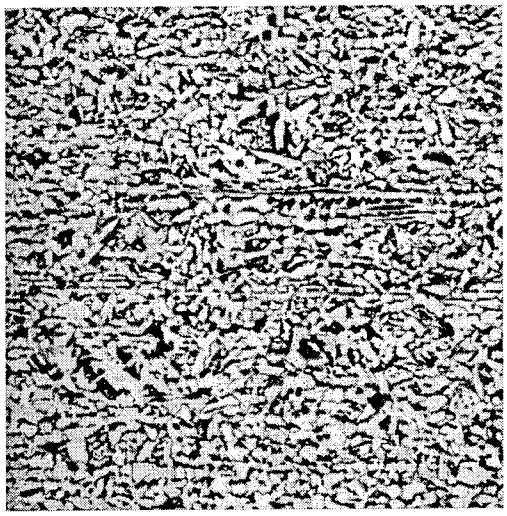

100X Picral + Nital Etch OB401

The typical microstructure consists of a somewhat banded mixture of equiaxed ferrite and pearlite. The grain size is ASTM 8.5. The steel exhibits centerline segregation with the microstructure in that region containing more pearlite.

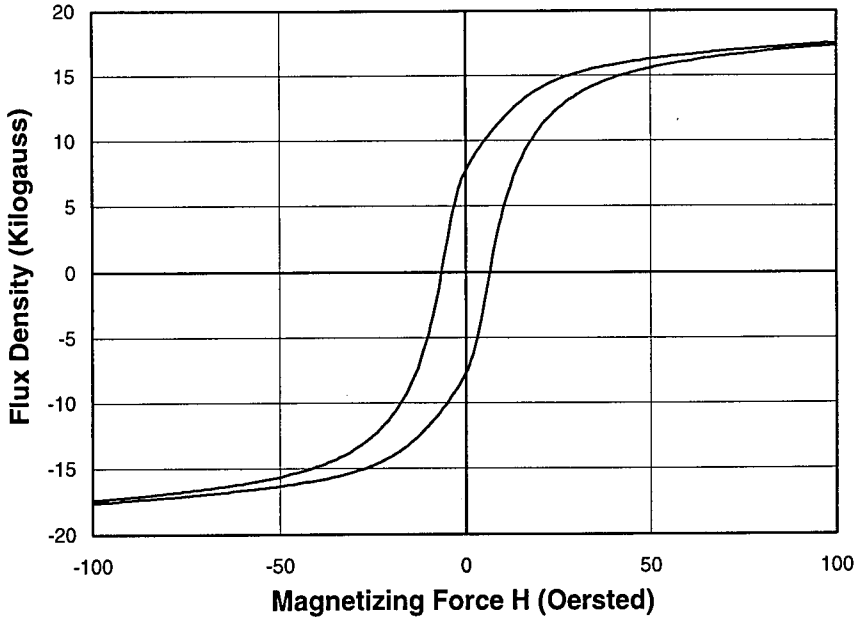

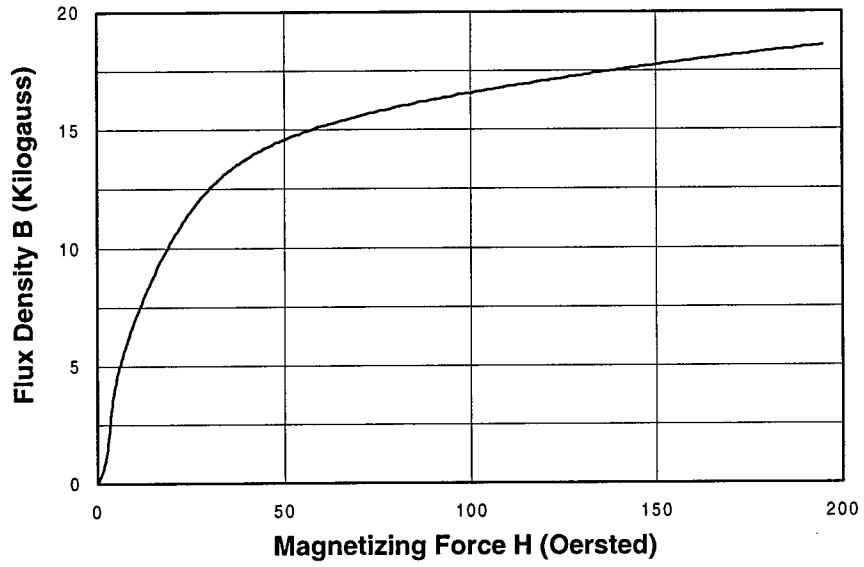

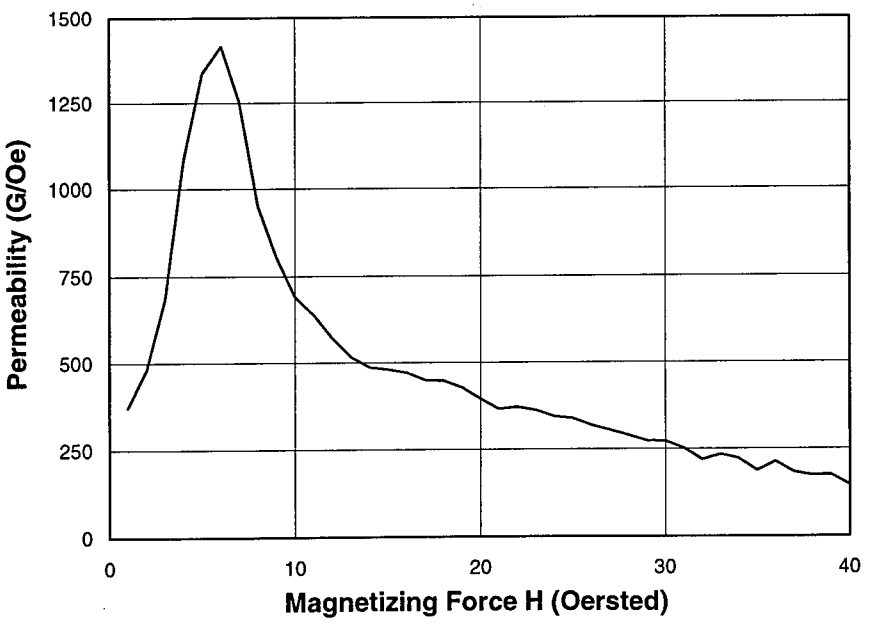

Material 24-46

Numerical Values		
Diameter		23.87 in.
Thickness		0.274 in.
Charpy		
Energy		26 ft-lbs
Shear		92%
Tensile		
Yield		48.5 ksi
Ultimate		67.9 ksi
Elongation		30%
Hardness (Rockwell B)		71
Grain Size (ASTM #)		8
Magnetic Measures		
Remanence		8,060 G
Coercivity		4.71 Oe
Permeability		1,480 G/Oe
H at Max Permeability		5 Oe
Chemical Composition		
Carbon	C	0.20%
Manganese	Mn	0.49%
Phosphorus	P	0.006%
Sulfur	S	0.021%
Silicon	Si	0.000%
Aluminum	Al	0.025%
Vanadium	V	0.000%
Columbium	Cb	0.003%

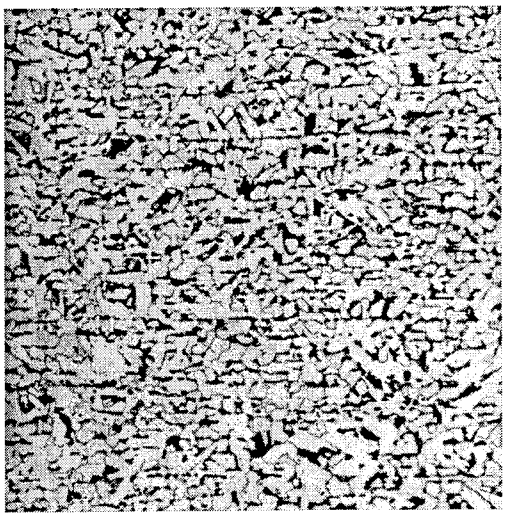

100X Picral + Nital Etch OB402

The microstructure consists of a somewhat banded mixture of equiaxed ferrite and pearlite. The grain size is ASTM 7.5.

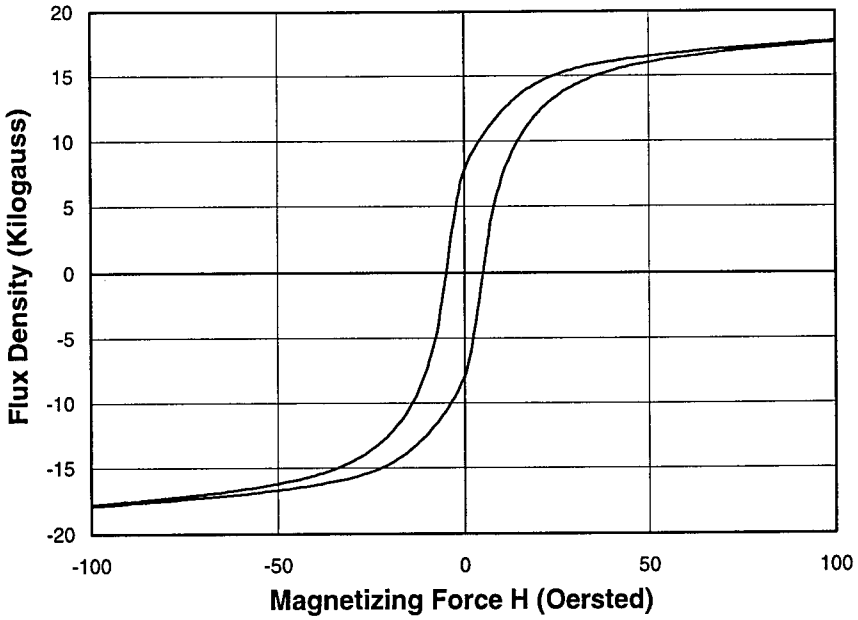

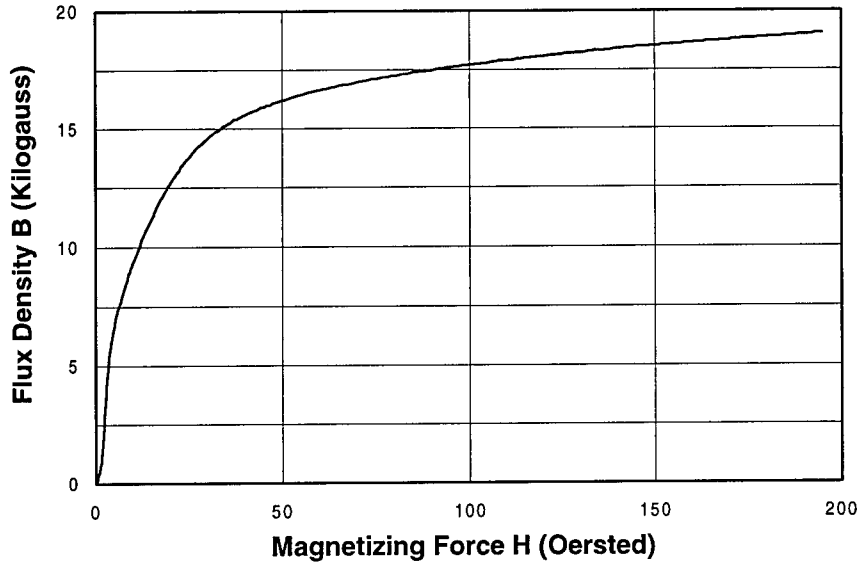

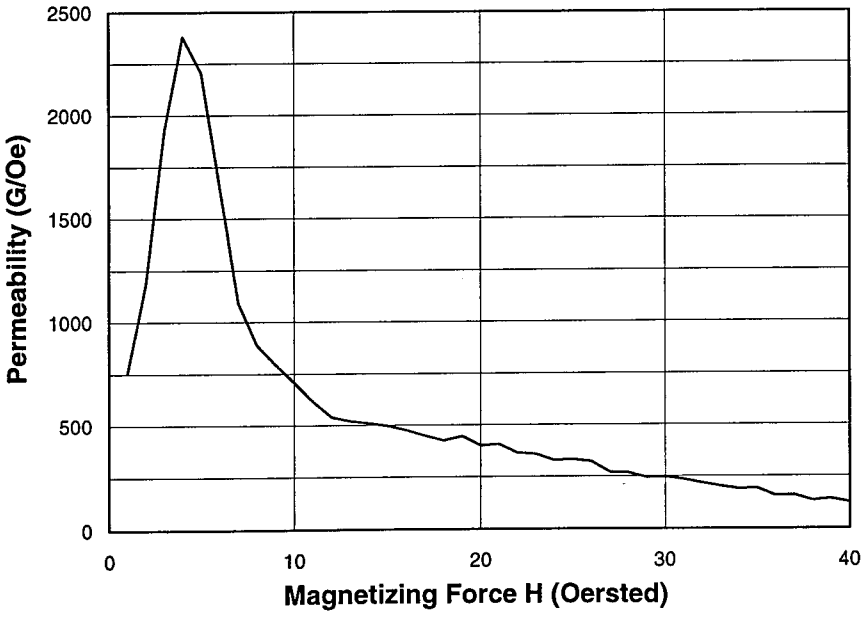

Material 24-47

Numerical Values		
Diameter		23.87 in.
Thickness		0.317 in.
Charpy		
Energy		63 ft-lbs
Shear		98%
Tensile		
Yield		63.8 ksi
Ultimate		80.8 ksi
Elongation		28%
Hardness (Rockwell B)		89.5
Grain Size (ASTM #)		11
Magnetic Measures		
Remanence		7,940 G
Coercivity		5.29 Oe
Permeability		1,100 G/Oe
H at Max Permeability		7 Oe
Chemical Composition		
Carbon	C	0.07%
Manganese	Mn	1.17%
Phosphorus	P	0.017%
Sulfur	S	0.005%
Silicon	Si	0.160%
Aluminum	Al	0.049%
Vanadium	V	0.002%
Columbium	Cb	0.000%

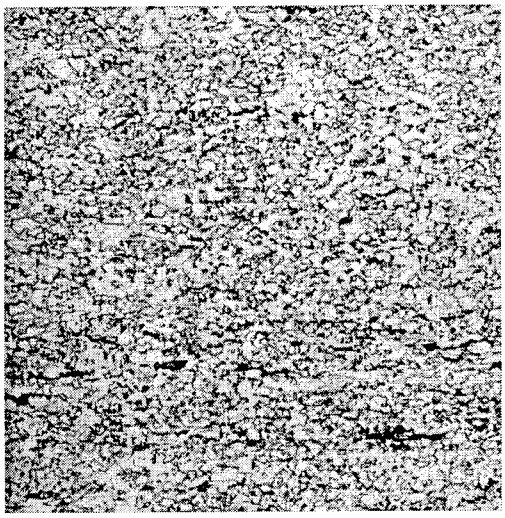

100X Picral + Nital Etch OB403

The microstructure consists of relatively fine-grained, equiaxed ferrite with patches of pearlite/bainite. The grain size is ASTM 10.5.

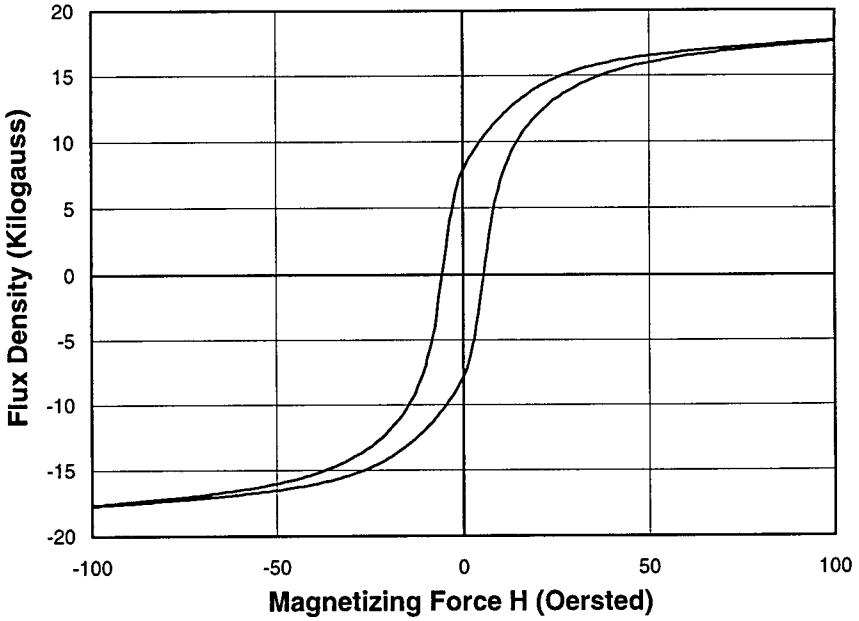

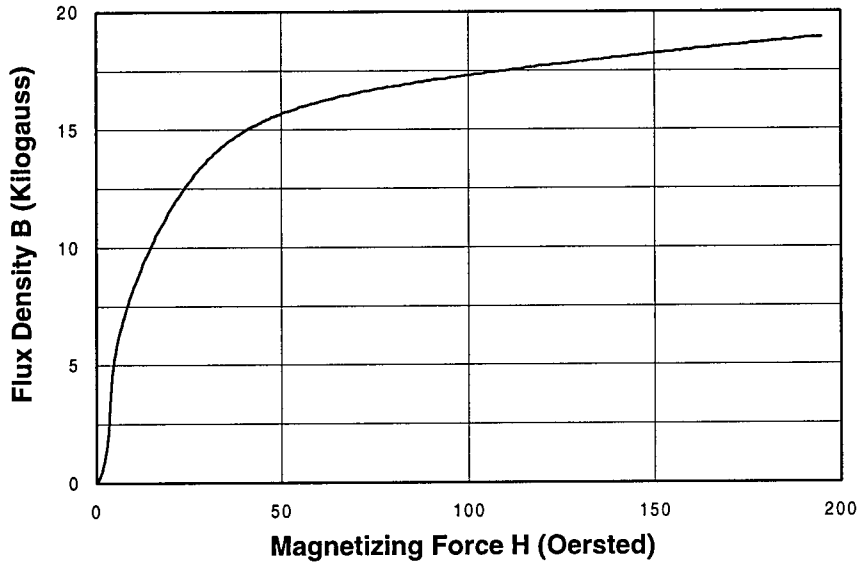

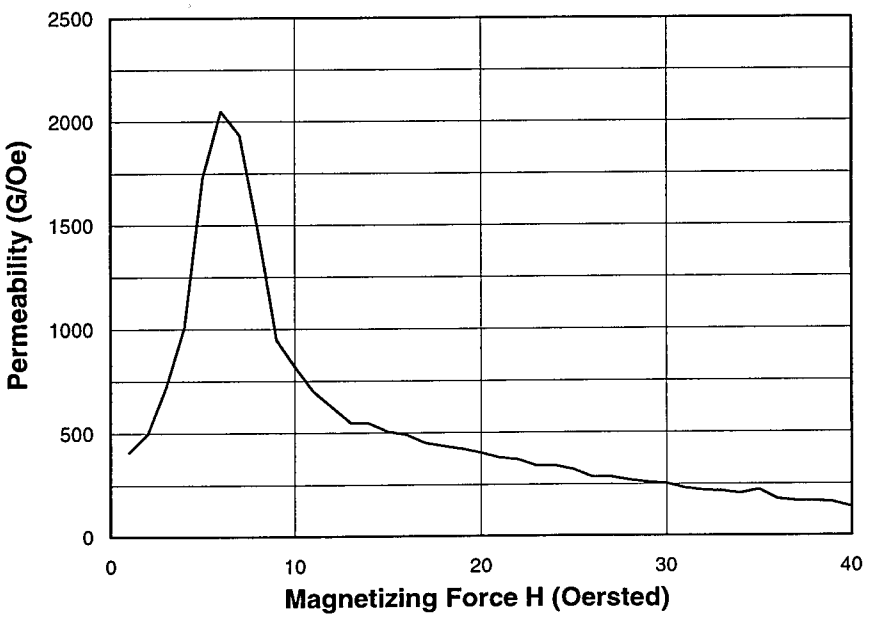

Material 24-50

Numerical Values		
Diameter		23.87 in.
Thickness		0.277 in.
Charpy		
Energy		33 ft-lbs
Shear		98%
Tensile		
Yield		47.8 ksi
Ultimate		63.5 ksi
Elongation		32.5%
Hardness (Rockwell B)		69.5
Grain Size (ASTM #)		8
Magnetic Measures		
Remanence		8,740 G
Coercivity		4.32 Oe
Permeability		1,590 G/Oe
H at Max Permeability		5 Oe
Chemical Composition		
Carbon	C	0.20%
Manganese	Mn	0.44%
Phosphorus	P	0.008%
Sulfur	S	0.028%
Silicon	Si	0.000%
Aluminum	Al	0.001%
Vanadium	V	0.000%
Columbium	Cb	0.003%

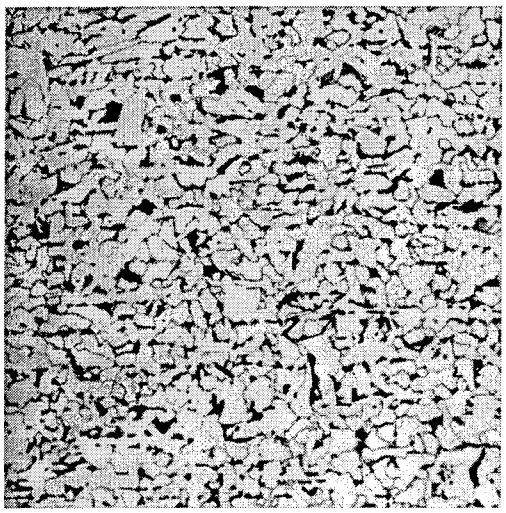

100X Picral + Nital Etch OB404

The microstructure consists of a slightly banded mixture of equiaxed ferrite and pearlite. The grain size is ASTM 8.

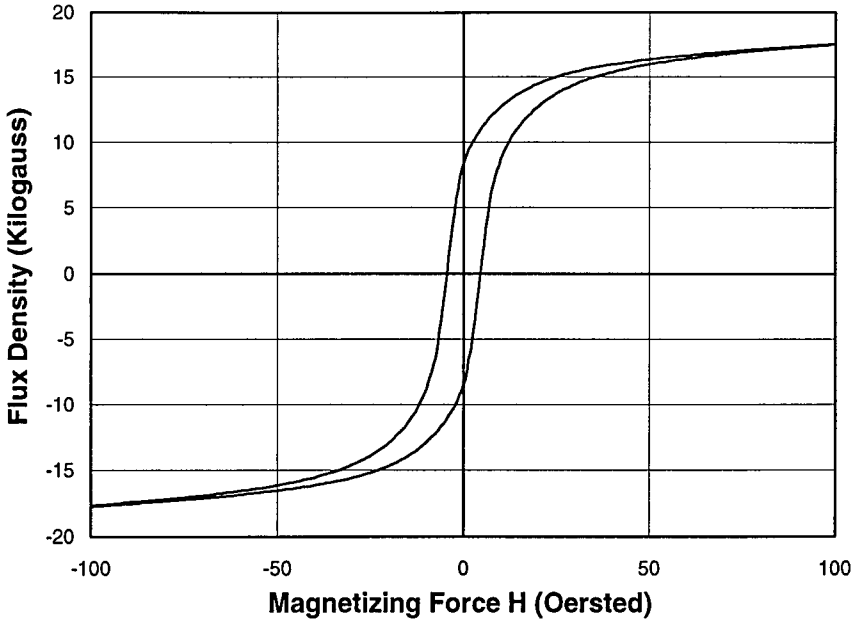

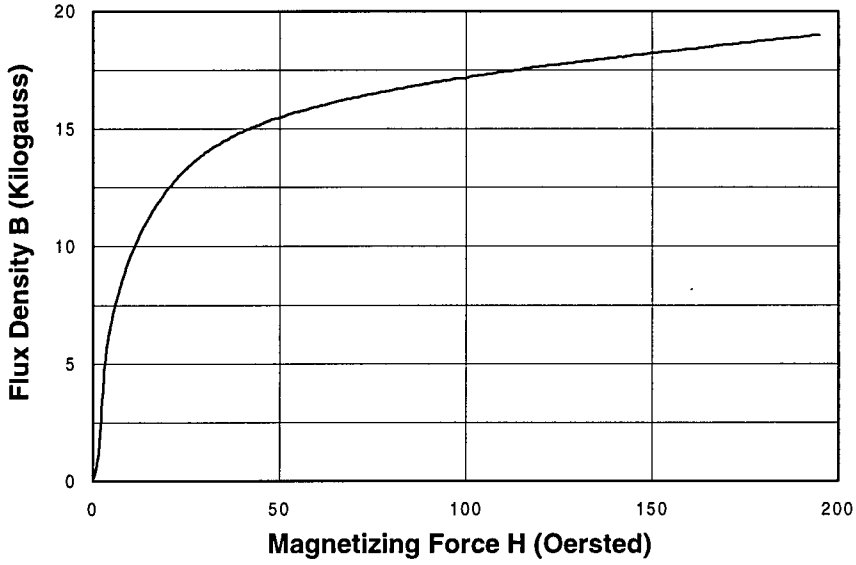

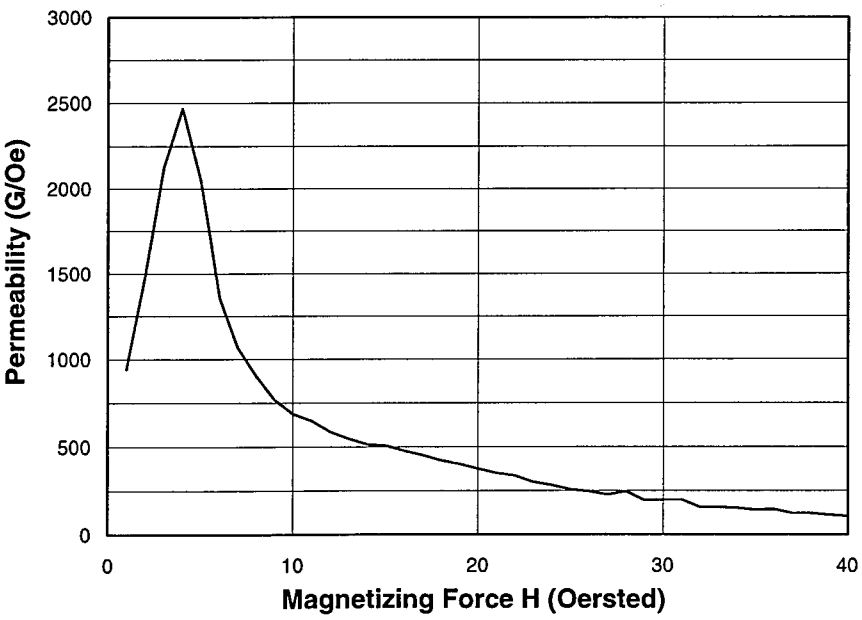

Appendix B

Results of Compression and Tension Testing of 12 Materials

MATERIAL 24-06

Compressive Loading

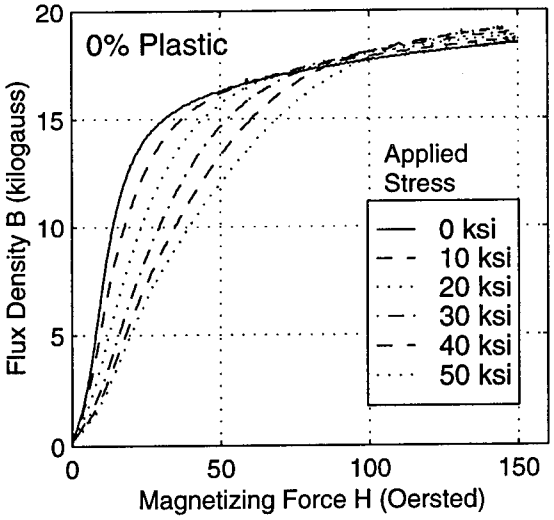

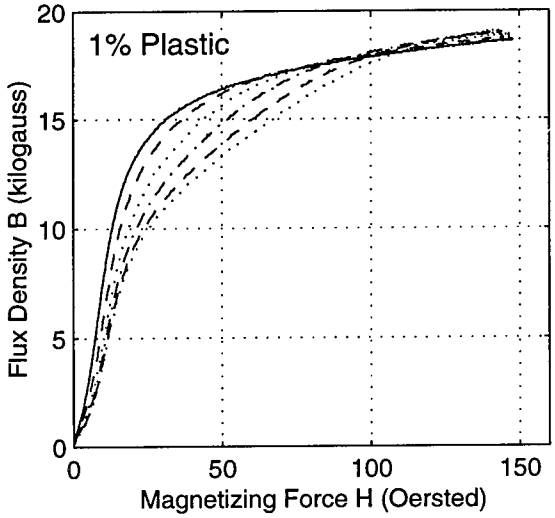

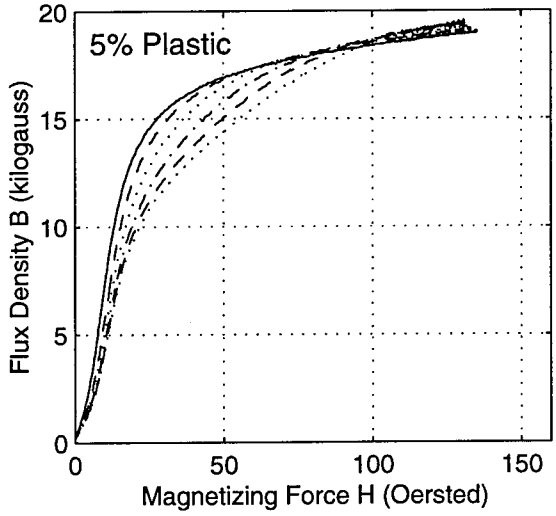

Tensile Loading

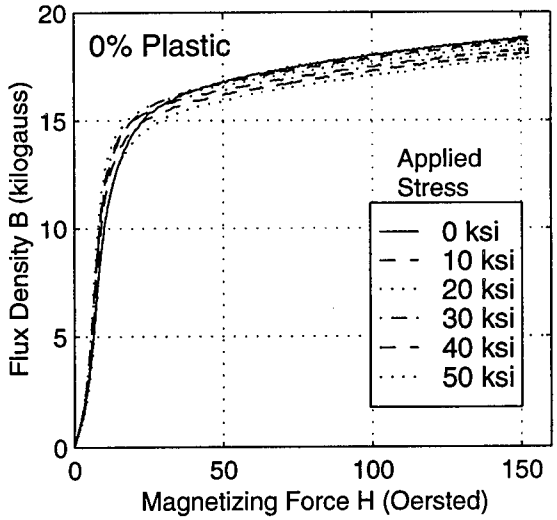

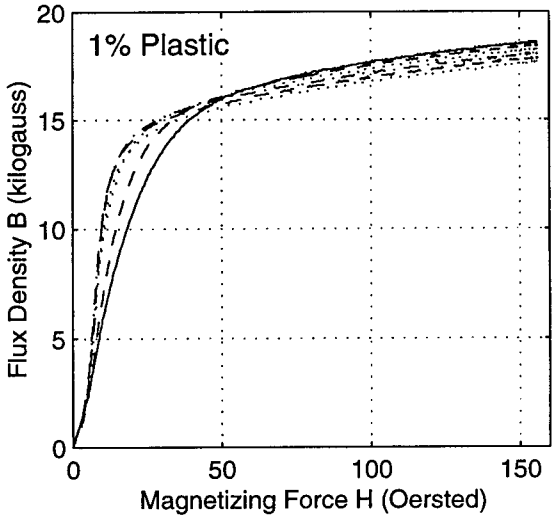

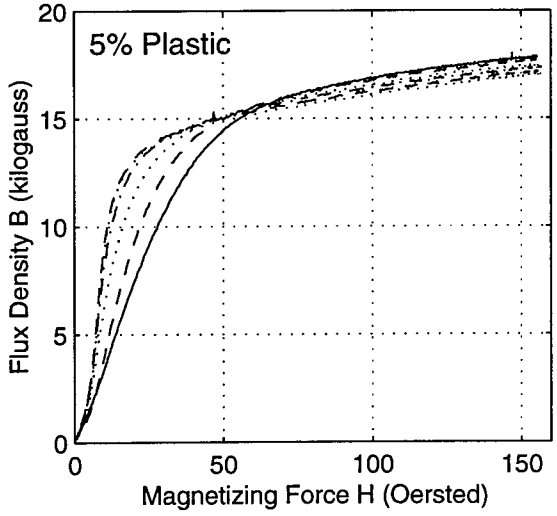

MATERIAL 24-06 (Cont'd)

Compressive Loading

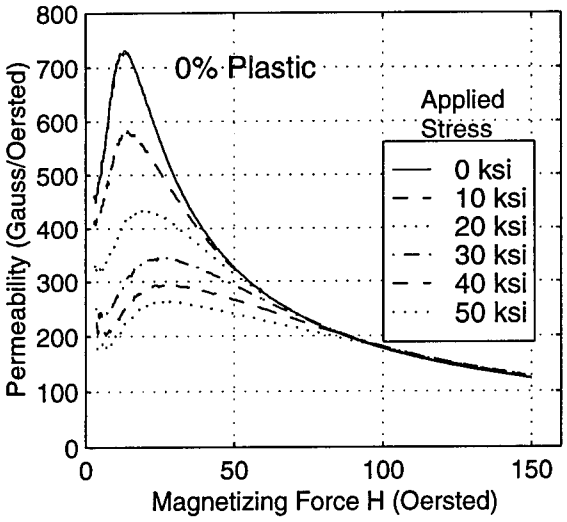

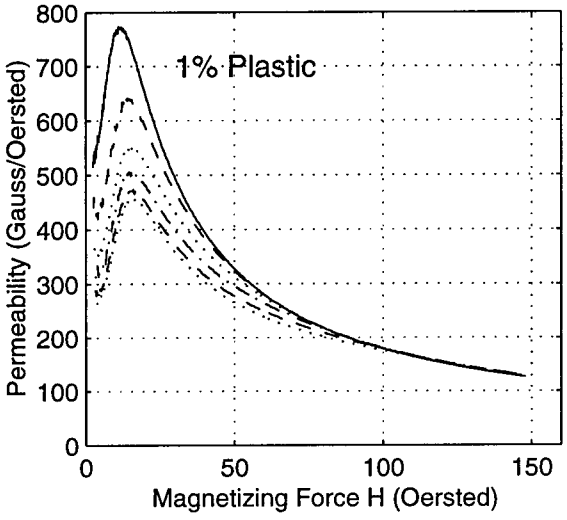

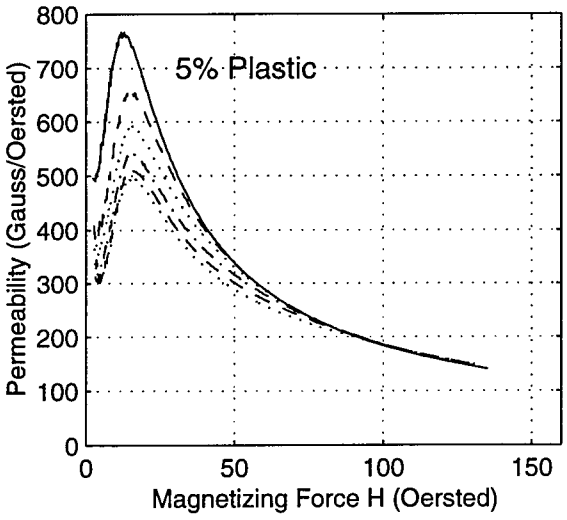

Tensile Loading

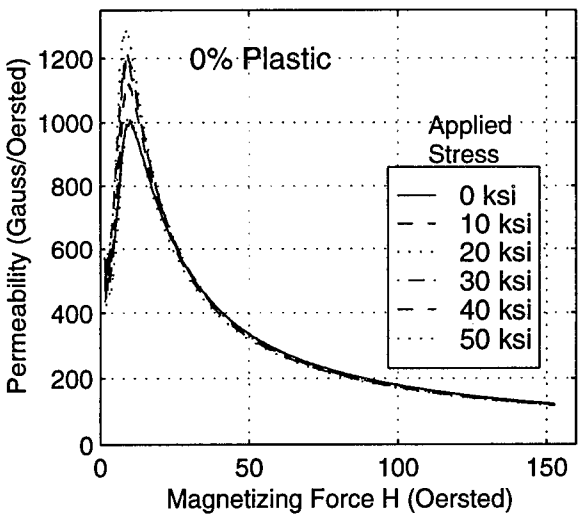

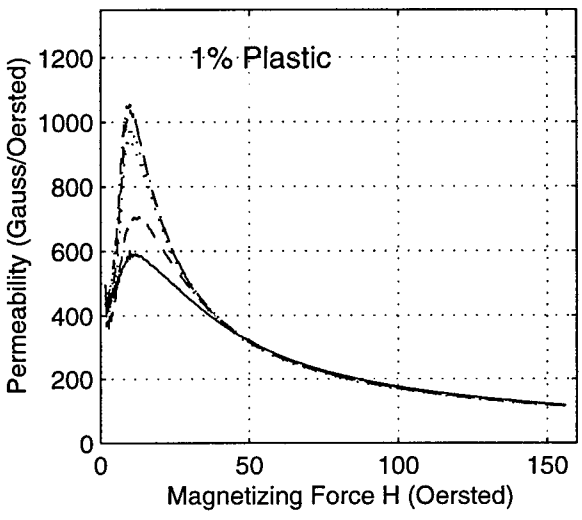

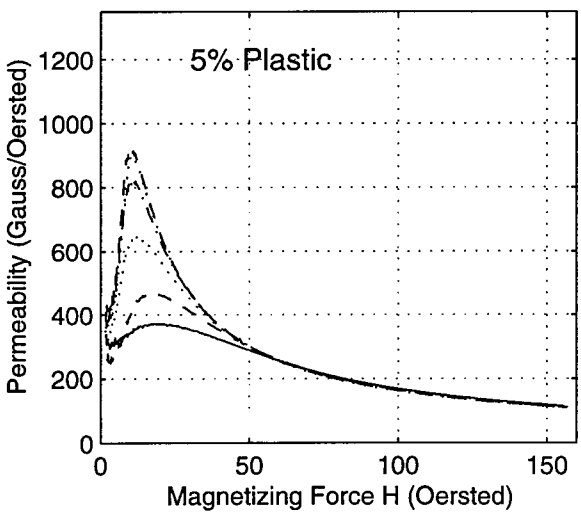

MATERIAL 24-06 (Cont'd)

Compressive Loading

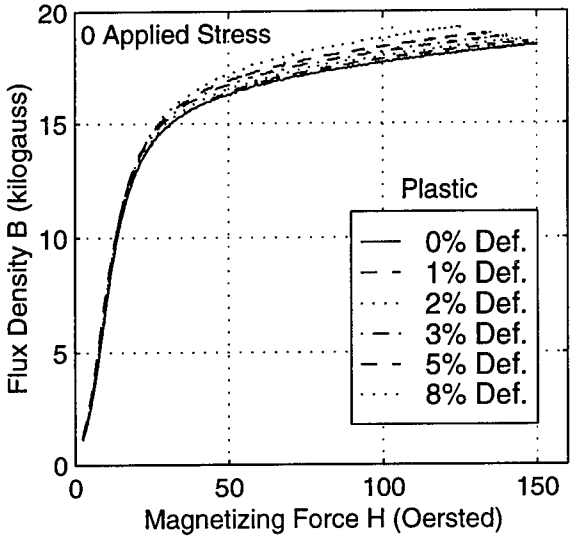

Tensile Loading

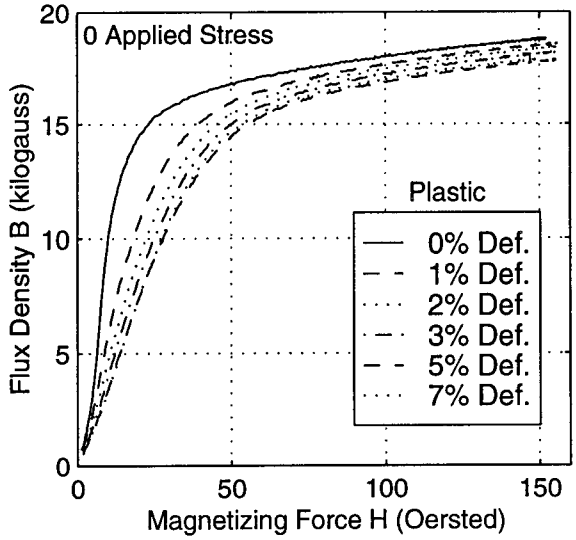

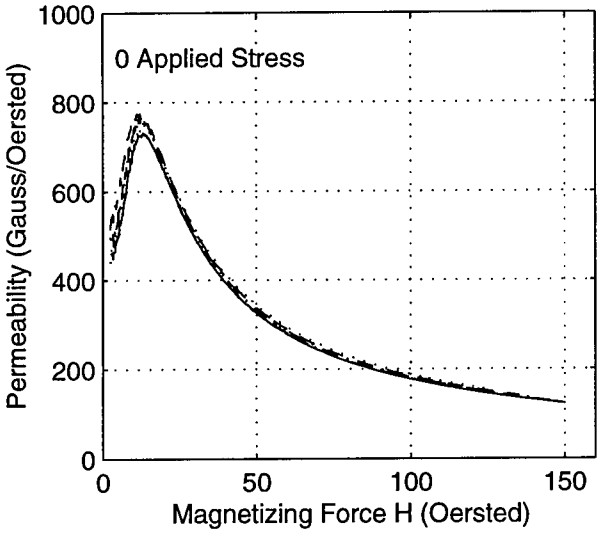

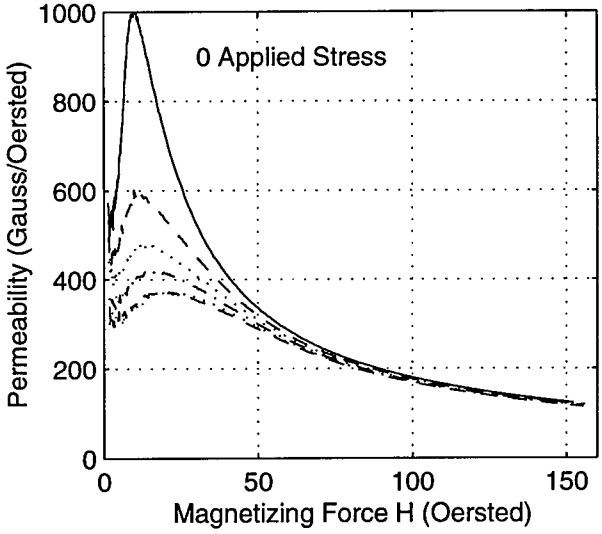

MATERIAL 24-08

Compressive Loading

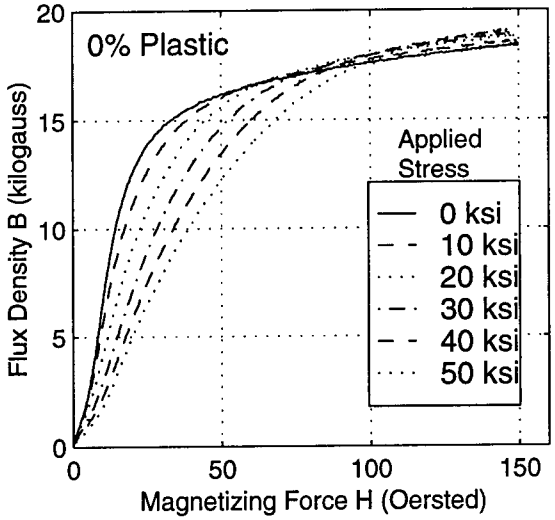

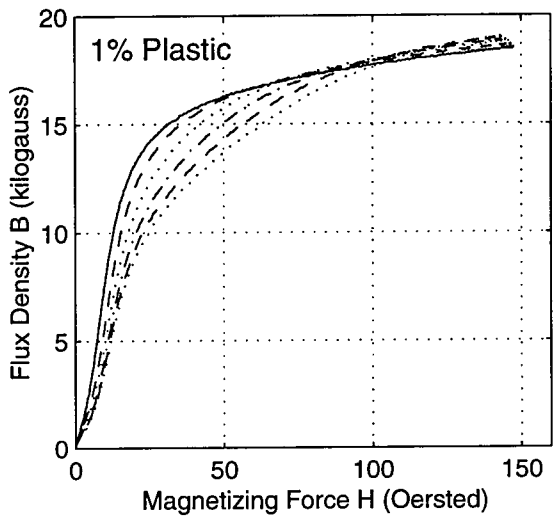

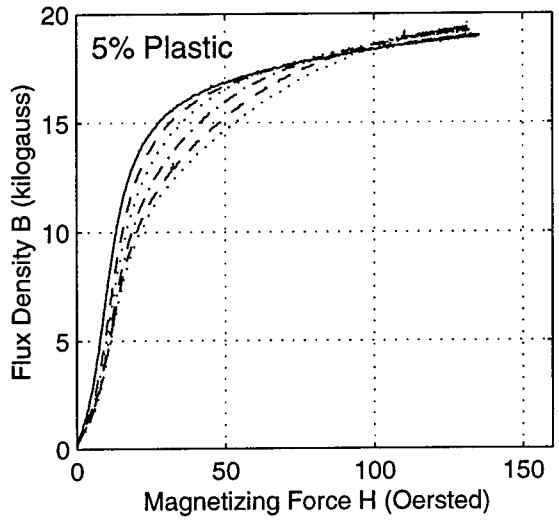

Tensile Loading

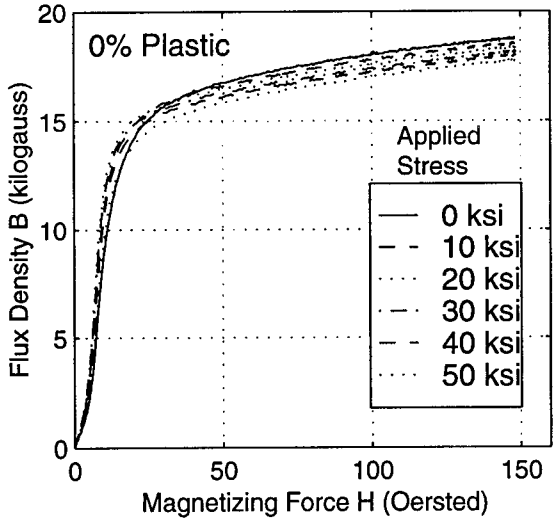

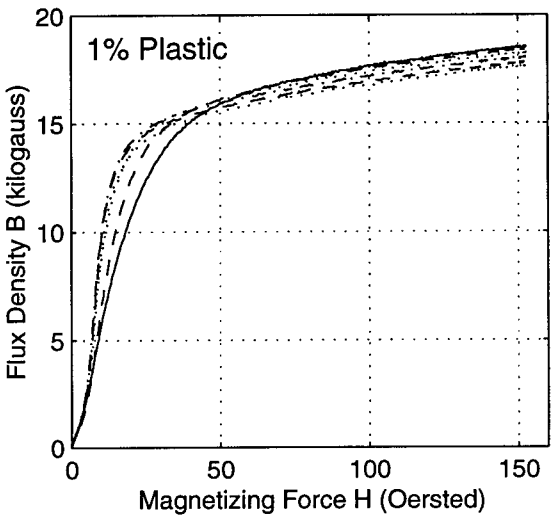

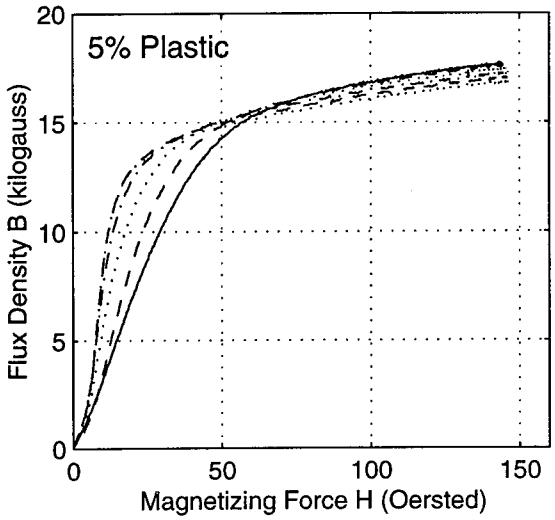

MATERIAL 24-08 (Cont'd)

Compressive Loading

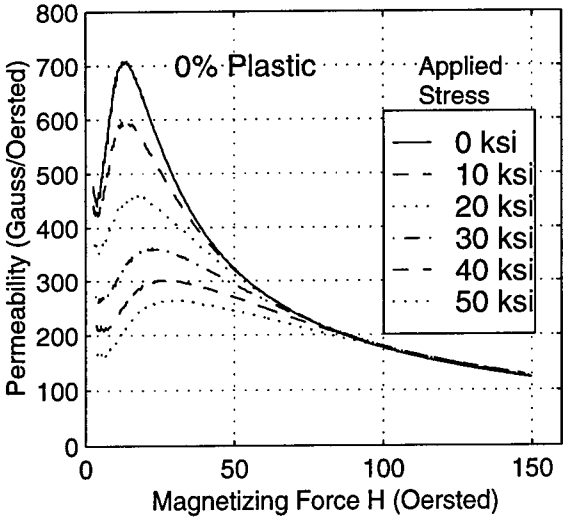

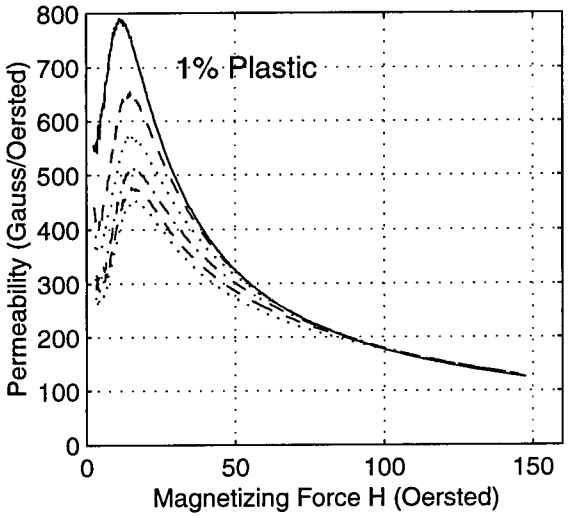

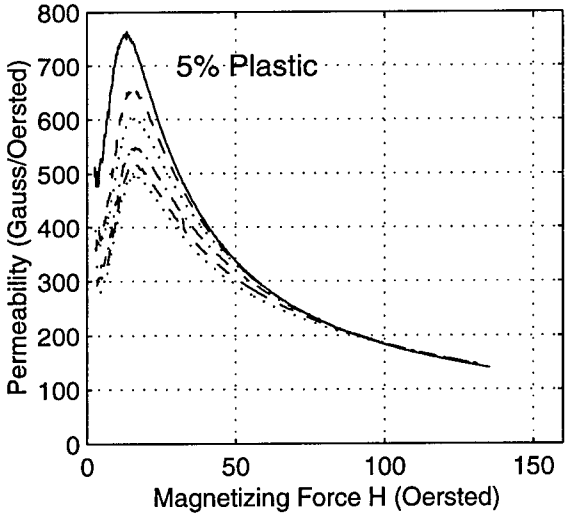

Tensile Loading

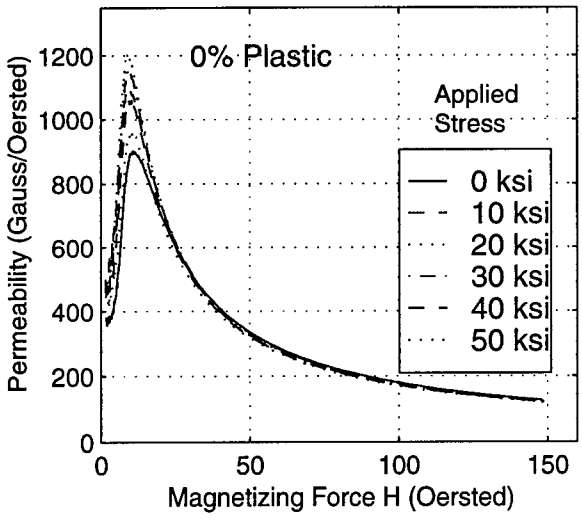

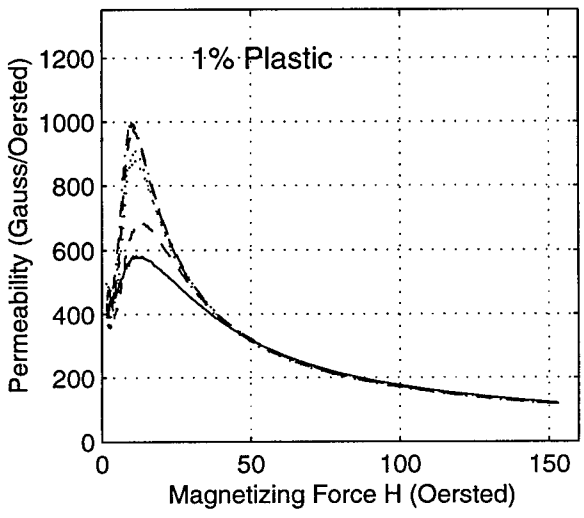

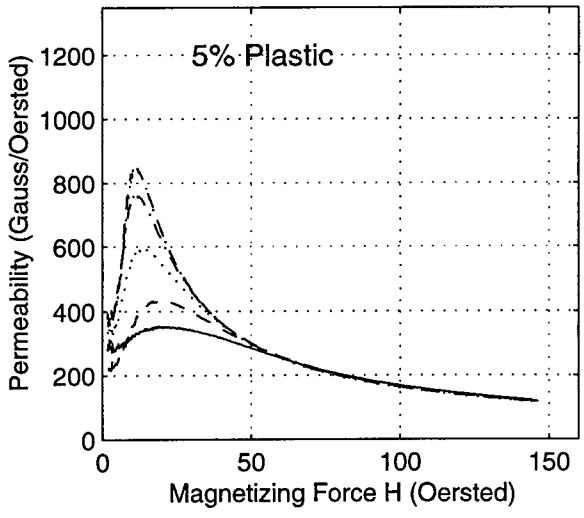

MATERIAL 24-08 (Cont'd)

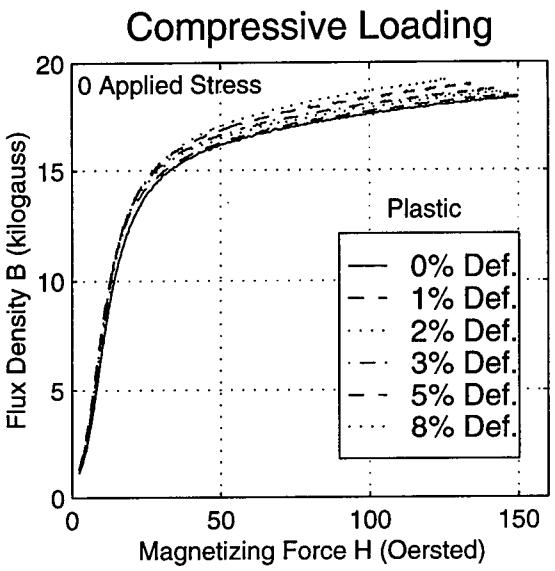

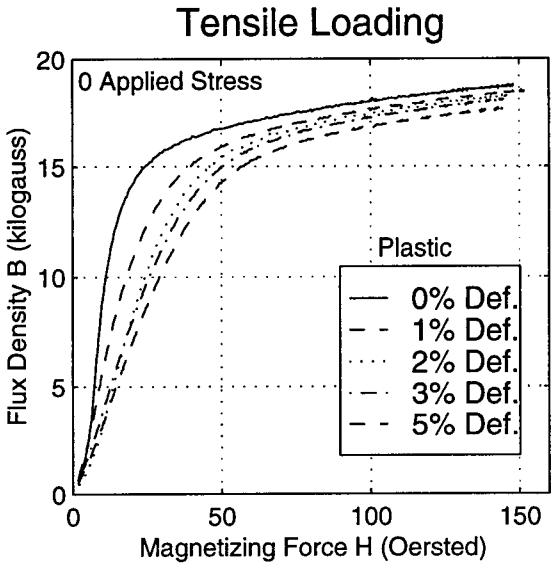

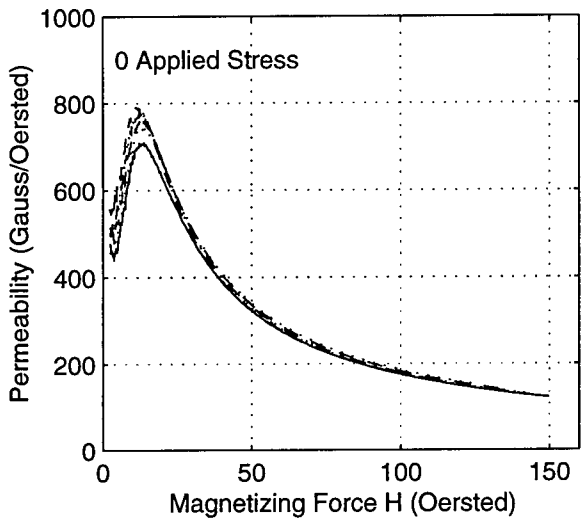

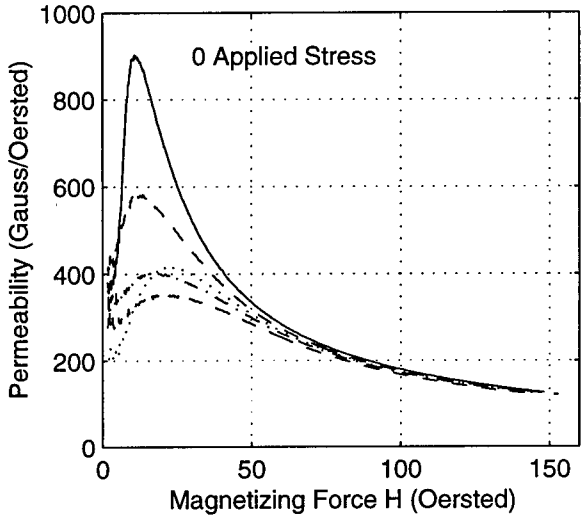

MATERIAL 24-10

Compressive Loading

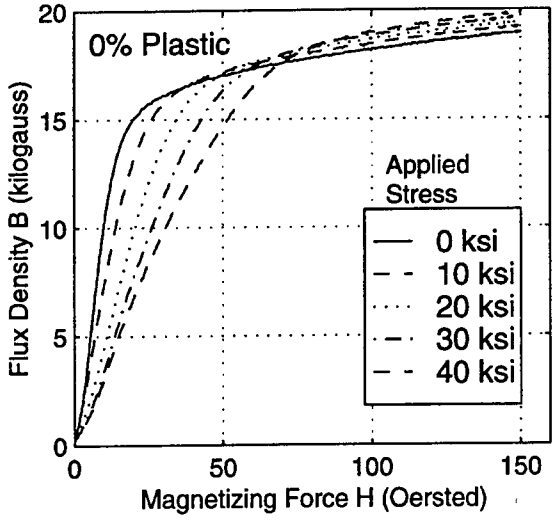

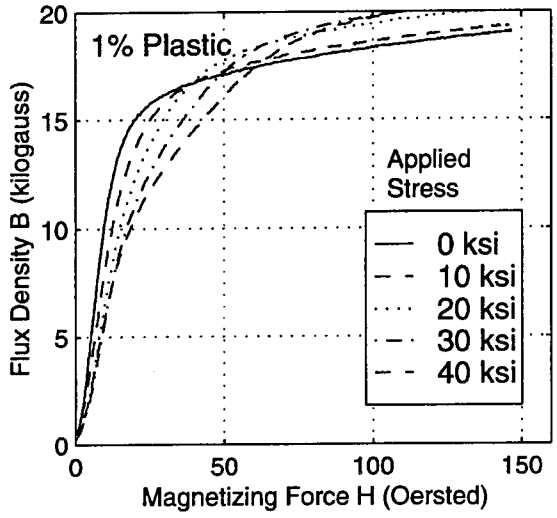

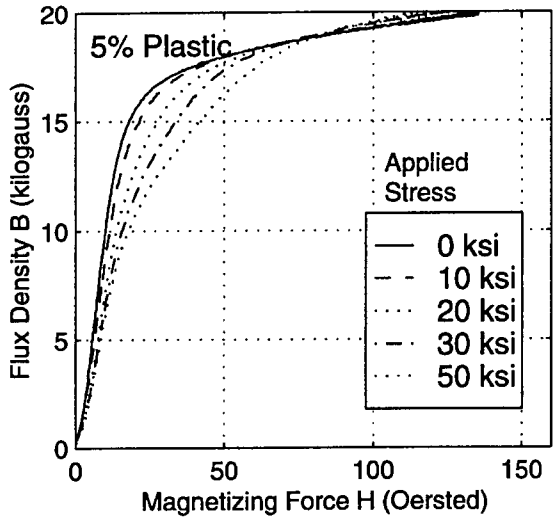

Tensile Loading

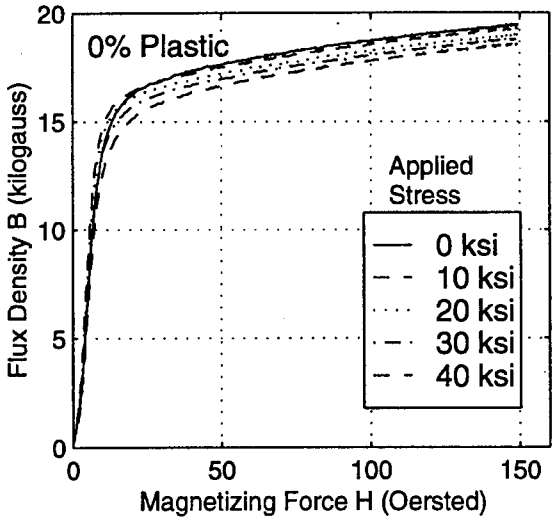

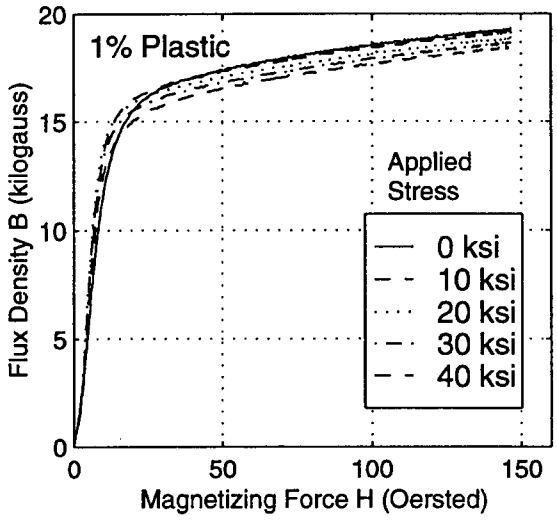

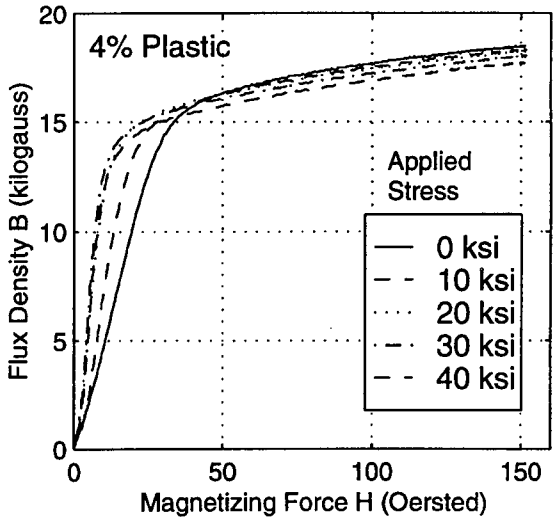

MATERIAL 24-10 (Cont'd)

Compressive Loading

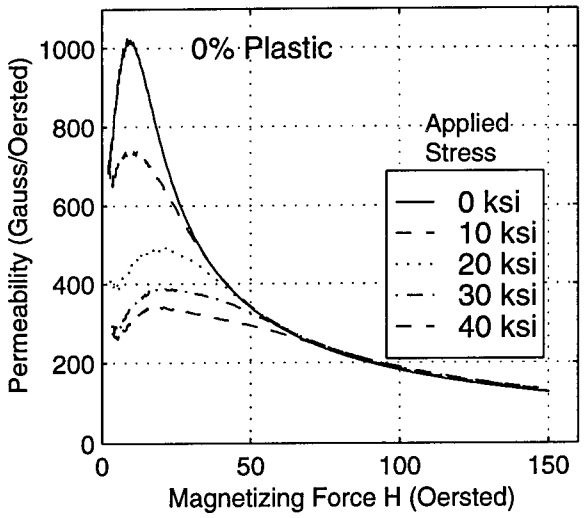

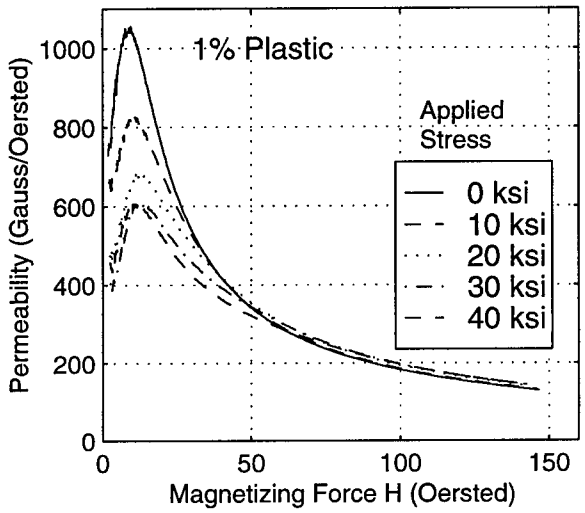

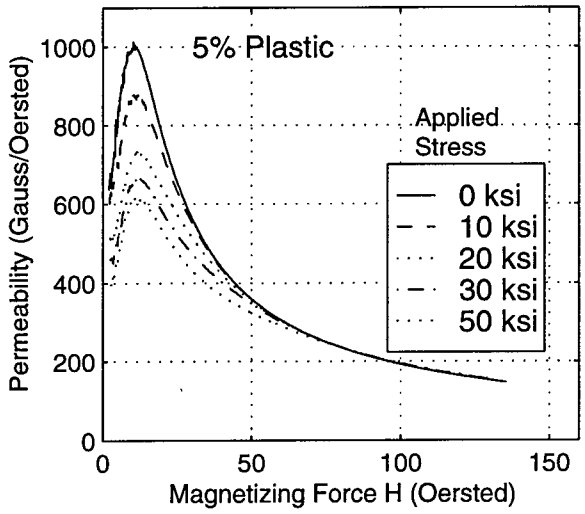

Tensile Loading

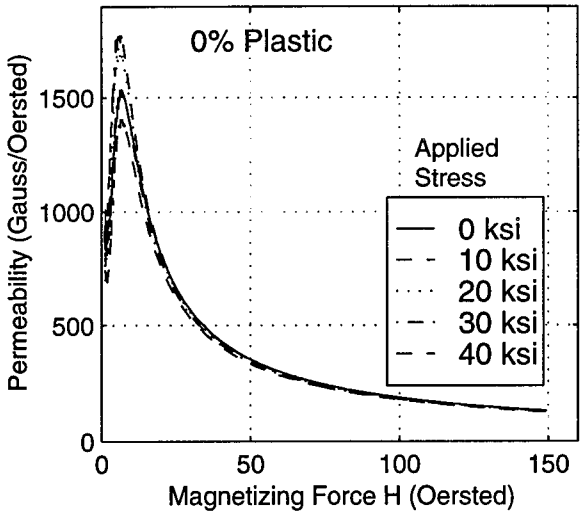

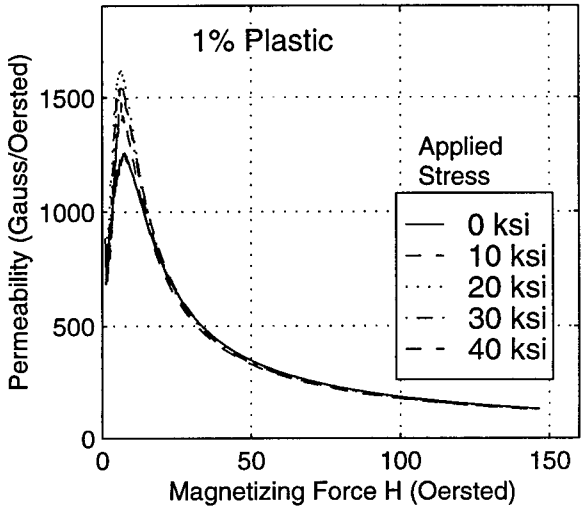

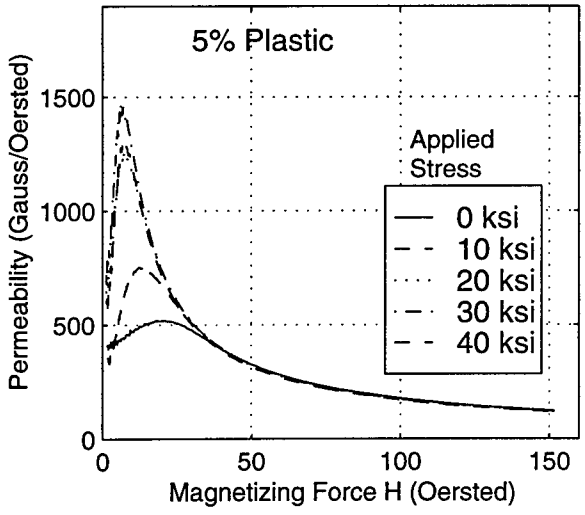

MATERIAL 24-10 (Cont'd)

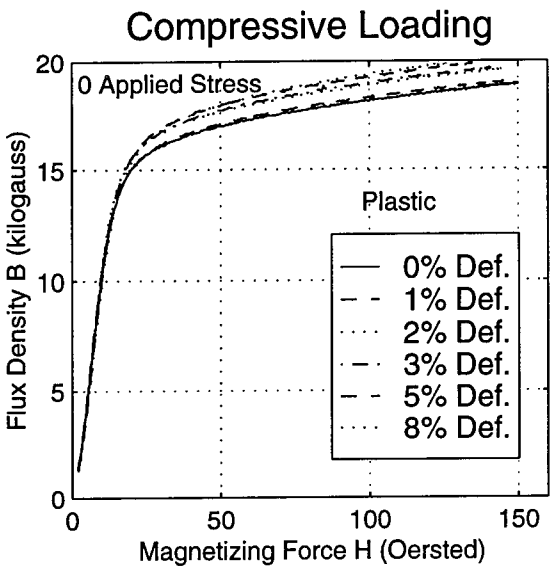

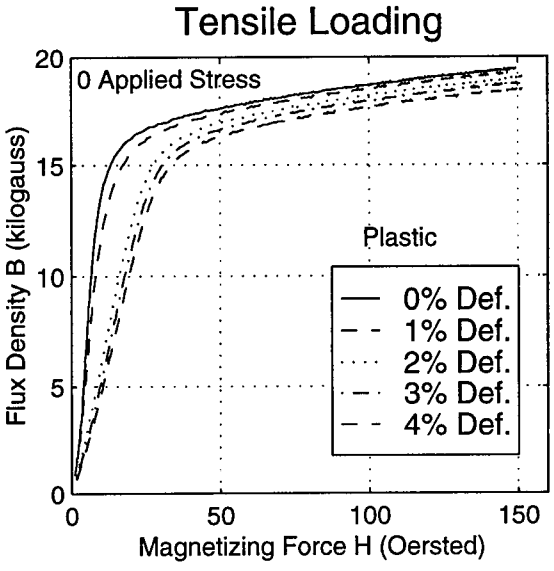

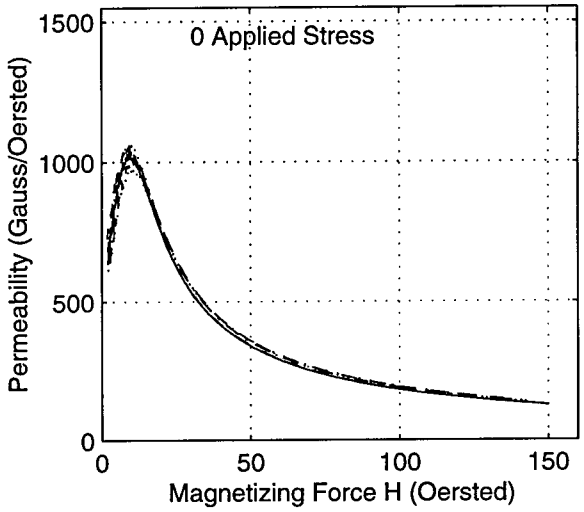

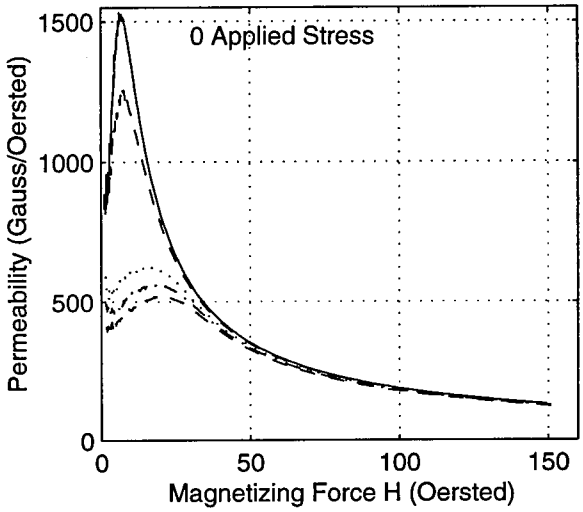

MATERIAL 24-11

Compressive Loading

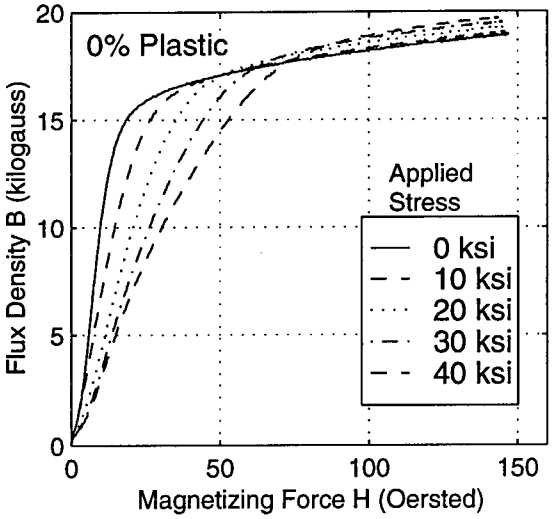

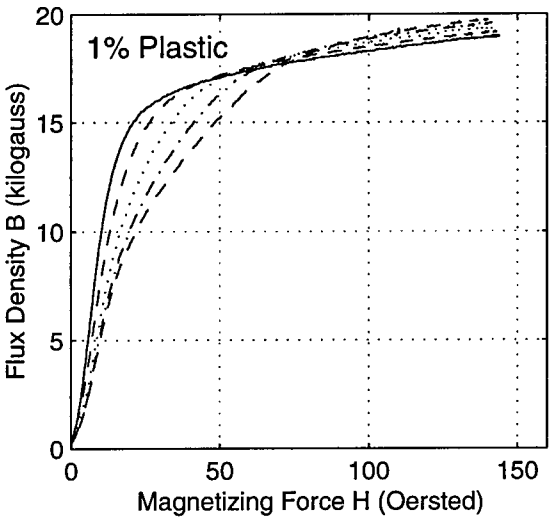

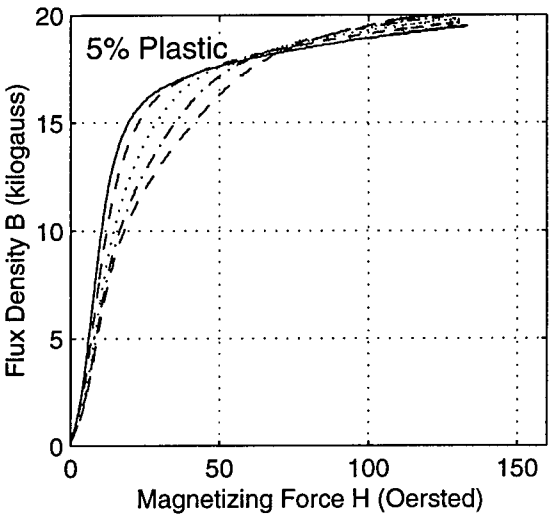

Tensile Loading

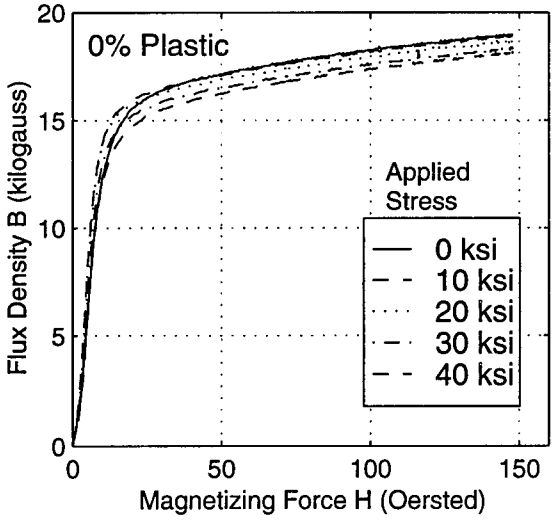

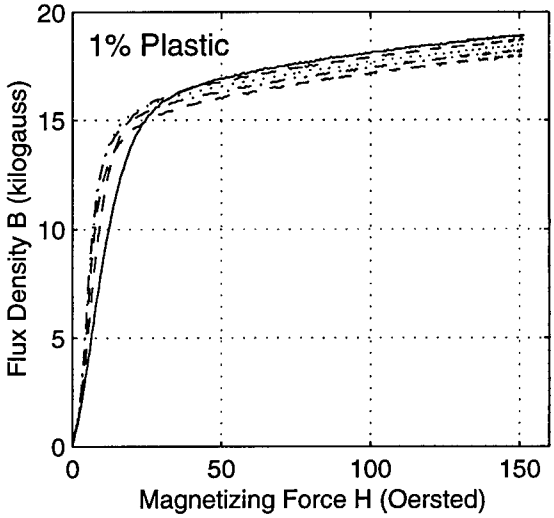

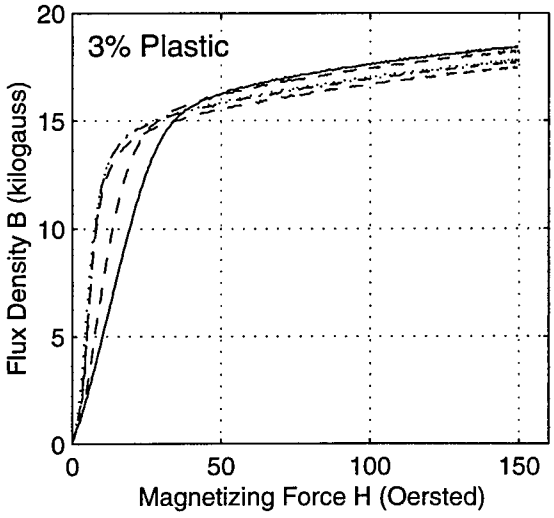

MATERIAL 24-11 (Cont'd)

Compressive Loading

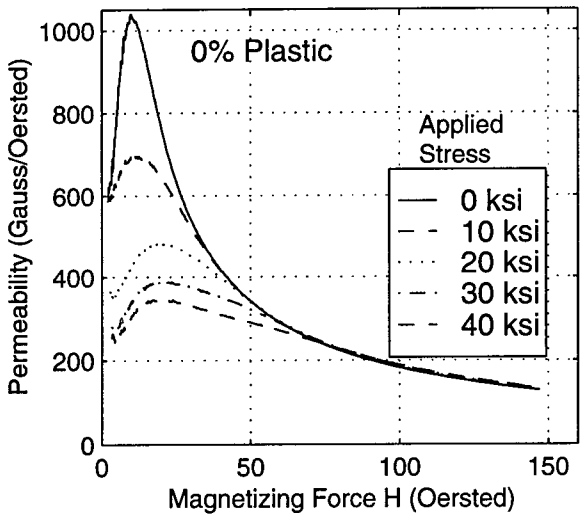

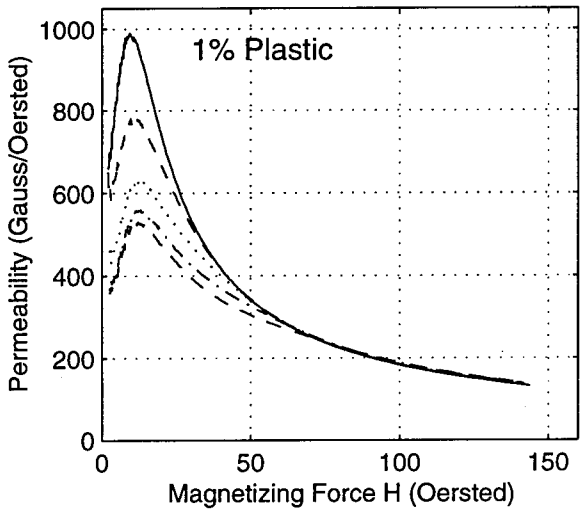

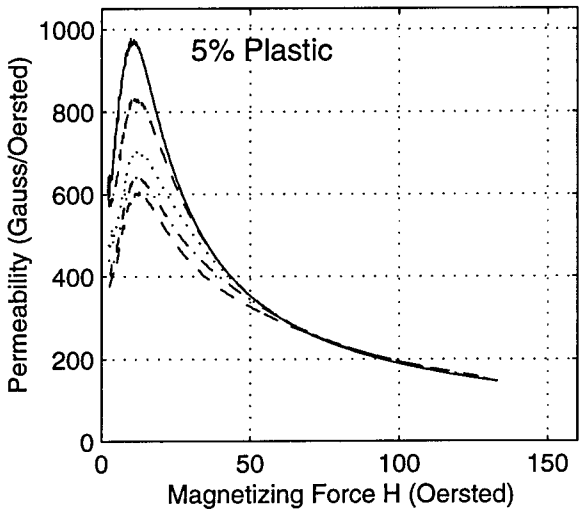

Tensile Loading

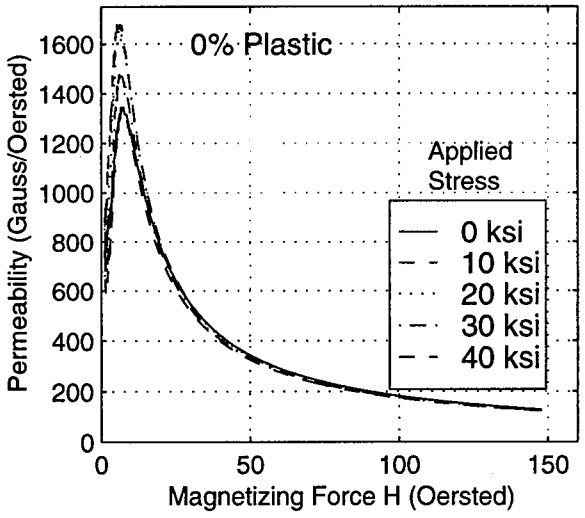

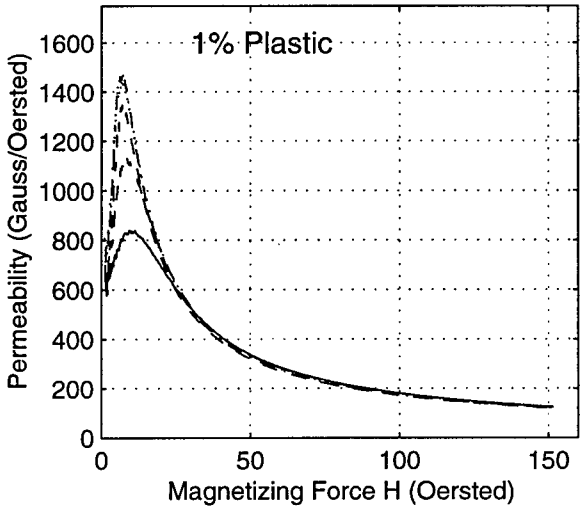

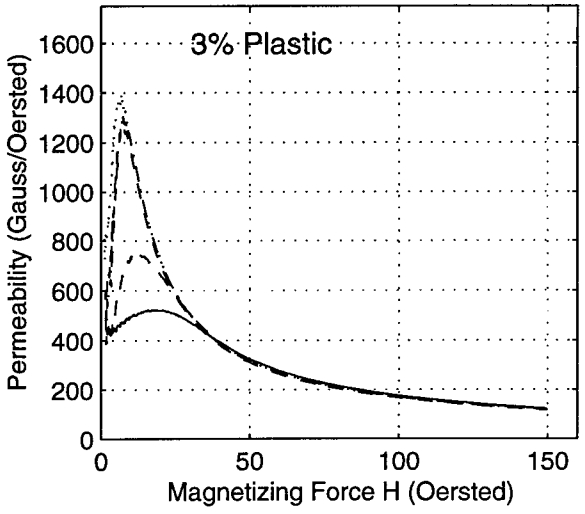

MATERIAL 24-11 (Cont'd)

Compressive Loading

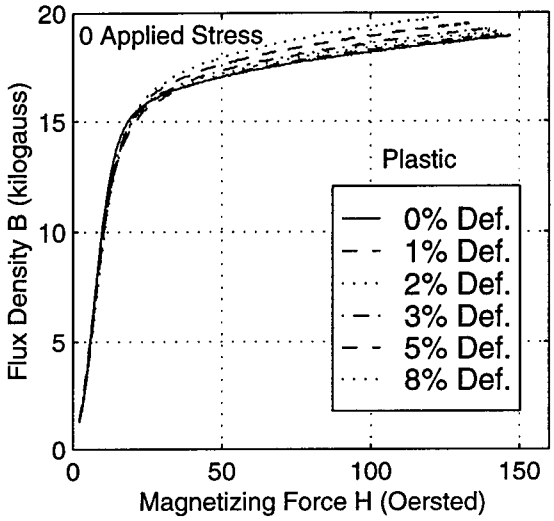

Tensile Loading

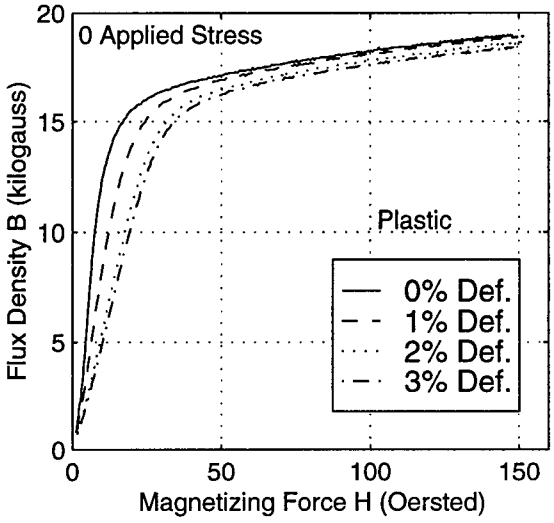

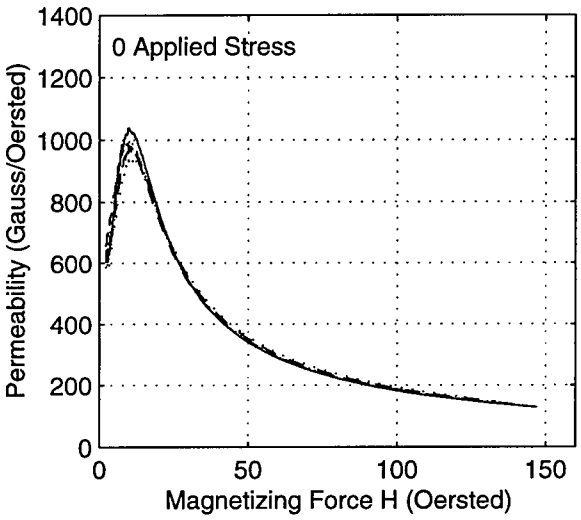

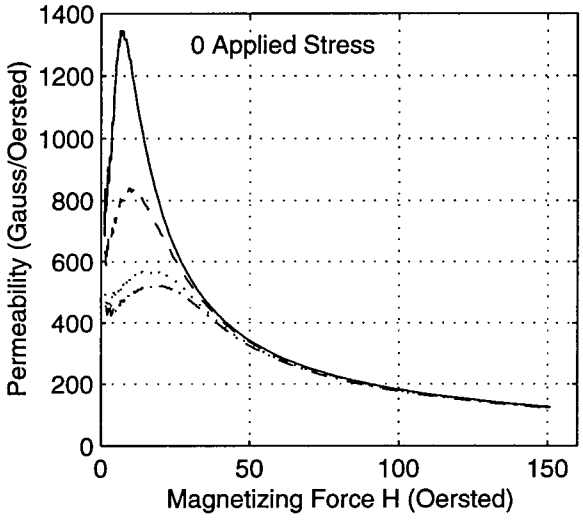

MATERIAL 24-13

Compressive Loading

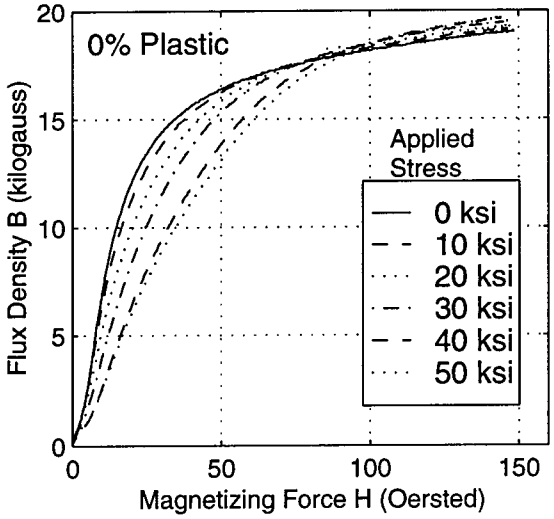

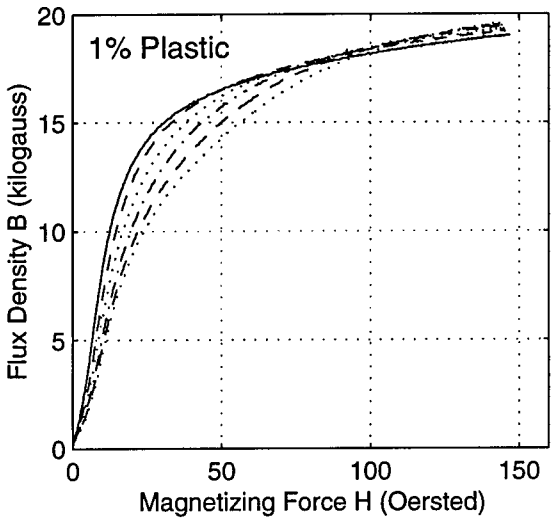

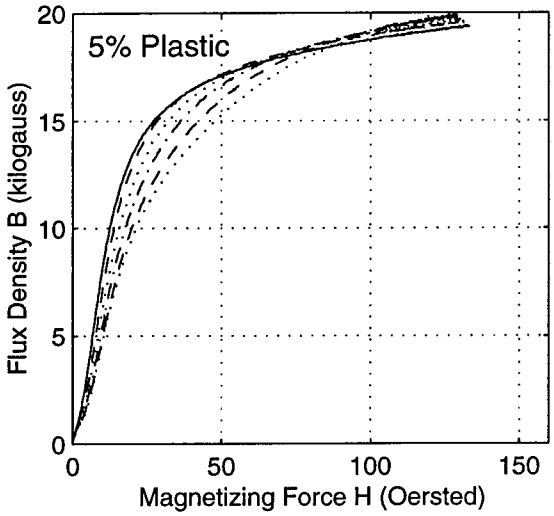

Tensile Loading

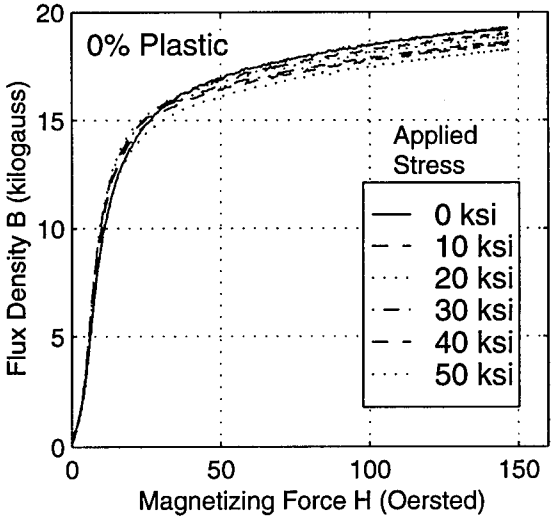

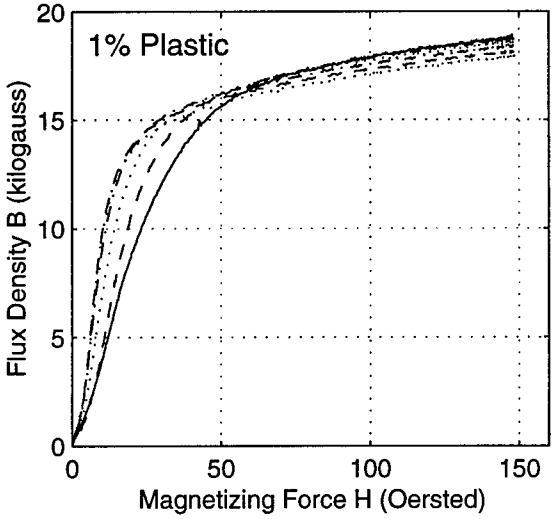

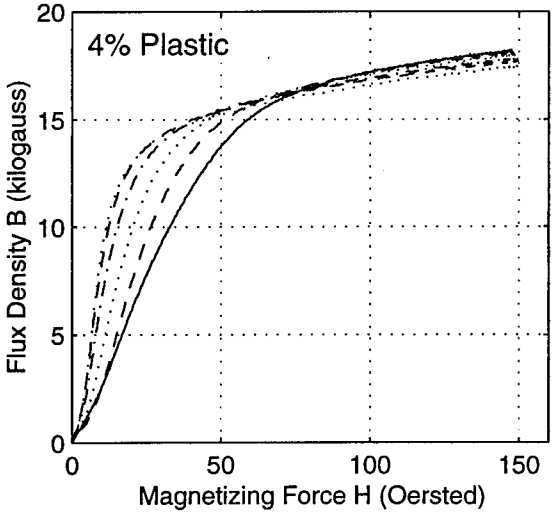

MATERIAL 24-13 (Cont'd)

Compressive Loading

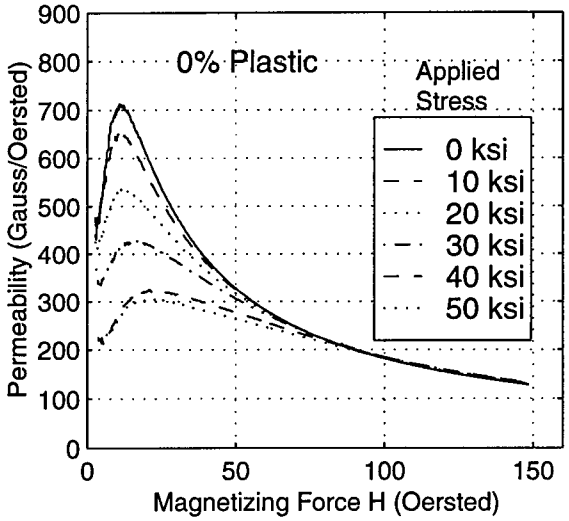

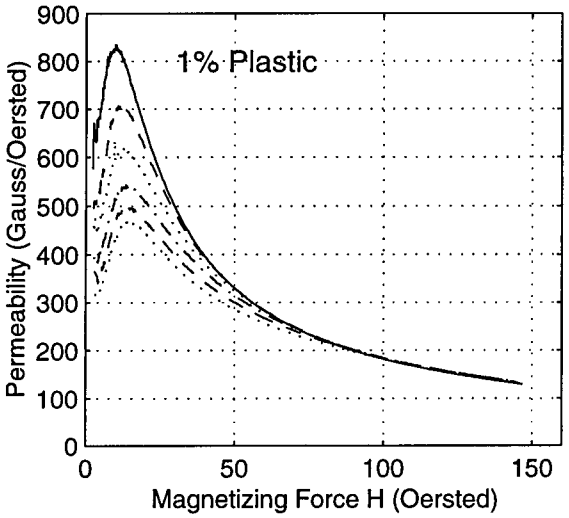

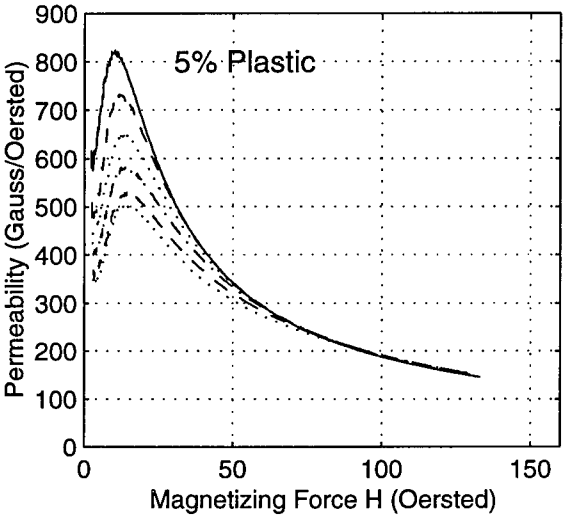

Tensile Loading

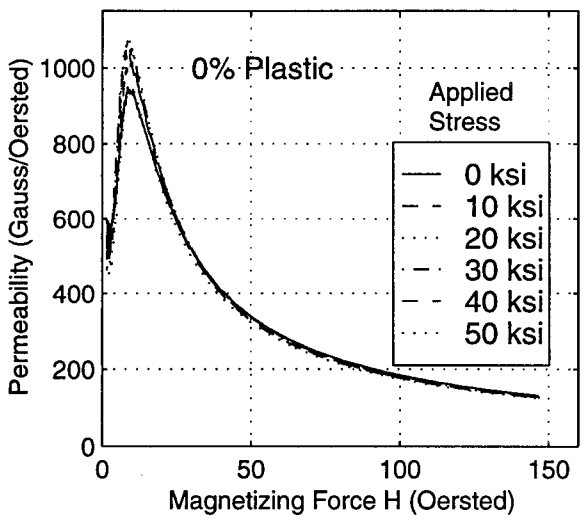

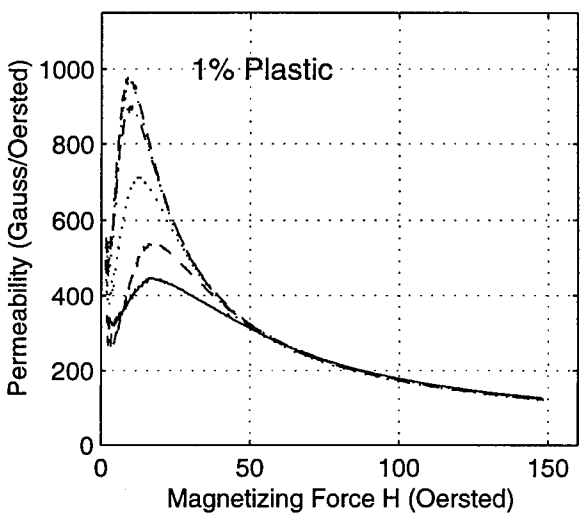

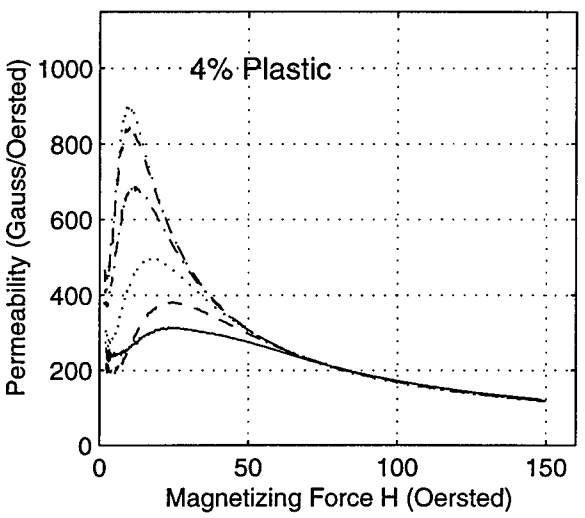

MATERIAL 24-13 (Cont'd)

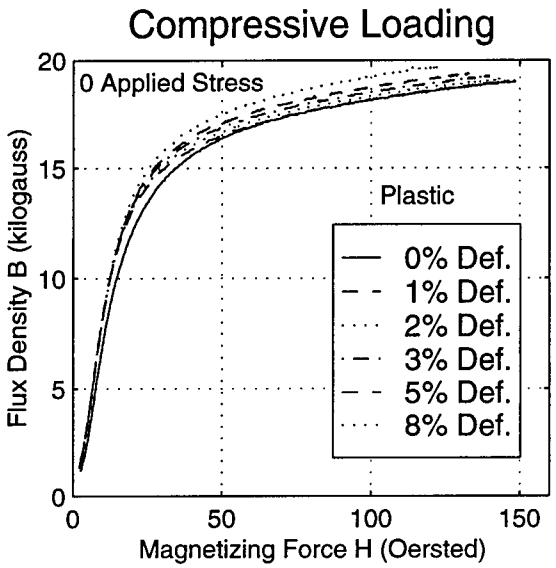

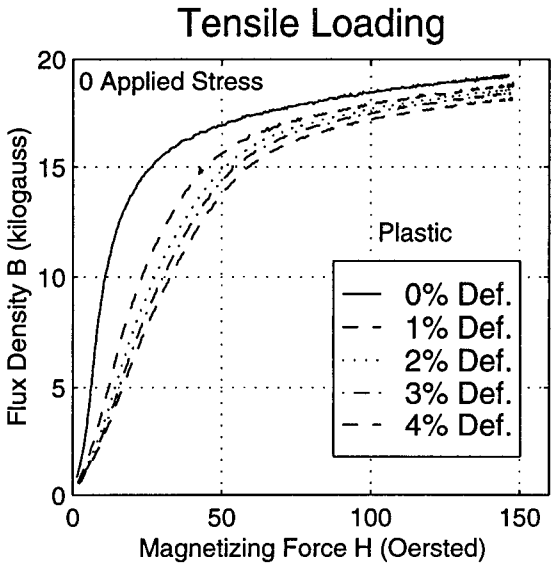

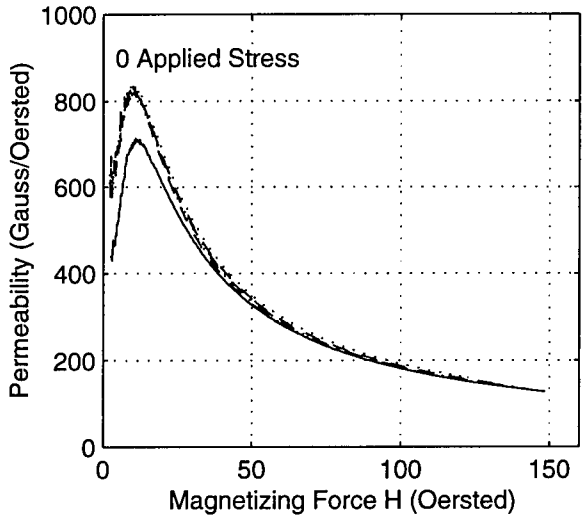

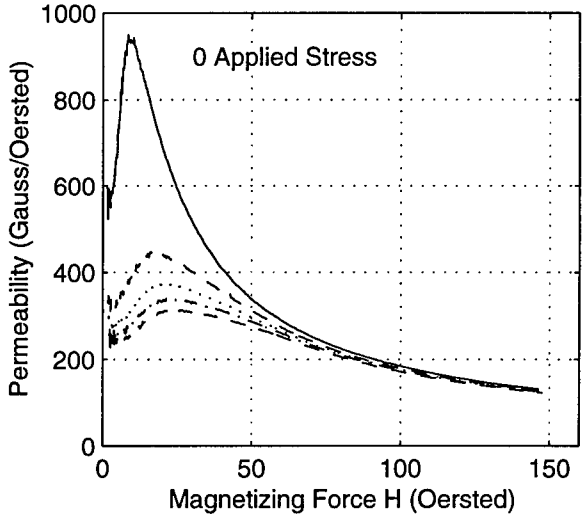

MATERIAL 24-17

Compressive Loading

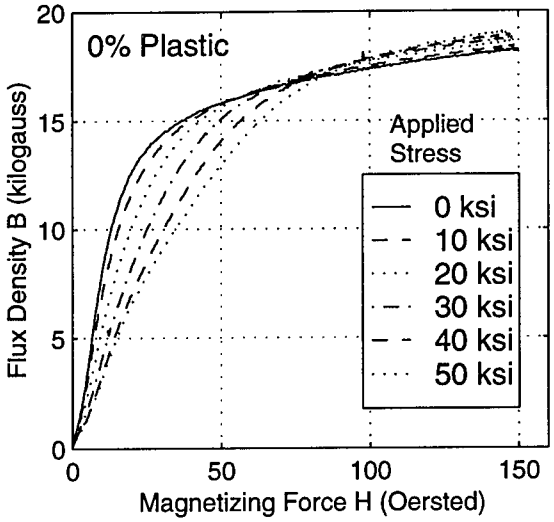

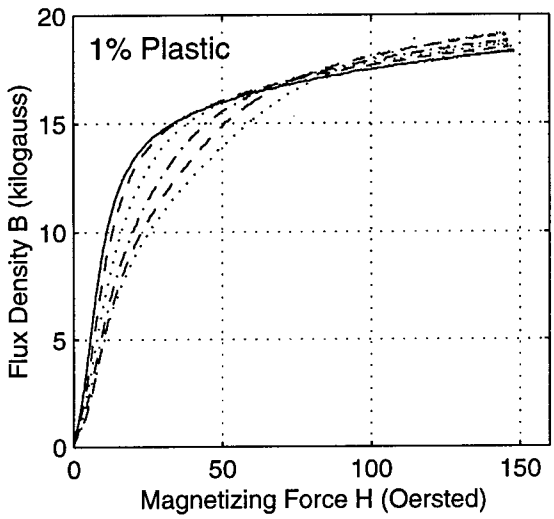

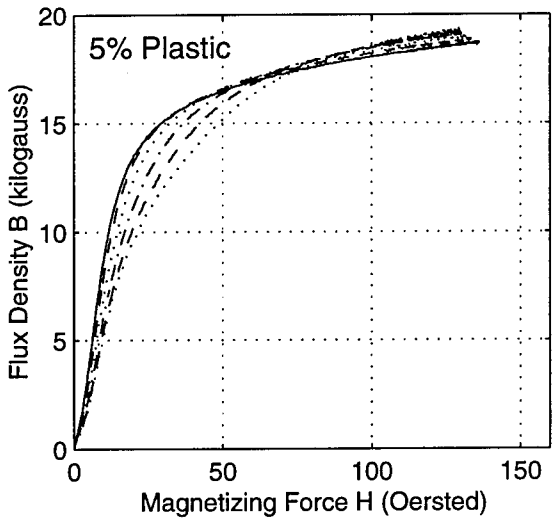

Tensile Loading

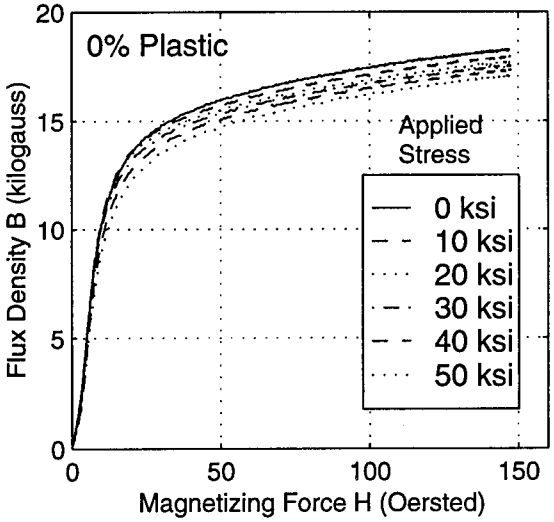

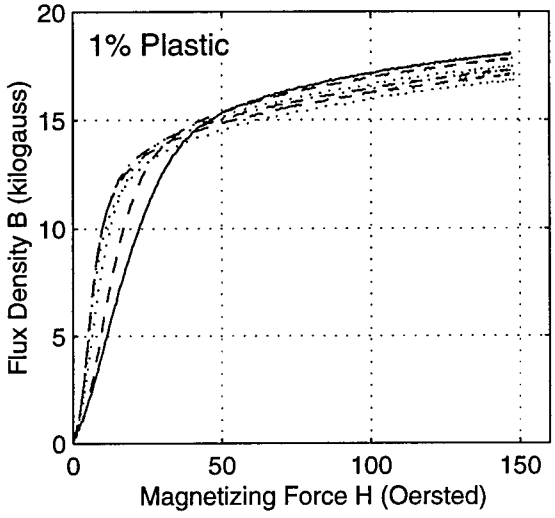

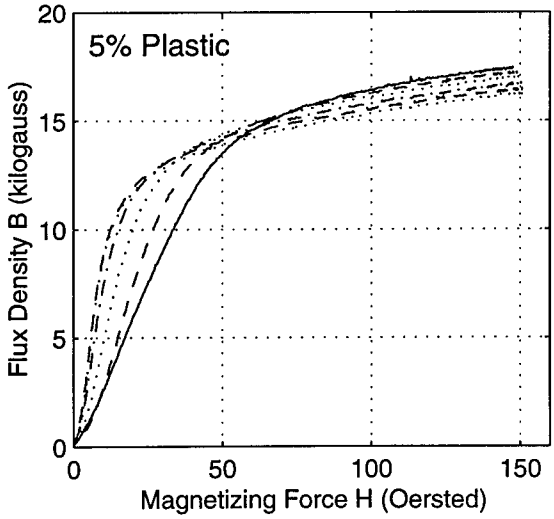

MATERIAL 24-17 (Cont'd)

Compressive Loading

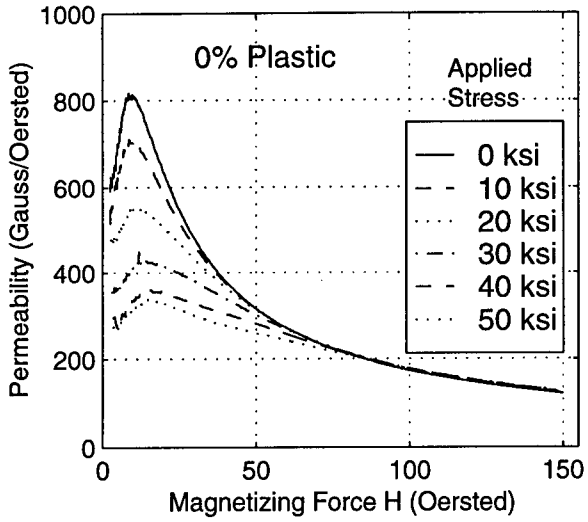

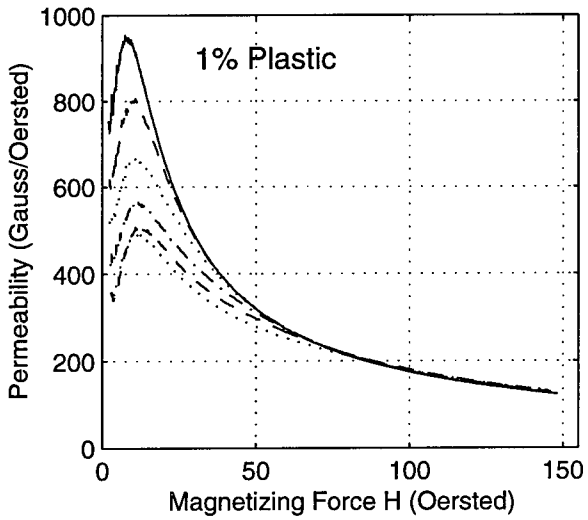

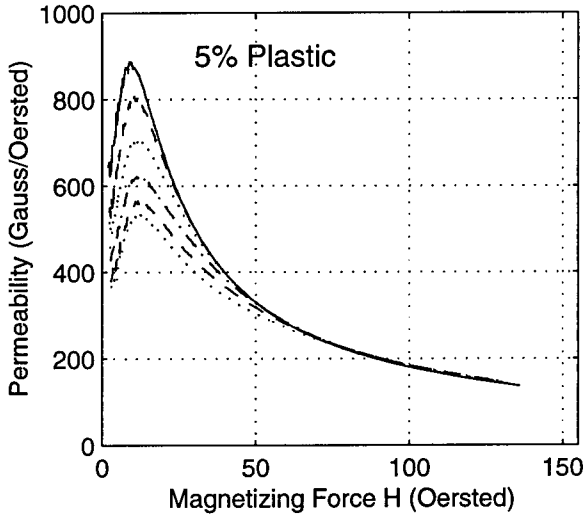

Tensile Loading

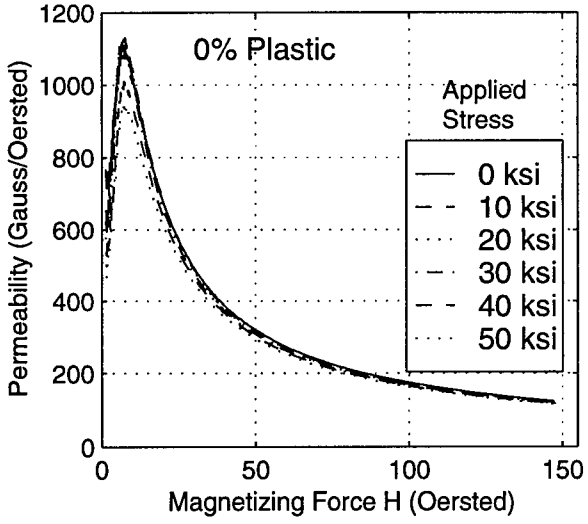

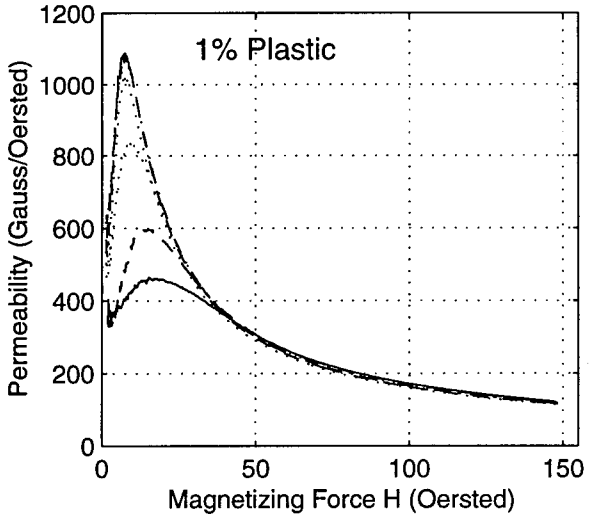

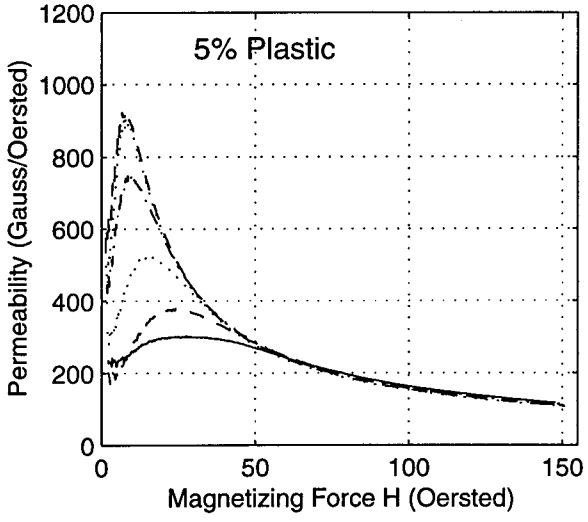

MATERIAL 24-17 (Cont'd)

Compressive Loading

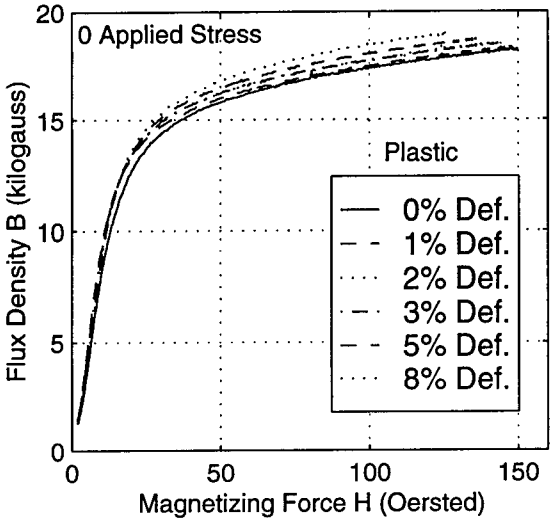

Tensile Loading

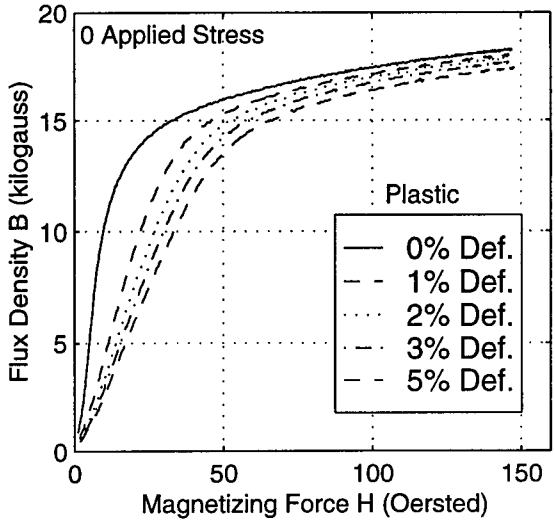

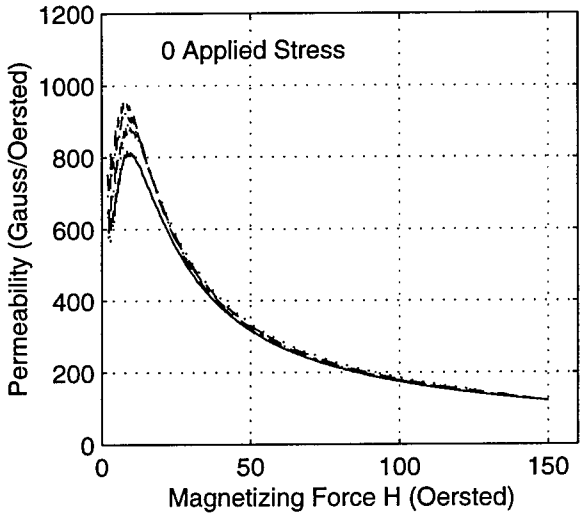

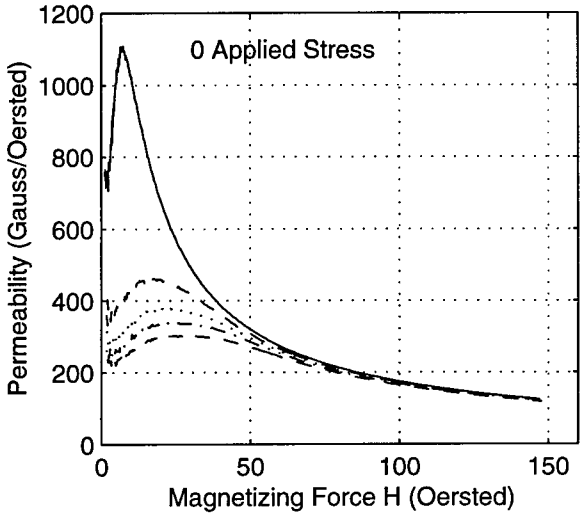

MATERIAL 24-18

Compressive Loading

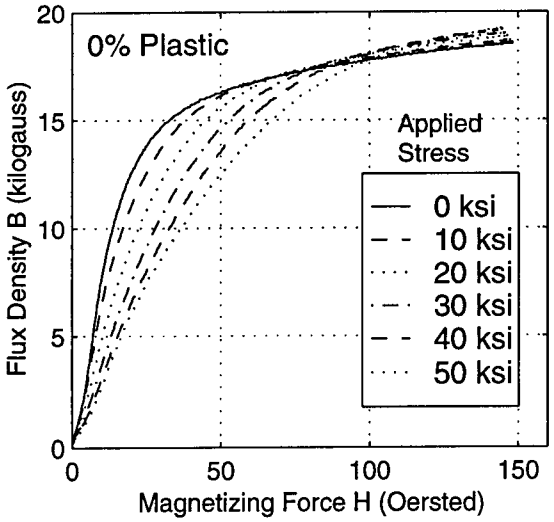

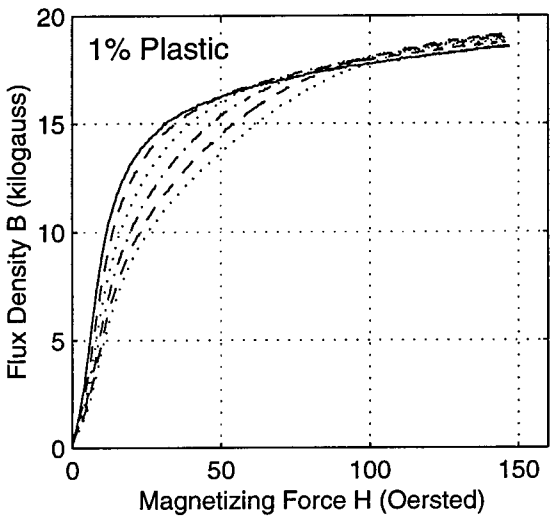

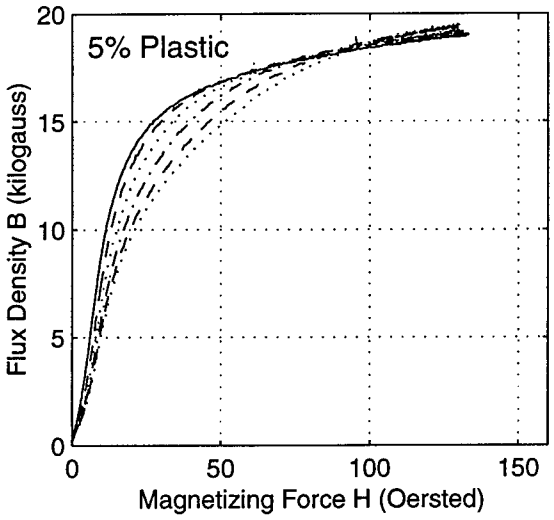

Tensile Loading

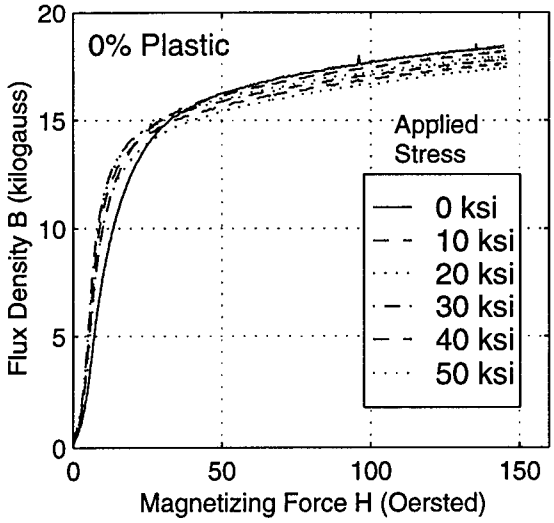

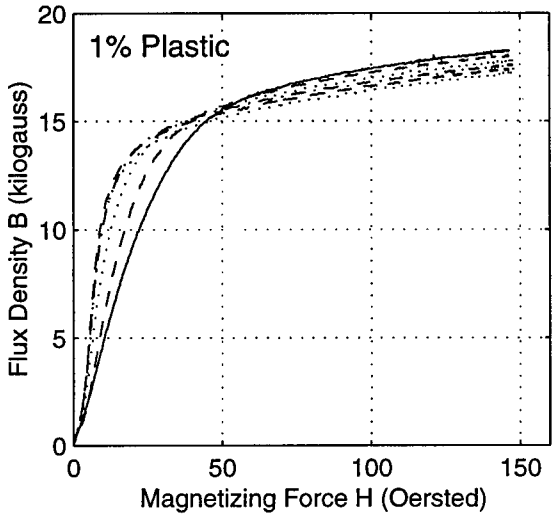

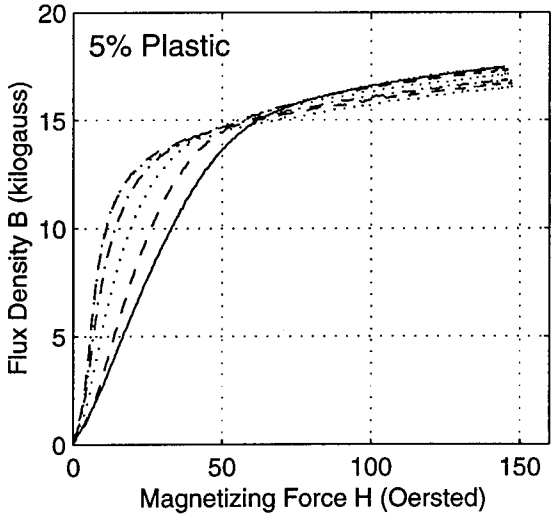

MATERIAL 24-18 (Cont'd)

Compressive Loading

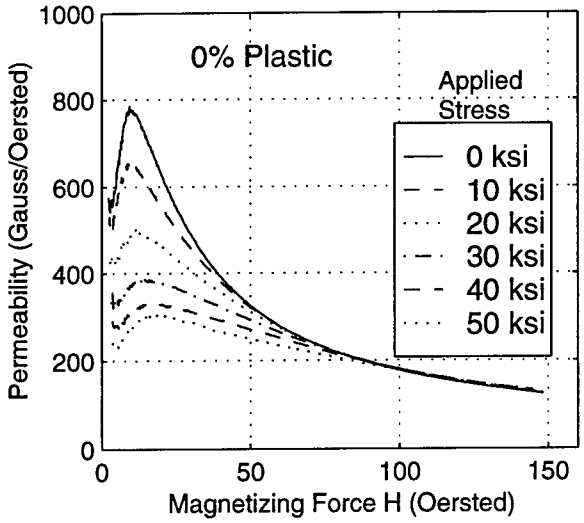

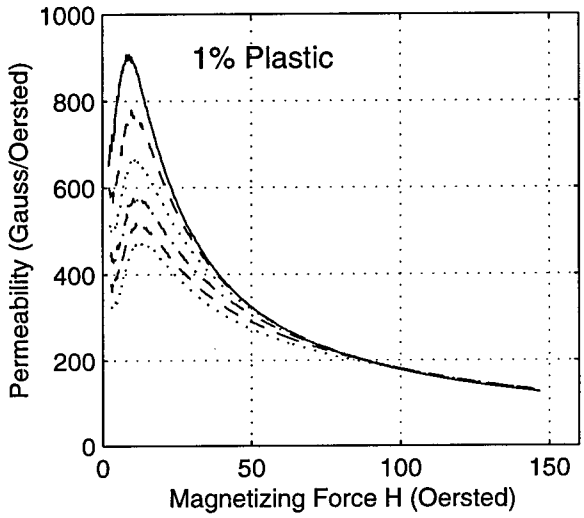

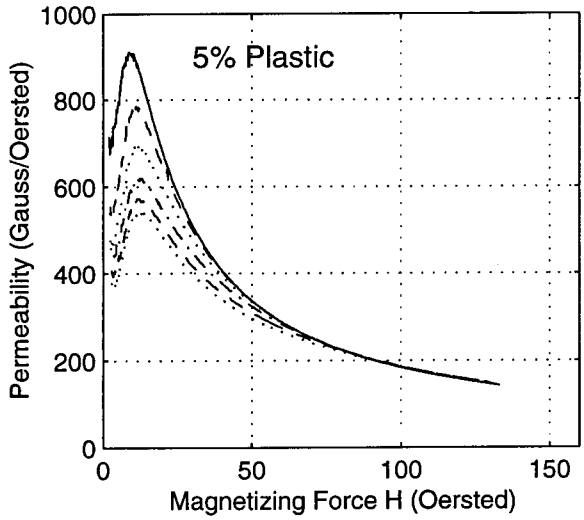

Tensile Loading

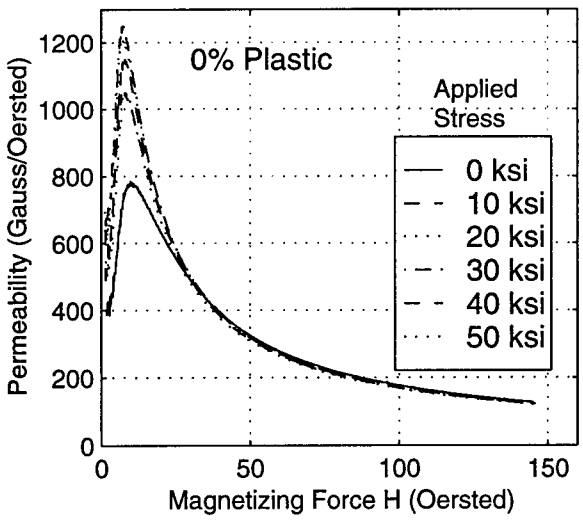

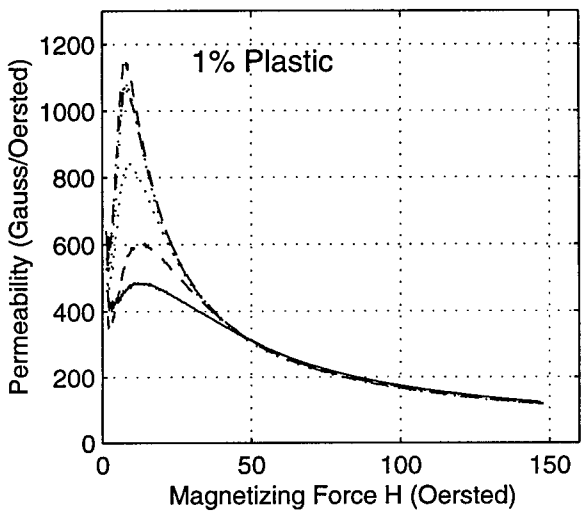

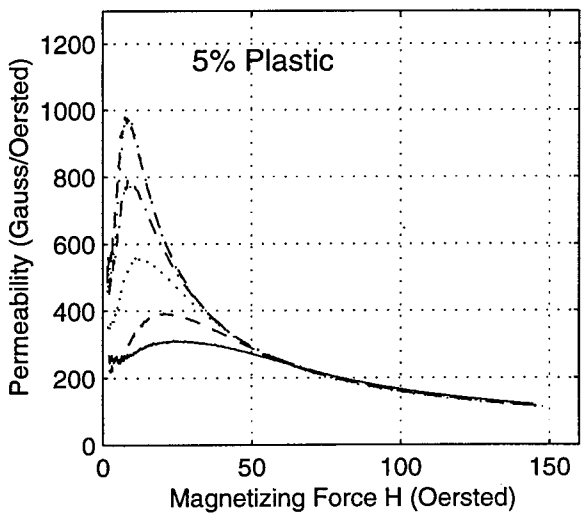

MATERIAL 24-18 (Cont'd)

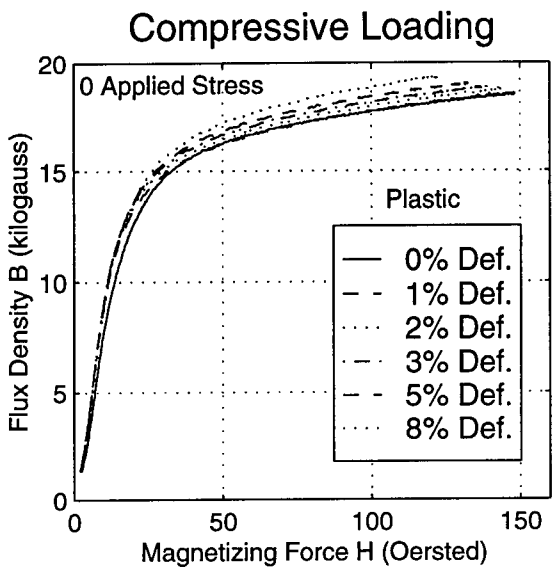

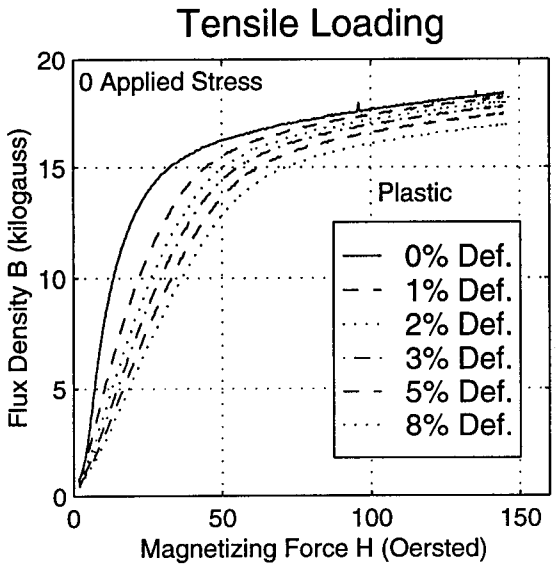

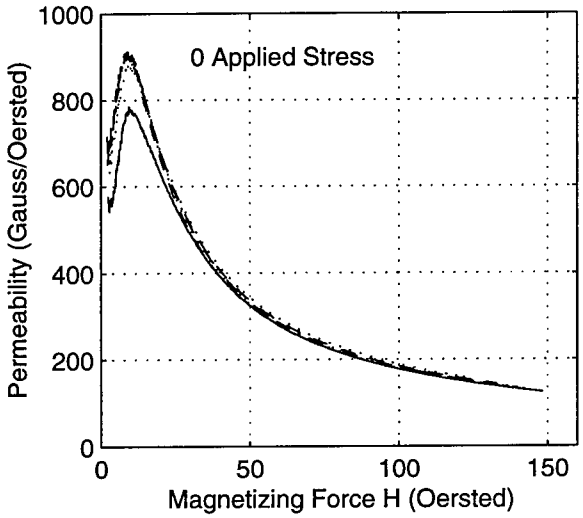

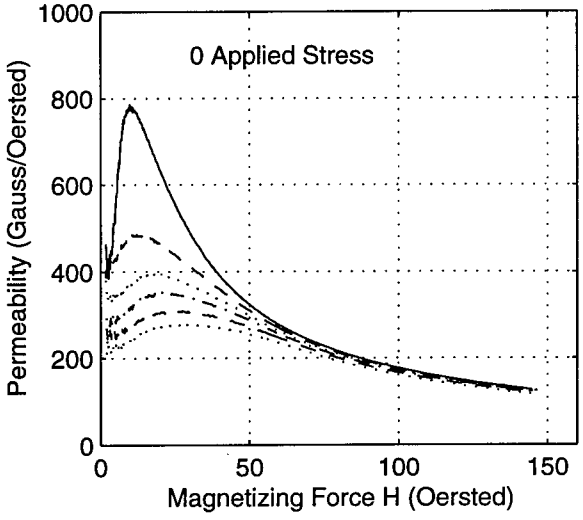

MATERIAL 24-22

Compressive Loading

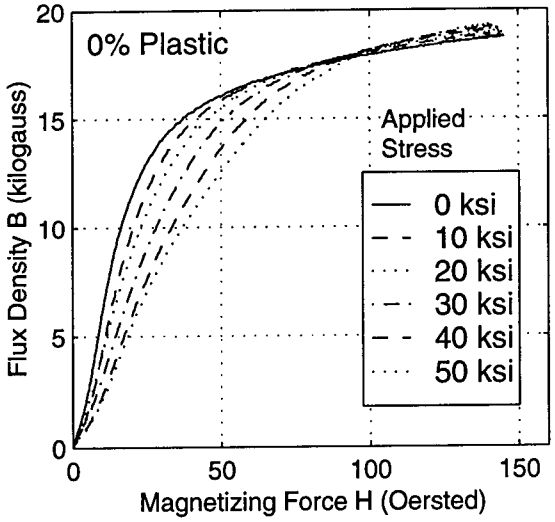

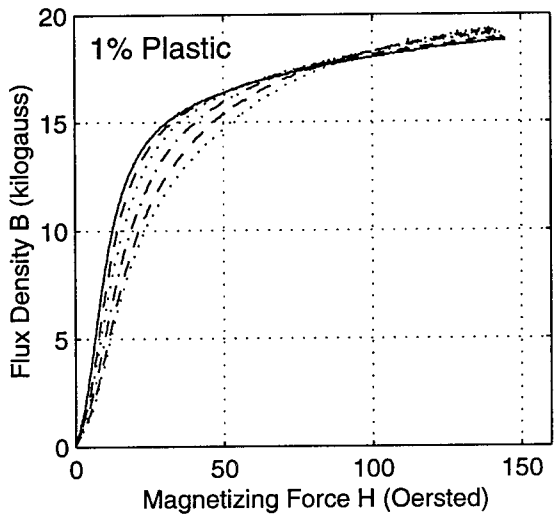

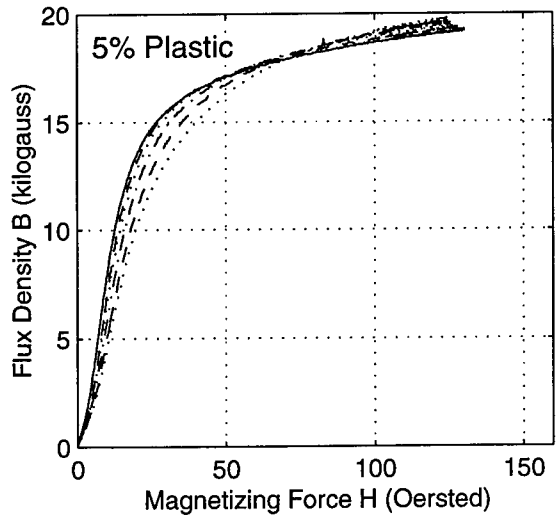

Tensile Loading

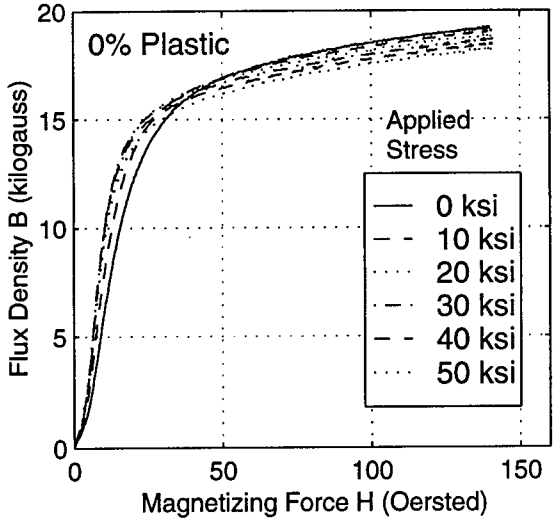

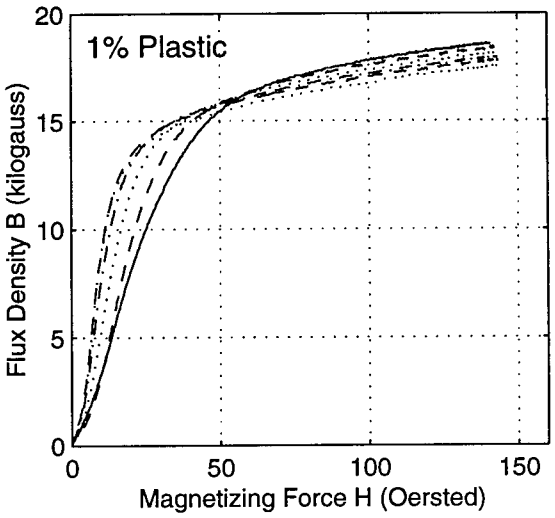

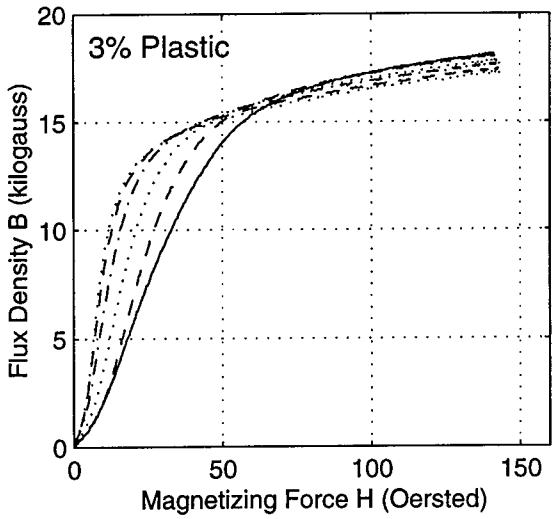

MATERIAL 24-22 (Cont'd)

Compressive Loading

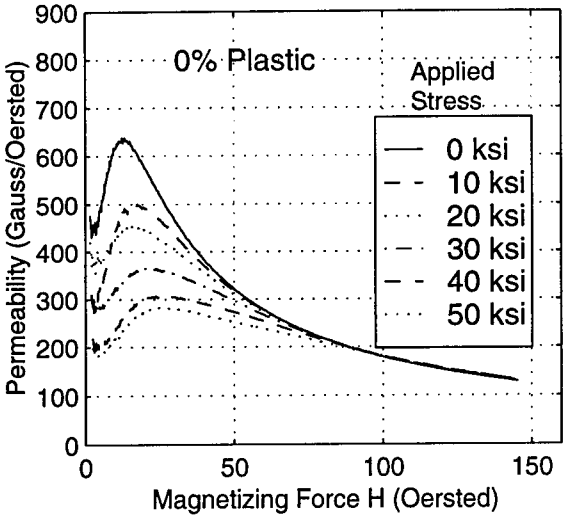

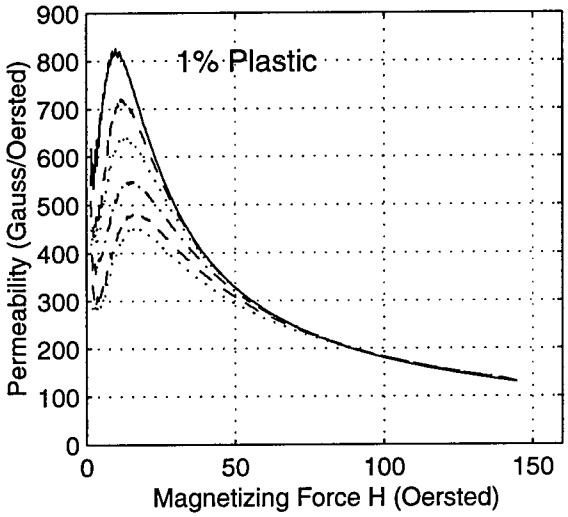

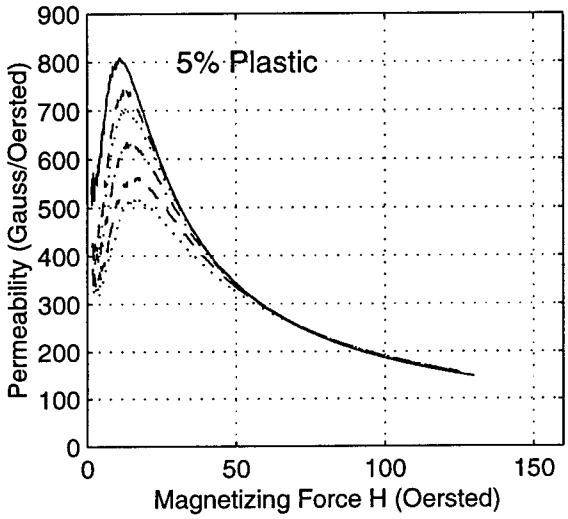

Tensile Loading

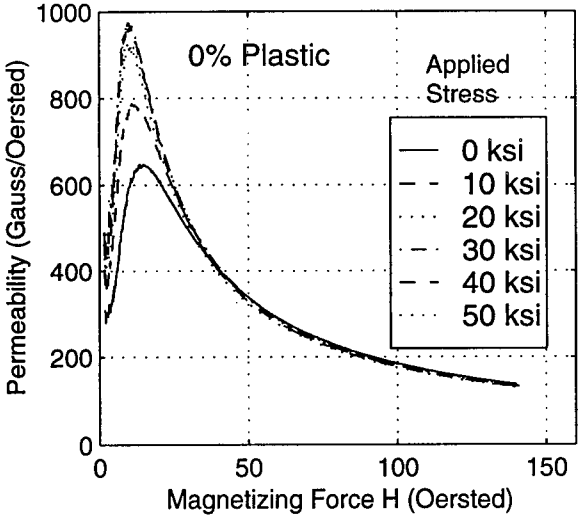

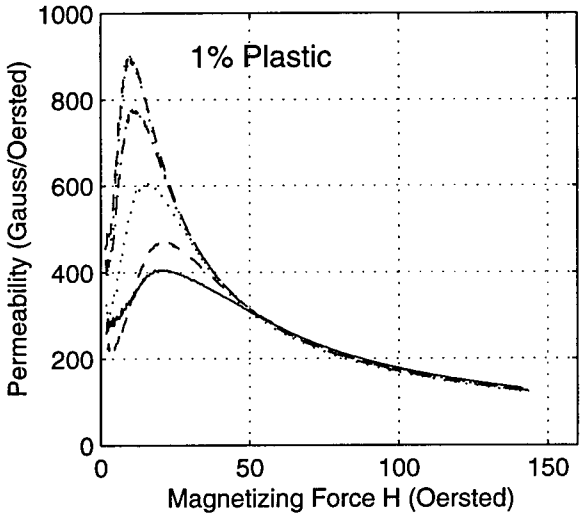

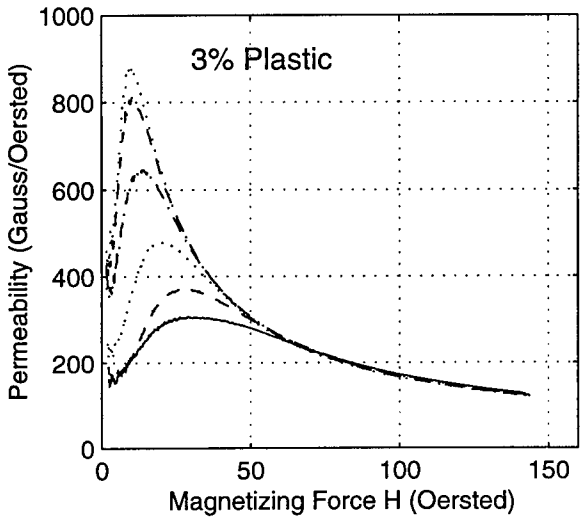

MATERIAL 24-22 (Cont'd)

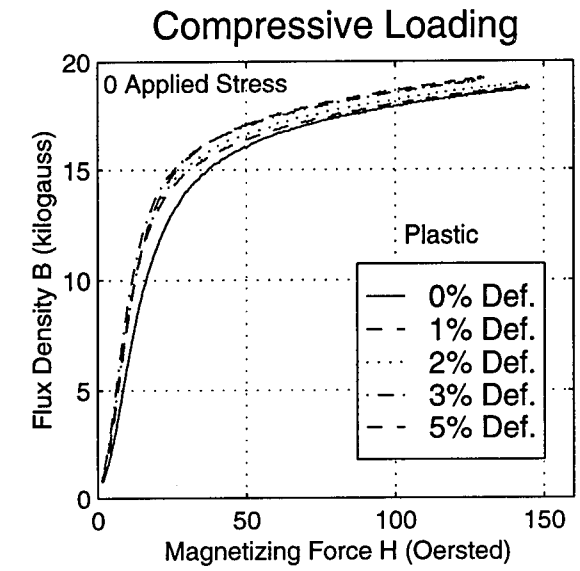

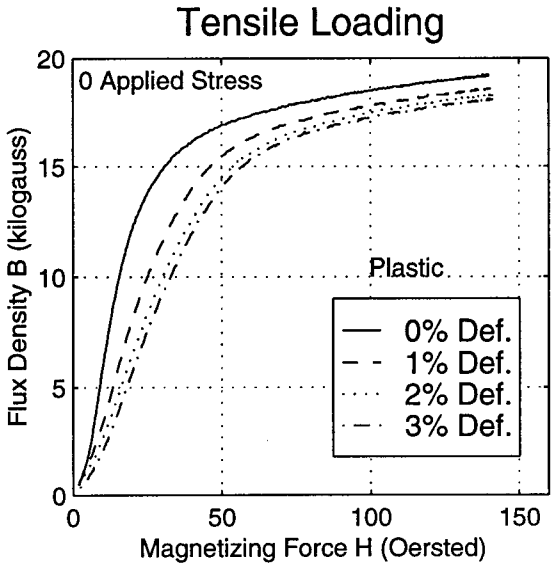

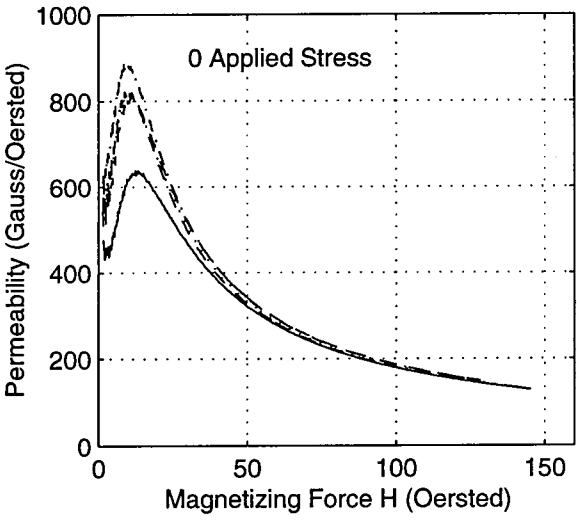

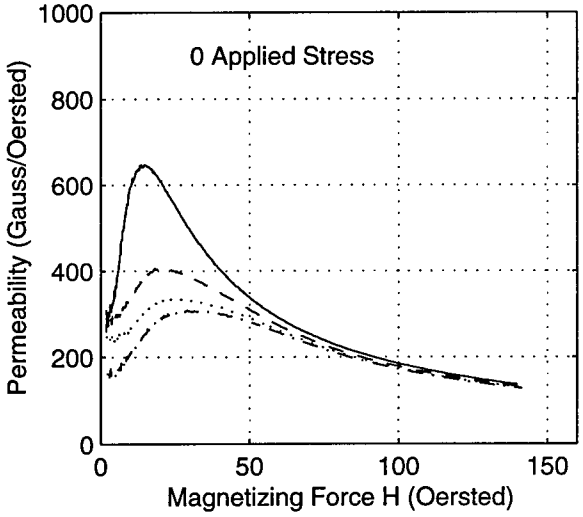

MATERIAL 24-31

Compressive Loading

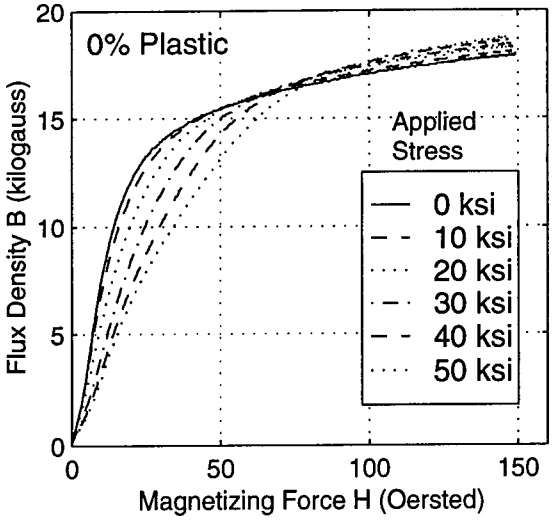

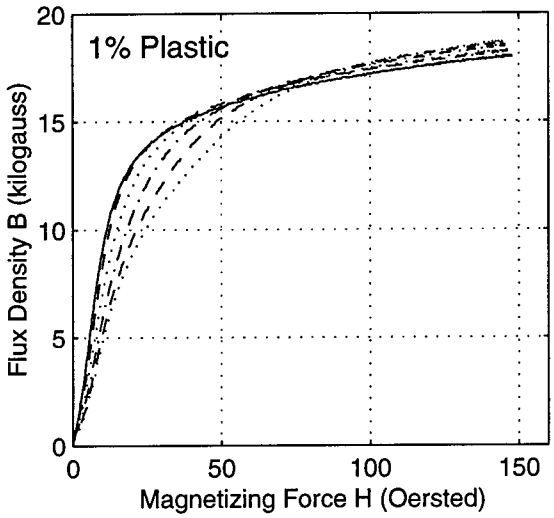

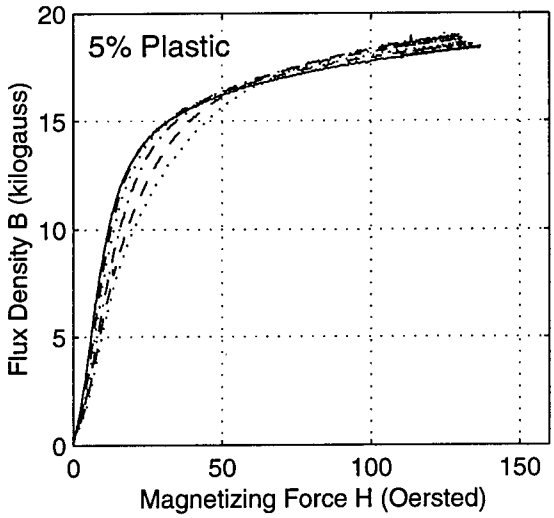

Tensile Loading

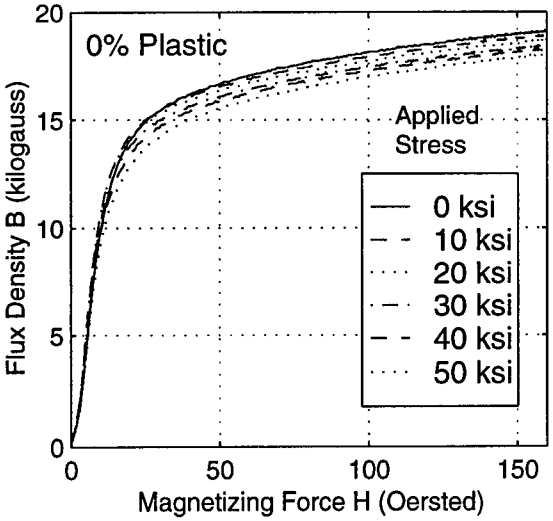

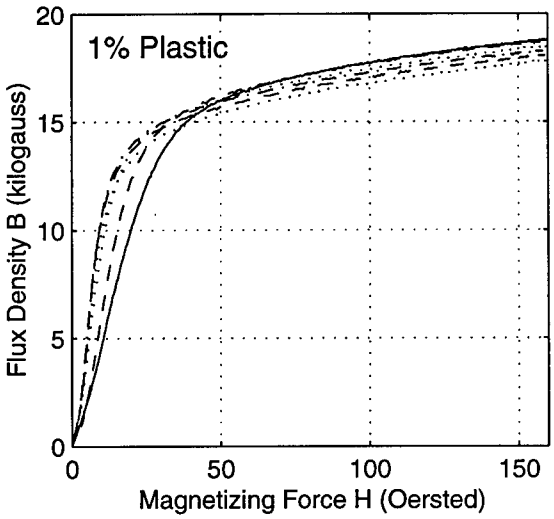

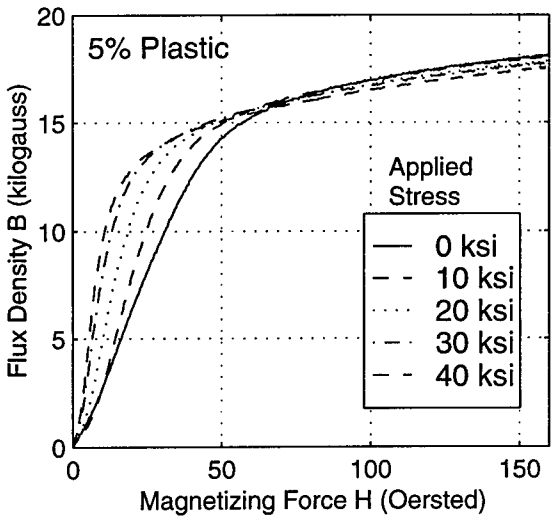

MATERIAL 24-31 (Cont'd)

Compressive Loading

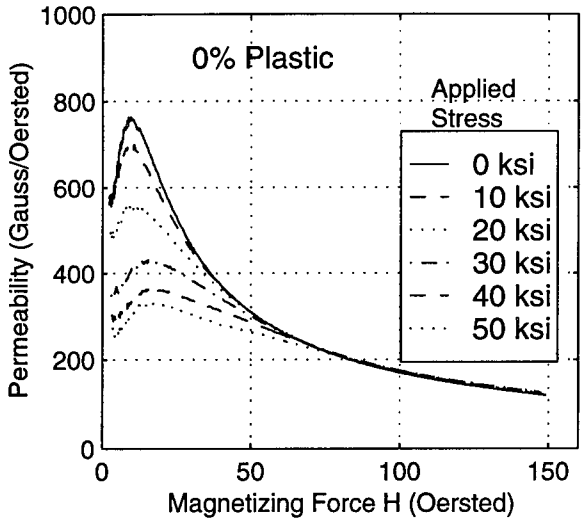

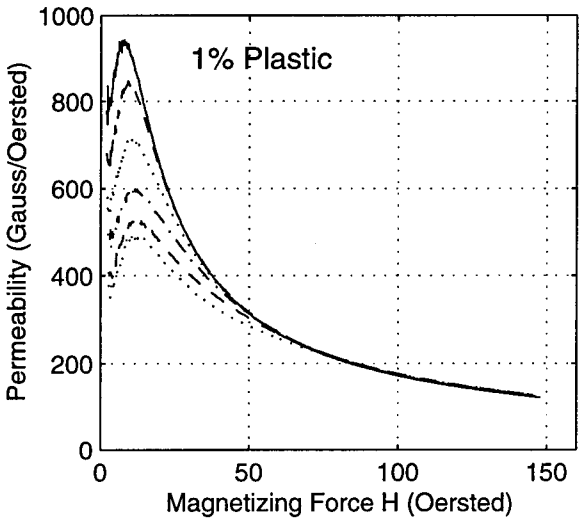

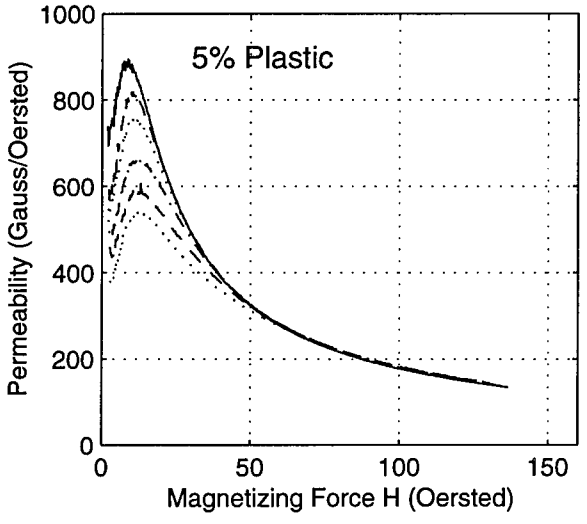

Tensile Loading

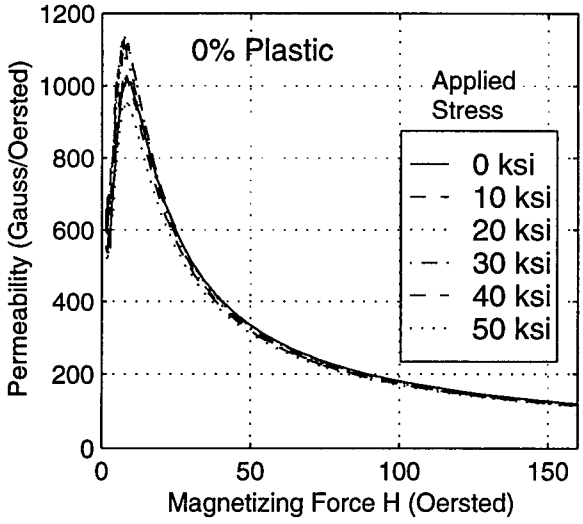

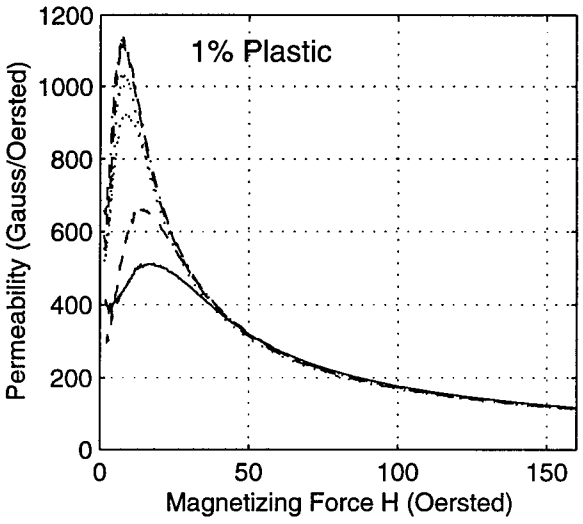

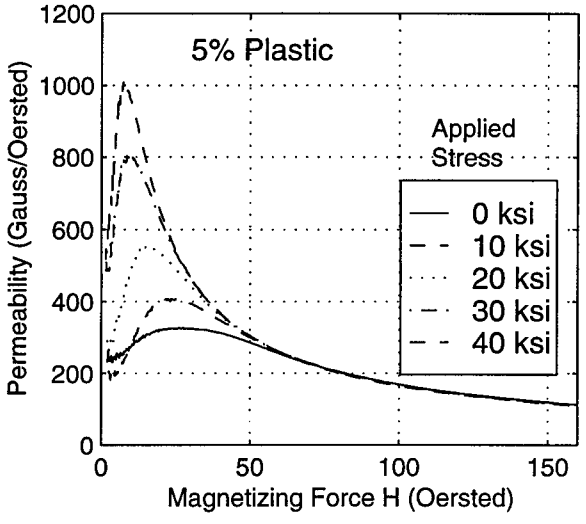

MATERIAL 24-31 (Cont'd)

Compressive Loading

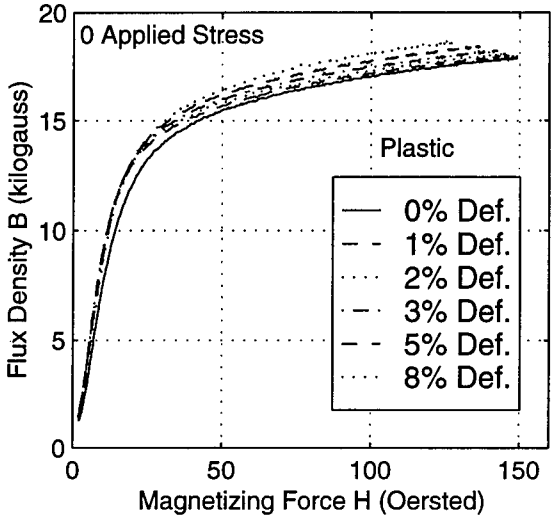

Tensile Loading

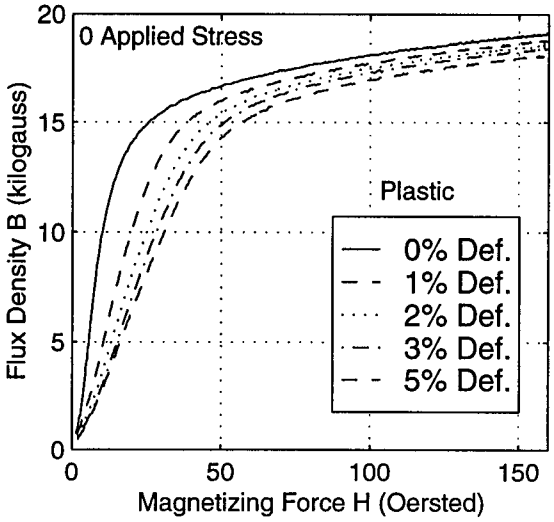

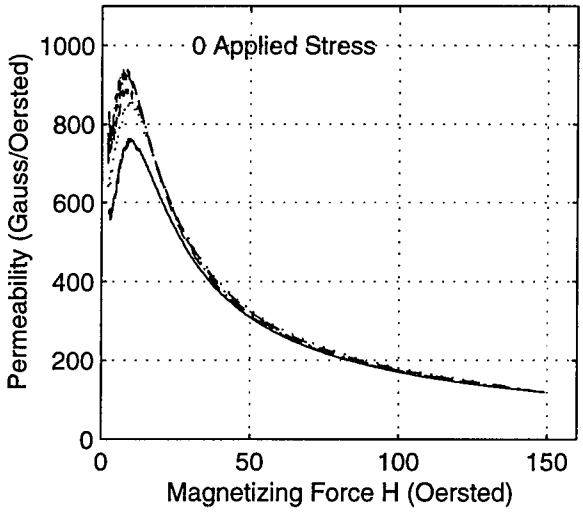

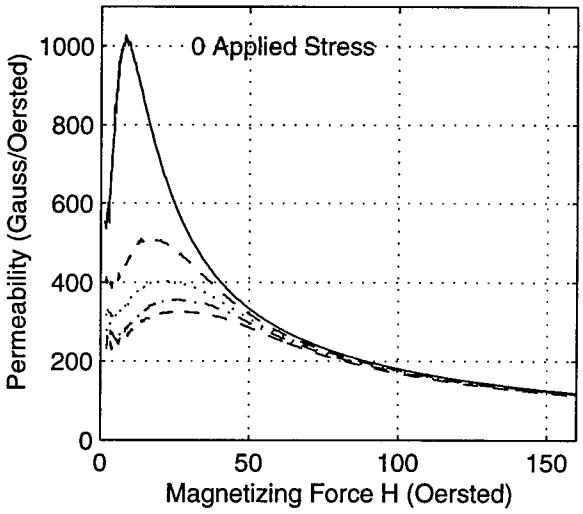

MATERIAL 24-35

Compressive Loading

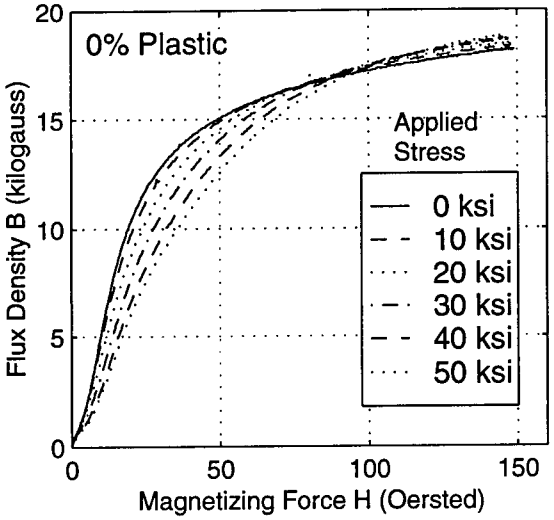

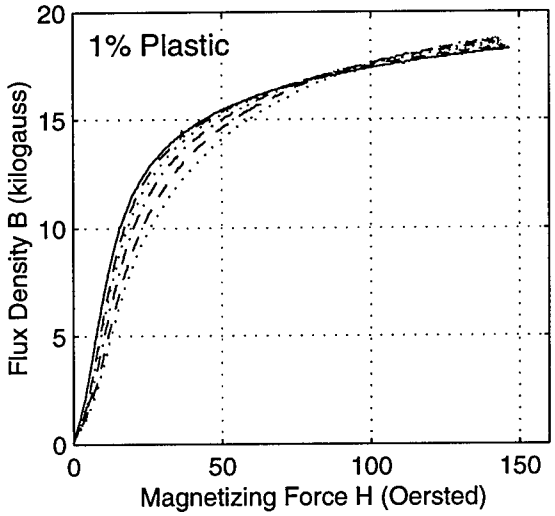

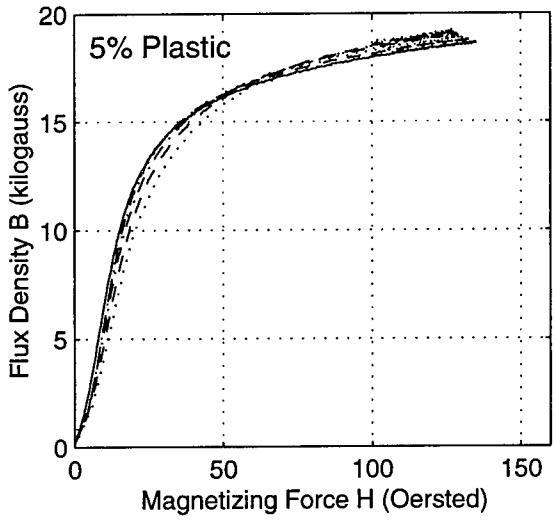

Tensile Loading

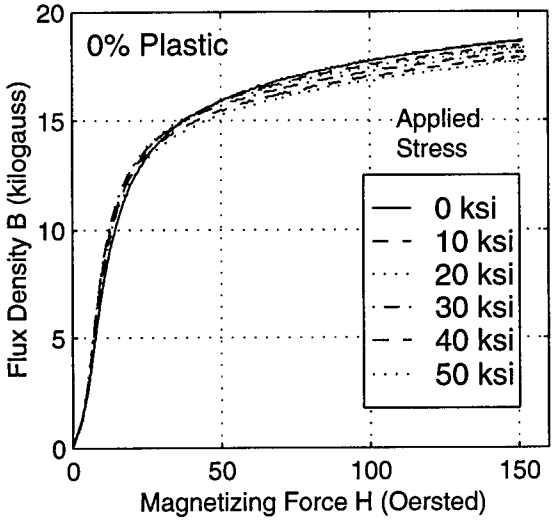

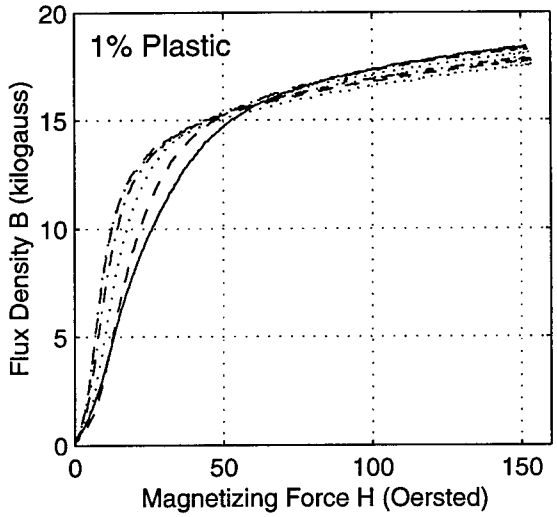

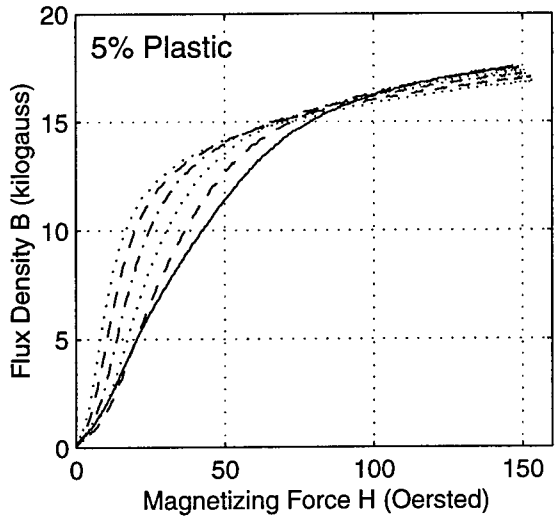

MATERIAL 24-35 (Cont'd)

Compressive Loading

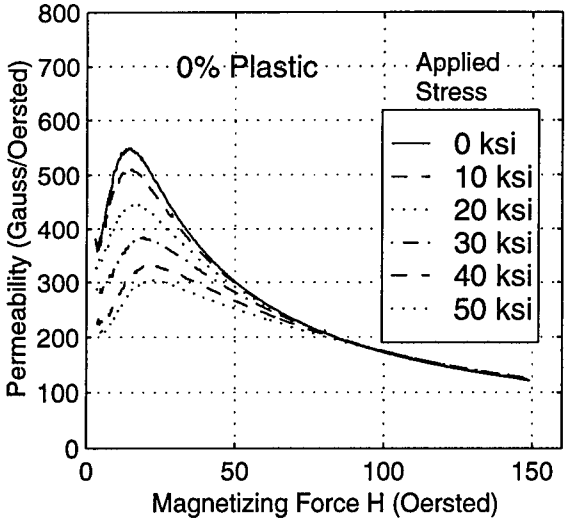

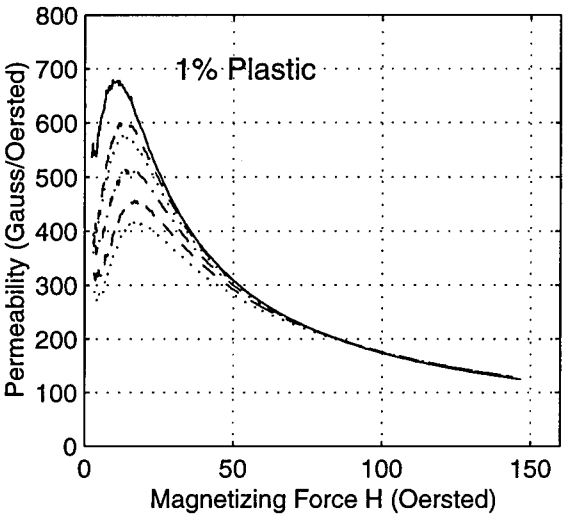

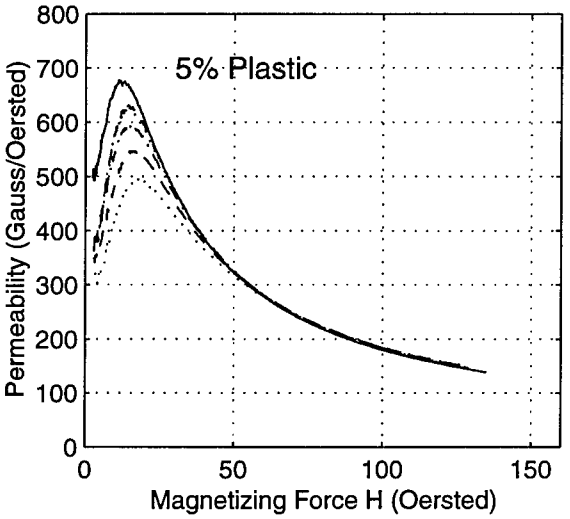

Tensile Loading

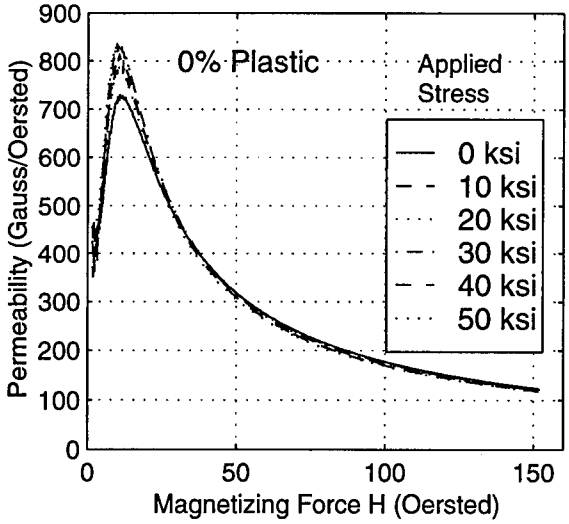

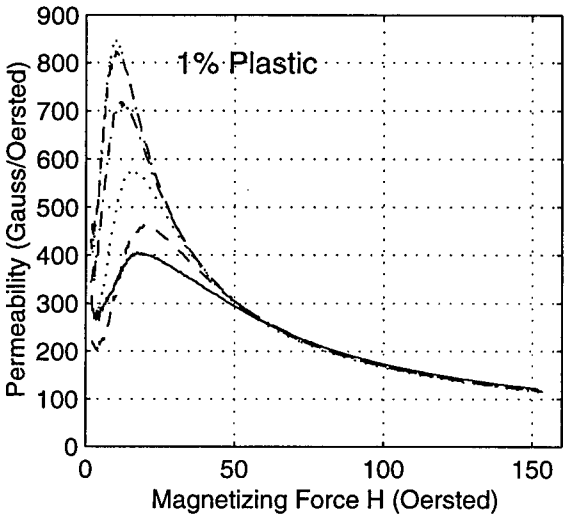

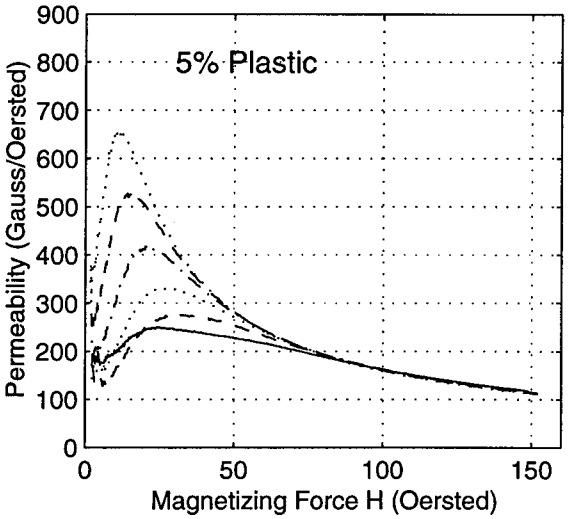

MATERIAL 24-35 (Cont'd)

Compressive Loading

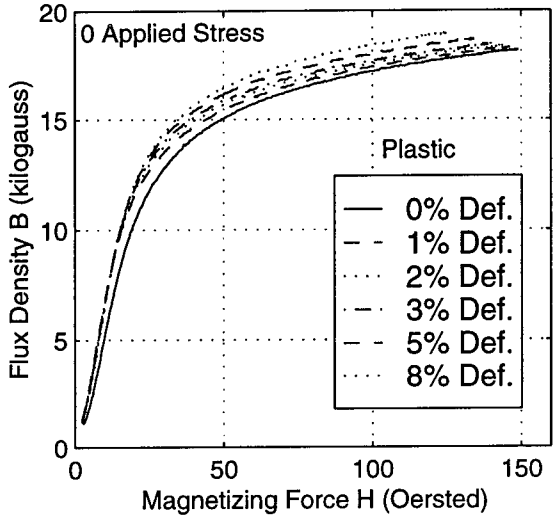

Tensile Loading

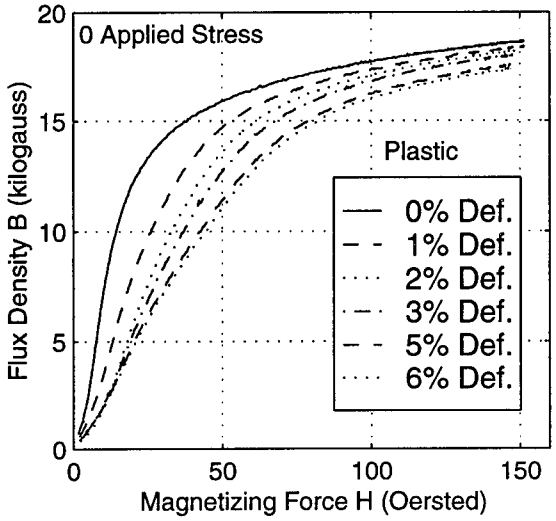

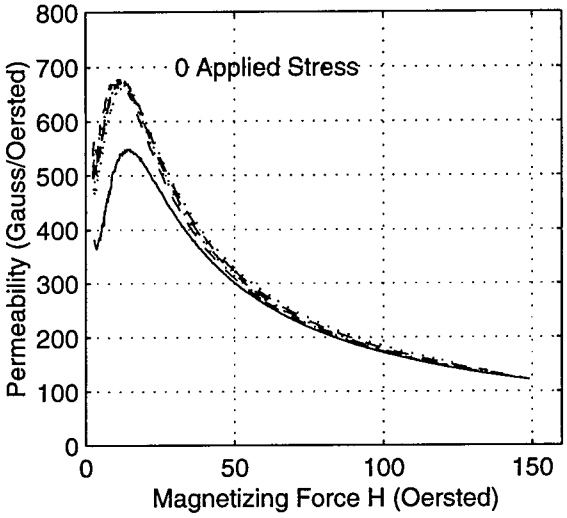

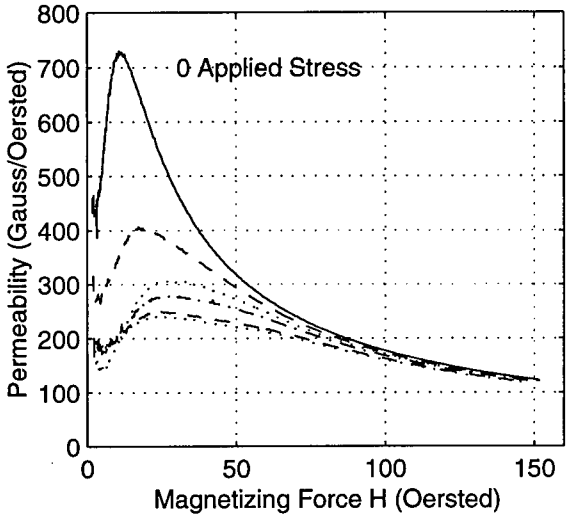

MATERIAL 24-36

Compressive Loading

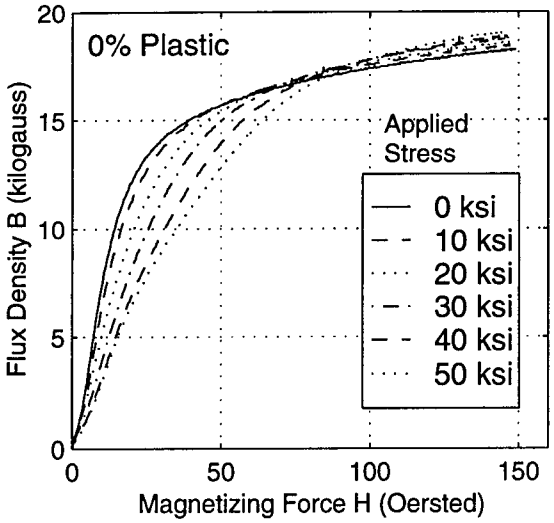

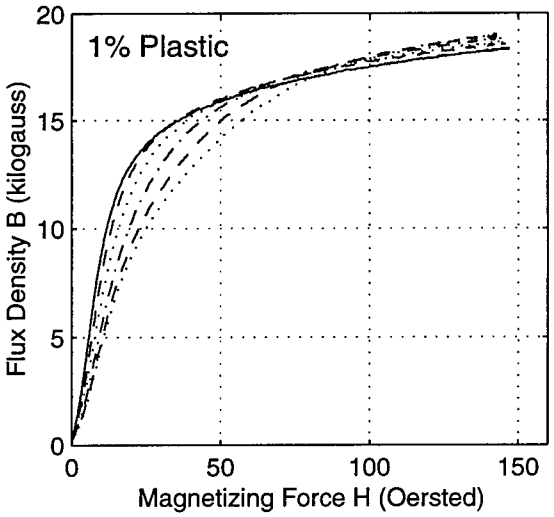

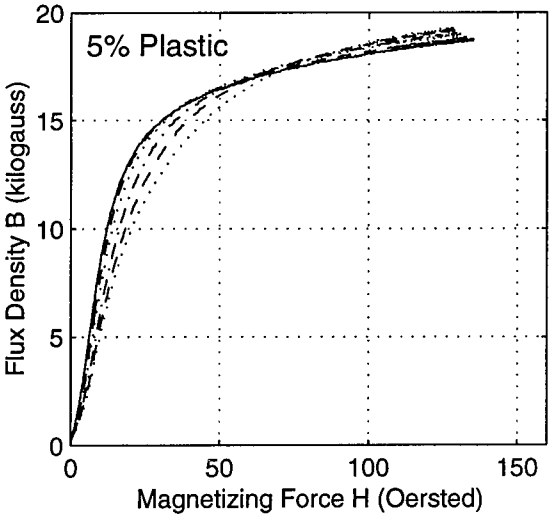

Tensile Loading

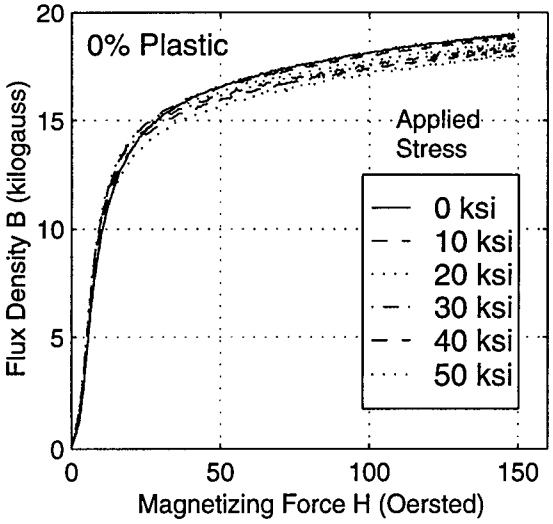

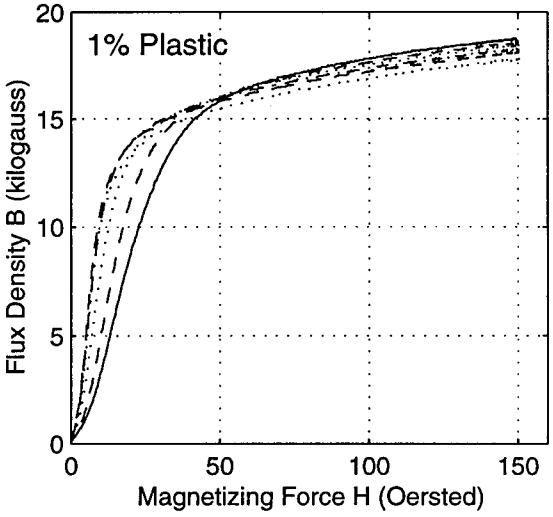

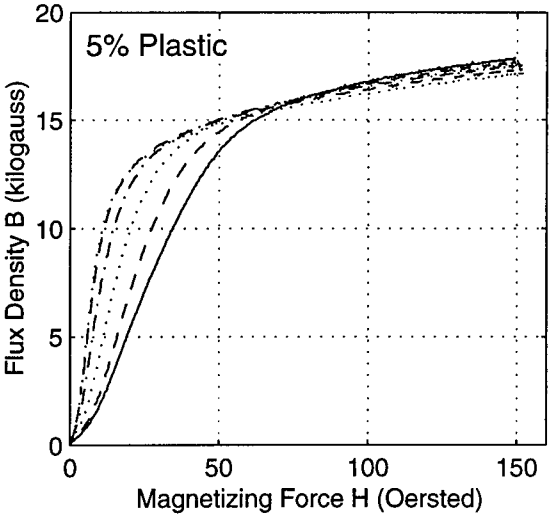

MATERIAL 24-36 (Cont'd)

Compressive Loading

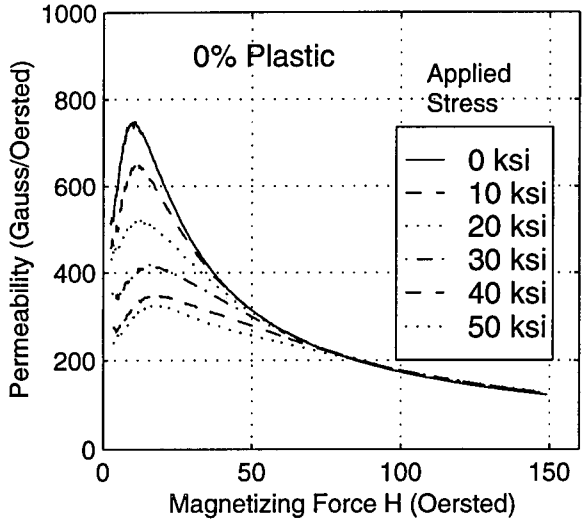

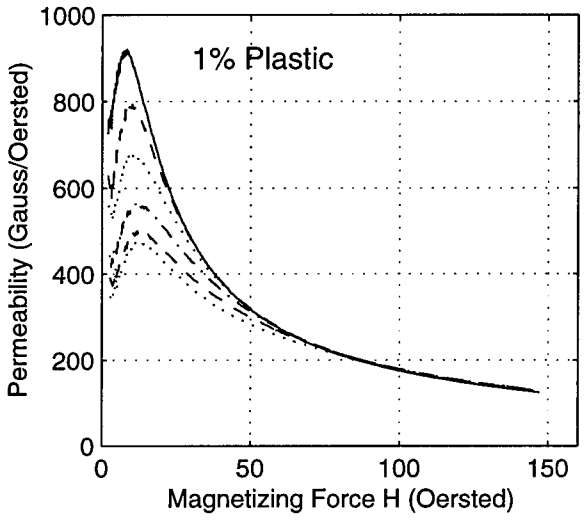

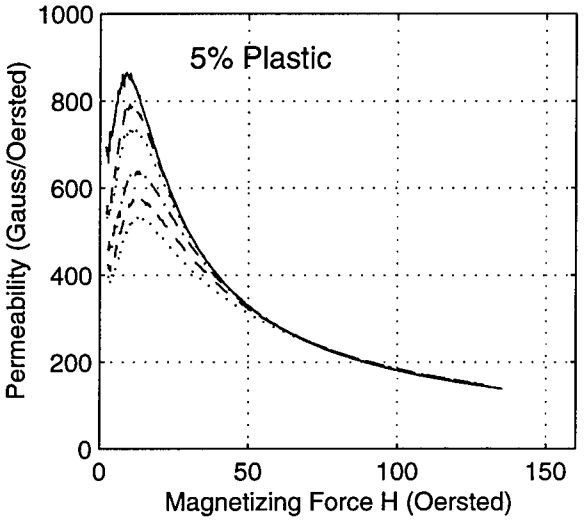

Tensile Loading

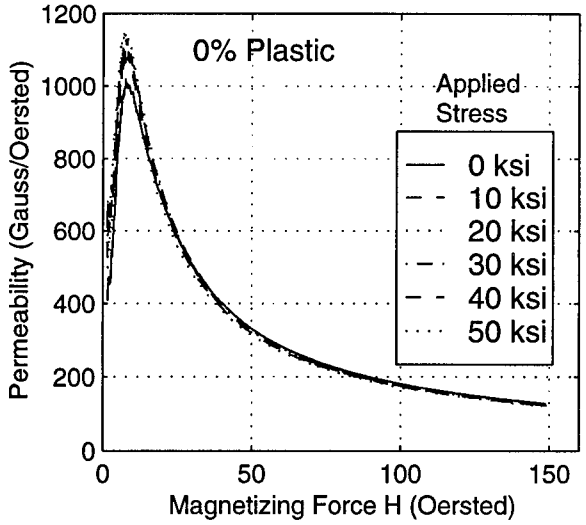

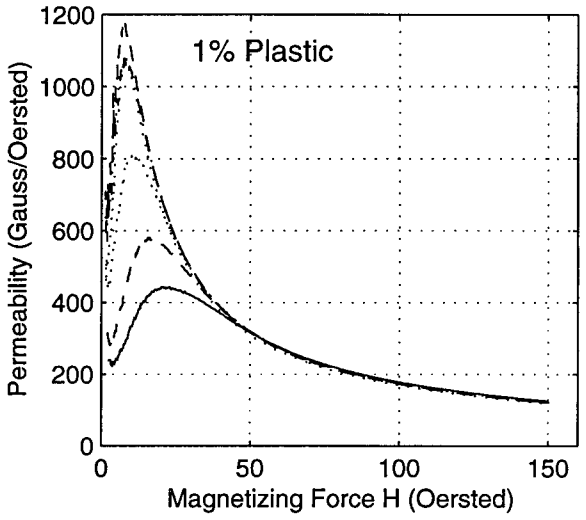

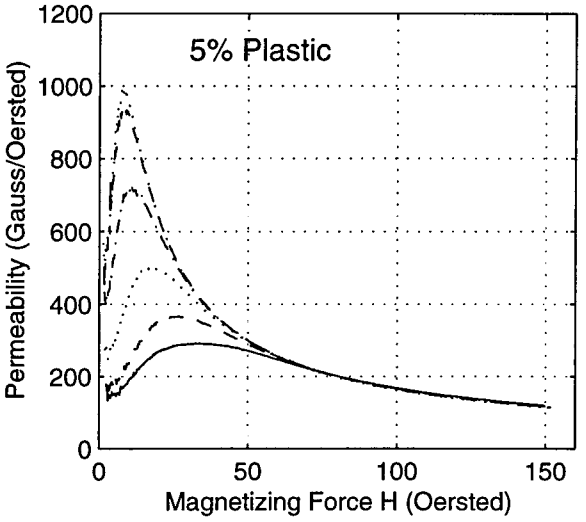

MATERIAL 24-36 (Cont'd)

Compressive Loading

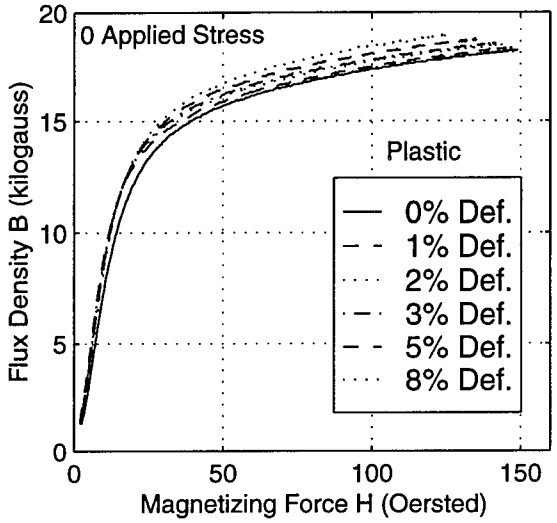

Tensile Loading

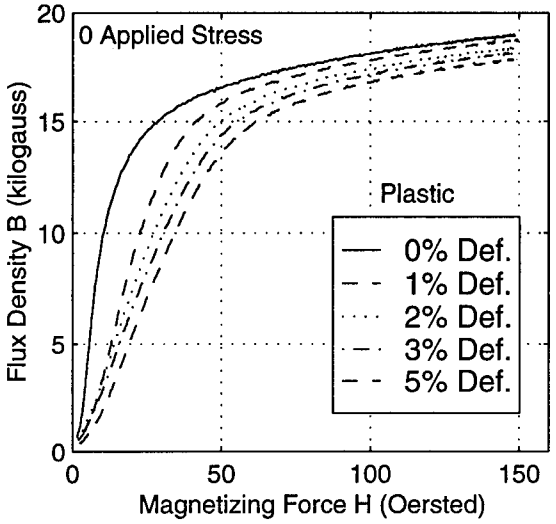

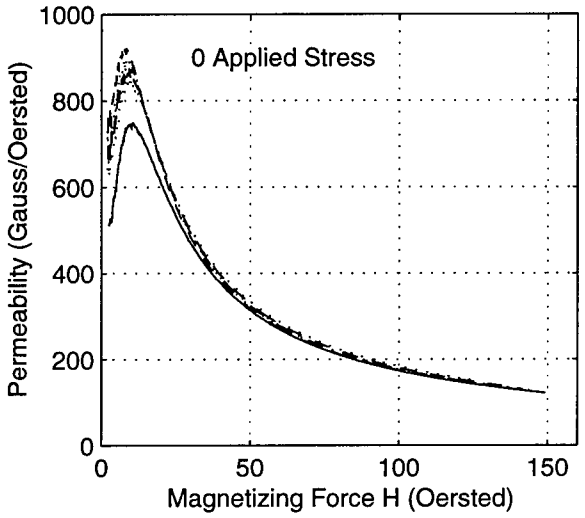

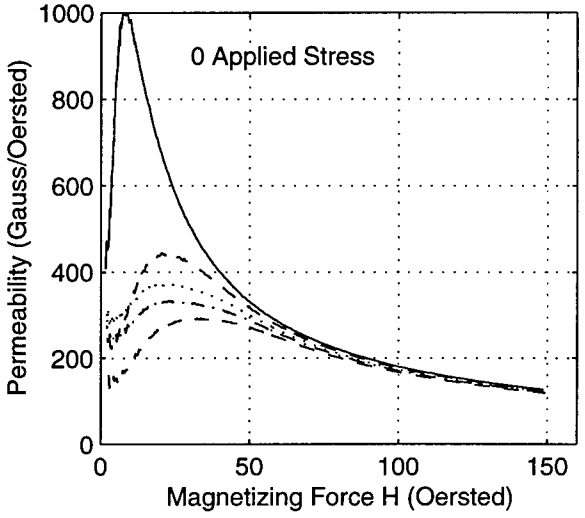

MATERIAL 24-43

Compressive Loading

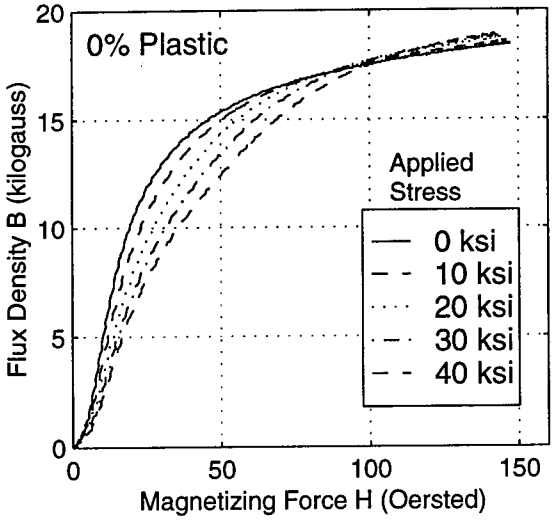

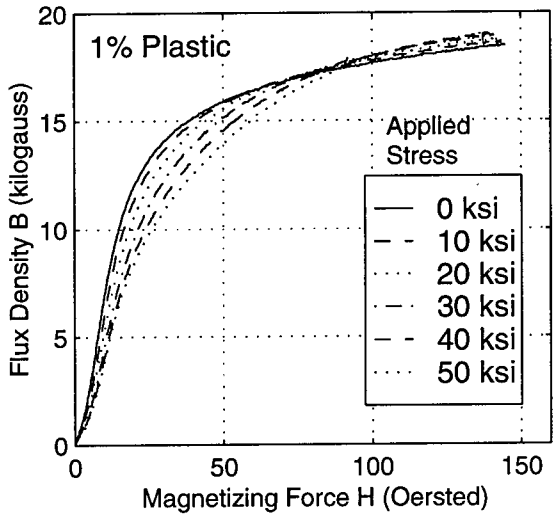

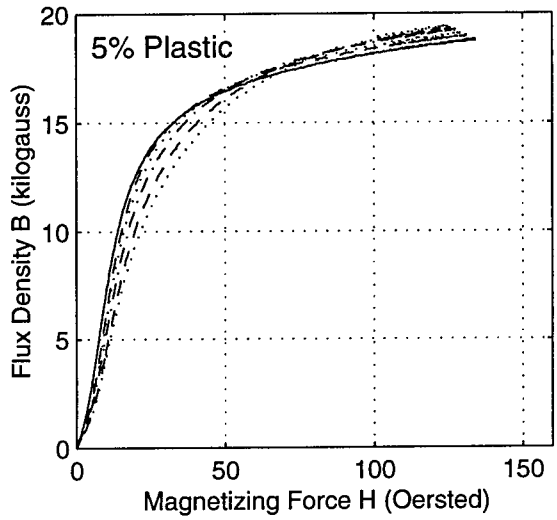

Tensile Loading

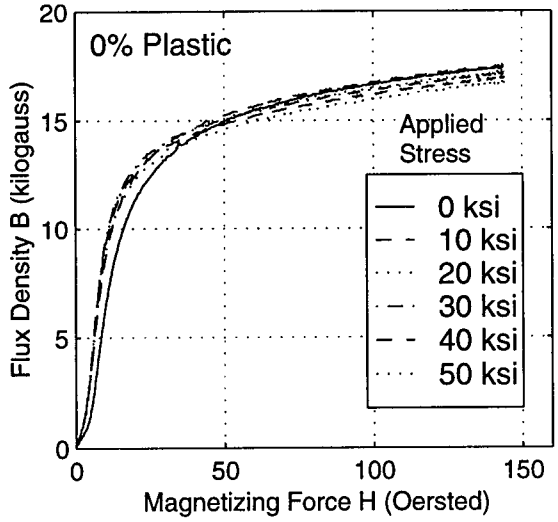

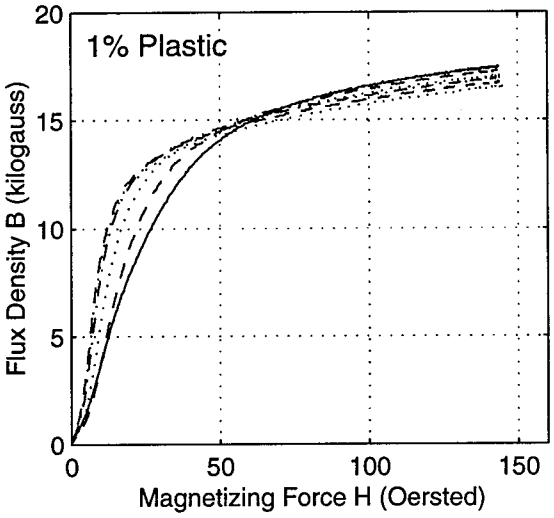

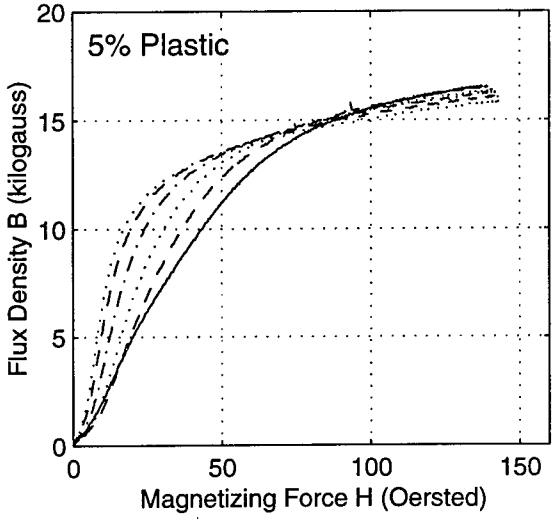

MATERIAL 24-43 (Cont'd)

Compressive Loading

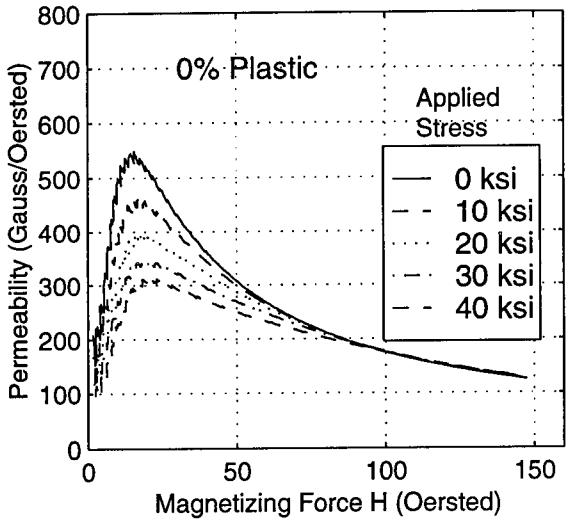

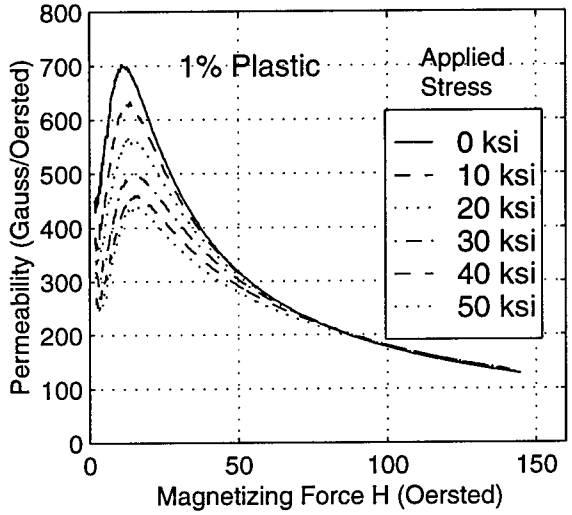

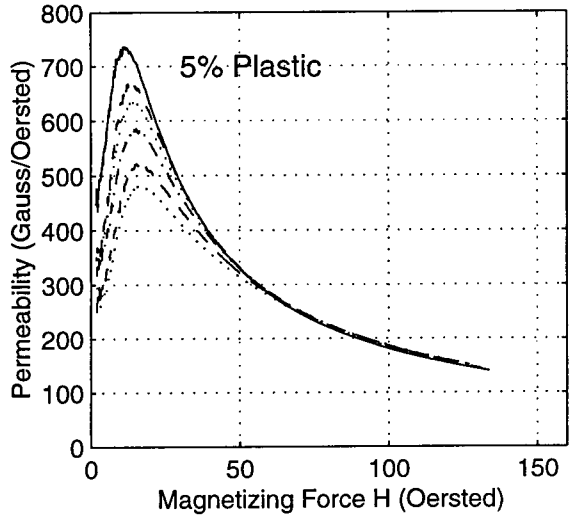

Tensile Loading

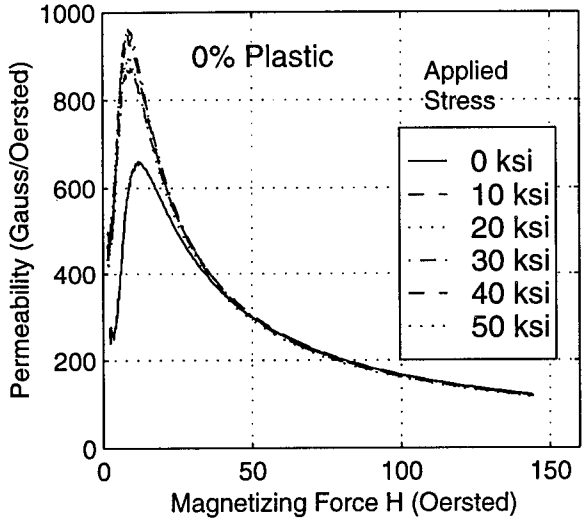

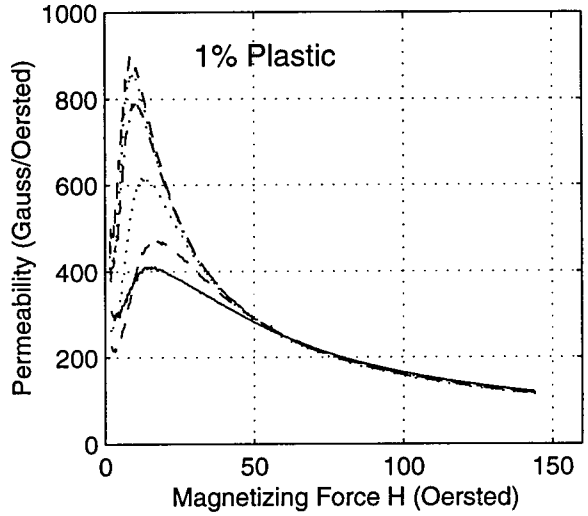

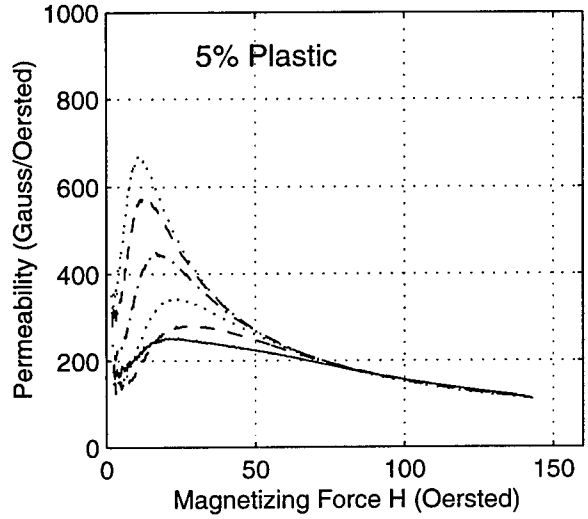

MATERIAL 24-43 (Cont'd)

Compressive Loading

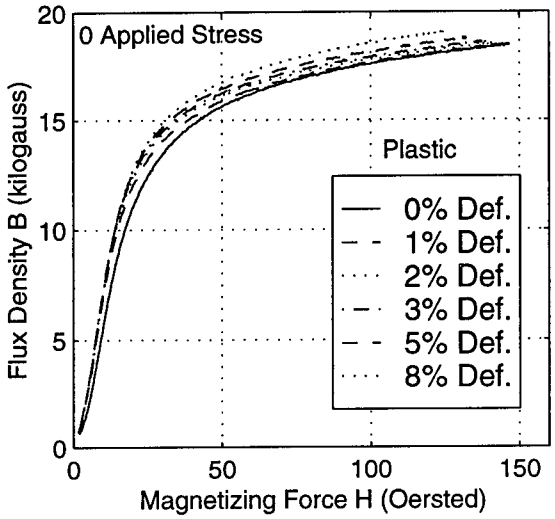

Tensile Loading